Non-Asymptotic Quantum Scattering Theory for Low-Dimensional Materials

Thesis by
Sathwik Bharadwaj

In Partial Fulfillment of the Requirements for the
Degree of
Doctor of Philosophy

WORCESTER POLYTECHNIC INSTITUTE
100 Institute Road, Worcester, Massachusetts 01609

2020

Sathwik Bharadwaj
ORCID: 0000-0001-8476-4152

Non-Asymptotic Quantum Scattering Theory for Low-Dimensional Materials

by

Sathwik Bharadwaj

A dissertation submitted to the faculty of

WORCESTER POLYTECHNIC INSTITUTE

in partial fulfillment of the requirements for the

Doctor of Philosophy

in

Physics

by

Sathwik Bharadwaj

July 2020

APPROVED:

L. R. Ram Mohan	P K Aravind
Prof. L. Ramdas Ram-Mohan Thesis Advisor	Prof. P. K. Aravind Committee Member
Germano Iannacchione	Ashwin Ramasubramaniam
Prof. Germano Iannacchione Committee Member	Prof. Ashwin Ramasubramaniam Committee Member

ACKNOWLEDGEMENTS

I am very grateful to many people who have helped me make this thesis possible. First, I would like to thank my advisor Prof. L. R. Ram-Mohan for the continuous guidance and support throughout my PhD. I appreciate the time and effort he has put to make my PhD experience productive and stimulating. I will always cherish the unique research experience I obtained under his guidance.

Over these years, I had the opportunity to work on a diverse set of collaborative projects. I would like to thank Prof. Ashwin Ramasubramaniam for his invaluable input towards the work presented in this thesis. We had numerous discussions which helped me bring many of the ideas to fruition. I also benefited a lot from stimulating interactions with Prof. John Albrecht, Prof. Leo Rodriguez, and Prof. Shanshan Rodriguez through several other projects.

I would also like to thank Prof. P. K. Aravind and Prof. Germano Iannacchione for agreeing to be a part of my thesis committee and providing useful feedback.

I express my gratitude to Prof. Tsuyoshi Ueta and the staff of Jikei University School of Medicine for the hospitality provided during my three months of stay in Japan. With Prof. Ueta, I had many engaging conversations on several topics that I plan to pursue even beyond my PhD.

I had the pleasure of interacting with several of my colleagues at the Center for Computational Nanoscience, WPI. It was a rewarding experience to pursue collaborative research with Dung Pham, Siddhant Pandey, Christopher Pierce, Muping Chen, Yuchen Wang, and Debanik Das.

I would also like to thank the staff of Academic and Research Computing team at WPI for providing the computational resources and technical support.

I would like to thank Aditi for being a constant source of support and motivation all these years.

Finally, I would like to thank Amma, Samu, and my grandparents for their love and care, and for always being supportive of my career.

ABSTRACT

Over the past few decades, solid-state devices have steered the field of nanoelectronics. The advancement in semiconductor technology has led to the development of classical integrated circuits, which follows the trend defined by Moore's law. However, in order to achieve the next generation of computing circuits, one requires to go beyond the limits of Moore's law. This has led to a revolution in the development of new quantum materials, and harnessing their physical properties. This new class of quantum materials constitutes low-dimensional systems such as semiconductor heterostructures and atomically thin two-dimensional (2D) materials. Tunability of the physical properties offered by these structures, makes them ideal candidates to host high-performance nanoelectronic circuits and quantum information platforms. In this thesis, we develop a scalable first-principles informed quantum transport theory to investigate the carrier transport properties of low-dimensional materials, and reveal their novel electronic and thermoelectric properties.

While first-principles calculations effectively determine the atomistic potentials associated with defects and impurities, they are ineffective for direct modeling of carrier transport properties at length scales relevant for device applications. Traditionally, scattering properties are obtained by applying the asymptotic boundary conditions. However, these boundary conditions do not account for the decaying evanescent mode contributions, that are crucial while determining the transport properties of low-dimensional systems. Here, we develop a novel non-asymptotic quantum scattering theory to obtain the transport properties in proximity to the scattering centers, for confined as well as open domain in one-, two- and three-dimensional systems. We then bridge this scattering theory and the $\boldsymbol{k}\cdot\boldsymbol{p}$ perturbation theory, with inputs from *ab-initio* electronic structure calculations, to construct a versatile multiscale formalism. The continuum nature of the formalism enables us to model realistic meso- and nano-scale devices.

The given formalism is applied to study electron scattering in quantum waveguides. Several interesting phenomena are revealed through our analysis. The Fano resonance profile for the transmission spectrum of both propagating and evanescent modes is observed. An enhancement of power factor far beyond the earlier proposed limits is obtained by embedding attractive impurities within the waveguide. A current rectification device is simulated, which is expected to find applications in quantum transport.

We further apply this formalism to reveal the novel electronic and thermoelectric properties of monolayer lateral transition-metal dichalcogenide (TMDC) heterostructures. We show that material inclusions in such heterostructures leads to enhancement of electron mobility by an order of magnitude larger than pristine TMDCs. The band alignment between the materials also enhances the thermoelectric figure-of-mertit (ZT) and power factor far beyond the pristine TMDCs. Our study opens new avenues for constructing ultra-efficient in-plane thermoelectric devices using lateral TMDC heterostructures.

TABLE OF CONTENTS

LIST OF ILLUSTRATIONS

Number *Page*

LIST OF TABLES

NOMENCLATURE

$\hbar$	Reduced Planck constant.
c	Speed of light in a vacuum inertial frame.
e	Charge of an electron.
h	Planck constant.
k_B	Bolzmann constant.
m_e	Mass of an electron.
1D	one-dimension/dimensional.
2D	two-dimensions/dimensional.
3D	three-dimensions/dimensional.
BCs	Boundary conditions.
DFT	Density functional theory.
DoF	Degrees of Freedom.
EPA	Envelope function approximation.
FEA	Finite element analysis.
LDA	Local-Density Approximations.
TMDC	Transition metal dichalcogenide.

Chapter 1

INTRODUCTION

1.1 Preface

Scattering phenomena are universal in their presence. The interaction between particles, and the determination of the forces between them through scattering experiments has been a central goal in understanding the physics of a system. Scattering experiments employ prepared initial states in collision phenomena and seek patterns in the final scattered states in order to deduce conclusions about the interaction properties. The scattering of waves in optical, acoustical, atomic and nuclear physics have a common methodology that has evolved into the present-day theory of scattering [1–8].

The traditional treatment of scattering considers an *ad-hoc* condition that the distance between scattering centers and the observer is asymptotically large. In Fig. 1.1, a scattering scenario is displayed. A plane wave from a source situated far from the scattering center initiates the scattering event. The outgoing waves are generated due to scattering are evaluated at a very large distance from the scattering center. At large distances, the solution wavefunction is expressed as a linear combination of the incoming and outgoing basis functions with undetermined amplitudes. A partial wave analysis is then performed in the asymptotic limit to obtain these amplitudes

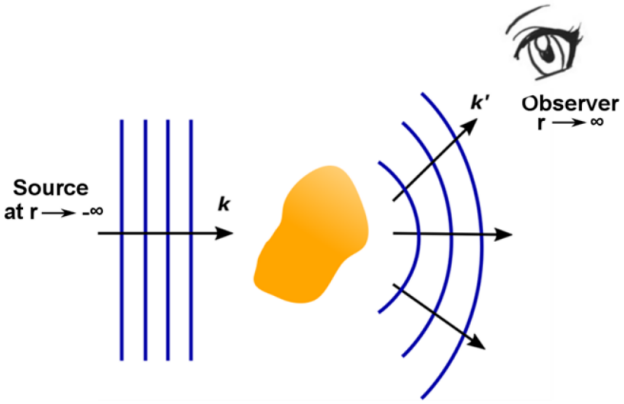

Figure 1.1: A prototypical scenario of scattering is depicted. Incoming plane wave from a source at infinity generates the outgoing waves. These outgoing waves are evaluated in the asymptotic limit.

in terms of the phase-shift parameters. For example, in the three-dimensional (3D) open domain, the wavefunction is expressed in terms of the spherical Hankel functions of the first kind $h_m^{(1)}(kr)$ [9]. We can then easily deduce the scattering amplitudes since all the Hankel functions have the same asymptotic form given by e^{ikr}/r, which represents the outgoing spherical wave [10] . Lord Rayleigh [11] developed this method for the first time in the context of acoustic scattering , and later it was extended to quantum mechanics by Faxen and Holtsmark [12].

In the asymptotic limit, only the radial component of the scattered current contributes to the cross-section. As a result, information about the angular current contributions [8], and the distance between target and observer is lost in this analysis. In reports by Dai *et al.,*[13, 14] it has been shown that a rigorous scattering treatment without the asymptotic approximations will introduce a modification factor to the scattering amplitude, and an additional phase factor to the scattered wavefunction. Moreover, we can show that in multiband scattering processes, the wavefunction will have contributions from not only the propagating waves, but also from the exponentially decaying evanescent waves [72]. This will be particularly prevalent in transport across heterointerfaces formed between the materials.

There has been a long history of providing a variational approach to scattering; Schwinger pioneered these efforts [16] while solving for electromagnetic fields in inhomogeneous waveguides for radar applications. In Schwinger's formalism, all the evanescent contributions vanish at the asymptotic limit, providing a closed form expression for the scattering phase shift [17]. Kohn [18], Rubinow [19], and Hulthén [20], have proposed variational methods for quantum systems involving expansion in global basis functions which satisfy asymptotic BCs. The variational parameters are determined by solving integral equations which are often difficult to evaluate. Occasionally we may encounter spurious resonance-like behavior [21]. Moreover, global basis functions do not have the flexibility of local finite-element interpolations to conform closely to the actual solution. Hence, their variational minima are always above the value obtained for a local basis set. The Schwinger variational method [22, 23] expresses the scattering T-matrix in terms of two square-integrable wavefunctions which satisfy the Lippman-Schwinger equation [24]. Here again global wavefunctions are used in this spectral basis approach, and the earlier comments apply to this case as well. A synopsis of this line of development has been given by Nesbet [25], and Adhikari [26]. Moreover, due to the asymptotic BCs used, these methods are not applicable to domains limited to nanoscale structures. They

cannot capture the presence of evanescent modes even when the defect potential is of finite range.

The works in this thesis develop a non-asymptotic description for quantum scattering theory and couch it in a fully variational framework that is particularly appropriate for meso- and nano-scale condensed matter systems. We re-examine aspects of preparing initial states and detecting the final states. The application of boundary conditions, the requirements of (probability) current conservation, the determination of decaying evanescent modes, and the near-field solutions are studied. Most of the nontrivial examples in scattering requires to go beyond purely analytical considerations. A detailed investigation of scattering effects in materials with our methods allow us to accurately predict the experimental outcomes.

Nanoelectronic devices based on low-dimensional materials offers avenues to construct integrated circuits beyond the limits of Moore's law [27, 28]. Atomically thin monolayers such as graphene [29], silicene [30], phospherene [31], transition metal dichalcogenides (TMDC) [32–34] have all been explored to construct high-performance field effect transistors, and these two-dimensional (2D) materials have shown great potential to succeed silicon in next generation computers. Accurate prediction of the transport properties in these materials is a crucial challenge to overcome before they can be used in practical devices [27].

Electron scattering due to imperfections, impurities, and phonons determine the carrier dynamics in materials. Carrier transport properties can also be engineered by creating potential patterns and quantum confinements, such as through the application of local potentials via STM/AFM tips [35, 36], surface functionalization by organic molecules [37, 39, 40], or through the geometrical confinement in heterostructures.

First-principles calculations such as the density functional theory (DFT) are highly effective in obtaining the electronic band structure, phonon dispersion relations, and the local potential distributions due to defects and impurities associated with the materials. In Fig. 1.2, as an example, we have displayed the contour plot of the potential distribution of a graphene monolayer with a circular vacancy, obtained using DFT calculations. This example shows that DFT can be used to precisely obtain the potential distributions in low-dimensional materials. Realistic devices in low-dimensional materials will constitute thousands of atoms. First-principles calculations are computationally demanding to model such devices, and will not scale accurately to determine the transport properties at such length-scales. Atomistic

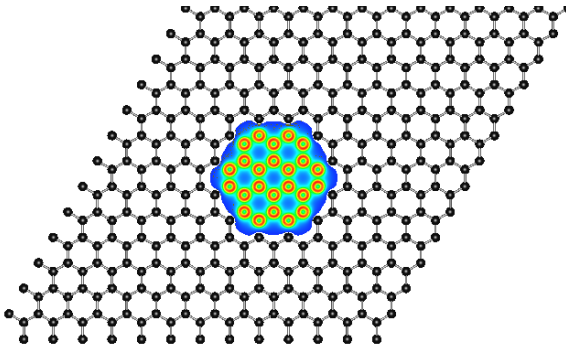

Figure 1.2: A contour plot of the potential distribution on a graphene monolayer with a circular vacancy is displayed. The potential distribution is obtained using DFT calculations.

tight-binding models are also too complex for simulating any device-scale applications. For example, complexity in modeling the transport properties of newly discovered bilayer 2D materials is significantly amplified, as more than 10^4 atoms contribute to the correlated behavior at magic angles [38]. Devices formed in materials typically constitute hundreds to thousands of atoms. In this thesis, we construct a multiscale quantum transport framework by bridging the novel non-asymptotic scattering theory with the $\boldsymbol{k} \cdot \boldsymbol{p}$ perturbation theory, supplemented with inputs from first-principles calculations. This formalism can easily scale into device dimensions. Hence it will be very useful to simulate nanoelectronics circuits in a variety of low-dimensional materials.

1.2 Overview of the thesis

In this section, we give a brief outline of the contents discussed in each of the chapters of this thesis.

Chapter 2

The non-asymptotic quantum scattering theory is developed for carrier scattering in one-dimensions. We describe the construction of absorbers around the scattering center to reduce the scattering BCs to simpler Dirichlet BCs. An absorption parameter is introduced and increased smoothly within the absorber, which leads to the damping of the wavefunction. Once we enclose the scattering region with absorbers, an electron source is introduced to initiate the scattering event. The differential equation developed here is solved using the action integral formulation, to provide a variational principles framework. Accuracy of our method is studied through a well known example of an electron scattering in double barriers.

Chapter 3

We develop the non-asymptotic quantum scattering theory in electron waveguides. We show that Cauchy (mixed) BCs are required to put the scattering theory into an action integral formulation. These complex BCs are reduced to simpler Dirichlet BCs by introducing totally absorbing "stealth regions." Material properties of these enclosing regions are optimized to give decaying solutions, so that the scattering amplitudes vanish at the finite boundaries. With the active scattering region now surrounded by absorbers, we construct an "electron antenna" to provide incident waves. In two-dimensional quantum waveguides, we obtain the scattered wavefunction for geometrically complex scattering centers, showing the flexibility of our method. The modal decomposition of reflected and transmitted waves allows us to obtain transmission coefficients for both propagating and evanescent modes. Using group theory, we develop selection rules for the scattered modes depending on the symmetry of the potential. Our method outperforms the limitations of traditional perturbative estimates, transfer-matrix, S-matrix discretizations, and other schemes to provide a complete non-asymptotic variational description for electron transport in quantum waveguides.

Chapter 4

We show that in electron waveguides, the Fano resonance profile associated with propagating modes have their analogs with evanescent modes as well. This is found to be an unusual and a universal effect for any attractive potential. Further, we show that quantum dots or attractive impurity potentials embedded in the interior of a quantum waveguide yields significantly large Seebeck coefficient (thermopower) and power factor. Hence, they are good candidates for enhancing the thermoelectric energy conversion efficiency. We study the effect of waveguide tapering on transport properties, and the effect of curvature on the transmission coefficients. We propose a nanoscale current rectification device in two-dimensions using tapered electron waveguides.

Chapter 5

We develop a scalable first-principles-informed quantum transport theory to investigate the carrier transport properties of 2D materials. We derive a novel non-asymptotic quantum scattering framework in 2D open domain to obtain the transport properties in proximity to the scattering centers. We then bridge our scattering framework with $\boldsymbol{k}\cdot\boldsymbol{p}$ perturbation theory, with inputs from *ab-initio* electronic

structure calculations, to construct a versatile multiscale formalism. The continuum nature of our formalism enables us to model realistic devices, scaling from hundreds to thousands of atoms. The given formalism also preserves the distance information between the observer and target, and accounts for the crucial contributions of decaying evanescent modes across heterointerfaces. We apply this formalism to study electron transport in lateral transition-metal dichalcogenide (TMDC) heterostructures and show that material inclusions can lead to an enhancement of mobility by an order of magnitude larger than pristine TMDCs.

Chapter 6

In this chapter, we study the thermoelectric performance of lateral TMDC heterostructures within a multiscale quantum transport framework. Both *n*-type and *p*-type lateral heterostructures are considered for all possible combinations of semiconducting TMDCs: MoS_2, $MoSe_2$, WS_2, and WSe_2. The band alignment between the materials is found to play a crucial in enhancing the thermoelectric figure-of-mertit (ZT) and power factor far beyond the pristine TMDCs. In particular, we show that the room-temperature ZT value of *n*-type WS_2 with WSe_2 triangular inclusions is five times larger than the pristine WS_2 monolayer. *p*-type $MoSe_2$ with WSe_2 inclusions is also shown to have a room-temperature ZT value about two times larger than the pristine $MoSe_2$ monolayer. The peak power factor values calculated here, are the highest amongst the gapped 2D monolayers at room temperature. Hence, we show that the 2D lateral TMDC heterostructures opens new avenues to construct ultra-efficient in-plane thermoelectric devices.

Chapter 7

In this chapter, we set up the framework to construct the non-asymptotic quantum scattering theory in 3D open domain. In 3D, we consider a spherical source, and the absorber to be a spherical shell. This framework allows us to model transport properties of devices hosted in bulk materials as well. By combining the methods developed in these chapters we achieve a scalable first-principles-informed quantum transport framework for simulating 1D, 2D, and 3D nano-devices.

Chapter 8

Concluding remarks are presented in this final chapter.

Chapter 2

SCATTERING IN ONE-DIMENSION

In this chapter, the non-asymptotic scattering theory is described for the simplest case of carrier scattering in one-dimensions. In Sec. 2.1, we describe the construction absorbers around the scattering center to simplify the boundary conditions, and define the region for computation. An absorption parameter is introduced and increased smoothly within the absorber, which leads to the damping of the wavefunction. This ensures that there is no reflection due to the absorbers. A procedure for including a source, *i.e.* an antenna, in the active region is also described in the same section. The differential equation developed here is solved through a generalized variational approach based on discretization of the action integral, described in Sec. 2.2. Concluding remarks are given in Sec. 2.3.

2.1 Boundary conditions: sources and absorbers

Let us briefly discuss scattering from a standard one-dimensional (1D) rectangular barrier and the corresponding boundary conditions (BCs). We consider an incoming plane wave with a given energy E and an amplitude a from a source at $x = -\infty$ (see Fig. 2.1). The reflected and transmitted wavefunctions are given by

$$\begin{aligned} \psi_1 &= ae^{ikx} + r\, e^{-ikx}, \\ \psi_3 &= te^{ikx}, \end{aligned} \tag{2.1}$$

where the wavevector $k = \sqrt{2m^*E/\hbar^2}$, and m^* is the effective mass of an electron.

We obtain the Cauchy (mixed) BCs at x_a and x_b that are given by

$$\begin{aligned} \left[\frac{d\psi_1(x)}{dx} + ik\psi_1(x)\right]_{x=x_a} &= 2ikae^{ikx}\Big|_{x=x_a}, \\ \left[\frac{d\psi_3(x)}{dx} - ik\psi_3(x)\right]_{x=x_b} &= 0. \end{aligned} \tag{2.2}$$

In numerical calculations, discretization of the scattering boundary leads to inaccuracies and a non-zero reflection from the boundary. Moreover, such BCs have to be applied at each point on the boundary which is cumbersome in 2 and 3 dimensions. This is formally resolved in the usual formulation by going to the asymptotic regime, at the price of having a larger scattering region and sacrificing the evanescent modes

in multiband wavefunctions. We can simplify the Cauchy BCs to Dirichlet BCs by introducing totally absorbing stealth regions as shown in Fig. 2.2.

We consider a complex electron effective mass

$$\overline{m} = m^* \left(1 + i\, \alpha(x)\right), \tag{2.3}$$

where $\alpha(x)$ is a cubic Hermite interpolation polynomial [41] varying smoothly from 0 to α_{max} within the stealth region and equal to 0 in the active (scattering) region. Let $\alpha(x_a) = \alpha(x_b) = 0$ and, $\alpha(x_L) = \alpha(x_R) = \alpha_{max}$ as shown in Fig. 2.3. The wave equation within stealth regions is given by

$$\frac{d}{dx}\left(\frac{1}{(1 + i\alpha(x))}\frac{d}{dx}\psi(x)\right) + k^2(1 + i\alpha(x))\psi(x) = 0. \tag{2.4}$$

Solutions to the above equation will have highly damped behavior due to suitably chosen $\alpha(x)$. Therefore we can ensure Dirichlet BCs on the outer boundaries of such stealth regions at $\psi(x_L) = \psi(x_R) = 0$.

No-reflection condition at the stealth interface

From optics we know that any abrupt interfaces give rise to reflections. Fabry-Pérot interference effects are observed when we have multiple interfaces [42]. The stealth regions are designed to simplify the BCs, and should not alter the physics within the active region. Hence we fix the parameters such that there is no reflection from any wave incident on the stealth interface.

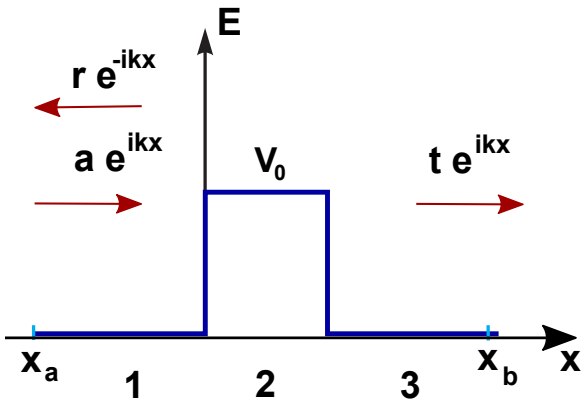

Figure 2.1: A schematic diagram of scattering by a 1D barrier of height V_0 is shown. We consider an incoming plane wave with an amplitude a and energy E. The corresponding wavevector is $k = \sqrt{2m^*E/\hbar^2}$. Here, r and t are the reflection and transmission amplitudes, respectively.

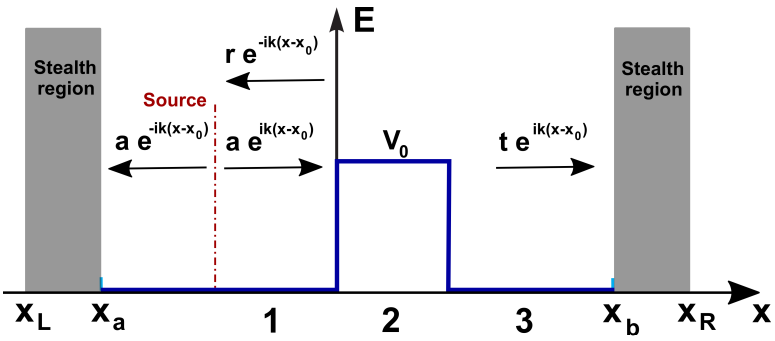

Figure 2.2: Scattering through a 1D barrier of height V_0 with stealth regions on either side of the barrier is shown. We consider a source at $x = x_0$ within the active region which injects an incoming wave with an amplitude a and the energy E in either direction. The corresponding wavevector is $k = \sqrt{2m^*E/\hbar^2}$. Here, r and t are the reflection and transmission coefficients, respectively.

In Fig. 2.4, we consider a 1D problem with a stealth interface at $x = 0$. In the active region $x < 0$, we have an incoming plane wave, of amplitude a and energy E, that emerged from a source at $x = -\infty$. A uniform stealth region is filled in the region $x > 0$. In general, at an interface we will have both transmitted and reflected waves. Let the electron effective mass in region 2 be $\overline{m} = m^*(1 + i\,\alpha)$, where α is the absorption parameter considered to be a constant for the moment. The total wavefunction is given by

$$\begin{aligned} \psi_1(x) &= ae^{ik_1x} + re^{-k_1x}, \;\; x < 0; \\ \psi_2(x) &= te^{ik_2x}, \;\; x > 0, \end{aligned} \tag{2.5}$$

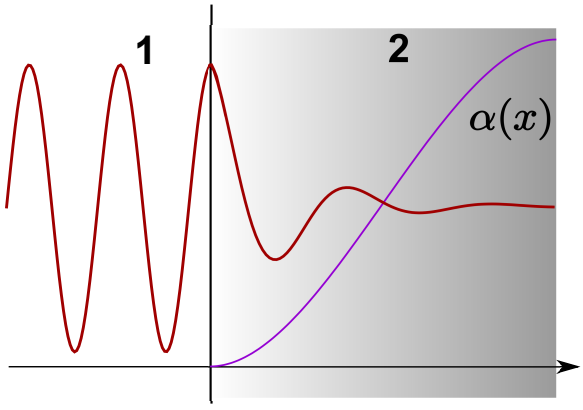

Figure 2.3: A plane wave incident from the active region decaying rapidly to zero within the absorber (shaded) is shown. The stealth function $\alpha(x)$ is a cubic Hermite polynomial that varies smoothly in the stealth region and is shown as a continuous curve.

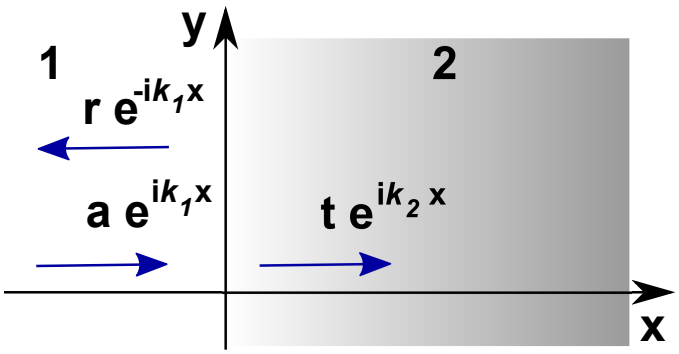

Figure 2.4: The transmission and reflection of electron waves at the stealth region interface are shown. Here k_1 and k_2 are the corresponding wavevectors in the regions 1 and 2, respectively. Also a, r and t are the incident, reflected and transmitted amplitudes, respectively.

where the wavevector $k_1 = \sqrt{2m^*E/\hbar^2}$, and k_2 is as yet undetermined. The differential equations satisfied by the wavefunction in the two regions are given by

$$\begin{aligned} \frac{d^2}{dx^2}\psi_1(x) + k_1^2\psi_I(x) = 0, \;\; x < 0; \\ \frac{d}{dx}\frac{m^*}{\overline{m}}\frac{d}{dx}\psi_2(x) + k_1^2\beta\psi_2(x) = 0, \;\; x > 0, \end{aligned} \tag{2.6}$$

where the parameter β is fixed later through the no-reflection condition. Continuity of the wavefunction at the interface $x = 0$ requires that

$$a + r = t. \tag{2.7}$$

The probability current continuity demands that the mass-derivative of the wavefunction be continuous [43]. Hence, we have the condition

$$i\frac{k_1}{m^*}(a - r) = i\frac{k_2}{\overline{m}}t. \tag{2.8}$$

From Eq. (2.7) and (2.8), the reflection coefficient is given by

$$r = a\left(\frac{k_1\overline{m} - k_2m^*}{k_1\overline{m} + k_2m^*}\right), \tag{2.9}$$

and *the no-reflection condition* is

$$k_2 = \frac{\overline{m}}{m^*}k_1 = (1 + i\alpha)\, k_1. \tag{2.10}$$

Substituting Eq. (2.5) in Eq. (2.6), we obtain a dispersion relation of the form

$$-\frac{m^*}{\overline{m}}k_2^2 + \beta k_1^2 = 0, \tag{2.11}$$

leading to $\beta = (1 + i\,\alpha)$. In practice, we consider the absorption parameter α to increase smoothly over the stealth region so that there are no sharp interfaces or jump conditions to generate any reflections. Therefore, the wave equation in the stealth region is given by

$$-\frac{\hbar^2}{2m^*}\frac{d}{dx}\left(\frac{1}{(1+i\alpha(x))}\frac{d\psi(x)}{dx}\right) - E\,(1+i\alpha(x))\,\psi(x) = 0, \tag{2.12}$$

with solutions of the form

$$\psi(x) \sim \exp\left(\pm ik_1\,x - k_1\int_0^{\pm x} dx'\alpha(x')\right). \tag{2.13}$$

We see that the solutions are highly damped, which allows us to apply Dirichlet BCs at the boundaries of the stealth regions. The mass-derivative continuity [43] in Eq. (2.6) for any interface at $x_0 > 0$ requires $\alpha(x)$ to satisfy a condition of the form

$$\left.\frac{1}{1+i\alpha(x)}\frac{d}{dx}\psi_2\right|_{x_0-0^+} = \left.\frac{1}{1+i\alpha(x)}\frac{d}{dx}\psi_2\right|_{x_0+0^+}. \tag{2.14}$$

Hence, the absorption parameter $\alpha(x)$ has to be a smooth function. We choose $\alpha(x)$ to be a cubic Hermite interpolation polynomial which varies smoothly from 0 to α_{max} within the stealth region as shown in Fig. 2.3. The width of the stealth region and α_{max} are optimized in such a way that the sum of reflection (R) and transmission (T) coefficients is closest to 1 up to a desired accuracy. In the absence of scatterers, we predetermine these parameters in a convenient manner. The *no-reflection condition* similar to Eq. (2.10) is valid even for scattering in 2D waveguides. In Fig. 2.5, we see that the percentage error decreases steadily as a function of the width of the stealth region. The error can be decreased further by increasing the thickness of the absorbers and increasing the mesh density. A choice of α_{max} can be made for all energies by having $\alpha_{max} \propto (E/1\,eV)\,\alpha_0$, where α_0 is a fixed constant. We note that creating absorbers surrounding the scattering center provides a convenient way of specifying the region where we are interested in determining the transport properties.

Schrödinger's equation with a source term

Having enclosed the scattering center with totally absorbing stealth regions, we now require an electron antenna or source within the active region which can inject plane waves of given energy E and amplitude a. A "driving term" on the right hand side is added to the standard Schrödinger equation to create a δ-function source at a given

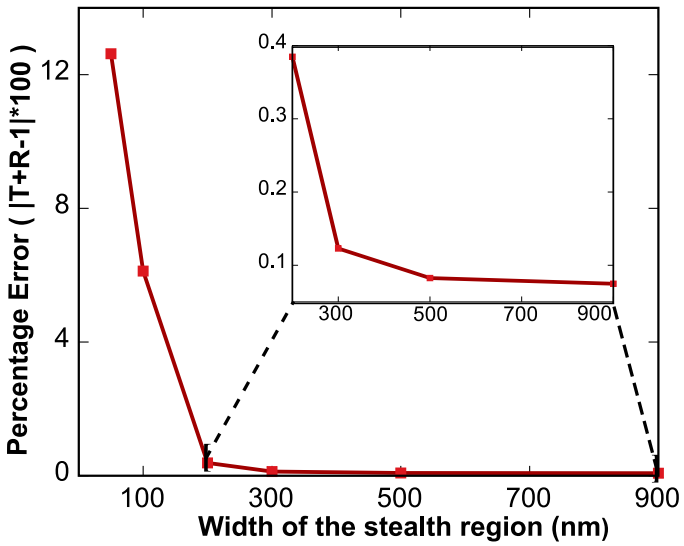

Figure 2.5: The percentage error $(T + R - 1) \times 100$ is plotted as a function of the width of the stealth region for scattering in a 2D waveguide. Here we choose the incoming energy to be 0.01eV, $\alpha_0 = 16$, and the mesh size ≈ 5000. We have employed $C^{(1)}$- continuous quintic Hermite interpolation polynomials on a triangle (see Appendix B) for all 2D calculations. The global matrix size is ~30000×30000.

location. The Schrödinger equation with a source term in the active region is given by

$$\left[-\frac{d}{dx}\left(\frac{\hbar^2}{2m^*}\frac{d}{dx}\right)+V(x)-E\right]\psi(x) = -S\frac{\hbar^2}{2m^*}\delta(x-x_0), \tag{2.15}$$

where x_0 is the location of the source within the active region and S is the source parameter. In the absence of any potential, the equation for Green's function $G(x-x_0)$ in the active region is given by

$$\left[-\frac{d}{dx}\left(\frac{\hbar^2}{2m^*}\frac{d}{dx}\right)-E\right] G(x-x_0) = -S\frac{\hbar^2}{2m^*}\delta(x-x_0). \tag{2.16}$$

The Fourier transform of $G(x - x_0)$ is defined by

$$G(x - x_0) = \frac{1}{2\pi}\int_{-\infty}^{\infty} dk'\, g(k')\, \exp(ik'(x - x_0)). \tag{2.17}$$

Substituting Eq. (2.17) in Eq. (2.16) and representing the δ-function in the Fourier space we obtain

$$g(k') = -\frac{S}{2k}\left[\frac{1}{k' - k - i\epsilon} - \frac{1}{k' + k + i\epsilon}\right], \tag{2.18}$$

where we have used the '$i\epsilon$' prescription to specify poles in the 1^{st} and 3^{rd} quadrants. Now the integral in Eq. (2.17) is determined such that for $x > x_0$ ($x < x_0$) we evaluate the contour integral in the upper (lower) half plane, as shown in Fig. 2.6, to obtain

$$G(x - x_0) = \frac{S}{2ik} \begin{cases} \exp(ik(x - x_0)), & x > x_0; \\ \\ \exp(-ik(x - x_0)), & x < x_0. \end{cases} \tag{2.19}$$

We are then able to identify the source parameter to be $S = 2ika$, where a is the amplitude and k is the wavevector for the incoming waves emerging on either side of the source located at $x = x_0$. Similar considerations in 2D and 3D lead to appropriate sources in any geometry.

2.2 The action integral formalism: a generalized variational approach

Casting Eq. (2.15) as an action integral allows us to solve readily using variational approaches. We first multiply Eq. (2.15) with a small variational $\delta\psi^*$, and integrate over dx between the limits x_L to x_R. We obtain an expression of the form

$$\delta\mathcal{L} = \int_{x_L}^{x_R} dx\ \delta\psi^*(x) \left[\left(-\frac{d}{dx}\left(\frac{\hbar^2}{2m^*}\frac{d}{dx}\right) + V(x) - E \right)\psi(x) + S\frac{\hbar^2}{2m^*}\delta(x - x_0) \right] = 0. \tag{2.20}$$

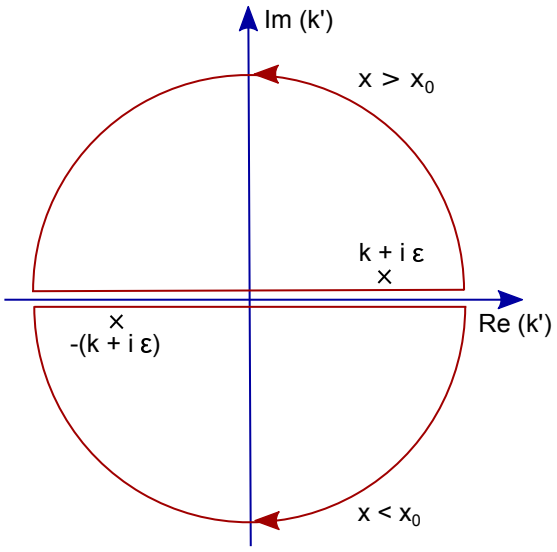

Figure 2.6: Poles and contours in the complex k'- space that are used to determine the integral in Eq. (2.17) are shown. For $x > x_0$ and $x < x_0$ we chose the contour and pole in the upper and lower half plane, respectively.

Applying integral by parts to the first term in the above expression, we obtain

$$\delta\mathcal{L} = \int_{x_L}^{x_R} dx \Bigg[-\frac{d\delta\psi^*}{dx}\left(\frac{\hbar^2}{2m^*}\right)\frac{d\psi}{dx} + \delta\psi^*\,(V(x)-E)\psi(x) + \delta\psi^* S\frac{\hbar^2}{2m^*}\delta(x-x_0)\Bigg] = 0. \tag{2.21}$$

We extract the variation term $\delta\psi^*(x)$ and obtain an expression

$$\delta\mathcal{L} = \Bigg[\int_{x_L}^{x_R} dx\; \delta\psi^*(x)\Big[\overleftarrow{\partial}_x \frac{1}{(1+\alpha(x))}\overrightarrow{\partial}_x + \frac{2m^*}{\hbar^2}\big[V(x) - E\,(1+i\alpha(x))\,\big]\Big]\psi(x) + \int_{x_L}^{x_R} dx\; \delta\psi^*(x) S\;\delta(x-x_0)\Bigg] = 0. \tag{2.22}$$

Hence, the action integral for the 1D scattering problem with sources and absorbers (corresponding to Eq. (2.15)) is given by

$$\mathcal{A} = T \times \Bigg[\int_{x_L}^{x_R} dx\; \psi^*(x)\Big[\overleftarrow{\partial}_x \frac{1}{(1+\alpha(x))}\overrightarrow{\partial}_x + \frac{2m^*}{\hbar^2}\big[V(x) - E\,(1+i\alpha(x))\,\big]\Big]\psi(x) + \int_{x_L}^{x_R} dx\; \psi^*(x) S\;\delta(x-x_0)\Bigg], \tag{2.23}$$

where, $\alpha(x)$ is taken to be 0 in the scattering region. We are solving the time-independent (steady-state) problem so that the time integral over the range $[0, T]$ in the action is simply T, and Dirichlet BCs are implemented at $x = x_L$ and $x = x_R$.

Finite element analysis (FEA) is a generalized variational approach in which we discretize the physical domain of interest into several small elements [41, 44, 45]. Within each element, we express the wavefunction as a linear combination of interpolation polynomials multiplied by as-yet undetermined coefficients that correspond to the value of the wavefunction at the vertices, called nodes of the elements that are line intervals in 1D and triangles or squares in 2D. We have used quintic Hermite interpolation polynomials for all calculations, for which the expansion coefficients are the wavefunction values and its derivatives at the nodes [41]. The additional derivative continuities allowed for in this case substantially increases the accuracy as compared with traditional Lagrange interpolation polynomials [26]. A detailed

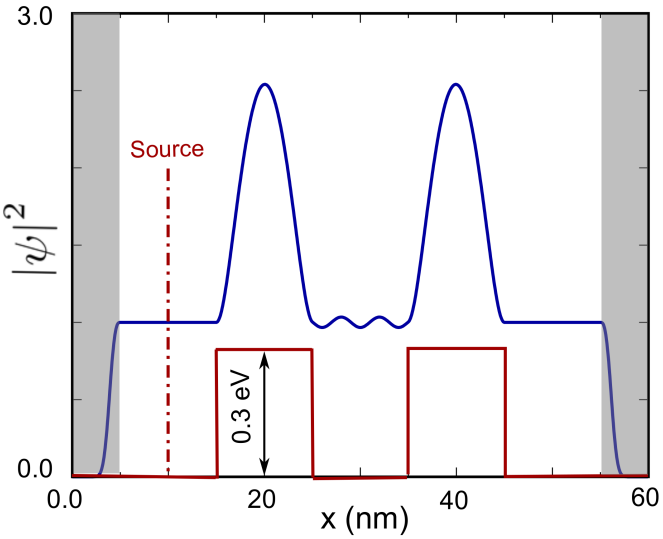

Figure 2.7: Probability distribution for the first above-barrier resonant state with incoming energy 0.355 eV is shown. The source is located at $x = 10$ nm. The stealth region is shaded in gray. The barrier heights and widths are taken to be 0.3 eV and 10 nm, respectively.

discussion on the derivation of interpolation polynomials is given in Appendix A. Sets of Lagrange and Hermite interpolation polynomials in one and two-dimensions are listed in Appendix B.

Discretization of the action integral in Eq. (2.23) within the finite element framework, and variation of the resulting action with respect to ψ^* leads to a system of linear equations of the form $M\,\Psi = b$, where Ψ is the column vector containing function values and derivatives of the wavefunction at the nodes, M is the corresponding coefficient matrix, and b is the column vector corresponding to the integral over the source term. We solve this matrix equation in a parallel computing environment [47–50] to obtain the total wavefunction throughout.

For scattering through a 1D single barrier, transmission coefficients are determined through our formalism and found to be accurate within 10^{-5} when compared with analytical results [51]. We can systematically increase the accuracy further through mesh size refinement (h-refinement), or by employing higher order interpolation polynomials (p-refinement) for convergence within the FEA.

As a test case, we consider an electron scattering through a 1D symmetric double barrier in GaAs. The effective mass of the electron is equal to $0.067\,m_e$, where m_e is the free electron mass. The barrier heights and widths are taken to be 0.3

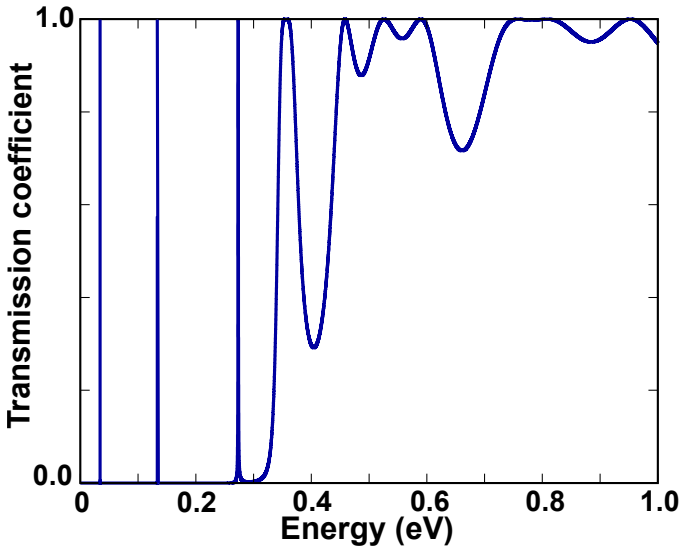

Figure 2.8: The transmission coefficient as a function of energy for a double barrier potential is shown. Each of the barriers is of height 0.3 eV with a width of 10 nm and are 10 nm apart.

eV and 10 nm, respectively. In Fig. 2.7, we plot the probability distribution for the first above-barrier resonant state corresponding to the energy 0.355 eV. Notice that the probability density reaches a maximum at each barrier due to Fabry-Pérot interference . Such resonances have been observed in several experiments involving superlattices and heterostructures [52–55]. Within the stealth regions (shaded) the wavefunction decays smoothly to zero as expected. In Fig. 2.8, we plot the well-known tunneling transmission coefficient profile [56, 57] as a function of incoming energy for the double barrier. Three resonant peaks that are observed below the barrier (0.3 eV) are attributed to the electron trapped inside the well between the two barriers.

We typically have ∼500 elements in 1D for these calculations, and the matrix size is 2000×2000 when we use quintic Hermite interpolation polynomials. At a given energy, the computational time is under 0.5 minutes and the matrix condition number is $\sim 10^{-6}$.

2.3 Conclusions

A typical text-book treatment of scattering involves an incoming prepared state from $x = -\infty$, and cross-sections are obtained by applying BCs in the asymptotic limit . In finite, nano-scale systems it is necessary to obtain solutions within a few wavelengths away from the scattering center. In this chapter, using the stealth

elements, we have redefined the quantum scattering problem with "sources and absorbers." In summary, we have shown that

1. the quantum scattering can be brought into the variational framework using the action integral formalism.

2. the use of stealth elements reduces the Cauchy BCs to simpler Dirichlet BCs at the periphery. In this way we substantially reduce the computational complexity. The parameter, α, is varied smoothly in the stealth region as a function of coordinates $\boldsymbol{r}$ for each energy E to ensure no reflection at the stealth interface.

3. Schrödinger's equation with a source term provides a way of designing a carrier antenna in the active region which inject the plane waves of a specified energy and amplitude while the active region is enclosed by absorbers.

4. the method provides a way of readily handling geometrically complex potentials and multiple scattering problems.

In confined geometries, the total wavefunction obtained through our analysis includes the contribution from evanescent modes. In two-dimensional or three-dimensional open domains, the stealth elements are placed around the scattering center in all directions and the source is located in the active region. These concepts will be discussed in the subsequent chapters.

Chapter 3

ELECTRON SCATTERING IN QUANTUM WAVEGUIDES: FORMALISM

In this chapter, we develop a non-asymptotic description for scattering in electron waveguides, and couch it in a fully variational framework that is particularly appropriate for nanoscale systems. This chapter is organized as follows. Motivation and a summary of the important results are provided in Sec. 3.1. In Sec. 3.2, we describe the electron scattering in quantum waveguides with sources and absorbers. We re-examine aspects of preparing initial states and detecting the final states. The application of boundary conditions, the requirements of (probability) current conservation, and the determination of evanescent (decaying) modes and near-field solutions are studied. In Sec. 3.3, we derive the selection rules for electron scattering in a quantum waveguide. Concluding remarks are given in Sec. 3.4.

3.1 Introduction

In confined nanostructures (such as quantum waveguides), the probability of evanescent contributions are lost when measured at the asymptotic limit . In the frequently used transfer-matrix and S-matrix methods , these contributions are explicitly introduced as matrix elements corresponding to a finite set of evanescent modes. However, the numerical value of computed transmission amplitudes depend on the number of modes taken into consideration. Also, these matrix methods have large discretization errors when employed for geometrically complicated distribution of scattering centers. Hence, we require a fully variational scattering approach that can determine the wavefunction accurately throughout the region of interest.

Disorder effects arise in quantum waveguides due to the presence of impurity and defect distributions. Electron transport in such systems are of great interest for several high-frequency device applications [58]. Such structures can be fabricated at low temperature in $Ga_{1-x}Al_xAs/GaAs$ and $LaAlO_3/SrTiO_3$ heterointerfaces [59] to generate high mobility two-dimensional (2D) electron gases . Carbon nanotubes can be used as multi-mode quantum waveguide [60]. The formalism and results developed here are applicable and relevant to study such meso- and nano-scale structures.

Here, we note the following:

1. Our formalism can be applied to model electron transport in confined geometries to obtain experimentally amenable results. While we are reporting results for one dimensional (1D) and two dimensional (2D) systems, the method can be extended to study three-dimensional (3D) scattering mechanisms. Scattering in 2D and 3D open domain will be discussed in the subsequent chapters.

2. We set up stealth (absorbing) regions to completely enclose the active region and effectively simplify the Cauchy BCs to Dirichlet BCs . Applying boundary conditions at the asymptotic limit are necessary in the conventional formulations. However, they are difficult to implement in numerical calculations. Introducing absorbers on either side of the potential distribution also eliminates the need for applying asymptotic BCs. Hence, we can also effectively investigate the "near-field" scattering effects.

3. Through group theory, we identify selection rules for modes contributing to the scattered wavefunction. Symmetry of the scattering potential effectively eliminates the presence of those modes that do not obey the selection rules.

4. A universal way of calculating the amplitudes of both propagating and evanescent modes has been described.

3.2 Scattering in 2D quantum waveguides

Let us consider a straight 2D mesoscopic waveguide of width w with wave propagation along the x-axis, as in Fig. 3.1. Let $V_c(y)$ and $U_0(x, y)$ be the confining waveguide potential and the scattering potential, respectively. $U_0(x, y)$ is non-zero only at the scattering center and $V_c(y)$ is given by

$$V_c(y) = \begin{cases} 0, & 0 \leq y \leq w; \\ \infty, & y < 0 \text{ and } y > w. \end{cases} \tag{3.1}$$

Electron waves are confined in the transverse direction and the solutions are those of the infinite potential well of width w in the y-direction. Therefore the energy for an incident wave in the n^{th} subband is expressed as

$$E_n = E_{x,n} + \frac{n^2\pi^2\hbar^2}{2m^*w^2}, \tag{3.2}$$

where n is the integer mode number for the incoming wave. We refer to $E_{y,n} = n^2\pi^2\hbar^2/(2m^*w^2)$ as the subband minimum corresponding to the band index n. The

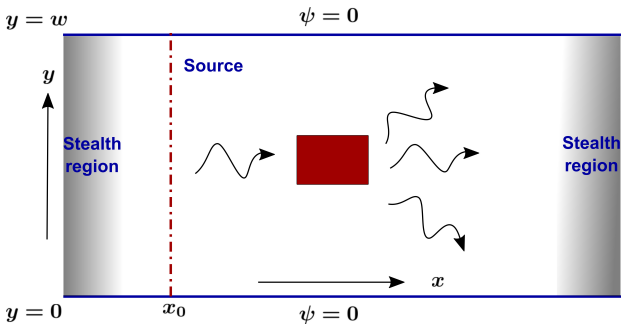

Figure 3.1: A schematic picture of scattering in a 2D waveguide of width w is shown. The stealth regions are placed at either end of the waveguide. The wave propagation is along the x-axis and the source is located x_0.

basis wavefunctions are of the form

$$\psi_n(x, y) = a_n \sqrt{\frac{2}{w}} \exp(ik_{xn}\, x) \sin\left(\frac{n\pi y}{w}\right), \tag{3.3}$$

which satisfies the dispersion relation given by

$$k^2 = k_{xn}^2 + \frac{n^2\pi^2}{w^2}, \tag{3.4}$$

where k_{xn} is the wavevector and a_n is the specified amplitude of the wave in the mode n. Note that in a straight empty waveguide, due to the translational symmetry , we will have only real values of k_{xn}. However, the presence of scattering centers breaks this symmetry, and this results in both real (propagating) and purely imaginary (evanescent) k_{xn} contributions in the spectrum.

For a given x these basis functions individually satisfy the Cauchy BCs of the form

$$\left[\frac{\partial \psi_n}{\partial x} - ik_{xn}\psi_n\right] = 0. \tag{3.5}$$

Note that the evanescent modes have a wavevector of the form $k_{xn} = iK_{xn}$, and satisfy BCs of the form $(\partial_x\psi_n + K_{xn}\psi_n) = 0$.

In section 2.1, we showed that such Cauchy BCs are essential for a variational formulation of scattering. In the analytical consideration of scattering such BCs are built into the solution by starting with an expansion in terms of the incoming and outgoing basis wavefunctions. In 2D and 3D, a partial wave analysis is then performed to obtain amplitudes and angular dependences in the *asymptotic limit*. This method was first developed by Rayleigh [11] in the context of sound waves, and later by Faxen and Holtsmark [12] for the scattering of electrons. For example, in

the 2D open domain, the scattered wavefunctions are expressed in terms of Hankel functions of the first kind $H_m^{(1)}(k\rho)$, all of which have the same asymptotic form [10] given by $e^{ik\rho}/\sqrt{\rho}$.

The mixed BCs can be used in the variational treatment of the scattering [61–64] as the current continuity condition for the Hankel function of each order. However, it is complicated to use such BCs in calculation [41]. This is because a derivative of the Hankel function of order n is linked to Hankel functions of order $n \pm 1$ through a recursion relation. Hence, the asymptotic form of the BCs is invoked. Moreover, in a numerical treatment the geometry discretization of the scattering boundary leads to inevitable inaccuracies and a non-zero reflection from the boundary. This is formally resolved in the usual formulation by going to the asymptotic regime, at the price of having a larger scattering region and sacrificing the evanescent modes in multi-band wavefunctions.

Here we propose a method to reduce mixed BCs to simpler Dirichlet BCs by creating absorbers (stealth regions) on either end of the waveguide as in Fig. 3.1. We consider a complex effective mass and smoothly vary the optimized mass parameters within these absorbers, constructed in such a way that there is no reflection from any wave incident on them (see section 2.1). The complex electron effective mass is considered to be of the form

$$\overline{m} = m^* \left(1 + i\, \alpha(x)\right), \tag{3.6}$$

where $\alpha(x)$ is a cubic Hermite interpolation polynomial varying smoothly from 0 to α_{max} within the stealth regions, and equal to 0 in the active (scattering) region. From the no-reflection condition (derived in section 2.1) we obtain the wave equation within stealth regions without any scattering centers as

$$\left[\frac{\partial}{\partial x}\frac{1}{(1+i\alpha(x))}\frac{\partial}{\partial x} + \frac{\partial^2}{\partial y^2} + k^2(1+i\alpha(x))\right]\psi(x,y) = 0.$$

Solutions to the above equation are required to have highly damped behavior, leading to Dirichlet BCs on the outer boundaries of such stealth regions.

Note that by introducing absorbers we can simplify the BCs, and define the region of interest without going into the asymptotic limits. However, they do not affect the scattering mechanism in the active region.

Once we enclose the active scattering region with absorbers, we require a source (an electron antenna) in the active region at $x = x_0$ to initiate the incoming plane waves

(see Fig. 3.1). This will be achieved by introducing a source term to the Schrödinger equation given by

$$\left[-\frac{\partial}{\partial x}\frac{\hbar^2}{2\overline{m}}\frac{\partial}{\partial x} - \frac{\hbar^2}{2\overline{m}}\frac{\partial^2}{\partial y^2} + V_c(y) + U_0(x,y) - E_n\right]\psi(x) = -S(y)\frac{\hbar^2}{2\overline{m}}\delta(x - x_0), \tag{3.7}$$

where $S(y)$ is a parameter specified along the source line; the effective mass $\overline{m} = m^*$ in the active region, and this is made into a smoothly varying complex function in the stealth regions as shown in Eq. (3.6).

The Green's function solution to the above equation generates the incoming plane waves. In section 2.1, we solve the Schrödinger equation with a δ-function source and show that the solutions are plane waves emerging on either side of the source located at $x = x_0$. Waves traveling in the negative x ($x < x_0$) direction will be absorbed by the stealth region, and the waves traveling in the positive x ($x > x_0$) direction initiate the scattering event. Hence in quantum waveguides, for a given incoming mode n, an incoming wave from the source is expected to be of the form

$$\psi_{in}(x,y) = a_n\sqrt{\frac{2}{w}}\sin\left(\frac{n\pi y}{w}\right)\begin{cases}\exp(ik_{xn}(x - x_0)), & x > x_0;\\ \\ \exp(-ik_{xn}(x - x_0)), & x < x_0.\end{cases} \tag{3.8}$$

Substituting Eq. (3.8) in Eq. (3.7) and integrating with respect to x around $x = x_0$ we obtain an expression for the source parameter given by

$$S(y) = 2ik_{xn}\,a_n\,\sin\left(\frac{n\pi y}{w}\right). \tag{3.9}$$

In general, the source parameter can include several modes to account for multimode electron transport. Note that in the forward direction ($x > x_0$), the wavefunction in Eq. (3.8) is equivalent to the standard incoming plane wave, except for a constant phase factor $\exp(-ik_{xn}\,x_0)$. Hence, by solving Eq. (3.7) we obtain the total wavefunction $\psi(x,y) = \psi_{in} + \psi_{scat}$ which includes the entire set of real (propagating) and, complex (evanescent) wavevector spectrum of the Hamiltonian.

Once we formulate the quantum scattering problem with *sources* and *absorbers*, we can utilize numerical methods to obtain the total wavefunction $\psi(x,y)$ throughout. We solve Eq. (3.7) using a generalized variation approach based on discretization of the action integral [41, 44, 45]. as shown in section 2.2. We note that our analysis

yields the total wavefunction which encodes contributions from the infinite number of propagating and evanescent modes, in contrast with the S - matrix approach where a choice is made for the limited number of modes to be included in the calculation.

To summarize, *using the method of sources (electron antenna) and absorbers (stealth regions) we have developed a rigorous scattering theory without any asymptotic approximations. The Schrödinger equation with a source term is amenable to a complete variational treatment using the discretization of the action integral.* Through this procedure we accurately obtain the total wavefunction. We can extract the individual transmission coefficients using the modal analysis described below.

Modal Analysis

It is of importance to obtain the individual transmission and reflection coefficients corresponding to each mode, to study various physical phenomena. Note that the evanescent modes are purely real functions, hence they will not contribute to the outgoing current J_{scat}. However, they contribute to the probability distribution $|\psi(x, y)|^2$. We determine the transmission and reflection coefficients through modal analysis using the orthogonality of sine functions. The modal analysis is carried out at either side of the potential distribution to obtain both reflection and transmission coefficients.

Let us consider the incoming wave to be in the mode n. The transmission amplitude for a mode m as a function of x measured to the right of the scattering potential is given by

$$t_{nm}(x) = \int_0^w dy \, \sin\left(\frac{n\pi y}{w}\right) \psi_{scat}(x, y). \tag{3.10}$$

Note that for an incoming mode n, all modes $m \leq n$ are propagating, and $m > n$ are evanescent. This can been seen from the dispersion relation given in Eq. (3.4). For propagating modes, the amplitude $t_{nm} \sim \exp(ik_{xn}x)$, hence the probability density $|t_{nm}|^2$ is independent of coordinates. However, for evanescent modes the amplitude $t_{nm} \sim \exp(-K_{xn}x)$, hence the probability density $|t_{nm}|^2$ is a coordinate dependent quantity.

Propagating modes

The transmission coefficient T_{nm} for a propagating mode m is defined as the ratio of transmitted mode current J^T_{nm} to the incoming current J_{inc}

$$T_{nm} = \frac{J^T_{nm}}{J_{inc}} = \frac{k_{xm}\,|t_{nm}|^2}{k_{xn}a_n^2}. \tag{3.11}$$

Similarly, the reflection coefficient R_{nm} for a propagating mode m is defined as the ratio of reflected mode current J^R_{nm} and the incoming current J_{inc}

$$R_{nm} = \frac{J^R_{nm}}{J_{inc}} = \frac{k_{xm}\,|r_{nm}|^2}{k_{xn}a_n^2}, \tag{3.12}$$

where r_{nm} is the reflection amplitude measured to the left of the scattering potential distribution analogous to Eq. (3.10). Note that T_{nm} and R_{nm} are independent of the coordinates, hence they survive even when the measurements are made at the asymptotic limit. From the current continuity condition, we know that

$$\sum_{m=1}^{m\leq n} \left(J^T_{nm} + J^R_{nm} \right) = J_{inc}, \tag{3.13}$$

where we take the sum over only propagating modes, since there is no current contribution from evanescent modes. Taking the ratio of J_{inc} on either side, and substituting the expression for transmission and reflection coefficients, we obtain

$$\sum_{m} \left(T_{nm} + R_{nm} \right) = 1. \tag{3.14}$$

Evanescent modes

To study the contribution of evanescent modes *we define the reflection and transmission coefficients* as

$$\begin{aligned} \tilde{T}_{nm} &= \frac{|t|^2_{nm}}{a_n^2} \sim \exp\left(-2K_{xm}\,|x|\right); \\ \tilde{R}_{nm} &= \frac{|r|^2_{nm}}{a_n^2} \sim \exp\left(-2K_{xm}\,|x|\right), \end{aligned} \tag{3.15}$$

where $K_{xn} = \sqrt{n^2\pi^2/w^2 - k^2}$ represents the evanescent wavevector. These coefficients represent the probability strength of each evanescent modes. Since these transmission coefficients are coordinate dependent, measurements have to be done at a specific finite distance to detect them. Hence, the conventional scattering theory with an asymptotic approximation is unable to include the evanescent wave contributions. We note that the transmission and reflection coefficient for the evanescent modes do not satisfy any current conservation rule similar to Eq. (3.14).

Through modal analysis we obtain all transmission and reflection amplitudes, hence we can construct a diagonal representation of the transfer-matrix [46]. Furthermore, for a given energy, the propagating modes are associated with the thresholds at lower

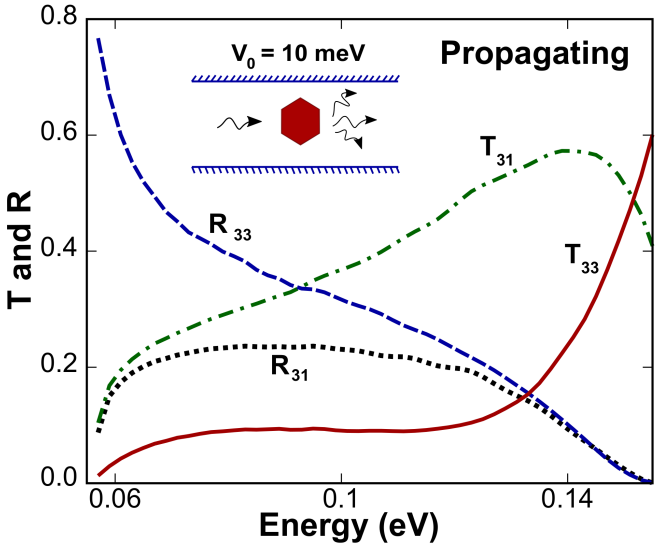

Figure 3.2: The transmission T_{3j} and reflection R_{3j} coefficients are shown as a function of energy for the propagating modes for scattering by a regular hexagonal barrier of side length = 5 nm. The incoming mode is $n = 3$ and the barrier height $V_0 = 10$ meV.

energy, and the evanescent modes are associated with the thresholds at energies higher than the incident energy. *Thus the transverse modes in the two cases are mutually exclusive and can be identified and separated.*

Throughout this chapter, we consider the width of the stealth region to be 900 nm, hence all calculations are accurate within 0.1% as shown in Fig. 2.5.

As a typical system, we consider scattering and transport in a 2D GaAs waveguide of width 30 nm. The corresponding lowest five subband minima are given by

$$E_{y,1} = 6.24 \text{ meV}, \quad E_{y,2} = 24.95 \text{ meV}, \quad E_{y,3} = 56.14 \text{ meV},$$
$$E_{y,4} = 99.80 \text{ meV}, \quad E_{y,5} = 155.94 \text{ meV}.$$

We note that the defect and impurity distribution can exist in any shape in nanostructures. With newer experimental techniques, it is possible to create and embed quantum dots of several possible shapes in waveguides. In this chapter while we treat specific potentials and geometries to discuss several universal phenomena, our method based on geometry discretization can be considered *for any complicated potential distributions*.

As a first example, we consider scattering through a regular hexagonal barrier with each side of length 5 nm. The regular hexagonal shape is considered for

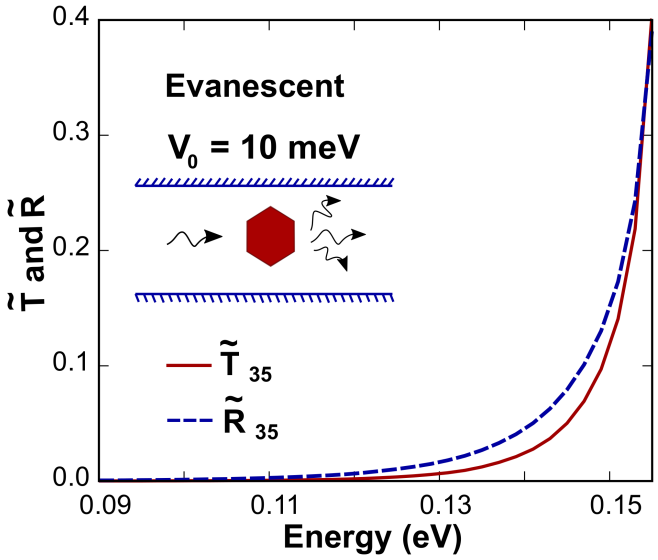

Figure 3.3: The transmission $\tilde{T}_{35}$ and reflection $\tilde{R}_{35}$ coefficients are shown as a function of energy for the *evanescent modes* for scattering through a regular hexagonal barrier of side length = 5 nm. The incoming mode is $n = 3$ and the barrier height $V_0 = 10$ meV. The modal analysis is done at $|x| = 10$ nm.

the potential because it has a non-trivial geometry and has the same transverse symmetry as that of the straight waveguide.[a] The use of symmetry arguments will be elaborated on in the following in greater detail. In Fig. 3.2 and Fig. 3.3, we plot the transmission coefficients as a function of energy for the propagating and evanescent modes, respectively. Here, we consider the incoming wave from the mode $n = 3$, and the modal analysis is done at $|x| = 10$ nm. Throughout this chapter, we have re-scaled the potential as $V_0 = m^* U_0/m_e$, where m_e is the fundamental electron mass. For GaAs, the effective mass $m^* = 0.067\, m_e$. Notice that only the odd modes (even parity) contribute; this is explained through the presence of a selection rule in the following section. In Fig. 3.3, we see that the evanescent modes contribute fairly symmetrically for both transmitted and reflected waves, and reach a maximum at the subband minimum ($E_{y,5}$) [65]. In Fig. 3.4, we show the exponential decay of evanescent waves with distance for an energy $E = 155$ meV. The observed wavevector obtained through a curve fitting matches the theoretical prediction. Note that the decaying behavior of transmission coefficients observed in Fig. 3.4 are consistent with Eq. (3.15).

[a] We chose a non-trivial geometry to show the flexibility of our method. This is not to be viewed as a limitation. In fact, the method transcends such geometrical considerations through discretization, and is a strength of our approach.

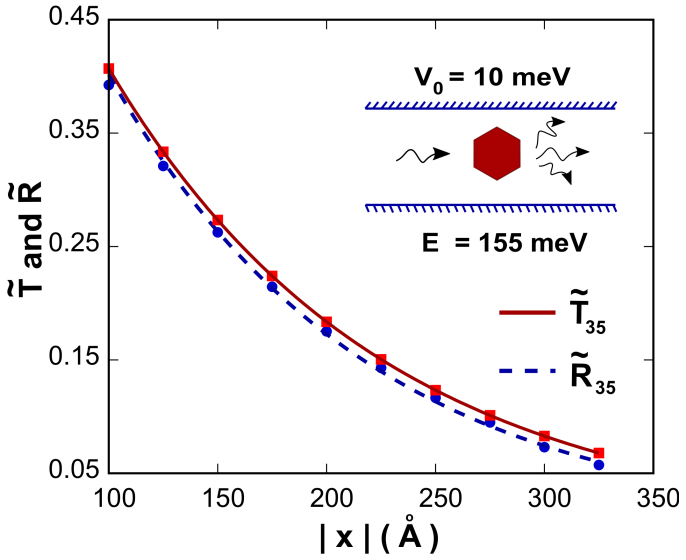

Figure 3.4: Decay of transmission ($\tilde{T}_{35}$) and reflection ($\tilde{R}_{35}$) coefficients for evanescent modes are shown as a function of x(Å) for $E = 155\,\text{meV}$ for scattering through a regular hexagonal barrier of side length = 5 nm. The incoming mode is $n = 3$ and the scattering potential is $V_0 = 10\,\text{meV}$. Here we carried out the modal analysis at every 25Å. Equations from the curve fitting are given by $\tilde{T}_{35} = 0.90208\,\exp(-2\times 0.00398\,x)$, and $\tilde{R}_{35} = 0.93368\,\exp(-2\times 0.00421\,x)$. Theoretically determined $K_{x5} = 0.00398/\text{Å}$, which is close to the fitted values.

In Fig. 3.5, we show the flow of the probability current density through the waveguide with a regular hexagonal barrier. Since the potential has C_{1h}-symmetry and the incoming mode is $n = 3$, the modes contributing to the scattered current are $n = 1$ and 3. This leads to a peaking of the current at the middle of the waveguide. This can be noted in the figure. Such analysis will influence the precision manipulation of electron beams via patterned defect engineering as a new functionality in microelectronics.

3.3 Selection rules for waveguide scattering

We seek a selection rule according to the symmetry of the scattering potential U_0, which determines the modes that contribute to the scattered wavefunction. For 2D waveguides we write the Hamiltonian as $H = H_0 + U_0$, where H_0 is the Hamiltonian corresponding to ballistic transport. We note that H_0 has C_{1h} symmetry; the corresponding character table is given in Table 3.1. Let $H_0\,|m\rangle = E_m\,|m\rangle$, where $|m\rangle$ is a basis function for an irreducible representation Γ_m of C_{1h}.

Let $U_{mn} = \langle m|\,U_0\,|n\rangle$ represent the matrix elements corresponding to the scattering potential. In general, $U_0(x, y)$ involve terms that transform according to different

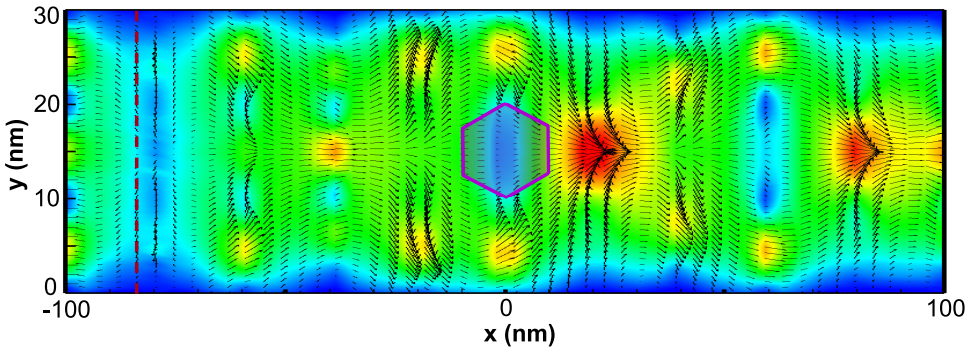

Figure 3.5: The probability current density at incoming energy $E = 155$ meV (which is just below the subband threshold at 155.94 meV) is plotted for scattering through a regular hexagonal barrier of side length = 5 nm. The incoming mode is $n = 3$, and the barrier height is $V_0 = 10$ meV. The line source located at $x = -80$ nm is represented by a dotted line. In this plot, the magnitude of probability current densities ranges from 0 to 0.06, which is represented by a continuous contour color coding varying from blue to red.

irreducible representations of C_{1h}. Let U_0 transform according to a representation Γ_V. We can then decompose Γ_V in terms of irreducible representations A' and A''. For simplicity, let Γ_V be one of the irreducible representations. *Then, from the basis-function orthogonality theorem for groups [66, 67], we state that U_{mn} vanishes unless* $\Gamma_m \otimes \Gamma_V \otimes \Gamma_n = A'$. Hence, in the scattering process only those modes which satisfy this condition contribute to the reflected and transmitted waves.

In case of a hexagonal scatterer, the scattering region (hexagon) is invariant under σ_h. Hence, $\Gamma_V = A'$. We know that in a 2D waveguide, odd(even) numbered modes

$C_{1h}(m)$	E	σ_h	Basis functions	
A'	1	1	x	x^2, y^2
A''	1	-1	y	xy

Table 3.1: The character table for the symmetry group C_{1h} along with the basis functions corresponding to the irreducible representations.

are in the irreducible representation $A'(A'')$. We see that

$$\begin{aligned} A' \otimes \Gamma_V \otimes A' &= A', \\ A'' \otimes \Gamma_V \otimes A'' &= A', \\ A' \otimes \Gamma_V \otimes A'' &= A''. \end{aligned} \tag{3.16}$$

Hence, when an incoming mode is odd (even) only odd (even) modes will contribute. This is evident from Figs. 3.2 and 3.3. We note that all modes contribute to the scattered wavefunction irrespective of the incoming mode only when $U_0(x, y)$ does not have the mirror symmetry (σ_h). For example, if we provide a geometrical perturbation through a small angular rotation to the hexagonal defect center, the original C_{1h} symmetry is lost and we observe that all modes open up to contribute to the scattered wavefunction.

3.4 Conclusions

We have developed a non-asymptotic, fully variational description for quantum scattering theory with sources and absorbers to study carrier transport in nanostructures with defects and impurities.

In traditional scattering theory, Cauchy BCs are required for an outgoing current. In two-dimensions, to apply Cauchy BCs we require the derivative of Hankel functions $\partial_\rho H_n(k\rho)$. The derivative $\partial_\rho H_n(k\rho)$ satisfies a recurrence formula. Hence, it will involve mixing of terms corresponding to the order n and $n \pm 1$. This cumbersome evaluation is usually avoided by invoking the asymptotic limit. In the asymptotic domain, all Hankel functions $H_n(k\rho)$ take the same form $\exp(ik\rho)/\sqrt{\rho}$ for all orders n. This simplification is remarkably effective for calculating the scattering amplitudes, and automatically yields the optical theorem. However, the evanescent modes do not contribute in the asymptotic domain, and hence are not accounted for in this usual formulation when applied for multiband scattering phenomena. In the present formalism, we eliminate the requirement of going to the asymptotic limit by enclosing the scattering region with absorbers. This provides a unique way of simplifying and applying BCs without affecting the accuracy of results. A modal analysis in the post-processing stage yields all the information associated with a partial wave analysis.

The method presented here goes beyond the existing S-matrix, R-matrix, and transfer-matrix approaches. The transfer matrix approach suffers from numerical errors due to exponentially growing matrix elements introduced by the evanescent

modes. In S-matrix and R-matrix approaches, the conductance value depends on the number of modes used for the calculation [68, 69]. In all these methods smooth potentials are discretized, and are considered to be a constant within each region for constructing the local matrices. Hence, these methods are not suited for treating complicated defect and impurity potential distributions. For example, hexagonal or circular potentials are not readily amenable to such discretization.

At times, boundary element methods are also invoked in scattering problems. However, one observes highly inaccurate results around the resonance energy values [70, 71]. Boundary integrals are cumbersome to handle when we include the evanescent modes. However, the variational approach presented in this chapter, based on discretization of the action integral provides a stable solution by converging quadratically to the actual value.

Lastly, we have described the selection rules for determining the modes contributing to the scattered wavefunction. Selection rules based on the symmetry of the potential effectively eliminate the presence of modes which do not obey the given symmetry.

Essentially, waveguides of any shape, with any complicated defects and impurity distributions can be modeled accurately with the method delineated in this chapter. In other words, this method based on the geometry discretization has a remarkable flexibility in its potential applications.

In the succeeding chapter, we apply our formalism to examine evanescent mode contributions to Fano resonance , and the enhancement of thermoelectric power. We also study the effect of geometrical tapering, and curvature on the transport properties of a quantum waveguide.

Chapter 4

ELECTRON SCATTERING IN QUANTUM WAVEGUIDES: APPLICATIONS

In this chapter, we present novel physics revealed through the application of the non-asymptotic scattering theory developed in the previous chapter. The organization of this chapter is as follows. A summary of concepts and results to be discussed in this chapter is presented in Sec. 4.1. In Sec. 4.2, we calculate the Fano interference profile arising due to the interaction between bound states in attractive potentials with the propagating and *evanescent* waves. The dependence of transmission and reflection coefficients on the variation of the scattering potential is discussed in Sec. 4.3. We compare our method with the Feshbach coupled-channel theory in Sec. 4.4 and show that the Feshbach coupled-channel theory predicts incorrect energy value of the transmission minimum, and the Fano line width. Section 4.5 is devoted to calculations of the conductance and Seebeck coefficient for scattering in quantum waveguides. A novel result is the calculation of transmission coefficients in tapered waveguides presented in Sec. 4.6. The effect of curvature on scattering in bent waveguides is studied in Sec. 4.7. Concluding remarks are provided in Sec. 4.8.

4.1 Introduction

In the previous chapter, we developed a non-asymptotic, variational description for quantum scattering theory with sources and absorbers, to study transport properties in quantum waveguides. The introduction of absorbing regions, "stealth regions," as we call them, for enclosing the active scattering region provides a unique way of simplifying and applying boundary conditions (BCs). The absorption parameter is smoothly increased so that there is no unwanted back-scattering from the stealth regions. Hence, the presence of near-field evanescent solutions are not eliminated from consideration. Furthermore, the calculations can be focused on the physical region without going to the asymptotic limit. We then obtain accurate solutions throughout the region under consideration. In this chapter:

1. We show that in quantum waveguides with attractive impurity potentials the Fano resonance profiles are observed for both propagating and evanescent modes.

2. We report results for the transport in tapered waveguides with different tapering angles, and study their dependency on the directionality of incoming waves. The transmission coefficients behave asymmetrically with respect to the injection ports. This configuration is readily achievable using split-gate geometry on semiconductor inversion layers. Hence our predictions can be verified experimentally.

3. We calculate the conductance, Seebeck coefficient, and power factors of waveguides with impurities, providing experimentally measurable quantities. We have shown that quantum dots or attractive impurity potentials embedded in the interior of a waveguide are good candidates for enhancing the thermoelectric energy conversion efficiency, since they yield large power factors around the subband minimum.

4.2 Attractive scatterers and Fano resonance

Fascinating physics arises when we apply our method of sources and absorbers [72] to study scattering in quantum waveguides with attractive scatterers. Let us consider a straight two-dimensional (2D) mesoscopic waveguide of width w with wave propagation along the x-axis. The hard wall confinement in the transverse y-direction is considered. Therefore the energy for a wave in the n^{th} subband is given by

$$E_n = E_{x,n} + \frac{n^2\pi^2\hbar^2}{2m^* w^2}, \tag{4.1}$$

where n is the integer mode number for the incoming wave. We refer to $E_{y,n} = n^2\pi^2\hbar^2/(2m^* w^2)$ as the subband minimum corresponding to the band index n. The dispersion relation for the wavevector k is given by

$$k^2 = k_{xn}^2 + \frac{n^2\pi^2}{w^2}, \tag{4.2}$$

where $k_{xn} = \sqrt{2m^* E_{x,n}/\hbar^2}$. The transmission and reflection coefficients between a propagating mode m and the incoming mode n are defined as [72]

$$T_{nm} = \frac{k_{xm}\,|t_{nm}|^2}{k_{xn} a_n^2}; \quad R_{nm} = \frac{k_{xm}\,|r_{nm}|^2}{k_{xn} a_n^2}, \tag{4.3}$$

where t_{nm}, r_{nm}, and a_n are the transmitted, reflected and, incoming amplitudes, respectively. In the presence of scattering centers, the total scattered wavefunction will have contributions from both propagating and evanescent modes. To study the

contributions from evanescent modes we define [72] the reflection and transmission coefficients as

$$\tilde{T}_{nm} = \frac{t_{nm}^2}{a_n^2} \sim \exp\left(-2K_{xm}\,|x|\right);$$
$$\tilde{R}_{nm} = \frac{r_{nm}^2}{a_n^2} \sim \exp\left(-2K_{xm}\,|x|\right), \tag{4.4}$$

where $K_{xn} = \sqrt{n^2\pi^2/w^2 - k^2}$ represents the evanescent wavevector. These coefficients represent the probability strength of each evanescent modes [72].

Only the propagating modes contribute to the probability current, and the evanescent modes being purely real functions will have vanishing current contributions. Therefore, through the conservation of probability current we obtain the relation $\sum_m (T_{nm} + R_{nm}) = 1$. We note that the transmission and reflection coefficients for the evanescent modes (given in Eq. (4.4)) do not satisfy any such summation rule [72].

As an example of a multiple scattering problem, we consider a 2D waveguide with three circular impurities each of radius 30 Å and a constant potential, $V_0 = -50$ meV. In Fig. 4.1, we observe an asymmetric Fano resonance [74] transmission profile for the propagating modes due to interference between scattering states in one subband and a bound state supported by a different subband [75–77], an effect analogous to that of atomic autoionization [78]. Multiple Fano resonances observed in Fig. 4.1 are a special feature of multiple scattering.

The Fano resonance profile in waveguides has been qualitatively explained for the propagating states with an attractive δ-potential scatterer through two-band models [75, 76]. Such a Fano resonance has been reported for special cases of scattering from a rectangular impurity potential [79, 80], from two antidots [81], the Pöschl-Teller[82] attractive impurity potential [83, 84], and an impurity in the bottleneck conduction channel [85]. Experimentally, asymmetric Fano resonances have been observed in single-electron transistors with droplets of confined electrons [86], crossed carbon nanotubes [87], and in quantum wires coupled to a quantum dot [88, 89].

Through the Feshbach coupled-channel [79, 80, 90] theory and an S-matrix approach it has been shown that one can derive a Briet-Wigner type formula with an additional asymmetry parameter for transmission coefficients of propagating modes [91]. However, we observe a characteristic resonance profile *even for the evanescent modes in either direction* which reach a maximum at the resonance as seen in

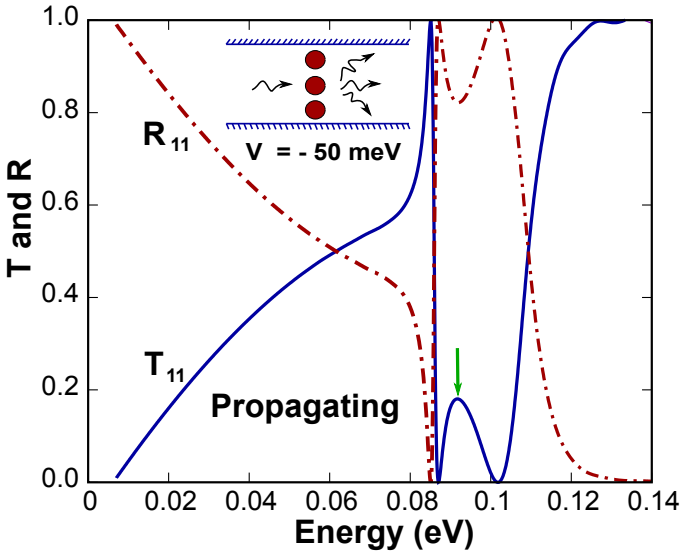

Figure 4.1: The transmission (T_{11}) and reflection (R_{11}) coefficients are shown as a function of energy for the propagating mode $n = 1$, with an incoming wave from the same mode, for scattering through three vertically aligned circular impurities of radius 3 nm whose centers are 10 nm apart, and depth -50 meV. The zero-transmission energy for T_{11} (E_R), the corresponding Fano q factor, and the line width Γ are given by $E_{R_1} = 0.087$ eV; $q_{R_1} = -1.1607$; $\Gamma_{R_1} = 0.001$ eV, and $E_{R_2} = 0.102$ eV; $q_{R_2} = 0.3229$; $\Gamma_{R_2} = 0.009$ eV, respectively.

Fig. 4.2. This is due to the interference between the quasi-bound metastable state and the evanescent modes. Notice that only the odd numbered modes contribute since the potential has C_{1h} symmetry, and the evanescent coefficients reach a maximum at the 5^{th} subband minimum (155.94 meV), as expected [72]. Such a profile was not found in all earlier theoretical simulations since they used asymptotic BCs [92]. In Section 4.4, we briefly discuss the Feshbach coupled-channel approach to derive the transmission coefficients with the Fano form and compare the results with our method. We find that there are small errors for the Fano parameters obtained through the Feshbach approach even for the simplest geometries. Moreover, the Feshbach approach is not amenable to a closed form solution, other than for very few potentials generated by simple geometrical structures [80].

In Fig. 4.1, we observe the Fano profile reversal at energy $E = 0.0917$ ev (marked by a green arrow in the plot). This can be quantified by noting the change of sign in the q-factor from -1.1607 to 0.3229. This q-reversal phenomenon has been widely studied in atomic physics, where the weak mixing of the interloper levels are attributed to such q-reversal observed in the Rydberg series spectrum [93, 94]. Connerade and Lane [94] have derived several conditions for such q-reversal. This

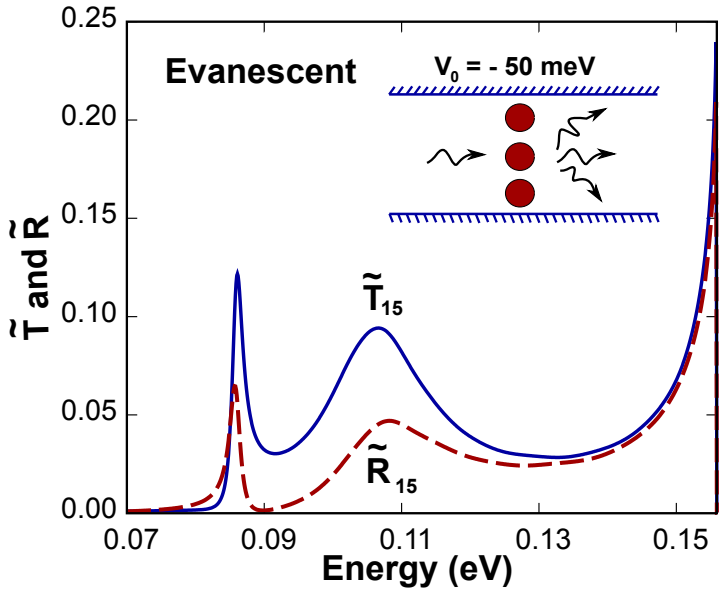

Figure 4.2: The transmission ($\tilde{T}_{15}$) and reflection ($\tilde{R}_{15}$) coefficients for evanescent modes are shown as a function of energy for the evanescent mode $n = 5$, with an incoming wave from the mode 1 at a distance $l = 10\,\text{nm}$, for scattering through vertically aligned three circular impurities of radius 3 nm whose centers are 10 nm apart, and whose potential depth is $V_0 = -50\,\text{meV}$.

phenomenon has also been identified in the transmission spectrum of quantum dots connected with 1D-channels [89, 95]. Such a change in parity is not observed for the evanescent modes which reach a maximum around the energy corresponding to the zero transmission.

In Fig. 4.3, we notice that for a hexagonal impurity[a] the Fano resonance profile changes parity while switching from the incoming mode 1 to the incoming mode 2. This is yet another type of q-reversal which occurs due to the change in symmetry of the incoming mode.

In Fig. 4.4, we plot the probability current at $E = 47\,\text{meV}$ for scattering through a hexagonal impurity with potential $V_0 = -10\,\text{meV}$ for an incoming mode 1. We observe that the current direction is unaltered since $T_{11} = 1$ at this energy due to the Fano resonance, as seen in Fig. 4.3(a). The magnitude of the probability current density has *diffraction spikes* due to the hexagonal shape of the impurity scattering potential, as seen in Fig. 4.4. Notice that when we have a repulsive hexagonal barrier, the probability current density will flow around the barrier [72]. On the

[a]All phenomena discussed in this chapter are essentially valid irrespective of the geometry of the potential. We have used a nontrivial hexagonal, circular or rectangular geometries to illustrate the universal behavior through our numerical work.

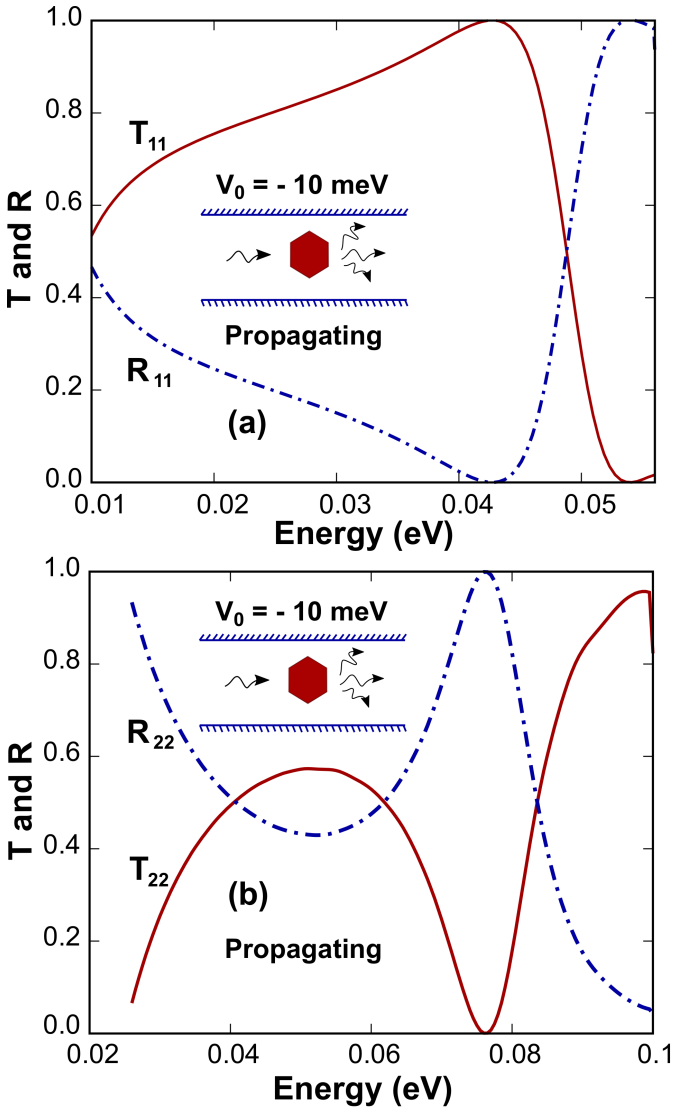

Figure 4.3: The transmission and reflection coefficients for propagating modes (a) T_{11} and R_{11}, and (b) T_{22} and R_{22} in transport through a hexagonal impurity with $V_0 = -10\,\text{meV}$ are plotted. Each side of the hexagon equals 5 nm. The zero-transmission energy (E_R), the Fano q-factor, and the line-width Γ are given by (a) $E_R = 0.055\,\text{eV}$; $q = -1.1384$; $\Gamma = 0.006\,\text{eV}$, and (b) $E_R = 0.0764\,\text{eV}$; $q = 0.3161$; $\Gamma = 0.008\,\text{eV}$.

other hand, with an attractive hexagonal potential, the current will reach a maximum at the center of the potential and form diffraction spikes emanating from its vertices.

In Fig. 4.5, we show the decay of evanescent modes $\tilde{T}_{24}$ and $\tilde{R}_{24}$ with distance for scattering through a hexagonal defect with $V_0 = -10\,\text{meV}$, at energy $E = 76\,\text{meV}$ at which $T_{22} = 0$ (see Fig. 4.3 (b)). Through exponential curve fitting we notice

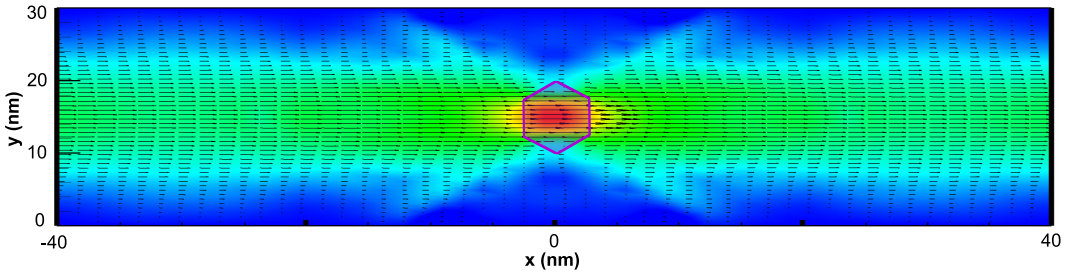

Figure 4.4: The probability current density at $E = 47\,\text{meV}$ for transport through a hexagonal impurity potential with $V_0 = -10\,\text{meV}$ for an incoming mode $n = 1$ is shown. At this energy $T_{11} = 1$ due to the Fano resonance, and hence we obtain an unperturbed current flow in the forward direction throughout. In this plot, the magnitude of the probability current density ranges from 0 to 0.065, which is represented by a continuous contour color coding varying from blue to red.

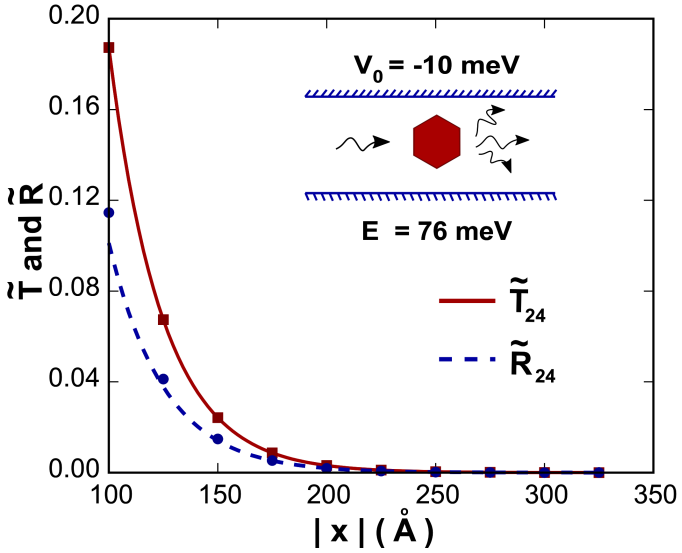

Figure 4.5: Decay of transmission ($\tilde{T}_{24}$) and reflection ($\tilde{R}_{24}$) coefficients for evanescent modes are shown as a function of x(Å) for $E = 76\,\text{meV}$ for scattering through a regular hexagonal impurity of side $= 50\,$Å. The incoming mode is $n = 2$ and the scattering potential is $V_0 = -10\,\text{meV}$. Here we carried out the modal analysis [72] at every 25Å. Equations from the curve fitting are given by $\tilde{T}_{24} = 11.18650 \exp(-2 \times 0.02045\, x)$, and $\tilde{R}_{24} = 5.18618 \exp(-2 \times 0.01969\, x)$. Theoretically determined $K_{x5} = 0.02045/\text{Å}$, which is close to the curve fit values.

that the evanescent modes have large amplitudes around the scattering center. Note that the decaying behavior of the transmission and reflection coefficient observed in Fig. 4.5 is consistent with Eq. (4.4).

4.3 Effect of varying potential on electron transmission

In this section, we discuss the effects of varying the potential on the transmission profile for both propagating and evanescent modes. We include the case of both attractive and repulsive scatterers. For a rectangular barrier, the coefficient T_{11} attains a resonance maximum which will shift towards the next allowed subband minimum ($E_{y,3} = 0.056\,\text{eV}$) with increase in the barrier height as shown in Fig. 4.6. We effectively have slowed down the waves in the barrier region by increasing the barrier height. Whereas for the evanescent waves, the maximum will be still at the next allowed subband minimum ($E_{y,3}$) and its maximum will increase with barrier height.

In Sec. 4.2, we discussed the emergence of the Fano profile for the transmission coefficients in the case of attractive scatterers. Here, we study the effect of varying the impurity potential for such a resonance. To illustrate this we study the scattering through a hexagonal impurity. In Fig. 4.7, we plot coefficients T_{22} and $\tilde{T}_{24}$ as a function of energy for different values of the potential barrier. We see that for weaker attractive potentials ($V_0 = -5\,\text{meV}$), we have a strong resonance with $T_{22} = 1$ near $E_{y,4} = 99.80\,\text{meV}$ (see Fig. 4.7). The resonance value decreases for more negative potential values, since the bound states move further below the continuum. For $V_0 = -120\,\text{meV}$, the Fano resonance profile disappears. Additional bound states may appear which can interact with scattering modes if we further deepen the well.

The evanescent mode ($\tilde{T}_{24}$) reaches a maximum when $T_{24} \approx 0$ which is much before the 4^{th} subband minimum ($E_{y,4}$) (see Fig. 4.7(b)). There are two governing conditions which lead to high amplitudes for the evanescent modes; (i) at the transmission minimum for the propagating modes the evanescent modes will have a peak, and (ii) they also tend to reach higher values at the subband minima. For $V_0 = -120\,\text{meV}$, $\tilde{T}_{24}$ has a much lower value since there is no Fano resonance, with the maximum value at the subband minimum.

4.4 Feshbach coupled-channel theory and Fano resonance

The Fano resonance for waveguide scattering with attractive scatterers are typically treated [79, 80, 91] within the Feshbach approach [90]. We compare the analytical expression for transmission coefficients obtained through this analysis and the nu-

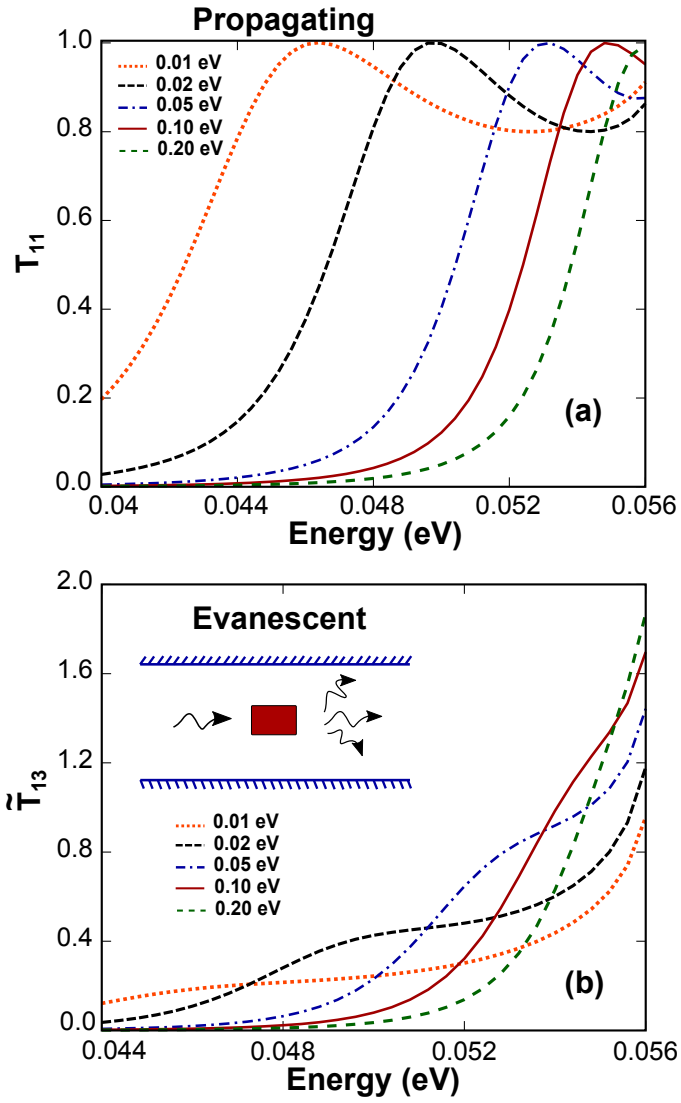

Figure 4.6: The transmission coefficients T_{11} and $\tilde{T}_{13}$ as a function of energy for a rectangular barrier with varying height are shown. A modal analysis [72] is done at $|x| = 10\,\text{nm}$ for the scattering coefficients.

merically calculated ones with our approach. In a 2D straight waveguide, we expand the scattered wavefunction in the form

$$\psi(x,y) = \sum_{n=1}^{\infty} \chi_n(x) \sin\left(\frac{n\pi\, y}{w}\right), \tag{4.5}$$

and the coupled-channel equation for $\chi_n(x)$ is given by

$$\left[-\frac{\hbar^2}{2m}\frac{d^2}{dx^2} + \left(E_{y,n} - E\right)\right]\chi_n(x) + \sum_{m=1}^{\infty} U_{nm}(x)\chi_m(x) = 0, \tag{4.6}$$

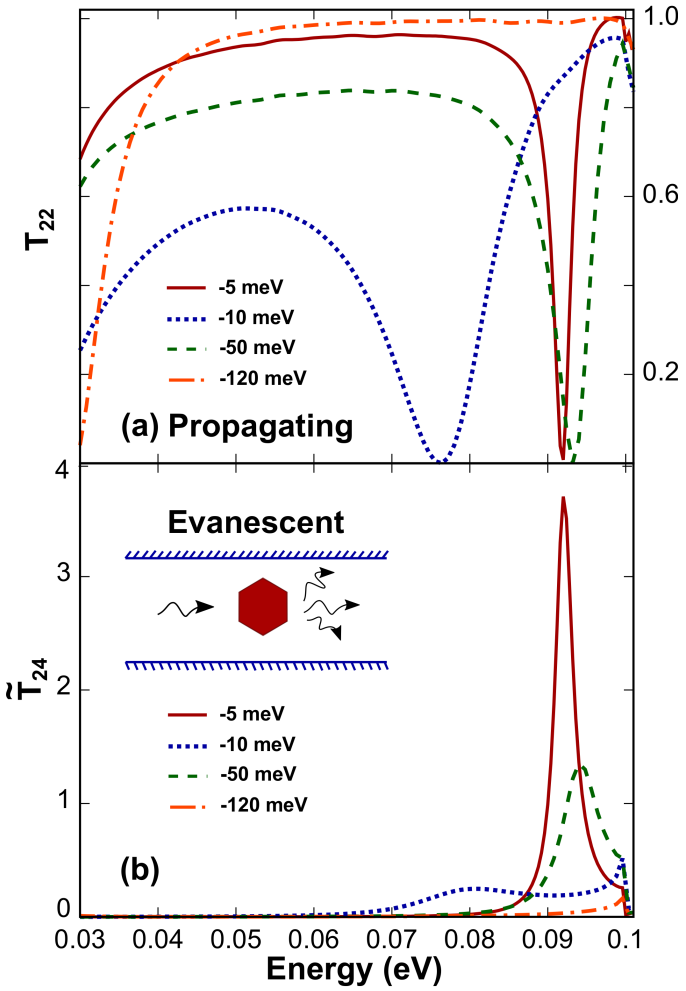

Figure 4.7: The transmission coefficients T_{22} and $\tilde{T}_{24}$ as a function of energy for a regular hexagonal impurity with a side length of 5 nm for different values of the potential are shown. A modal analysis is done at $|x|$ =10 nm for the scattering coefficients.

where $U_{nm}(x) = \int_0^w dy\ \sin(n\pi/w)V_0(x,y)\sin(m\pi/w)$ is the coupling matrix element. In order to compare our method with other methods and results we consider the *simplest* potential of the form

$$V_0(x,y) = \begin{cases} -\alpha\,\delta(x), & |y - w/2| \le y_s, \\ \\ 0, & \text{otherwise}, \end{cases} \tag{4.7}$$

where w is the waveguide width and $y_s < w/2$ is the range. Numerically, we specify the above potential by having several nodal values along the line $x = 0$, and $|y - w/2| < y_s$. Through this procedure, the $\delta(x)$ dependence of the potential is

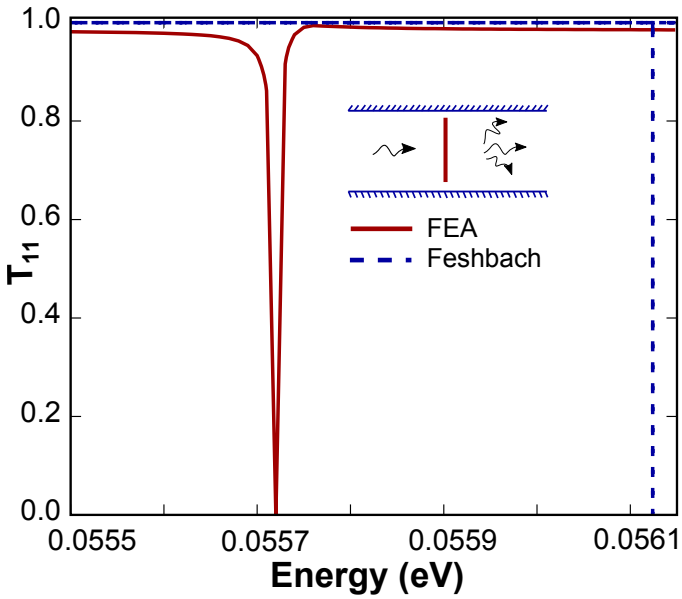

Figure 4.8: The transmission coefficient T_{11} is plotted as a function of energy obtained using our method (continuous curve) and using the Feshbach approach (dashed curve) for $\alpha = -0.01$ eV m and $y_s = 10$ nm for a straight waveguide of width 30 nm. The Fano parameters determined through (i) Feshbach calculations are $E_R = 0.05612$ eV, $q = 0.0046$, and $\Gamma = 0$ eV, (ii) our formalism are $E_R = 0.05572$ eV, $q = 0.0047$, and $\Gamma = 3.4 \times 10^{-6}$ eV. The difference between the parameters obtained through our method and the Feshbach approach is within 3 %.

integrated out in the action integral. The coupling matrix element is

$$U_{nm}(x) = -\alpha\delta(x)\, u_{nm};$$
$$u_{nm} = \int_{-y_s+w/2}^{y_s+w/2} dy\ \sin(n\pi/w)\sin(m\pi/w). \tag{4.8}$$

The off-diagonal (in m, n) matrix elements occur when the potential has a finite range $2y_s$ that is less than the width w of the waveguide. The potential has C_{1h} symmetry, and hence only the odd-modes are relevant to our analysis. For an incoming wave in mode 1 let us study the scattering within the energy interval $E_{y,1} < E < E_{y,3}$. We retain only the first two bands, the propagating ($n = 1$) and the evanescent ($n = 3$) in Eq. (4.6). If the coupling matrix element U_{13} is absent, we write

$$\left[-\frac{\hbar^2}{2m}\frac{d^2}{dx^2} + U_{11}(x)\right]\chi_1^0(x) = (E - E_{y,1})\chi_1^0(x). \tag{4.9}$$

Hence the formal solution to $|\chi_1\rangle$ is given by

$$|\chi_1\rangle = \left|\chi_1^0\right\rangle + \hat{G}_1 U_{13}\,|\chi_3\rangle\,, \tag{4.10}$$

where $\langle x|\chi_1^0\rangle = \chi_1^0(x)$, is the solution to Eq. (4.9), and $\hat{G}_1$ is the Green's function operator given by

$$\hat{G}_1 = \left[\frac{\hbar^2}{2m}\frac{d^2}{dx^2} + E - E_{y,1} - U_{13} + i\epsilon^+\right]^{-1}. \tag{4.11}$$

We use the *ansatz* [91, 120] $\chi_3(x) = \tilde{t}_{13}\,\Phi_0(x)$, where $\tilde{t}_{13}$ is the evanescent amplitude and $\Phi_0(x)$ is the bound state solution to the equation:

$$\left[-\frac{\hbar^2}{2m}\frac{d^2}{dx^2} + U_{33}(x)\right]\Phi_0(x) = (\mathcal{E} - E_{y,3})\Phi_0(x), \tag{4.12}$$

where $\mathcal{E}$ is the bound state energy. Solving Eqs. (4.9), (4.11) and (4.12) we obtain the transmission amplitudes in the form

$$\begin{aligned} t_{11} &= t\,\frac{(E-\mathcal{E})}{(E-(\mathcal{E}+\Delta)+i\Gamma)},\\ \tilde{t}_{13} &= \frac{\mathcal{F}}{(E-\mathcal{E}+i\,\eta)}, \end{aligned} \tag{4.13}$$

where the corresponding parameters are listed in Table 4.1.

$\mathcal{E} = E_{y,2} - \dfrac{m\alpha^2 u_{33}^2}{2\hbar^2}$;	$t = \dfrac{ik_1}{\left(ik_1 + \dfrac{m\alpha\,u_{11}}{\hbar^2}\right)}$,
$\Delta = \left(\dfrac{\alpha^4 m^3}{\hbar^6}\right)\left(\dfrac{u_{33}u_{11}u_{13}^2}{k_1^2 + \dfrac{m^2\alpha^2 u_{11}^2}{\hbar^4}}\right)$;	$\mathcal{F} = -\alpha\,t\,u_{13}\sqrt{\dfrac{u_{33}m\alpha}{\hbar^2}}$,
$\Gamma = \left(\dfrac{\alpha^3 m^2}{\hbar^4}\right)\left(\dfrac{u_{33}u_{13}^2 k_1}{k_1^2 + \dfrac{m^2\alpha^2 u_{11}^2}{\hbar^4}}\right)$;	$\eta = \alpha^3 u_{13}^2 u_{33}\,t\,\dfrac{m^2}{k_1\hbar^4}$.

Table 4.1: The Fano parameters corresponding to the amplitudes defined in Eq. (4.13) are listed, where $k_1 = \sqrt{2m(E_R - E_1)/\hbar^2}$.

Within the resonance approximation [80], we have the transmission coefficient

$$T_{11} = |t_{11}|^2 = |t|^2\,\frac{(E-\mathcal{E})^2}{(E-\mathcal{E}-\Delta)^2 + \Gamma^2}. \tag{4.14}$$

Let the quasi-bound state energy $E_R = \mathcal{E} + \Delta$, and we define the reduced variables

$$\epsilon = \frac{(E - E_R)}{\Gamma}; \qquad q = \frac{\Delta}{\Gamma}, \tag{4.15}$$

where the Fano q-factor determines the asymmetry of the line shape, and Γ represents the line-width. With this reduction we obtain

$$T_{11} = |t|^2 \frac{(\epsilon + q)^2}{\epsilon^2 + 1}, \tag{4.16}$$

which has the standard Fano form [74, 78, 91]. When $T_{11} = 0$ (at $E = \mathcal{E}$), we see that the evanescent amplitude $\tilde{t}_{13}$ reaches a maximum, as seen in Fig. 4.7.

In Fig. 4.8, we compare the transmission coefficient T_{11} obtained using our method and the Feshbach approach. We observe that the Feshbach approach has a small error in predicting the energy value of the transmission minimum and the Fano line width Γ is under-estimated, as compared with our approach. This is evident already for the simplest δ-potential. We expect to have significant errors with such coupled-channel theory when we consider geometrically more complex potentials. This is because the Feshbach approach is essentially a two-band model, whereas our method incorporates contributions from all the subbands. Moreover, such analytical methods are not amenable to a solution, other than for a very few potentials generated by simple geometrical structures. We note that our method transcends any such geometrical complications and is expected to yield accurate results.

4.5 Enhancement of power factor through defects and impurities

Consider transport through a multichannel lead connected to reservoirs at equilibrium attached to the waveguide on either end. The conductance G and the Seebeck coefficient (thermopower) S, for a given chemical potential μ_F and temperature T, calculated using the Landauer-Büttiker formalism [96–102] are given by

$$G(\mu_F, T) = \frac{2e^2}{h} \sum_i \int_0^\infty dE \left(-\frac{df}{dE}\right) T_i(E), \tag{4.17}$$

and

$$S(\mu_F, T) = \frac{k_B}{e} \frac{\sum_i \int_0^\infty dE \left(-\frac{df}{dE}\right) T_i(E) \left(\frac{E - \mu_F}{k_B T}\right)}{\sum_i \int_0^\infty dE \left(-\frac{df}{dE}\right) T_i(E)}, \tag{4.18}$$

where, f is the Fermi-Dirac distribution function, k_B is the Boltzmann constant, e is the fundamental electron charge and T_i is the transmission probability from all

channels to the channel i given by $T_i = \sum_j T_{ij}$. In the low temperature limit, these expressions reduce to a simpler form [103, 104] given by

$$G(\mu_F, T = 0) = \frac{2e^2}{h} \sum_i T_i(\mu_F) = \frac{2e^2}{h} \sum_{i,j} T_{ij}(\mu_F),$$
$$S(\mu_F, T) = \frac{(k_B \pi)^2}{3e} T \frac{d}{dE} (\ln G(E, 0)) \Big|_{E=\mu_F}. \tag{4.19}$$

We evaluate the conductance and the Seebeck coefficient as functions of the chemical potential in the case of attractive and repulsive scatterers for different values of the potential. It is essential to determine both G and S to characterize the energy conversion efficiency by the dimensionless figure of merit (ZT) given by

$$ZT = \frac{GS^2}{\kappa} T, \tag{4.20}$$

where κ is the thermal conductance of the material which includes phonon and electron contributions.

In Fig. 4.9, we plot the conductance as a function of chemical potential for different heights of a hexagonal barrier. Conductance will no longer preserve the quantization, and it will be suppressed as we increase the barrier height. Near the subband minima we observe the Ramsauer-Townsend type resonance due to the high probability of evanescent modes [65, 105]. In Fig. 4.10, we plot the thermopower as a function of the chemical potential for different heights of a hexagonal barrier. We see that the thermopower reaches high positive values at low energies around the subband minima. Increase in the barrier height can slightly increase the values of the Seebeck coefficient though its profile remains the same. The power factor (GS^2) will be close to 1 around the second subband minimum, and will not vary much with the barrier height (see Fig. 4.11).

In the case of attractive scatterers, resonant dips are observed for the conductance (see Fig. 4.12) at the subband minima which are attributed to the formation of quasi-bound states whose energies are determined by finding poles of the Green's function for the system [68, 106]. We see that the conductance decreases and the resonant dips disappear as we deepen the negative potential. The quasi-bound states lead to both positive and negative values for the Seebeck coefficient around the subband minima (see Fig. 4.13). Notice that the maximum value of the thermopower decreases as we deepen the negative potential. From Fig. 4.14, we see that the power factor can

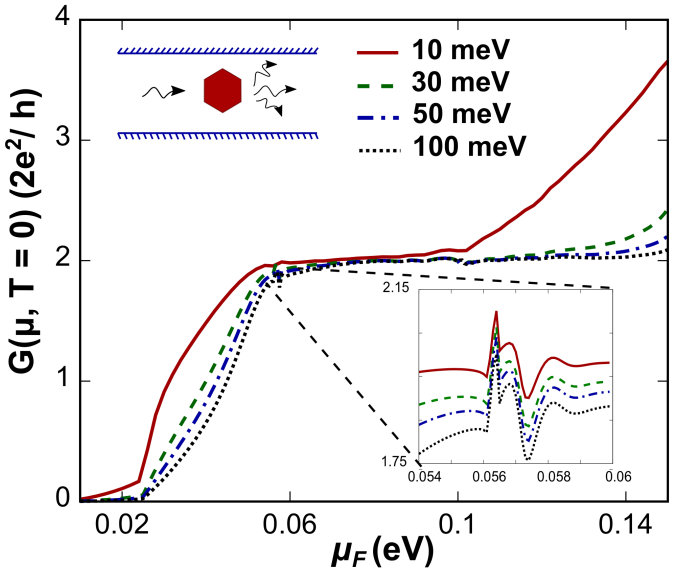

Figure 4.9: The conductance $G(\mu_F, T = 0)$ as a function of the chemical potential μ_F for scattering from a regular hexagonal barrier defect with a side of length 5 nm. We have shown the conductance for four different potential values. Within the inset we have shown $G(\mu_F, T = 0)$ between the range $0.054 - 0.06$ eV.

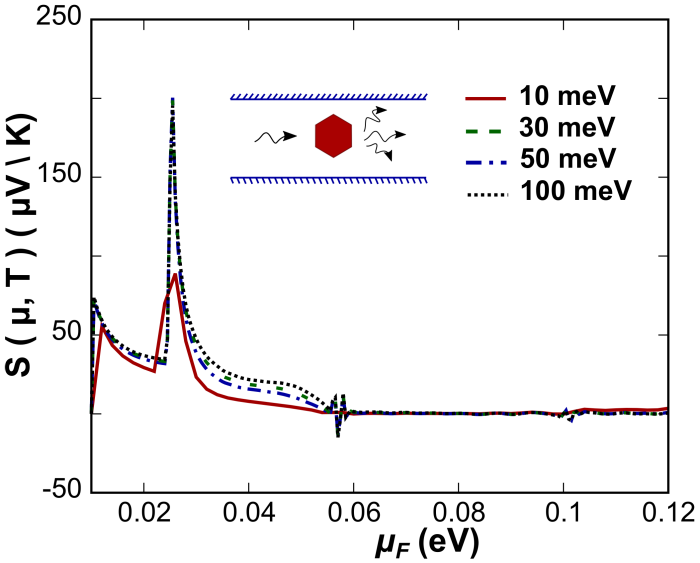

Figure 4.10: The Seebeck coefficient $S(\mu_F, T)$ (in units of μV/ K) as a function of the chemical potential μ_F for scattering from a regular hexagonal barrier defect with side length 5 nm evaluated at T=10 K is shown. The thermopower for four different potential values are displayed.

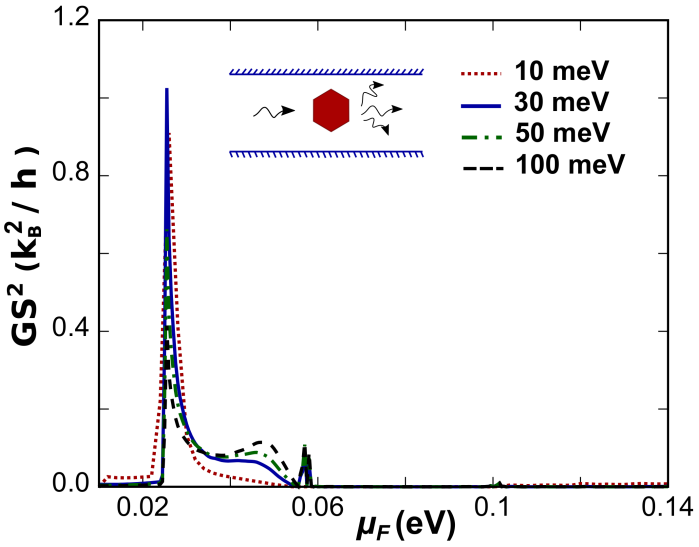

Figure 4.11: The power factor GS^2 (in units of k_B^2/h) as a function of the chemical potential μ_F for scattering from a regular hexagonal barrier defect with side length 5 nm evaluated at temperature $T = 10\,K$. We have shown the power factor for four different potential values.

reach large values around the subband minima in the case of impurity scatterers. We obtain multiple peaks at each subband minimum since the Seebeck coefficient has multiple resonances.

Transport in a waveguide, with attractive impurities or quantum dots being present, provides the means of obtaining large Seebeck coefficients and the power factor. This will be of interest in thermoelectric applications [107, 108], and these can be extended to spatially confined nanostructures. Having an attractive impurity distribution surpasses the limits on the power factor asserted earlier [109] in the case of ballistic transport.

We note that the Landauer-Büttiker conductance formula in the present form will not take into account changes in the potential arising from a charge accumulation due to the evanescent modes. It would require a self-consistent solution [110] of the Schrödinger-Poisson equation to calculate the additional potential which depends on the probability density of carriers in the evanescent modes. This issue will be addressed separately in the near future.

4.6 Tapered waveguides

Next, we study the ballistic transport in a tapered waveguide. In this case, the energy levels for local subband minima at one end are lower or higher than the subbands

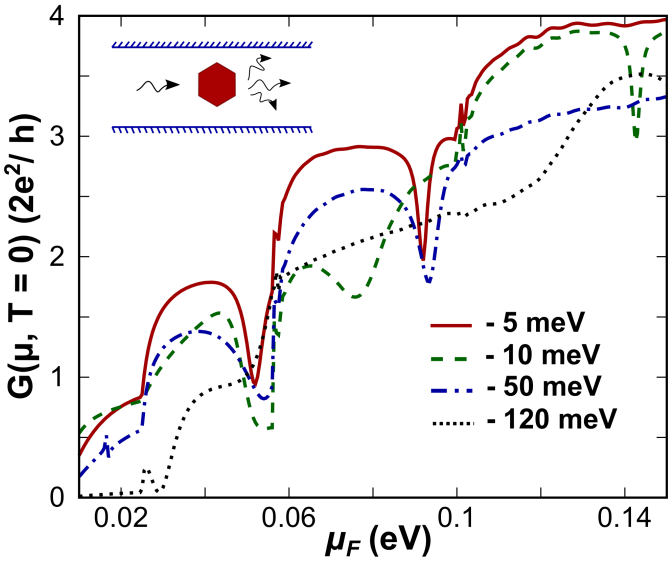

Figure 4.12: The conductance $G(\mu_F, T = 0)$ as a function of the chemical potential μ_F for scattering from a regular hexagonal impurity with a side length 5 nm is shown. The conductance for four different potential values is displayed. We observe the formation of resonant dips at the subband minimum which disappear for $V_0 = -120$ meV.

at the other end. Hence, new propagating and evanescent modes will emerge in the scattered wavefunction. A tapered waveguide will still preserve the C_{1h} symmetry if the tapering angle is the same in either direction. Therefore, contributions from different modes still follow the selection rules discussed in Sec. 3.3.

In Fig. 4.15, we plot the transmission and reflection coefficients for the tapered waveguide with a left end of width 50 nm, and the right end of width 10 nm. We choose our incoming energy below the first subband minimum (56.14 meV) of the right end. We perform the modal analysis [72] at either end of the waveguide to obtain the scattering amplitudes. Since this set up does not allow any transmission of propagating waves below 56.14 meV, we observe only contributions for the current coming from the reflection coefficients R_{11} and R_{13}. However, we observe a fairly high amplitude for the evanescent transmission coefficient $\tilde{T}_{11}$ due to the tapering. Evanescent modes lead to electron localization in the waveguide, thereby altering the potential through a change in the local electron distribution. *Since we have evanescent modes only in the transmission direction, tapered waveguides provide the means of changing the conductance while keeping the current constant.*

Next, we study the transport from a smaller to a wider cross-sectional waveguide. In Fig. 4.16, we plot the transmission coefficients for three different tapering angles.

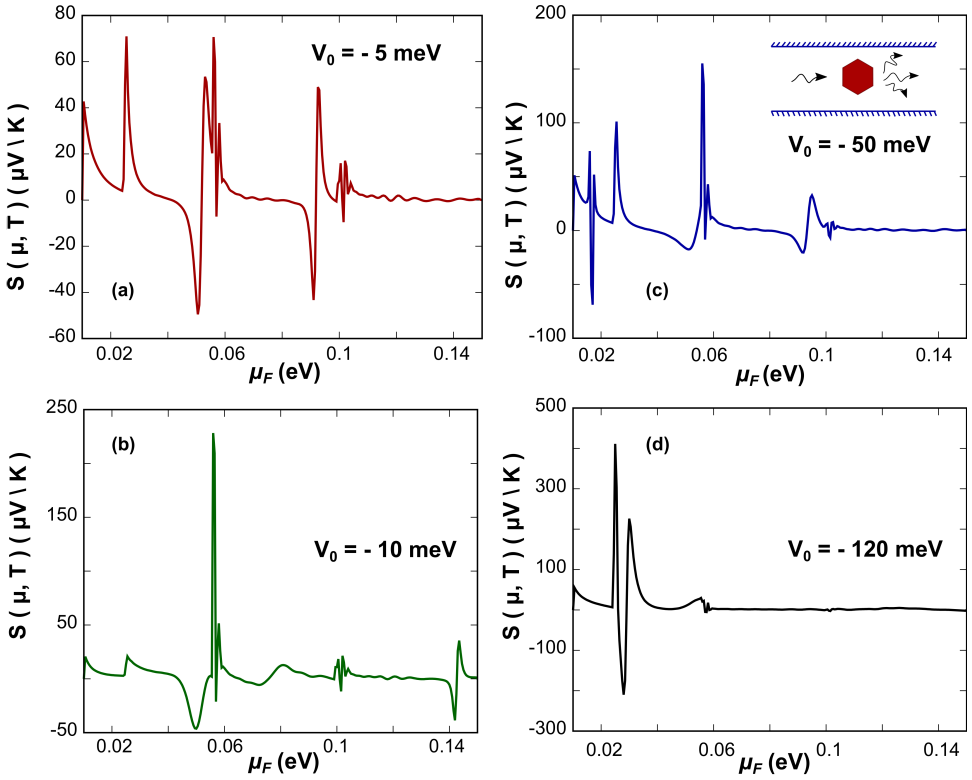

Figure 4.13: The Seebeck coefficient $S(\mu_F, T)$ (in units of μV/K) as a function of the chemical potential μ_F for scattering from a regular hexagonal impurity with side length 5 nm evaluated at T=10 K is shown. $S(\mu_F, T)$ for four different potential values are displayed. We can obtain large Seebeck coefficient by deepening the value of negative potential.

For our choice of incoming energies we observe only propagating modes since a wider cross-section has all subband minima below the incoming subband minimum for the smaller cross-section. We see that only the 1^{st}, 3^{rd} and 5^{th} modes contribute, again as per the selection rules (refer Sec. 3.3).

Though our incoming mode is $n = 1$, we observe other odd number modes because of the coupling generated to these modes from the tapering boundaries of the waveguide.

At $E_{y,3} = 56.14$ meV for the incoming mode, we observe a strong resonance in the transmission profiles. By increasing the tapering angle we can decrease the contribution from mode 1, while contributions from the 3^{rd} and the 5^{th} mode increase. *The tapered waveguide provides a new way of developing a nanoscale rectifier since the currents through it that are initiated at either end are inequivalent.* This is seen in Figs. 4.15 and 4.16.

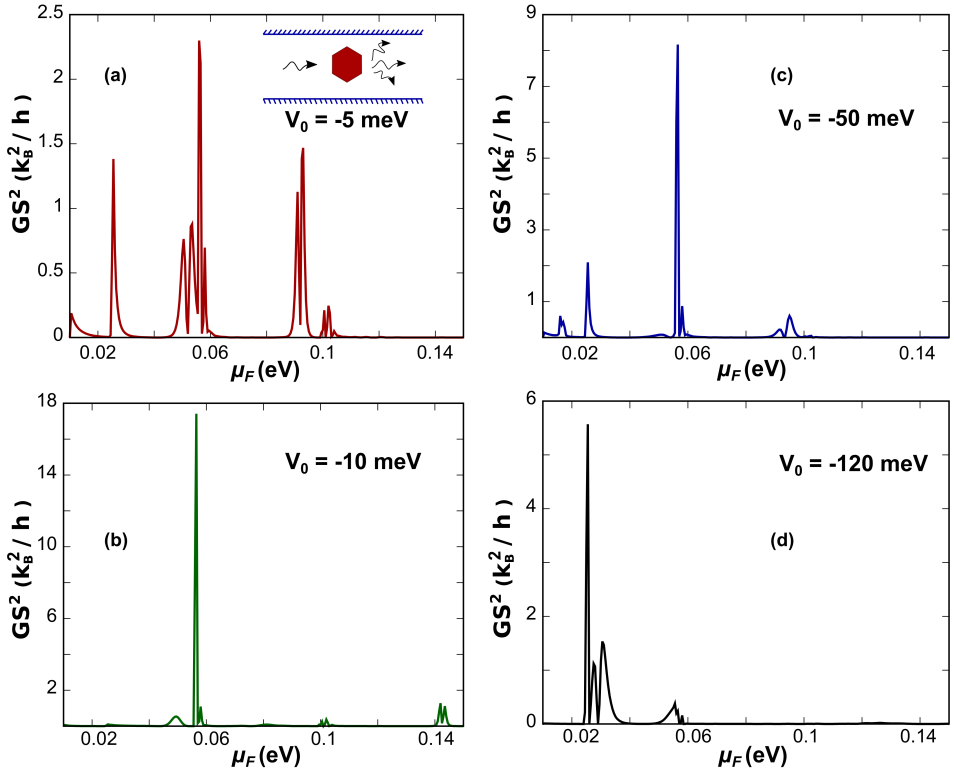

Figure 4.14: The power factor GS^2 (in units of (k_B^2/h)) as a function of the chemical potential μ_F for scattering from a regular hexagonal impurity with side length 5 nm evaluated at a temperature $T = 10\,K$ is shown. We have shown the power factor for four different potential values. We can obtain large power factors around the subband minima.

4.7 Curved waveguides

While designing electronic circuits, invariably we will have channels with bends connecting different straight waveguides. Goldstone and Jaffe [111] have shown that the curved channels in 2D and twisted tubes in 3D can support bound states. Schult *et al.* [112] found the presence of bound states in a classically unbound system of crossed wires. We expect to have evanescent modes even in the ballistic transport through empty curved or crossed channels since the translational symmetry is broken. It has been shown that we can obtain a series of Fano lines in an empty curved waveguide due to curvature effects [113]. Olendski and Mikhailovska [114] have shown the presence of a Fano resonance profile when a quantum dot is embedded in a uniformly curved waveguide. Such calculations are done by solving the wave equation in the circular coordinate system, and the potential is taken to be circularly symmetric. In our method, we have no such constraints since we work with a discretized space. As an example we obtain the transmission coefficients for

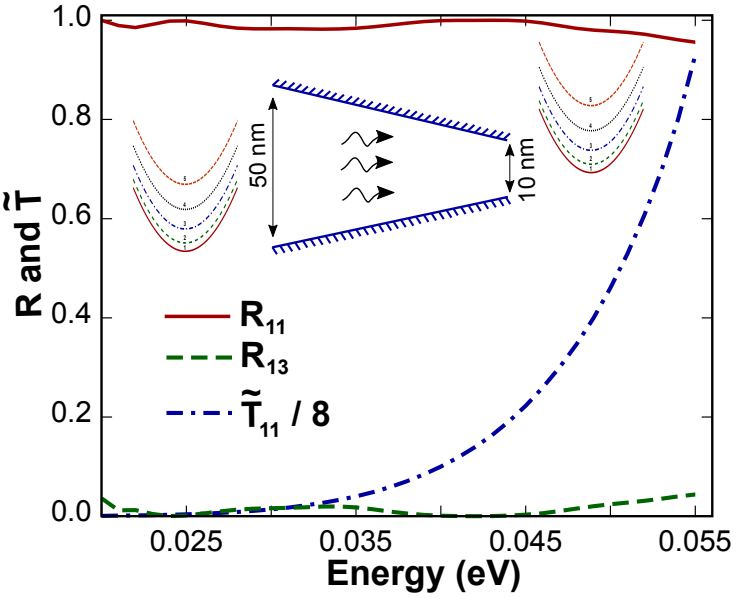

Figure 4.15: The reflection and transmission coefficients for a tapered waveguide with an incoming wave from the end of width 50 nm to the outgoing end of width 10 nm are shown.

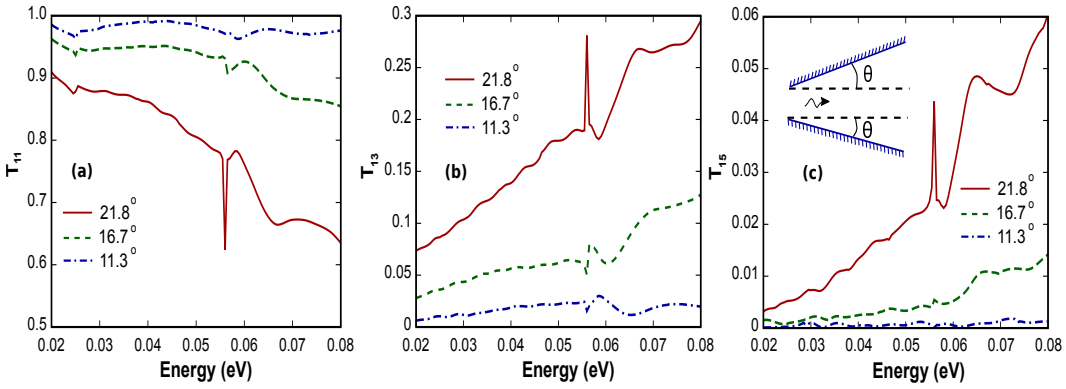

Figure 4.16: The transmission coefficients for the propagating modes (a) T_{11}, (b) T_{13}, and (c) T_{15} as a function of energy are plotted for a tapered waveguide going from the smaller (30 nm) to a wider cross-section for three different tapering angles.

different bending angles in a curved waveguide with an embedded square quantum dot.

In Fig. 4.17, we plot the transmission coefficients T_{11}, $\tilde{T}_{12}$, $\tilde{T}_{13}$ and $\tilde{T}_{14}$ for scattering from a square quantum dot of dimensions 20×20 nm and a potential $V_0 = -10$ meV. The bent geometry of the waveguide does not have C_{1h} symmetry, hence all modes contribute to the wavefunction. Since the energy is taken to be below $E_{y,2} = 0.0249$ eV, we have only one propagating mode ($n = 1$). We see several transmission

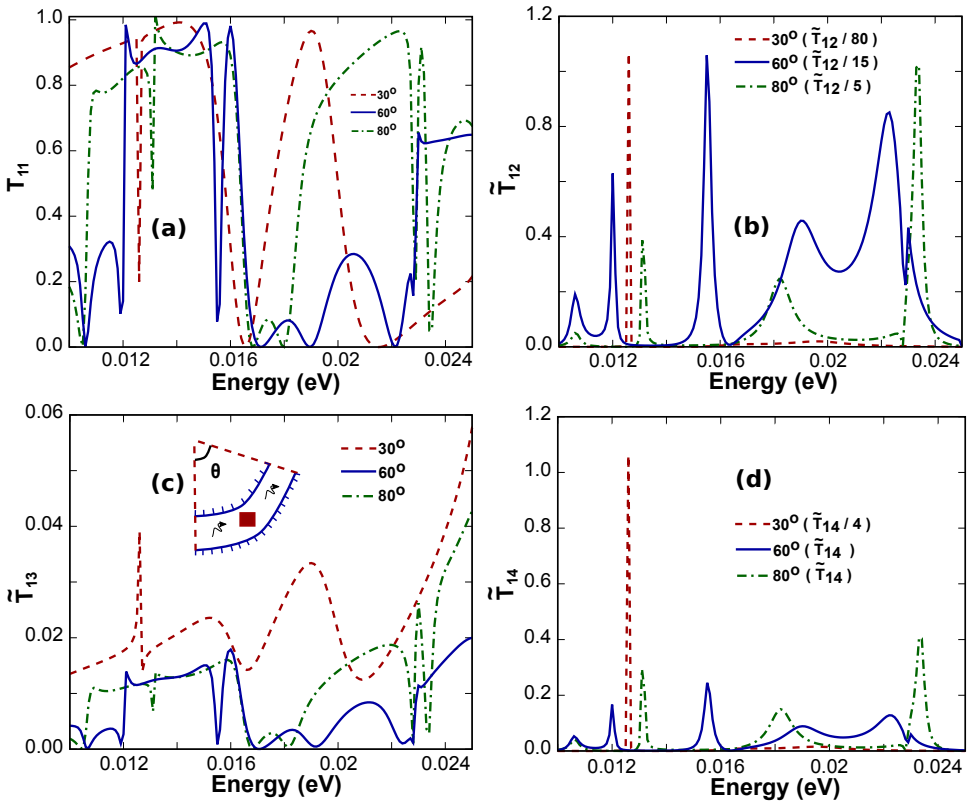

Figure 4.17: The transmission coefficients for the propagating mode (a) T_{11}, and for the evanescent modes (b) $\tilde{T}_{12}$, (c) $\tilde{T}_{13}$, and (d) $\tilde{T}_{14}$ are plotted as a function of energy for a curved waveguide of width 30 nm embedded with a square quantum dot of dimensions 20×20 nm. The potential within the quantum dot $V_0 = -10$ meV.

dips for T_{11} due to the Fano effect. As explained earlier, such a dip in the propagating mode leads to a high probability for evanescent modes. For a curvature angle of $\theta = 30^o$, $\tilde{T}_{12}$ will be as large as 85 at $E = 0.0126$ eV. The probability of evanescent modes decreases with the curvature angle as seen in Figs. 4.17(b), (c) and (d). We note the formation of Fano line profiles even for the evanescent modes around the transmission minima.

4.8 Conclusions

We have shown that in quantum waveguides with attractive scatterers, there are two dominant characteristics of the evanescent modes: (i) the evanescent modes reach a maximum at the subband minimum, and (ii) the evanescent modes have large amplitudes around the zero-transmission resonance energy. A universal way of calculating amplitudes of both propagating and evanescent modes is described. We have displayed the Fano resonance profile *for both propagating and evanescent*

modes for the case of scattering from impurities. This effect can be explicitly evaluated for any attractive scattering potential. The resonance formula for the two cases are derived in Section 4.4.

Earlier theoretical developments were constrained by the need for analytical techniques, limiting considerations to δ-function potential. With our method, we can easily overcome this artificial limitation. Moreover, electron transport in a waveguide with multiple scattering centers are not an issue anymore. Since we are espousing a numerical calculation, there is no additional step required as in earlier considerations, such as repeatedly invoking the Born approximation [115].

We have described the scattering mechanism in tapered and curved waveguides. These 2D waveguides can be fabricated on inversion layers of hetero-interfaces which hosts 2D electron gas, and by designing appropriate gate geometries. Thus, the results can be readily confronted with experimental outcomes. In tapered waveguides, the direction of the incoming current has a broken inversion symmetry. This provides a unique situation of possible current rectification throughout the device geometry.

We can include the effect of an external magnetic field using a local gauge which acts as a multiplicative term for the matrix elements [116]. This generates rapidly converging results even in the presence of a magnetic field. The usual gauge-invariant substitution for the momentum operator leads to a quadratic diamagnetic potential which is troublesome to evaluate at large distances from the orbit center. The Ueta method [116] circumvents this problem. Similarly, the Dresselhaus [117] and Rashba [118] spin-orbit effects can be incorporated as additive terms in the action integral. Absorption effects can be deftly included in our method by introducing a negative imaginary part to the potential [119]. Such a scheme will account for gate-contacts in 2D inversion layers, where the gate-contacts siphons off the probability current going across the device.

Calculations of conductance, Seebeck coefficient, and power factors can directly predict experimentally measurable quantities. Lastly, we have shown that quantum dots or attractive impurity potentials embedded in the interior of a waveguide are good candidates for fabricating thermoelectric devices since they yield large power factors around the subband minima.

Chapter 5

SCALABLE FIRST-PRINCIPLES-INFORMED QUANTUM TRANSPORT THEORY IN TWO-DIMENSIONAL MATERIALS

This chapter is organised as follows. In Sec. 5.2, we develop a non-asymptotic quantum scattering theory based on sources and absorbers. With this setup, we obtain the total wavefunction that includes both propagating and evanescent band contributions. This formalism is extended to a multiband framework, by integrating with it the $\boldsymbol{k}\cdot\boldsymbol{p}$ perturbation theory with inputs from DFT calculations. This will be explained further in Sec. 5.3. In Sec. 5.4, we describe the method to evaluate the scattering times within the relaxation time approximation. In that section we will also explain the method to include the thermal properties in our formalism through deformation potentials obtained through DFT calculations. In Sec. 5.5, we apply our formalism to study transport properties in lateral TMDC heterostructures. We observe the emergence of Fano resonances in 2D materials with material inclusions. We also study the mobility of electrons in lateral heterostructures for a family of TMDC monolayers. Concluding remarks are given in Sec. 5.6.

5.1 Introduction

Density-functional theory (DFT) [122] provides a parameter-free method for the electronic structure calculations, and accurately determine the atomistic potentials associated with heterointerfaces, defects, and impurities. However, DFT is ineffective for direct modeling of carrier transport properties at length scales relevant to device applications. There have been efforts to provide an atomistic quantum transport framework based on the tight-binding methods [123], plane-wave representation of the empirical pseudo-potentials [124], and DFT-based non-equilibrium Green's function techniques [125, 126]. However, such simulations are limited to a small number of atoms, ranging from few hundreds to thousands, and can be computationally expensive. Moreover, scattering across the material interfaces will have significant contributions from the decaying evanescent modes. Traditional scattering calculations will not be able to account for these crucial contributions, since the probabilities of evanescent modes vanish at the asymptotic limit where the boundary conditions BCs) are applied to determine the scattering amplitudes. Hence, we require a scattering framework where the scattering properties are evaluated in

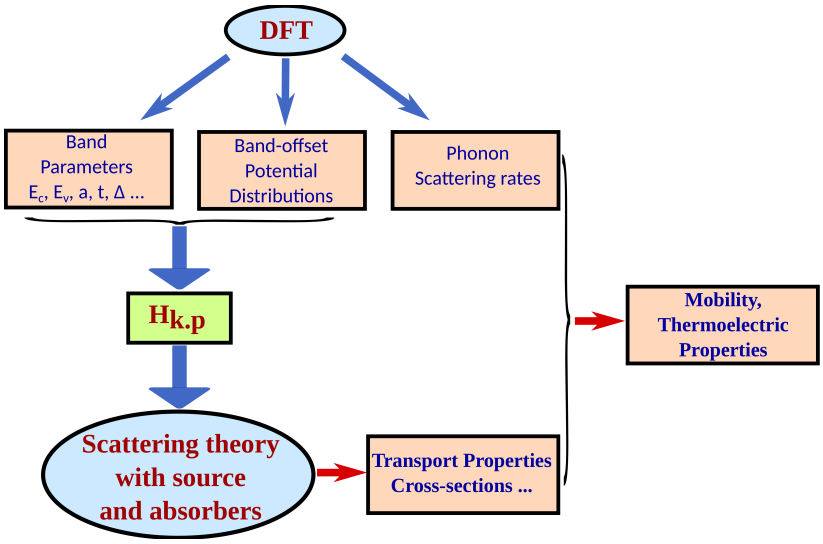

Figure 5.1: Flowchart of the quantum transport framework discussed in this chapter.

proximity to scattering centers.

In this chapter, alternatively, we setup a first-principles-informed continuum quantum transport theory. We first develop a novel non-asymptotic quantum scattering theory for the open domain. We show that bridging our scattering theory framework and the $\boldsymbol{k} \cdot \boldsymbol{p}$ perturbation theory, using inputs from *ab-initio* electronic structure calculations provides a versatile multiscale formalism. This formalism can easily scale into device dimensions. Hence it will be very useful to simulate and design electron optics, and nanoelectronics platforms. In Fig. 5.1, we display the flowchart of the quantum transport framework discussed in this chapter. The band parameters, potential distributions, and phonon scattering rates are obtained through DFT calculations. These quantities will be an input to the $\boldsymbol{k} \cdot \boldsymbol{p}$ Hamiltonian which is then solved using the non-asymptotic quantum scattering theory. By combining the carrier scattering rate obtained through our calculations with the phonon scattering rate obtained though first-principles calculations, we can accurately obtain the mobility and thermoelectric performance of the devices.

In Fig. 5.2, we consider a heterointerface formed between MoS_2 and WS_2 monolayers. From the electronic structure calculations, we know that MoS_2 ($E_c = -4.31$ eV) has a lower conduction band minimum than WS_2 ($E_c = -3.97$ eV) monolayer. Hence, when an electron with energy $-4.31\,\text{eV} \leq E < -3.97\,\text{eV}$ is injected from the MoS_2 to the WS_2 monolayer, transport occurs only through the evanescent modes. These evanescent modes are placed within the bandgap and will have

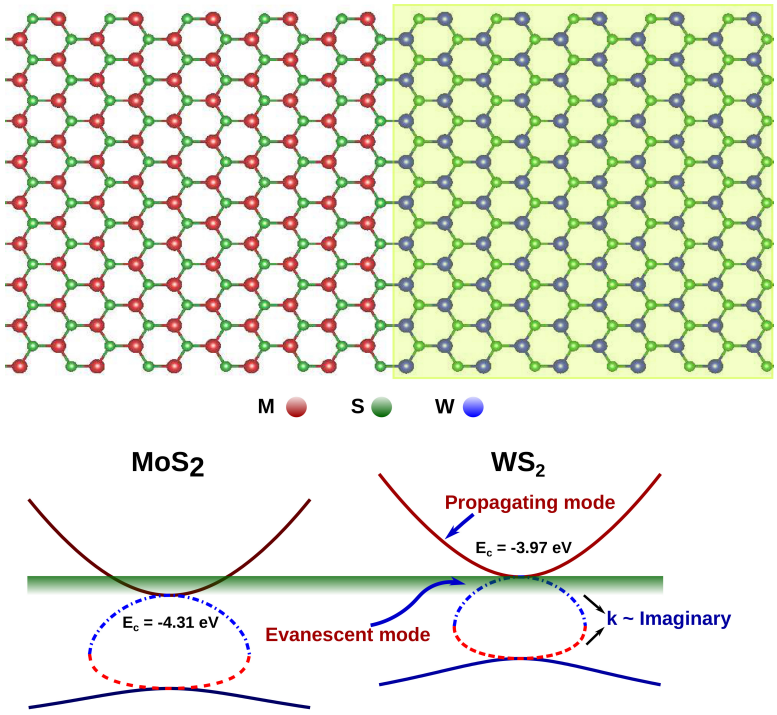

Figure 5.2: A schematic representation of the heterointerface between MoS_2 and WS_2 monolayers is shown. We also display their corresponding conduction and valence bands near the $K-$point. MoS_2 ($E_c = -4.31\,\text{eV}$) has a lower conduction band minimum than WS_2 ($E_c = -3.97\,\text{eV}$). Hence, below the energy $-3.97\,\text{eV}$, electron transport across the interface occurs only through evanescent modes.

purely imaginary wavevectors. This results in exponentially decaying contributions to the scattered wavefunction. Traditional scattering calculations will not be able to account for these crucial contributions, since the probabilities of evanescent modes vanish at the asymptotic limit where the boundary conditions are applied to determine the scattering amplitudes. We then require a new quantum scattering framework that will accurately compute both the evanescent modes and angular current contributions in the near-field of the scattering center.

5.2 Construction of sources and absorbers

Our first aim is to formulate a framework to obtain the scattering properties without applying asymptotic boundary conditions (BCs). In the conventional variational formulation of the scattering theory, asymptotic BCs are applied either by mapping the far-field partial wave expansion into the near-field region [63], or by approximating the Sommerfeld radiation conditions [10, 127]. However, both of these approaches fail to account for the decaying evanescent solutions, since they inherit

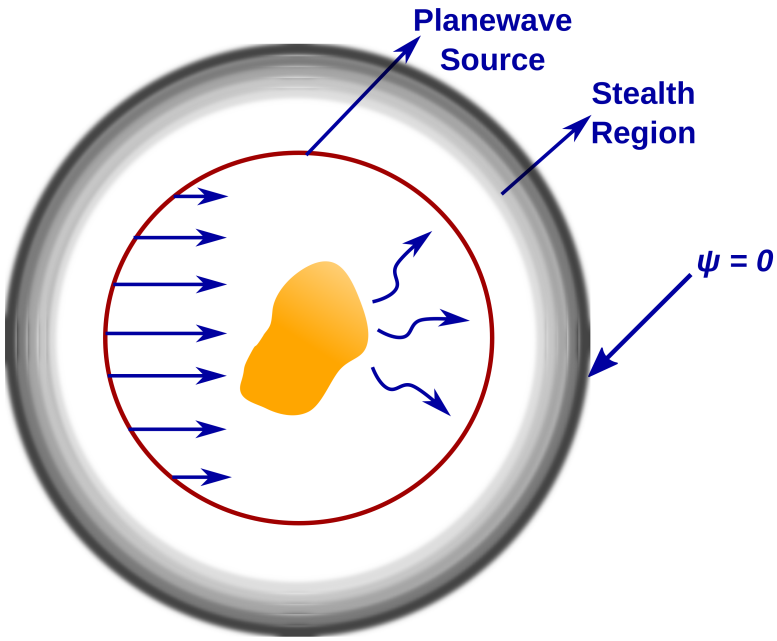

Figure 5.3: Schematic representation of the construction of a circular source (red line) and absorber (gray region, also known as the stealth region) around a scattering center (green shaded region). We can apply Dirichlet boundary conditions at the boundary of the absorber. Amplitudes on the source circle are chosen as per Eq. (5.10), so that the plane waves are injected into the region confining the scattering center.

the asymptotic BCs.

Previously, for electron scattering in waveguides, we proposed a method to reduce the scattering BCs to Dirichlet BCs by creating absorbers (stealth regions) on either end of the waveguide [72]. An extension of this technique to 2D open domain is achieved here by creating circular absorbers around the scattering center, as shown in Fig. 5.3. Within the absorber, we perform a coordinate transformation $\rho \rightarrow \rho\,(1 + i\alpha(r))$, and an energy transformation $E \rightarrow E\,(1 + i\alpha(r))$. Here, $\alpha(r)$ is the cubic Hermite interpolation polynomial varying smoothly from 0 to α_{max}. Through such transformation, it has been shown that the no-reflection condition is satisfied [72], and the absorber will not reflect any wave back into the active region confined within the absorber. Therefore, scattering properties in the active region remain unaffected with the presence of the absorber. As a result of such a transformation, the wavefunction will decay rapidly within the absorber, and we can apply the Dirichlet BCs at the boundary of the absorber. Through this technique, we can confine the computational domain, and preserve the near-field nature of the wavefunction in the region confined by the absorber (scattering region), that are

otherwise lost due to the application of asymptotic BCs.

Once we enclose the active scattering region with the absorber, we require a source (an electron antenna) in the active region to initiate the incoming plane waves (see Fig. 5.3). This is achieved by introducing a source term in the Schrödinger equation. In order to derive this source term, we start with the Green's function equation for the Schrödinger operator in the 2D circular coordinate system given by

$$\left[\frac{1}{\rho}\frac{\partial}{\partial\rho}\left(\rho\frac{\partial}{\partial\rho}\right)+\frac{1}{\rho^2}\frac{\partial^2}{\partial\phi^2}+k^2\right]G(\boldsymbol{\rho},\boldsymbol{\rho'}) = S(\rho',\phi')\,\frac{\delta\left(\rho-\rho'\right)}{\rho'}\,\delta\left(\phi-\phi'\right), \tag{5.1}$$

where $S(\rho',\phi')$ is the source term whose form is yet to be determined, the wavevector $k=\sqrt{2m^*E/\hbar^2}$, E is the incoming energy, and m^* is the effective mass. We expand the Green's function in the Fourier form given by

$$G(\boldsymbol{\rho},\boldsymbol{\rho'}) = \frac{1}{2\pi}\sum_{m=-\infty}^{\infty} e^{im(\phi-\phi')}g_m(\rho,\rho'). \tag{5.2}$$

Inserting this into Eq. (5.1) we obtain

$$\frac{1}{2\pi}\sum_{m=-\infty}^{\infty} e^{im(\phi-\phi')}\left[\frac{1}{\rho}\frac{\partial}{\partial\rho}\left(\rho\frac{\partial g_m}{\partial\rho}\right)+\left(k^2-\frac{m^2}{\rho^2}\right)g_m\right] = S(\rho',\phi')\,\frac{\delta\left(\rho-\rho'\right)}{\rho'}\,\delta\left(\phi-\phi'\right). \tag{5.3}$$

Multiplying Eq. (5.3) by $e^{-im\phi}$ and integrating over ϕ from 0 to 2π we obtain

$$\left[\frac{1}{\rho}\frac{\partial}{\partial\rho}\left(\rho\frac{\partial g_m}{\partial\rho}\right)+\left(k^2-\frac{m^2}{\rho^2}\right)g_m\right] = S(\rho',\phi')\,\frac{\delta\left(\rho-\rho'\right)}{\rho'}. \tag{5.4}$$

The radial part $g_m(\rho,\rho')$ is the Green's function for the one-dimensional Sturm Liouville operator [128], and will be of the form

$$g_m(\rho,\rho') = A_m\begin{cases} J_m(k\rho)H_m(k\rho'), & \rho\le\rho' \\ J_m(k\rho')H_m(k\rho), & \rho>\rho' \end{cases}, \tag{5.5}$$

where, $J_m(k\rho)$ and $H_m(k\rho)$ are the Bessel and Hankel function of first kind, respectively. We determine the coefficient A_m by applying the jump condition at $\rho=\rho'$ given by

$$\left.\frac{\partial g_m}{\partial\rho}\right|_{\rho'+\epsilon} - \left.\frac{\partial g_m}{\partial\rho}\right|_{\rho'-\epsilon} = \frac{S(\rho',\phi')}{\rho'},$$
$$A_m\,\mathcal{W}\left[J_m(k\rho'),H_m(k\rho')\right] = \frac{S(\rho',\phi')}{\rho'}, \tag{5.6}$$

where, the Wronskian $\mathcal{W}\left[J_m(k\rho'), H_m(k\rho')\right] = 2i/\pi\rho'$. Thus

$$A_m = -\frac{i\pi}{2}\, S(\rho', \phi'). \tag{5.7}$$

Substituting Eqs. (5.5) and (5.7) into Eq. (5.2), we obtain the total Green's function of the form

$$G(\boldsymbol{\rho}, \boldsymbol{\rho'}) = -\frac{i}{4}\, S(\rho', \phi') \times \sum_{m=-\infty}^{\infty} e^{im(\phi-\phi')} \begin{cases} J_m(k\rho) H_m(k\rho'), & \rho \le \rho' \\ J_m(k\rho') H_m(k\rho), & \rho > \rho' \end{cases},$$

By using the additional theorem for Bessel functions we have

$$G(\boldsymbol{\rho}, \boldsymbol{\rho'}) = -\frac{i}{4}\, S(\rho', \phi')\, H_0(k\left|\boldsymbol{\rho} - \boldsymbol{\rho'}\right|). \tag{5.8}$$

We note that $H_0(k\left|\boldsymbol{\rho} - \boldsymbol{\rho'}\right|)$ represents the wave originating from the point source at $\boldsymbol{\rho'}$. As shown in Fig. 5.3, to obtain a circular source we integrate $G(\boldsymbol{\rho}, \boldsymbol{\rho'})$ over the angular coordinate ϕ' from 0 to 2π. Hence the wavefunction emerging from the circular source is given by

$$\psi_{in}(\rho, \rho') = -\frac{i}{4} \int_0^{2\pi} d\phi' S(\rho', \phi')\, H_0(k\left|\boldsymbol{\rho} - \boldsymbol{\rho'}\right|). \tag{5.9}$$

Our aim is to generate plane waves propagating in the forward direction from the circular source within the region $\rho \le \rho'$. Hence we choose the source term

$$S(\rho', \phi') = \frac{2i}{\pi} \sum_{n=-\infty}^{\infty} \frac{i^n\, e^{in\phi'}}{H_n(k\rho')}. \tag{5.10}$$

Now, substituting the above form into Eq. (7.11) we obtain

$$\psi_{in} = \sum_{m=-\infty}^{\infty} i^m\, e^{im\phi} \begin{cases} J_m(k\rho) & , \quad \rho \le \rho'; \\ \dfrac{J_m(k\rho')}{H_m(k\rho')} H_m(k\rho), & \rho > \rho', \end{cases} \tag{5.11}$$

where we have utilized the orthogonal properties of the function $e^{in\phi'}$. We know the expansion of plane wave $e^{ikx} = e^{ik\rho\cos\phi} = \sum_{m=-\infty}^{\infty} e^{im\phi} i^m J_m(k\rho)$. Hence

$$\psi_{in} = \begin{cases} e^{ikx} & , \quad \rho \le \rho'; \\ \displaystyle\sum_{m=-\infty}^{\infty} e^{im\phi} i^m \frac{J_m(k\rho')}{H_m(k\rho')} H_m(k\rho), & \rho > \rho', \end{cases} \tag{5.12}$$

we obtain plane waves impinging on the scattering center from a circular source at $\rho = \rho'$, as shown in Fig. 5.3. The wavefunction in the $\rho > \rho'$ region will simply get absorbed by the stealth region.

Once we formulate the quantum scattering theory with the *source* and *absorber*, we can employ numerical methods to obtain the total wavefunction ψ. In the presence of a scattering potential, we obtain the total wavefunction $\psi = \psi_{in} + \psi_{sc}$. Here, ψ_{sc} will include both the radial and angular current contributions. ψ_{sc} will also the evanescent solutions in case of an absorbing scattering potential or in case of multiband scattering processes, as discussed in the next section.

Throughout this chapter, we have solved the Hamiltonian equation by casting it into an action integral. This action integral is solved using finite element analysis (FEA) [41, 44–46]. In FEA, we discretize the physical domain of interest into small elements. Within each element, we express the wavefunction as a linear combination of interpolation polynomials multiplied by undetermined coefficients. These coefficients correspond to the value of the wavefunction and their derivatives at the vertices (nodes) of the element. With this approach, one can systematically increase the accuracy through mesh size refinement (h-refinement) or by employing higher order interpolation polynomials (p-refinement).

Scattering cross-section length at a finite distance

The differential cross-section is determined by dividing the scattered flux by the incoming flux, given by

$$\frac{d\sigma}{d\phi} = \frac{\mathbf{J}^{\text{sc}} \cdot d\mathbf{S}}{J_{\text{in}}}, \tag{5.13}$$

where $\mathbf{J}^{\text{sc}}$ is the scattered current, and $J_{\text{in}} = \hbar k/m^*$ is the magnitude of the current from the incoming plane wave. In the traditional scattering theory, the detector is at infinity, and the outgoing wave in 2D is a circular wave of the form $e^{ik\rho}/\sqrt{\rho}$. When the observer is at a finite distance ρ, the outgoing wave-front incident on the observer will have both radial and angular components. The surface element $d\mathbf{S}$ is considered to be orthogonal to the outgoing current [13, 14]. In 2D scattering,

$$\begin{aligned} \mathbf{J}^{\text{sc}} \cdot d\mathbf{S} &= J^{\text{sc}}\mathbf{n} \cdot dS\mathbf{n}, \\ &= J^{\text{sc}}\sqrt{g}d\phi, \end{aligned} \tag{5.14}$$

where g is the determinant of the metric $g_{\mu\nu}$. In 2D circular coordinate system

$$\sqrt{g} = \rho\sqrt{1 + \frac{1}{\rho^2}\left(\frac{d\rho}{d\phi}\right)^2}. \tag{5.15}$$

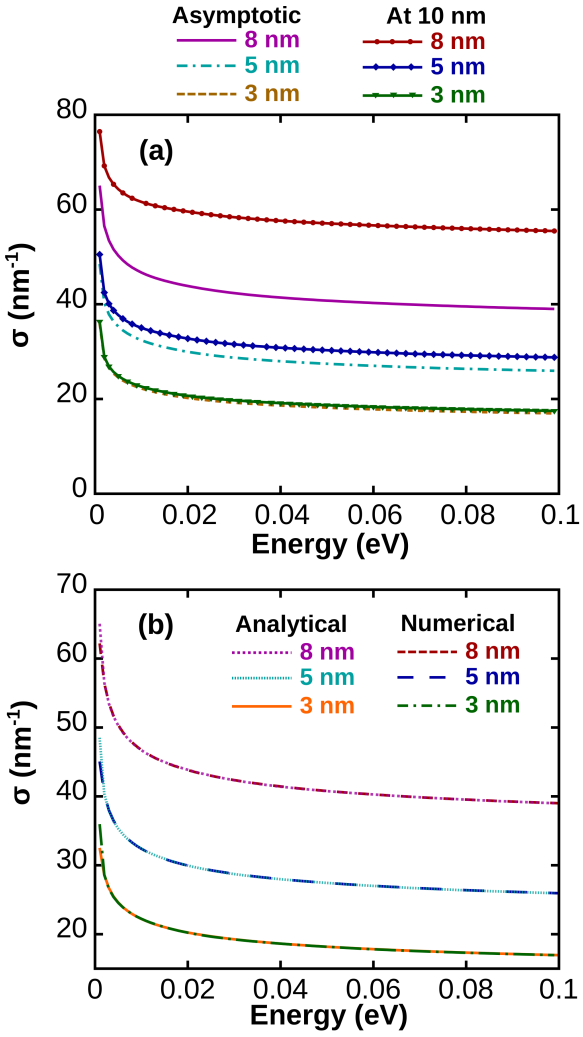

Figure 5.4: (a) Scattering cross-section length obtained through our scattering formalism is plotted as a function of incoming energy. Here, the dotted line represents the cross-section measured by an observer at infinity, whereas the continuous line represents the cross-section measured by an observer at a finite distance 10 nm. Radius of the hard circle potential considered here are equal to 8 nm, 5 nm and 3 nm. (b) The analytical result through partial wave analysis, and the numerical result obtained through our calculation for the scattering cross-section in hard circle potential is plotted as a function of energy.

Hence,

$$\mathbf{J}^{\mathrm{sc}} \cdot d\mathbf{S} = J^{\mathrm{sc}} \sqrt{1 + \frac{1}{\rho^2}\left(\frac{d\rho}{d\phi}\right)^2}\, \rho\, d\phi, \tag{5.16}$$

where

$$J_{\rho}^{\mathrm{sc}} = \frac{\hbar}{m}\, \mathrm{Im}\left(\psi_{sc}^{\dagger} \frac{\partial \psi_{sc}}{\partial \rho}\right),$$
$$J_{\phi}^{\mathrm{sc}} = \frac{\hbar}{m}\, \mathrm{Im}\left(\frac{\psi_{sc}^{\dagger}}{\rho} \frac{\partial \psi_{sc}}{\partial \phi}\right).$$

In order to compare with the expression given in the standard scattering theory, we would like to express the scattered flux in Eq. (5.16) only in terms of the scattering current components. We know that

$$\frac{\partial}{\partial x} = \cos\phi \frac{\partial}{\partial r} - \frac{\sin\phi}{r}\frac{\partial}{\partial \phi},$$
$$\frac{\partial}{\partial y} = \sin\phi \frac{\partial}{\partial r} + \frac{\cos\phi}{r}\frac{\partial}{\partial \phi}. \tag{5.17}$$

Hence we can express the scattered current as

$$\mathbf{J}^{\mathrm{sc}} = \begin{bmatrix} J_x^{\mathrm{sc}} \\ J_y^{\mathrm{sc}} \end{bmatrix} = \begin{bmatrix} \cos\phi & -\sin\phi \\ \sin\phi & \cos\phi \end{bmatrix} \cdot \begin{bmatrix} J_{\rho}^{\mathrm{sc}} \\ J_{\phi}^{\mathrm{sc}} \end{bmatrix}. \tag{5.18}$$

Now let us take that the surface of revolution for the scattered current, expressed in a parametric form given by $\rho = \rho(\phi)$. The tangential vector at a point on this surface will be of the form

$$\mathbf{t} = \begin{bmatrix} -\rho(\phi)\sin\phi \\ \rho(\phi)\cos\phi \end{bmatrix}. \tag{5.19}$$

The normal vector will be

$$\mathbf{n} = \frac{\partial \mathbf{t}}{\partial \phi} = \begin{bmatrix} -\rho(\phi)\cos\phi - \dfrac{\partial \rho(\phi)}{\partial \phi}\sin\phi \\ -\rho(\phi)\sin\phi + \dfrac{\partial \rho(\phi)}{\partial \phi}\cos\phi \end{bmatrix}. \tag{5.20}$$

Hence the scattered current is given by

$$\mathbf{J}^{\mathrm{sc}} = J^{\mathrm{sc}} \frac{\mathbf{n}}{|\mathbf{n}|} = \frac{J^{\mathrm{sc}}}{\sqrt{\rho^2 + \left(\dfrac{\partial \rho}{\partial \phi}\right)^2}} \begin{bmatrix} -\rho(\phi)\cos\phi - \dfrac{\partial \rho(\phi)}{\partial \phi}\sin\phi \\ -\rho(\phi)\sin\phi + \dfrac{\partial \rho(\phi)}{\partial \phi}\cos\phi \end{bmatrix}. \tag{5.21}$$

Equating Eq. (5.18) and (5.21) we obtain the angular components of the scattered as

$$J_\rho^{\rm sc} = \frac{-\rho J^{\rm sc}}{\sqrt{\rho^2 + \left(\frac{\partial\rho}{\partial\phi}\right)^2}},$$

$$J_\phi^{\rm sc} = \frac{\frac{\partial\rho}{\partial\phi} J^{\rm sc}}{\sqrt{\rho^2 + \left(\frac{\partial\rho}{\partial\phi}\right)^2}}. \tag{5.22}$$

Hence we find that

$$\frac{J_\phi^{\rm sc}}{J_\rho^{\rm sc}} = -\frac{1}{\rho}\frac{d\rho}{d\phi}. \tag{5.23}$$

By substituting this relation to Eq. (5.16) we obtain

$$\mathbf{J}^{\rm sc}\cdot d\mathbf{S} = J^{\rm sc}\sqrt{1+\left(\frac{J_\phi^{\rm sc}}{J_\rho^{\rm sc}}\right)^2}\,\rho\,d\phi. \tag{5.24}$$

We know that $J^{\rm sc} = \sqrt{\left(J_\rho^{\rm sc}\right)^2 + \left(J_\theta^{\rm sc}\right)^2} = J_\rho^{\rm sc}\left[1+\left(J_\phi^{\rm sc}/J_\rho^{\rm sc}\right)^2\right]$. Substituting this relation for $J^{\rm sc}$ in Eq. (5.24) we obtain

$$\mathbf{J}^{\rm sc}\cdot d\mathbf{S} = J_\rho^{\rm sc}\left[1+\left(\frac{J_\phi^{\rm sc}}{J_\rho^{\rm sc}}\right)^2\right]\rho\,d\phi, \tag{5.25}$$

and the differential cross-section length is given by

$$\frac{d\sigma}{d\phi} = \frac{\mathbf{J}^{\rm sc}\cdot d\mathbf{S}}{J_{\rm in}} = \frac{J_\rho^{\rm sc}\left[1+\left(\frac{J_\phi^{\rm sc}}{J_\rho^{\rm sc}}\right)^2\right]\rho}{J_{\rm in}}. \tag{5.26}$$

Note that as the source and observer are pushed to infinity ($\rho\to\infty$),

$$\begin{aligned} J_\phi^{\rm sc} &\to 0,\\ J^{\rm sc} &\to \frac{\hbar}{m^*}\frac{|f|^2}{\rho},\\ \frac{d\sigma}{d\phi} &\to \frac{|f|^2}{k}, \end{aligned} \tag{5.27}$$

where f is scattering amplitude. Hence, we obtain the standard definition of the differential cross-section length [9] in the limit $\rho\to\infty$.

To validate our scattering formalism, we consider the case of 2D scattering from a hard circle. The hard circle potential is given by

$$V(\rho) = \begin{cases} 0, & \rho \leq a \\ \infty, & \rho > a \end{cases}, \tag{5.28}$$

where, a is the radius of the circle. Through partial wave analysis, we can obtain a closed form result for the scattering cross-section length σ measured at the asymptotic distance as described in the next subsection. In Fig. 5.4(b), we compare the analytical result (see Eq. (5.32)), and the result obtained through our formalism. We see that these results match accurately. Behavior of σ at low and high energy limits observed in Fig. 5.4(b) are discussed in the next subsection.

In Fig. 5.4(a), we plot the cross-section length obtained from an observer at a very large distance (asymptotic limit), and at a finite distance 10 nm. We see a significant difference between between their quantitative values. In case of the hard circle potential, difference between the asymptotic and non-asymptotic predictions increases with decreasing distance between the observer and the hard circle. In Fig. 5.4(a), we see that the deviation between the prediction at the asymptotic limit, and for the observer at 10 nm is maximum for the hard circle radius of 8 nm. This is because the effective distance from the hard circle and the observer is least for 8 nm potential. Thus confirming that in nanoscale systems it is especially important to employ the non-asymptotic scattering theory developed here to obtain accurate transport properties. In chapter 7, we derive the source term for the non-asymptotic scattering theory in three-dimensions (3D). Such analysis in 3D can be employed to obtain transport properties in bulk materials.

Scattering from a Hard circle potential

In this section, we discuss the analytical results for the scattering from a hard circle potential in 2D. Even though, this problem has been addressed before in the literature [170, 171], they have not discussed the limiting behaviors. Furthermore, some of their work contains minor errors.

The hard circle potential of radius a in a 2D space is given by

$$V = \begin{cases} \infty, & \rho \leq a \\ 0, & \rho > a \end{cases}. \tag{5.29}$$

The solution wavefunction for the above potential will be of the form

$$\psi(\rho,\phi) = \begin{cases} 0, & \rho \le a \\ e^{ik\rho\cos\phi} + \sum_{n=-\infty}^{\infty} c_n\, e^{in\phi} H_n(k\rho), & \rho > a \end{cases}. \tag{5.30}$$

To determine the coefficients c_n, we utilize the boundary condition $\psi(a,\phi) = 0$. Hence,

$$c_n = \frac{-i^n J_n(ka)}{H_n(ka)}, \tag{5.31}$$

where we have used the expansion of the planewave $e^{ik\rho cos\phi} = \sum_{n=-\infty}^{\infty} (i^n) e^{in\phi} J_n(k\rho)$. Through partial wave analysis, we obtain the total cross-section length given by

$$\sigma = \frac{4}{k} \sum_{n=-\infty}^{\infty} \frac{|J_n(ka)|^2}{|H_n(ka)|^2}. \tag{5.32}$$

To compare the quantum mechanical calculations with classical mechanics predictions, we consider the cross-section length in the high energy limit $ka >> 1$. We know that,

$$\begin{aligned} J_n(ka) &\xrightarrow[ka\to\infty]{} \sqrt{\frac{2}{\pi ka}} \cos\left(ka - \frac{n\pi}{2} - \frac{\pi}{4}\right), \\ H_n(ka) &\xrightarrow[ka\to\infty]{} \sqrt{\frac{2}{\pi ka}}\; e^{\,i\left(ka - \frac{n\pi}{2} - \frac{\pi}{4}\right)}. \end{aligned} \tag{5.33}$$

Therefore,

$$\sigma \simeq \frac{4}{k} \sum_{n=-\infty}^{\infty} \cos^2\left(ka - \frac{n\pi}{2} - \frac{\pi}{4}\right). \tag{5.34}$$

Classically, the particle will not be deflected by the potential if the impact parameter $b > a$. The angular momentum L_ϕ will follow the limit $\left|L_\phi\right| = n\hbar \le \hbar ka$. Hence, we can restrict the sum in Eq. (5.34) between the limits $-ka \le n \le ka$. With this simplification we obtain the cross-section length

$$\sigma \simeq 4a, \tag{5.35}$$

which is twice the classical mechanics prediction [170].

To obtain the low energy limit ($ka << 1$) of the cross-section length, we retain only the first term ($n = 0$) in the series given in Eq. (5.32). In this limit,

$$\begin{aligned} J_0(ka) &\xrightarrow[ka\to 0]{} 1, \\ H_0(ka) &\xrightarrow[ka\to 0]{} \frac{2}{\pi} \ln(ka). \end{aligned} \tag{5.36}$$

Hence,

$$\sigma \simeq \frac{\pi^2}{k} \frac{1}{(\ln(ka))^2}. \tag{5.37}$$

This is not an analytic function. This can be explained as follows. We know that the incoming current $J_{\text{in}} = \hbar k/m^* \xrightarrow[ka\to 0]{} 0$. In the long wavelength limit, the scattered current $J^{\text{sc}} \sim 1/(\ln(ka))^2 \xrightarrow[ka\to 0]{} 0$. Hence, we obtain a $0/0$ form in the total cross-section length, which does not have a convergent value. Therefore, as $k \to 0$, cross-section length will diverge even though the scattering current vanishes.

5.3 Envelope function scattering theory with sources and absorbers

The low energy dynamics of the charge carriers in semiconducting materials can be described by the $\boldsymbol{k} \cdot \boldsymbol{p}$ Hamiltonian [129–132]. This Hamiltonian provides an accurate characterization of the energy dispersion around the high-symmetry points of the Brillouin Zone, in terms of a small number of input band parameters. These band parameters are taken from the database [133] obtained from DFT and many-body perturbation theory calculations. In this section, we describe the scattering theory for the envelope functions for the $\boldsymbol{k} \cdot \boldsymbol{p}$ Hamiltonian.

The $\boldsymbol{k} \cdot \boldsymbol{p}$ Hamiltonian effectively captures the coupled dynamics of the conduction and valence bands around the high-symmetry points of the Brillouin Zone. This is also the region in which we are most interested in determining the transport properties. Effects of remote bands can be easily included by using the Löwdin perturbation theory [134]. Effects due to strain, magnetic field, and spin-orbit coupling are included as additional input parameters. Being a long-wavelength theory, $\boldsymbol{k} \cdot \boldsymbol{p}$ perturbation theory is well suited to simulate transport properties in device-relevant scales.

Let us consider the Hamiltonian equation of the form

$$\begin{aligned}(H_0 + V_0 + V_d - E) \cdot \psi_{nk} \\ = S(\rho', \phi')\, \eta_{scale}\, \mathbb{A}_{nk}\, \frac{\delta(\rho - \rho')}{\rho'},\end{aligned} \tag{5.38}$$

where $S(\rho', \phi')$ is the source term defined in Eq. (5.10), $\mathbb{A}_{nk}$ is the incoming amplitude, n is the band-index, k is the wavevector, and η_{scale} is a scale factor whose form is as yet to be derived. Here, V_0 is the cell periodic potential, and V_d is the defect/impurity potential obtained from DFT calculations. In the envelope function approximation (EFA), the general form of the wavefunction and the incoming amplitudes are expressed as a linear combination of a finite number of bands

[129, 135, 136], given by

$$\psi_{nk} = \sum_{m=0}^{\mathrm{n}band} F_m \, u_{mk},$$
$$\mathbb{A}_{nk} = \sum_{m=0}^{\mathrm{n}band} a_m \, u_{mk}, \tag{5.39}$$

where F_m is the slowly-varying envelope function, u_{mk} is the cell-periodic Bloch function, a_m is the incoming amplitude, and n$band$ is the number of bands considered. Here, the expansion is at a fixed k value, and we will assume from now on that the expansion is around $k = 0$. Within the framework of EFA, we perform 'cell-averaging' by integrating over each unit cell in the crystal. Bloch functions satisfy Schrödinger's equation with band-edge energies, and results in:

$$\int_{cell} d^2\rho \, u^{\dagger}_{n0} \cdot u_{m0} = \delta_{mn},$$
$$\int_{cell} d^2\rho \, u^{\dagger}_{n0} \, (H_0 + V_0) \cdot \, u_{m0} = E_m \delta_{mn},$$
$$\int_{cell} d^2\rho \, u^{\dagger}_{n0} \boldsymbol{p} \cdot u_{m0} = \boldsymbol{p}_{mn}, \tag{5.40}$$

where $\boldsymbol{p}_{mn}$ is the momentum matrix. This averaging procedure results in the equation of the form

$$\left[\left\langle \mathbf{H}_{kp} \right\rangle_{cell} + (V_d - E)\,\mathbf{1}\right] \cdot \mathbb{F} = S(\rho', \phi')\, \eta_{\mathrm{scale}}\, \mathbb{A}\, \frac{\delta(\rho - \rho')}{\rho'}, \tag{5.41}$$

where $\left\langle \mathbf{H}_{kp} \right\rangle_{cell}$ is the $\boldsymbol{k} \cdot \boldsymbol{p}$ Hamiltonian, and $\mathbf{1}$ is the identity matrix. From now on we denote $\left\langle \mathbf{H}_{kp} \right\rangle_{cell}$ simply as $\mathbf{H}_{kp}$. The envelope function is $\mathbb{F} = \begin{pmatrix} F_1 & F_2 \ldots \end{pmatrix}^T$, and the incoming amplitude is $\mathbb{A} = \begin{pmatrix} a_1 & a_2 \ldots \end{pmatrix}^T$. In the absence of the defect potential V_d, the incoming amplitudes satisfy an equation of the form

$$\left[\mathbf{H}_{kp} - E\,\mathbf{1}\right] \cdot \mathbb{A} = 0. \tag{5.42}$$

Hence, for an given energy we can obtain $\mathbb{A}$ by solving the above matrix equation. Note that Eq. (5.42) represents the standard $\boldsymbol{k}\cdot\boldsymbol{p}$ Hamiltonian equation for the pristine material.

We also need to obtain an expression for the scale factor η_{scale} employed in Eq. (5.41). For simplicity let us consider the $\boldsymbol{k} \cdot \boldsymbol{p}$ Hamiltonian in one-dimension (1D). The expression we obtain here for 1D will translate into higher dimensions as well. Let us consider the equation

$$\left[\mathbf{H}_{kp}(x) - E\mathbf{1}\right] \cdot \mathbb{F} = S\, \eta_{\mathrm{scale}} \mathbb{A}\, \delta(x), \tag{5.43}$$

where, the source term in 1D is given by $S = 2ik_1$ [41, 72], where k_1 is the incoming wavevector. The solution to the above equation in terms of the Fourier components is given by

$$\mathbb{F}(x) = \frac{1}{2\pi}\int dk\, e^{ikx} 2ik_1\, \eta_{scale}\, \frac{adj(\mathbf{H}_{kp} - E\mathbf{1})\cdot\mathbb{A}}{Det(\mathbf{H}_{kp} - E\mathbf{1})}. \tag{5.44}$$

Let us constrain $\mathbf{H}_{kp}$ be a 2×2 matrix, with eigenenergies given by E_c and E_v. Then

$$\mathbb{F}(x) = \frac{ik_1}{\pi}\,\mathbb{A}\,(E_c - E_v)\int dk\, \frac{e^{ikx}\eta_{scale}}{(k^2 - k_1^2)(k^2 - k_2^2)...(k^2 - k_N^2)}, \tag{5.45}$$

where $k_1, k_2...k_N$ are the solution wavevector for the determinantal equation $Det(\mathbf{H}_{kp} - E\mathbf{1}) = 0$. The Hamiltonian $\mathbf{H}_{kp}$ can include terms in higher order k (such as $k, k^2, k^3...$), and hence the determinant equation will have N roots. Hence, we choose

$$\eta_{scale} = \frac{(k^2 - k_2^2)...(k^2 - k_N^2)}{(E_c - E_v)}, \tag{5.46}$$

so that the the incoming wavefunction $\psi(x)$ will have the form

$$\psi(x) = \mathbb{A}e^{ik_1 x}. \tag{5.47}$$

The expression derived in Eq. (5.46) will follow for 2D and higher dimensions as well.

We cast Eq. (5.41) into an action integral, and solve the equation within the variational framework. The advantages of the action integral formulation are that there is no ambiguity about reordering of operators for symmetrization [137], and we can easily evaluate the conserved current using the gauge-variational approach introduced by Gell-Mann and Levy [138] and used extensively by us [137] (see discussion below). This action integral is solved using the finite element analysis.

Action integral formation

In this section, we explain the action integral formulation employed to solve Eq. (5.41). Let us consider a general form of the $\boldsymbol{k}\cdot\boldsymbol{p}$ Hamiltonian in a 2D material given by

$$\mathbf{H}_{kp} = \mathbf{A}_{xx}k_x^2 + \mathbf{A}_{yy}k_y^2 + \mathbf{A}_{xy}k_xk_y + \mathbf{B}_xk_x + \mathbf{B}_yk_y + \mathbf{C}, \tag{5.48}$$

where $\mathbf{A}_{xx}, \mathbf{A}_{yy}, \mathbf{A}_{xy}, \mathbf{B}_x, \mathbf{B}_y, \mathbf{C}$ are the coefficient matrices, $k_x = -i\partial_x$, and $k_y = -i\partial_y$. For simplicity, we have considered only the terms up to the second order

derivatives. With this Hamiltonian, the action integral corresponding to Eq. (5.41) is given by

$$\mathcal{A} = \int d^2\rho\, \mathbb{F}^\dagger \cdot \mathbf{L}_{kp} \cdot \mathbb{F} + \int d^2\rho\, S(\rho', \phi')\, \eta_{scale}\, \mathbb{F}^\dagger \cdot \mathbb{A}\, \frac{\delta(\rho - \rho')}{\rho'}, \tag{5.49}$$

where $\mathbf{L}_{kp}$ is the Lagrangian operator given by

$$\mathbf{L}_{kp} = \Big[\overleftarrow{\partial}_x \mathbf{A}_{xx} \vec{\partial}_x + \overleftarrow{\partial}_y \mathbf{A}_{yy} \vec{\partial}_y + \frac{1}{2}\left(\overleftarrow{\partial}_x \mathbf{A}_{xy} \vec{\partial}_y + \overleftarrow{\partial}_y \mathbf{A}_{xy} \vec{\partial}_x\right) + \frac{i}{2}\left(\overleftarrow{\partial}_x \mathbf{B}_x - \mathbf{B}_x \vec{\partial}_x\right) + \frac{i}{2}\left(\overleftarrow{\partial}_y \mathbf{B}_y - \mathbf{B}_y \vec{\partial}_y\right) + \mathbf{C}\Big],$$

where $\overleftarrow{\partial}$ and $\vec{\partial}$ represent the derivative operator acting on the functions appearing to the left and right side, respectively. This will ensure the correct operator ordering at the material interface [137].

Across a material interface, the envelope wavefunction, and the probability current has to be continuous. The continuity of the envelop function is ensured by using Hermite interpolation polynomials in our calculations, which will have both first and second derivative continuity [73]. The probability current is evaluated using a gauge-variational approach that is commonly used in high energy/particle physics. Following Gell-Mann and Levy [138], we perform a transformation of the envelop function with respect to an arbitrary gauge function of the form, $\mathbb{F} \rightarrow \mathbb{F}\, e^{i\Lambda(\rho)}$. With this transformation, we obtain the conserved current

$$J_x = \mathbb{F}^\dagger \cdot \frac{\delta\, \mathbf{L}_{kp}}{\delta\, \partial_x \Lambda} \cdot \mathbb{F},$$
$$J_y = \mathbb{F}^\dagger \cdot \frac{\delta\, \mathbf{L}_{kp}}{\delta\, \partial_y \Lambda} \cdot \mathbb{F}. \tag{5.50}$$

The interfacial potential is obtained from the DFT calculations, and will be continuous across the interface. Hence, this conserved current will also be continuous.

5.4 Relaxation time approximation

Within the Boltzmann transport formalism, important transport properties such as the mobility, conductance and Seebeck coefficeints are expressed in terms of the total relaxation time $\tau(E)$. To determine $\tau(E)$, we need to consider both the intrinsic and extrinsic scattering rates. The extrinsic scattering rate arises from the potential scattering. According to the Matthiessen's law

$$\frac{1}{\tau(E)} = \frac{1}{\tau_e(E)} + \frac{1}{\tau_{ph}(E)}, \tag{5.51}$$

where, τ_e is the extrinsic carrier scattering time, and τ_{ph} is the total intrinsic scattering time arising from all the acoustic and optical phonon mode contributions.

Carrier scattering time

Through kinectic theory [139], for elastic scattering processes in 2D, τ_e is given by

$$\tau_e(E) = \frac{1}{n_d\, \sigma_m\, \langle v \rangle}, \tag{5.52}$$

where n_d is the disorder density, $\langle v \rangle$ is the average velocity, and σ_m is the momentum scattering cross-section defined as

$$\sigma_m = \int_0^{2\pi} \frac{d\sigma}{d\phi} (1 - \cos\phi)\; d\phi, \tag{5.53}$$

where, $d\sigma/d\phi$ is the differential cross-section length. The average incident velocity is

$$\langle v \rangle = \frac{1}{\pi} \int_{-\pi/2}^{\pi/2} d\beta\, v\, \cos\beta, \tag{5.54}$$

where $v = |\nabla_k E_n(k)|\,/\hbar$ is the carrier velocity, and β is the angle between the velocity vector and the longitudinal axis. For example, for a uniform velocity distribution, $\langle v \rangle = 2v/\pi$.

Phonon scattering time

First-principles calculations provide a convenient way of determining the phonon scattering times by computing the deformation potentials of the crystal lattice [140]. In 2D materials, the phonon scattering rate from the longitudinal and transverse acoustic phonons is given by [141–143]

$$\frac{1}{\tau_{ph,0}} = \frac{m^* D_1^2\, k_B T}{\hbar^3\, \rho_{2D}\, c_s^2}, \tag{5.55}$$

where m^* is the effective mass, D_1 is the first-order deformation potential, T is the absolute temperature, ρ_{2D} is the 2D ion mass density, and c_s is the sound velocity of the acoustic phonons. The intervalley acoustic phonon and optical phonon rates are expressed in terms of the zero-order deformation potential D_0, and is given by

$$\frac{1}{\tau_{ph,1}} = \frac{m^* D_0^2}{2\hbar^2 \omega_\xi \rho_{2D}} \left(e^{\hbar\omega_\xi / k_B T} \Theta(E - \hbar\omega_\xi) + 1 \right) f_\xi^{BE}, \tag{5.56}$$

where Θ is the Heaviside step function, ω_ξ is the phonon frequency, and f_ξ^{BE} is the Bose-Einstein distribution function for the phonon mode ξ. Effect of the

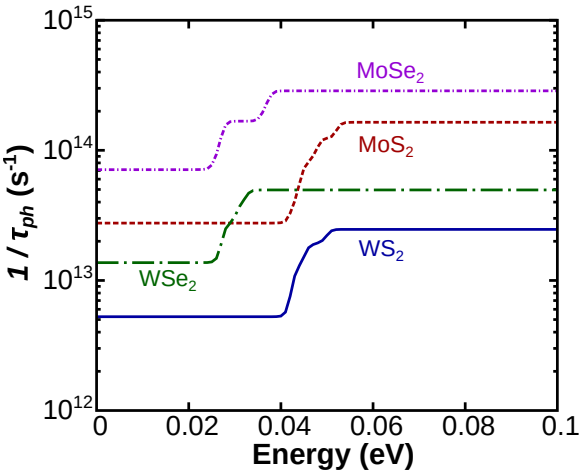

Figure 5.5: The total phonon scattering rates for the K-valley electrons are plotted as a function of energy for TMDCs at temperature $T = 300$ K. Scattering rates are calculated using the deformation potentials listed in Ref. [141–143].

Fröhlich interaction can be implicitly added to the deformation potential [142]. We neglect the first-order optical deformation potential contributions, that are typically small while compared to the values from Eqs. (5.55) and (5.56). Hence the total intrinsic phonon scattering rate is computed by summing over the all phonon modes, $\tau_{ph}^{-1} = \sum_{\xi} \tau_{\xi}^{-1}$.

In Fig. 6.3, we have plotted the total intrinsic phonon scattering rate at room temperature for TMDC monolayers. We have included deformation potentials for the acoustic and optical phonon modes corresponding to the transition $K \rightarrow \{K, K', Q, Q'\}$. Emergence of contributions from optical phonon modes are observed as steps in the scattering rate. We observe that $MoSe_2$ (WS_2) has the strongest (weakest) interaction with phonons in the family of TMDC monolayers. WX_2 has a greater electrical conductivity than MoX_2. These observations and scattering rate values are consistent with previous first-principles study in the literature [141, 142].

5.5 Transport properties in TMDC heterostructures

Transition metal dichalcogenides have attracted tremendous recent interest in fabricating high-mobility nanoelectric circuits [144–146]. In contrast to graphene, TMDCs host massive Dirac fermions due to their direct bandgap, which negates the probability of Klein tunneling [147]. Strong coupling between spin and valley degrees of freedom are observed in TMDCs due to their lack of inversion symmetry [148]. This makes them interesting candidates to realize valleytronic devices as well

[149].

Similar crystal structure and comparable lattice constants observed in MX_2 (M = Mo, W; X = S, Se) monolayers have motivated the study of TMDC-based quantum confinement and heterostructures [121, 150–155] . Experimentally, such lateral heterostructures can be realized through multistep chemical vapor deposition techniques, bottom up synthesis, and micromechanical techniques [156–165]. Ability to pattern the material inclusions in these systems provides an enhanced level of control over their electrical properties. Hence, they have a great potential to realize in-plane transistors, photodiodes, cascade lasers, and CMOS circuits.

As shown in Fig. 5.2, mismatch between the band-offsets at a heterointerface between two TMDC monolayers breaks the translational symmetry of the system. Hence the evanescent modes (with complex wavevector) contribute significantly to their transport properties. Therefore, in 2D lateral heterostructures the carrier scattering calculations have to carried out using the method described in Sec. 5.3. In TMDCs, a seven-band $\boldsymbol{k}\cdot\boldsymbol{p}$ model can accurately capture the most important dispersion features of the conduction (CB) and valence (VB) bands [166]. We can the apply Löwdin perturbation theory [134] to reduce the seven band model into a two-band model corresponding to the lowest CB and highest VB. Here, we keep the terms upto second-order in the diagonal element in the Hamiltonian corresponding to the basis set $\{|\phi_c, s, \eta\rangle, |\phi_v, s, \eta\rangle\}$. Here, $s = \pm 1$ is the spin index, and $\eta = \pm 1$ denotes the valley $\pm K$. C_{3h} symmetry dictates that the Hamiltonian should have the form

$$H_{kp} = H_0 + at\left(\eta\, k_x\hat{\sigma}_x + ik_y\hat{\sigma}_y\right) - \lambda\,\eta\frac{(\hat{\sigma}_z - 1)}{2}s, \tag{5.57}$$

where $\hat{\sigma}$ denotes the Pauli matrices, a is the lattice constant, t is the effective hopping integral, λ is the spin-orbit (SO) parameter, and H_0 is given by

$$H_0 = \begin{bmatrix} E_c + \alpha_s k^2 & 0 \\ 0 & E_v + \beta_s k^2 \end{bmatrix}. \tag{5.58}$$

Here, α_s, β_s are the material parameters, and E_c and E_v are the CB minima and the VB maxima, respectively. The $\boldsymbol{k}\cdot\boldsymbol{p}$ theory is corrupted with the occurrence of spurious solutions. We have utilized the Foreman transformations [167] to eliminate the spurious solutions, and hence, we consider $\beta_s = 0$. In Table 6.2 we have listed all the $\boldsymbol{k}\cdot\boldsymbol{p}$ parameters used in our calculations for MoS_2. WS_2, $MoSe_2$, WSe_2 monolayers. We have neglected strain matrix elements since MoS_2 ($MoSe_2$) and WS_2 (WSe_2) have comparable lattice constants. Material parameters between the

	E_c (eV)	E_v (eV)	a (Å)	t (eV)	λ (eV)	$\alpha_+(\alpha_-)$ (eV·Å^2)
MoS_2	-4.31	-5.89	3.184	1.059	0.073	-5.97(-6.43)
WS_2	-5.97	-5.50	3.186	1.075	0.211	-6.14(-7.95)
$MoSe_2$	-3.91	-5.23	3.283	0.940	0.090	-5.34(-5.71)
WSe_2	-3.61	-4.85	3.297	1.190	0.230	-5.25(-6.93)

Table 5.1: The $\boldsymbol{k}\cdot\boldsymbol{p}$ parameters used in our calculations are listed. These parameters were obtained from the previously reported first-principles study [133, 166].

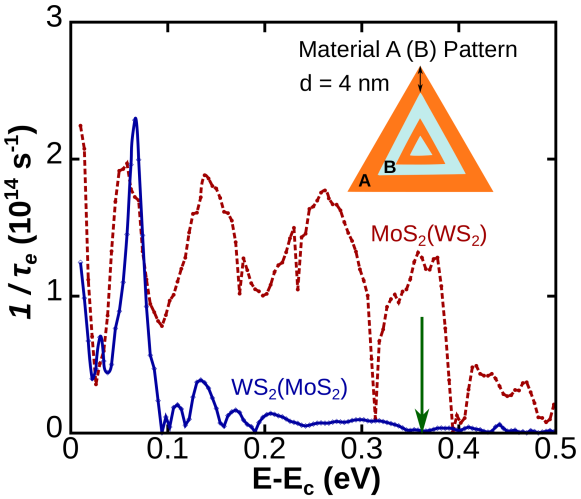

Figure 5.6: Electron scattering rate is plotted as a function of energy for $MoS_2(WS_2)$ and $WS_2(MoS_2)$ triangular heterostructures. A(B) material pattern is displayed in the inset. The material parameters are employed here are listed in Table 6.2, and $n_d = 10^{12}\,\mathrm{cm}^{-2}$. Width of each layer is taken to be 4 nm. Scattering rates are calculated using the envelope function scattering theory discussed in Sec. 5.3.

two layers are smoothly interpolated through the self-consistent potential distribution obtained from the DFT calculations.

In Fig. 5.6, we have plotted the electron scattering rate for a 2D triangular superlattice between MoS_2 and WS_2 monolayers. There have been experimental efforts to realize such structures through lateral epitaxy [164]. MoS_2 has a lower CB minimum compared to WS_2 (see Table 6.2). Hence, for energies below -3.97 eV (marked by a green arrow in Fig. 5.6) transport in WS_2 layers can occur only through the evanescent modes. Evanescent wavevectors are the purely imaginary k roots of the

$\boldsymbol{k}\cdot\boldsymbol{p}$ Hamiltonian defined in Eq. (6.2). Firstly, we observe that the WS_2 (MoS_2) structure has a lower scattering rate (higher lifetime) while compared to the MoS_2 (WS_2) structure. This is because an electron injected from the WS_2 layer can scatter off through the additional propagating conduction channels available from MoS_2 inclusions. We observe that for transport in the MoS_2 (WS_2) structure, above the incoming energy $E > -3.97\,\text{eV}$ ($E - E_c = 0.34\,\text{eV}$, marked by an arrow in Fig. 5.6), corresponding to the CB minima of WS_2, the electron scattering rate decreases significantly, since the evanescent modes disappear above this energy. The resonances observed in the MoS_2 (WS_2) structure, below the energy $E < -3.97\,\text{eV}$ are due to the interaction with the trapped electron states within the WS_2 barrier.

For transport in the WS_2 (MoS_2) structure, we observe maxima and minima in the electron scattering rate around $E - E_c = 0.1\,\text{eV}$ (see Fig. 5.6). This marks the occurrence of Fano resonance in the transmission profile, an effect analogous to that of atomic autoionization [74], first observed in the context of inelastic electron scattering by a helium atom. Analogous Fano profiles are observed around the subband minima of a quantum waveguide with attractive potentials [15]. Here, the MoS_2 inclusion acts as a quantum well and leads to the formation of quasi-bound metastable states. Interaction between the propagating modes and the quasi-bound states leads to the Fano resonance. Multiple Fano resonances are observed when we have a superlattice of WS_2 and MoS_2 layers as shown in Fig. 5.7. Formation of Fano resonances leads to an enhancement in the thermoelectric figure-of-merit far beyond the pure 2D monolayers. This phenomenon will be discussed in detail in a subsequent chapter [168].

Lastly, we study the mobility of electrons in the TMDC heterostructures. Around the K-valley, the CB is isotropic and parabolic in nature. Hence, the mobility can be defined as

$$\mu = \frac{e}{m^*}\frac{1}{n}\int dE\, g(E)\, E\, \tau(E)\left(-\frac{\partial f(E)}{\partial E}\right), \tag{5.59}$$

where, the 2D carrier density $n = \int dE\, g(E)\, f(E)$, $g(E)$ is the density of states, and the Fermi-Dirac distribution is $f(E) = (1 + \exp[(E - E_F)/k_BT])^{-1}$. Due to the parabolic nature of CB, we consider constant $g(E) = g_s g_v m_K^*/2\pi\hbar^2$, where g_s and g_v ($g_v = 1, 2$ for VB, CB) are the spin and valley degeneracies, respectively. In Fig. 5.8, we plot the total mobility (including both phonon and electron contributions) at room temperature for the n-type TMDC monolayers with triangular inclusions. The density of triangular inclusions is considered to be $n_d = 10^{12}\,\text{cm}^{-2}$. We observe an enhancement in the mobility at low carrier density. The WS_2 monolayer with MoS_2

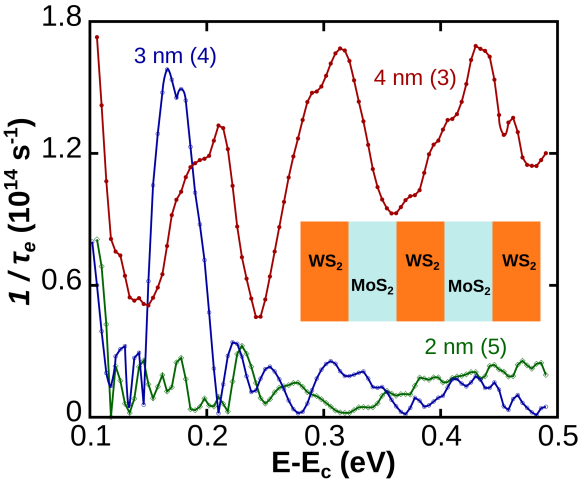

Figure 5.7: Electron scattering rate is plotted as a function of energy for WS_2-MoS_2 lateral heterostructures. Electrons are initiated from the WS_2 layer. Here, the notation 4 nm(3) represents that there are 3 periods of WS_2 and MoS_2 layers, and each layer has a width 4 nm. The material parameters employed here are listed in Table 6.2 and $n_d = 10^{12}\,\mathrm{cm}^{-2}$. Scattering rates are calculated using the envelope function scattering theory discussed in Sec. 5.3.

inclusion will have the highest mobility amongst the considered combinations. This can be attributed to two main factors: 1) additional CB channels available from MoS_2 inclusions enhance the electron scattering lifetime, 2) WS_2 monolayer has the highest phonon scattering lifetime amongst the family of TMDC monolayers (see Fig. 6.3). The MoS_2 monolayer with WS_2 inclusion will have relatively lower mobility. This is because the evanescent modes, being real functions will not contribute to the probability current, and hence, suppress the overall mobility. We also note that the mobility observed here in WX_2 monolayers with triangular inclusions is an order of magnitude larger than the phonon-limited mobility, and the mobility calculated in layers with charged vacancies. In charged vacancies, Coulomb contributions suppress the mobility [169]. Hence, short-range potentials such as the inclusions considered here are promising candidates to realize high-mobility devices.

5.6 Conclusions

We have developed a non-asymptotic quantum scattering theory using a novel method of sources and absorbers. The Cauchy boundary conditions that are necessary in the variational formulation of scattering are reduced to simpler Dirichlet boundary conditions by constructing a perfect absorber (stealth region) around the scattering centers. This will also allow us to define a finite computational domain.

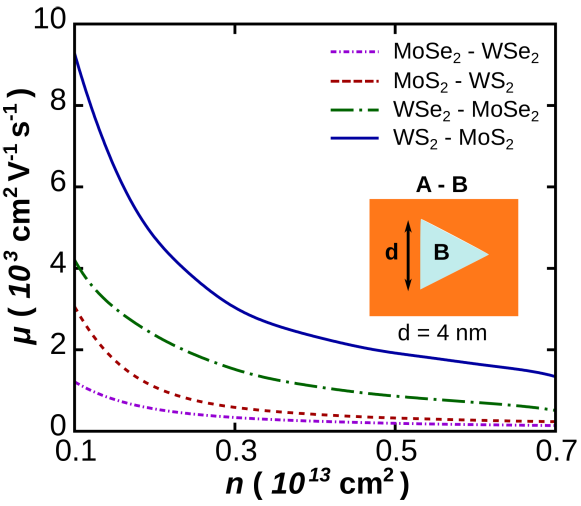

Figure 5.8: Electron mobility at room temperature is plotted as a function of 2D carrier density for the triangular inclusions in TMDC heterostructures. The material parameters employed here are listed in Table 6.2 and $n_d = 10^{12}\,\mathrm{cm}^{-2}$.

In the conventional scattering theory, the scattering properties are determined at the asymptotic distance. This will result in the loss of evanescent mode contributions in multiband scattering processes, and when we have absorbing scattering potentials. Introducing an absorber will facilitate the evaluation of the scattering properties at a finite distance, and it will preserve the distance information between the observer and the scattering center. Once we enclose the active scattering region with the absorber, we require a carrier source that will generate plane-waves in order to initiate the scattering event. We have derived the expression for the circular source term introduced in the right-hand side of the Hamiltonian equation.

We have shown that even for the simplest case of scattering from a hard circle potential, the cross-section length measured at a finite distance using our formalism, and at the asymptotic distance obtained through the analytical formulation will have significant differences in their numerical values. The carrier scattering time is inversely proportional to the cross-section length. Hence, our formalism will be of great interest in nanoscale systems, where the transport measurements are made in proximity to the scattering centers.

We have shown that bridging our scattering theory framework with the $\boldsymbol{k}\cdot\boldsymbol{p}$ perturbation theory, with inputs from *ab-initio* electronic structure calculations, provides a versatile multiscale formalism. The continuum nature of our formalism will enable the modeling of realistic devices, scaling from hundreds to thousands of atoms. Carrier scattering rates obtained through our formalism combined with the phonon

scattering rates obtained through DFT calculations can accurately calculate the thermoelectric properties of the nano-devices. Hence it will be very useful to design and simulate nanoelectronics circuits using 2D materials.

We obtained the phonon scattering rates for MX_2 (M = Mo, W; X = S, Se) monolayers through deformation potential calculations. We observed that the WS_2 ($MoSe_2$) has the highest (lowest) phonon scattering time in the family of MX_2 monolayers. This observation is consistent with other first-principles study in the literature.

As an application of our formalism, we studied the transport properties in lateral TMDC heterostructures. Material inclusions in TMDCs acts as a short-range scattering centers. We observed the emergence of novel Fano resonances for the first time in 2D materials, when the MoS_2 is encapsulated within the WS_2 monolayer. MoS_2 inclusion here acts as a quantum well, and forms the quasi-bound states that will interact with the propagating modes.

Lastly, we studied mobility as a function of carrier density in a family of TMDC layers with triangular inclusions. Here WS_2 monolayer with MoS_2 inclusions is observed to have the highest mobility by an order of magnitude larger than the phonon-limited mobility. Hence, these lateral TMDC heterostructures should be explored as candidates to realize high-mobility devices.

Chapter 6

BOOSTING THERMOELECTRIC EFFICIENCY IN LATERAL TRANSITION-METAL DICHALCOGENIDE HETEROSTRUCTURES

In this chapter, we apply the scalable first-principles informed quantum scattering theory developed earlier to study the thermoelectric properties of lateral transition metal dichalcogenide heterostructures . In Sec. 6.1, we provide the motivation to study the thermoelectric performance in 2D lateral heterostructures. The methods employed here to calculate the thermoelectric properties are detailed in Sec. 6.2. In Sec. 6.3, we describe the main results and discuss the enhancement of the thermoelectric performance in lateral TMDC heterostructures far beyond the pristine TMDCs. Concluding remarks are provided in Sec. 6.4.

6.1 Introduction

Thermoelectric devices can play a pivotal role in fulfilling future demands for clean energy [172–174]. A good thermoelectric material must have a high thermoelectric figure-of-merit ZT, defined as

$$ZT = \frac{\sigma S^2 T}{\kappa_e + \kappa_{ph}}, \tag{6.1}$$

where T is the absolute temperature, σ is the electrical conductance, S is the Seebeck coefficient, κ_e is the electronic thermal conductivity, and κ_{ph} is the lattice phonon thermal conductivity. In bulk materials, the value of ZT is limited by σ and S varying in inverse proportion, and κ_e and σ varying in direct proportion (Wiedemann-Franz law) [175]. Hence, for a long period of time thermoelectricity was believed to be an inefficient source of energy for practical application [176]. However, the works of Hicks and Dresselhaus [177–179] illustrated that in nanostructures one could achieve a substantial increase in the value of ZT by reducing the dimensionality of the system. The density of electron states per unit volume increases in lower dimensions, thereby resulting in an enhancement in ZT [180]. Since then the field of thermoelectricity has focused on: a) increasing S and σ independently through quantum confinement effects, and b) decreasing κ_{ph} by systematically controlling phonon contributions [181]. Additionally, other techniques such as band-gap engineering [182], carrier-pocket engineering [183], energy filtering [184], and semimetal–semiconductor

transition [185] have been developed to engineer the thermoelectric properties of nanostructures.

Traditionally, semiconductor superlattices and heterostructures have been used to construct efficient thermoelectric devices. However, in such structures, it is experimentally difficult to achieve the efficiency predicted by the theory, since a large number of parameters have to be optimized [186]. In this regard, two-dimensional (2D) materials such as graphene and transition-metal dichalcogenides (TMDC) have attracted tremendous attention due to their unique physical and chemical properties [187]. The high degree of flexibility of 2D materials to tune the electrical and thermal properties, makes them ideal candidates for thermoelectric applications. The prototypical 2D material, graphene, has exhibited a power factor (PF) value as high as 34.5 $\mathrm{mWm^{-1}K^{-2}}$ at room temperature [188]. However, it has limited thermoelectric applications due to the extremely high thermal conductivity ($2000 - 4000\ \mathrm{Wm^{-1}K^{-1}}$ for freely suspended samples at room temperature [189, 190]). In comparison, monolayer (1L) TMDCs maintain a very low thermal conductance due to significantly lower phonon mean free paths [191, 192]. Hence, TMDCs have tremendous potential to realize in-plane thermoelectric and Peltier cooling devices.

There have been several first-principles studies in the literature, calculating the thermoelectric quantities in 1L and layered TMDCs [193–199]. *p*-type MoS_2 1L and *n*-type WSe_2 1L were observed to have maximum ZT values at room temperature, and at higher temperatures, respectively. Also, bilayer MoS_2 is observed to have a PF of 8.5 $\mathrm{mWm^{-1}K^{-2}}$, which is highest amongst the materials with a non-zero bandgap [198]. Yet the conductance and ZT values observed in TMDCs are much lower than the corresponding quantities in traditional thermoelectric materials, such as Bi_2Te_3, and phonon-glass electron-crystals [108]. There are opportunities to boost the thermoelectric performance in TMDCs through the formation of heterostructures.

Similar crystal structure and comparable lattice constants observed in MX_2 (M = Mo, W; X = S, Se) monolayers have motivated the construction of lateral TMDC heterostructures. Experimentally, such structures are fabricated through multi-step chemical vapor deposition techniques [158–162], one-pot synthesis [163], and omnidirectional epitaxy [164]. In traditional thermoelectric materials, such as Bi_2Te_3, quantum confinement through the formation of heterostructures have been demonstrated to enhance the figure-of-merit [200, 201]. We can anticipate such an enhancement in lateral 2D TMDC heterostructures as well.

In this chapter, we study the thermoelectric performance of lateral TMDC het-

erostructures within a multiscale quantum transport framework with inputs from first-principles calculations. We specifically consider triangular inclusions (see Fig. 6.1), since 2D TMDCs are typically grown as triangular flakes. We study both *n*-type and *p*-type lateral heterostructures, for all possible combinations of semiconducting TMDC monolayers: MoS_2, $MoSe_2$, WS_2, and WSe_2. *n*-type WS_2 with WSe_2 triangular inclusions is found to have $ZT \approx 1$ at room temperature, which is five times larger than ZT value of pristine *n*-type WS_2 1L. The peak power factor for the lateral TMDC heterostructures obtained here, are the highest amongst the gapped 2D 1L reported at room temperature till date.

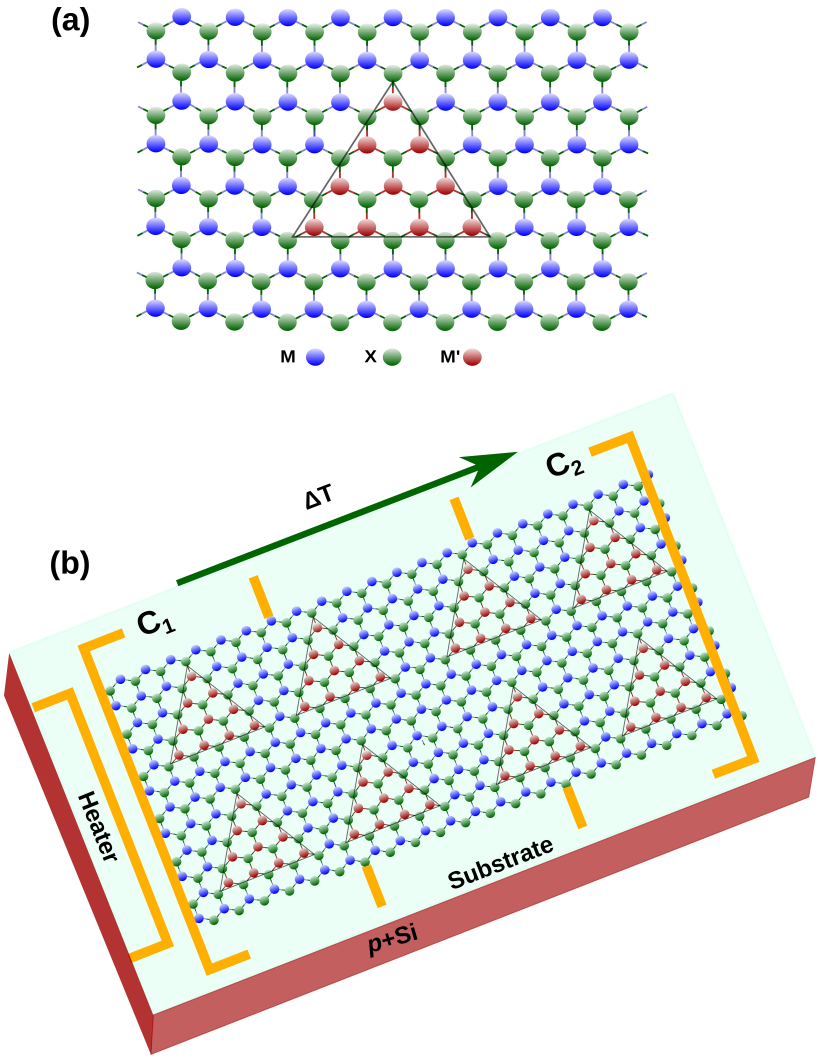

Figure 6.1: A schematic representation of (a) a triangular inclusion in 2D materials is displayed. Here, $M'X_2$ material is confined within the MX_2 matrix. (b) an in-plane thermoelectric device using lateral TMDC heterostructures is shown. 2D monolayer is placed on an oxide substrate that can be grown on *p*+silicon material.

6.2 Methods

To determine the thermoelectric quantities in Eq. (6.4) we need to determine the density of states $g(E)$ and the total scattering time $\tau(E)$. The density of states $g(E)$ is computed from DFT calculations. The phonon and electron scattering contributions of $\tau(E)$ are determined independently.

DFT calculations were performed, using the Vienna Ab Initio Simulation Package (VASP) [205, 206], to obtain the density of states for the various TMDC monolayers studied here. Core and valence electrons were modeled using the projector-augmented wave (PAW) method [207, 208] and the local density approximation [209, 210] was used to describe electron exchange and correlation. The kinetic energy cutoff was set to 500 eV and a Gaussian smearing of 0.1 eV was used for Brillouin-zone integrations. The Brillouin zones were sampled using an $18 \times 18 \times 1$ Γ-centered k-point mesh. The lattice parameters for the TMDC monolayers were fixed at the bulk experimental parameters [MoS_2: [211]; $MoSe_2$: [212]; WS_2 & WSe_2: [213]]. As semilocal functionals underestimate the fundamental gaps of semiconductors, the density of states were shifted, a posteriori, to match the quasi-particle gaps reported in Ref. [133].

The deformation potentials obtained using the first-principles calculations [141, 142] were employed to compute both the acoustic and optical phonon mode contributions. We have included the zeroth order acoustic and optical, and first order acoustic mode contributions. Effect of the Fröhlich interaction is implicitly added to the deformation potential [142]. The total τ_{ph} is determined using the reciprocal sum of these contributions as prescribed by Matthiessen's law. Further details of these calculations can be found in Ref. [214].

For elastic scattering processes in 2D, the kinetic definition of τ_e is given by $\tau_e(E) = 1/(n_d \sigma_m \langle v \rangle)$, where n_d is the disorder density, $\langle v \rangle$ is the average velocity, and σ_m is the momentum scattering cross-section. $\langle v \rangle = 2v/\pi$ for a uniform incoming velocity distribution. σ_m is determined using a multiscale quantum transport framework [214]. Carrier scattering in lateral heterostructures occurs via both propagating and evanescent modes. Standard scattering calculations cannot account for these crucial contributions of decaying evanescent modes, since their probabilities vanish at the asymptotic limit, where the boundary conditions are applied to determine the scattering amplitudes. On the other hand, our methodology accurately includes these contributions since we have circumvented the need for the asymptotic boundary conditions by introducing absorbers around the scattering centers.

	E_c (eV)	E_v (eV)	a (Å)	t (eV)	λ (eV)	$\alpha_+(\alpha_-)$ eV·Å^2	m_K^c (m_e)	m_K^v (m_e)
MoS_2	-4.31	-5.89	3.184	1.059	0.073	-5.97(-6.43)	0.45	0.53
WS_2	-5.97	-5.50	3.186	1.075	0.211	-6.14(-7.95)	0.3	0.34
$MoSe_2$	-3.91	-5.23	3.283	0.940	0.090	-5.34(-5.71)	0.53	0.58
WSe_2	-3.61	-4.85	3.297	1.190	0.230	-5.25(-6.93)	0.33	0.36

Table 6.1: The band parameters used in our calculations are listed. These parameters were obtained from the previously reported first-principles study [133, 166].

Scattering properties are determined through a 2-band $\boldsymbol{k}\cdot\boldsymbol{p}$ Hamiltonian of the form

$$H_{kp} = H_0 + at\left(\eta\, k_x\hat{\sigma}_x + ik_y\hat{\sigma}_y\right) - \lambda\,\eta\frac{(\hat{\sigma}_z - 1)}{2}s, \tag{6.2}$$

where $\hat{\sigma}$ denotes the Pauli matrices, a is the lattice constant, t is the effective hopping integral, λ is the spin-orbit (SO) parameter, and H_0 is given by

$$H_0 = \begin{bmatrix} E_c + \alpha_s k^2 & 0 \\ 0 & E_v \end{bmatrix}. \tag{6.3}$$

Here, α_s is a material parameter, and E_c and E_v are the CB minimum and the VB maximum at the K-valley, respectively. All the material parameters employed in this chapter are listed in Table 6.2. A detailed discussion of the quantum transport framework employed here is described in Ref. [214]. The quantum transport calculations combined with the Boltzmann transport theory determine σ, S and κ_e (see Eq. (6.4)). To determine the ZT factor we also require the phonon thermal conductivity κ_{ph} (see Eq. (6.1)). Typically κ_{ph} is computed through the phonon dispersion relations. We have utilized the κ_{ph} values listed in Ref. [192], that are obtained using DFT calculations.

6.3 Results

Nature of scattering in TMDC heterostructures

In our calculations, the thermoelectric properties are evaluated using the Boltzmann transport theory under the relaxation time approximations. Within this framework, the kinetic definitions of the conductance, Seebeck coefficient, and the electrical

thermal conductivity are given by

$$\begin{aligned} \sigma &= e^2 \mathcal{I}_0, \\ S &= \frac{1}{eT}\frac{\mathcal{I}_1}{\mathcal{I}_0}, \\ \kappa_e &= \frac{1}{T}\left[\mathcal{I}_2 - \frac{\mathcal{I}_1^2}{\mathcal{I}_0}\right], \end{aligned} \tag{6.4}$$

with

$$\mathcal{I}_n = \int dE\, v^2\, \tau(E)\, g(E)\, (E-\mu_F)^n \left(-\frac{\partial f_0}{\partial E}\right), \tag{6.5}$$

where e is the elementary charge, $g(E)$ is the density of states, $v = |\nabla_k E_n(k)|/\hbar$ is the carrier velocity, $f_0(E) = 1/(1+e^{(E-\mu_F)/k_BT})$ is the Fermi-Dirac distribution function, μ_F is the Fermi level, and $\tau(E)$ is the total scattering time. The density of states $g(E)$ is extracted from the electronic band structure obtained using the density functional theory (DFT) calculations within the local-density approximations (LDA). Figure 6.2 displays the density of states as a function of energy for MoS_2, WS_2, $MoSe_2$ and WSe_2 1L. $g(E)$ is normalized with the unit-cell area and the corresponding layer thickness. The PF and ZT value are sensitive to the small variations of $g(E)$ near the band edges.

To determine $\tau(E)$, we need to consider both the intrinsic and extrinsic scattering rates. According to the Matthiessen's law

$$\tau(E)^{-1} = \tau_e(E)^{-1} + \tau_{ph}(E)^{-1}, \tag{6.6}$$

where τ_e is the extrinsic carrier scattering time arising from the material inclusions, and τ_{ph} is the total intrinsic scattering time arising from all the acoustic and optical phonon mode contributions. The intrinsic scattering rate τ_{ph} is assumed to remain unaltered from the pristine 1L, a commonly used assumption while studying nanostructured thermoelectric materials [204].

Figure 6.3 shows the total phonon scattering time versus energy at room temperature for pristine n-type and p-type 1L TMDCs. We have included the acoustic and optical phonon modes corresponding to the transition $K \rightarrow \{K, K', Q, Q'\}$, via corresponding zeroth and first-order deformation potentials (see Methods for details). The optical phonon modes emerge as steps in the scattering rate. In the family of TMDC 1L, $MoSe_2$ (WS_2) has the strongest (weakest) interaction with phonons. In general, WX_2 has a greater phonon-limited electrical conductivity than MoX_2.

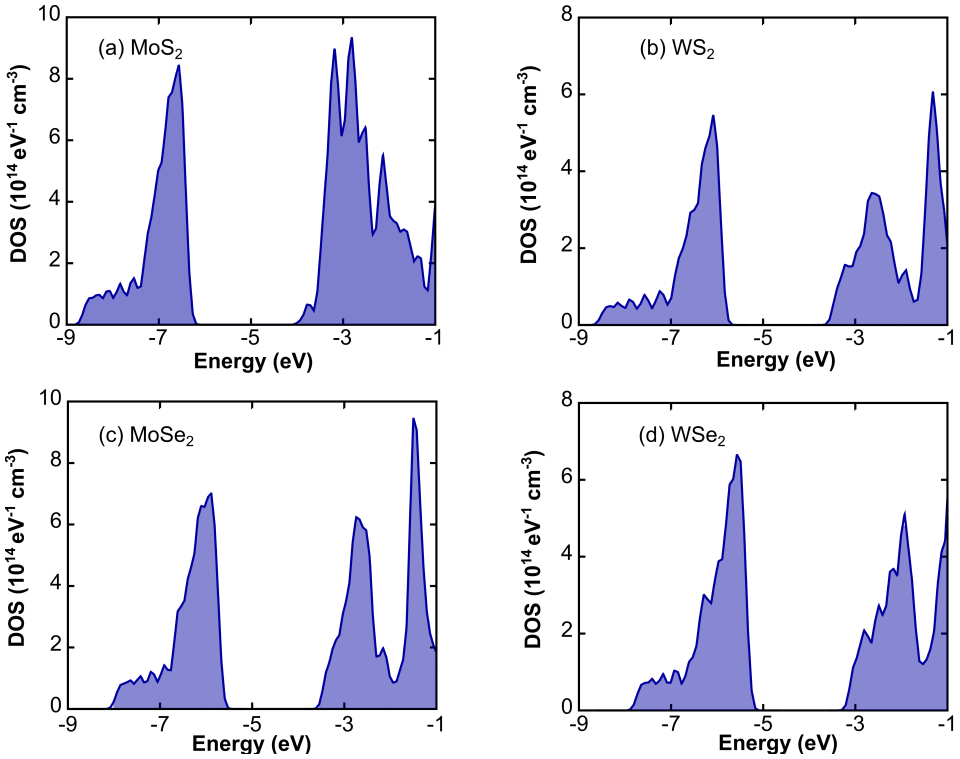

Figure 6.2: Density of states per unit energy per unit area obtained from DFT calculations is plotted as a function of energy for 1L (a) MoS_2, (b) WS_2, (c) $MoSe_2$, and (d) WSe_2. DFT calculations were performed within local-density approximations (LDA), and the spin-orbit effects are neglected. Hence, all bands are doubly degenerate.

These observations and scattering times are consistent with other first-principles studies reported in the literature [141, 142].

To calculate the carrier scattering time τ_e, we have employed a multiscale quantum transport framework informed by first-principles calculations described in Ref. [214]. Material inclusions break the translation symmetry of the system. Hence, the scattering in these structures can occur via both propagating (real wavevector) and evanescent modes (purely imaginary wavevector). As an example, in Fig. 6.4, we have plotted the heterointerface formed between MoS_2 and WS_2 1L. Electronic structure calculations dictate that MoS_2 1L ($E_c = -4.31$ eV) has a lower conduction band (CB) minimum than WS_2 ($E_c = -3.97$ eV) 1L. When an electron in the CB with energy $-4.31\,\text{eV} \leq E < -3.97\,\text{eV}$ is injected from the MoS_2 to WS_2 1L, scattering occurs only through the evanescent modes. Similarly, for carriers in the valence band of p-type WS_2, with energy $-5.50\,\text{eV} \geq E > -5.89\,\text{eV}$ (corresponding to the valence band maximum of MoS_2) only evanescent modes are available for scatter-

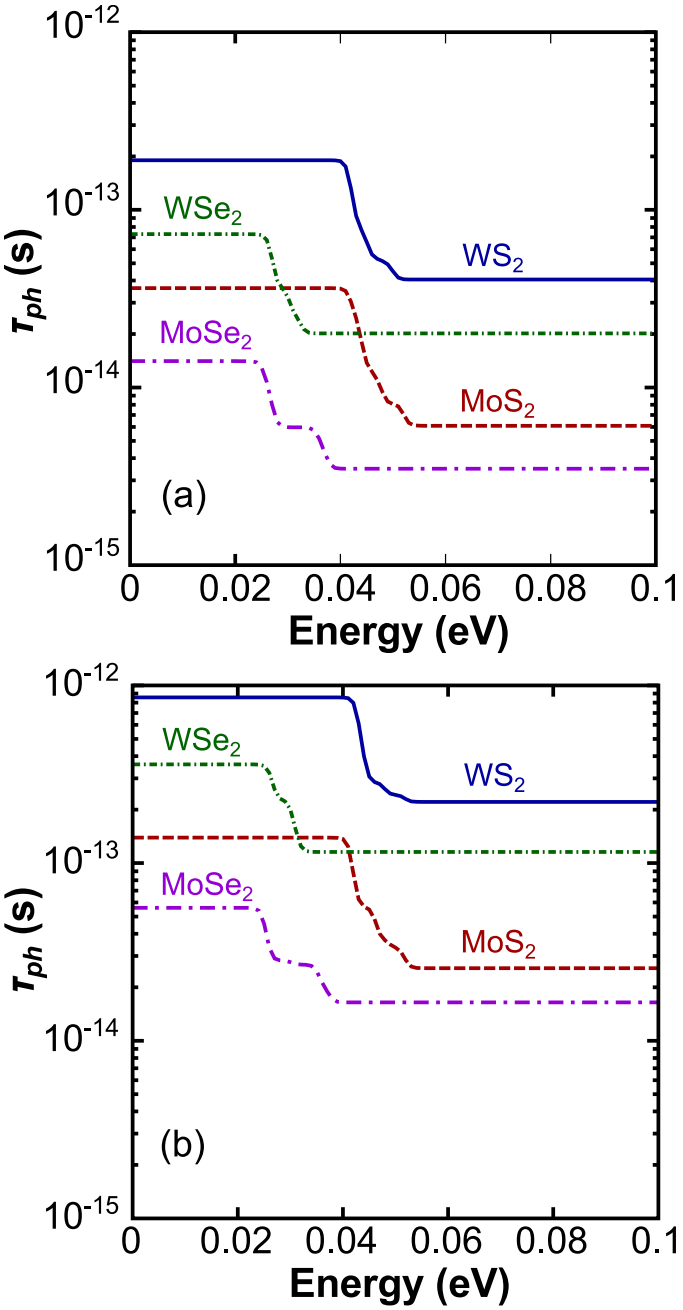

Figure 6.3: The total phonon scattering time versus energy for (a) K-valley electrons, and (b) K-valley holes are plotted for TMDCs at temperature $T = 300$ K. Scattering times are calculated using the deformation potentials listed in Ref. [141–143].

ing. Evanescent modes are situated within the bandgap, and result in exponentially decaying contributions to the scattered wavefunction.

Thermoelectric quantities in Eq. (6.4) are directly proportional to the total scattering time $\tau(E)$. Figure 6.5 displays the electron scattering rate, $1/\tau_e$ as a function of

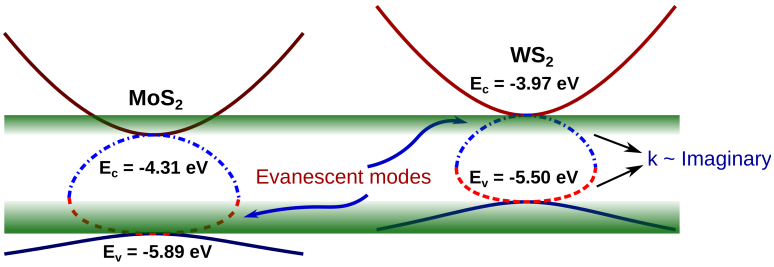

Figure 6.4: The conduction and valance band near the $K-$point are plotted for MoS_2 and WS_2 1L. In the presence of scattering centers, below the energy -3.97 eV (for n-type MoS_2), and above the energy -5.89 eV (for p-type WS_2) carrier transport across the interface occurs only through the evanescent bands.

energy in four different n-type material combinations. We see that $WS_2(MoS_2)$ has a higher scattering time (inverse of the scattering rate) while compared to $MoS_2(WS_2)$. A similar trend is followed by $WSe_2(MoSe_2)$ and $MoSe_2(WSe_2)$ 1L as well.

Power factor and ZT values in TMDC heterostructures

The main results for the peak power factor and ZT values for the n-type and p-type TMDC lateral heterostructures are listed in Table 6.2 and Table 6.3, respectively. In these tables, the notation A(B) represents that the material B inclusions are confined within the matrix of the material A. The material inclusion is considered to be an equilateral triangle, and optimized at the side length 8 nm. Throughout our calculations the density of inclusions is consider to be $n_d = 10^{12}$ cm^{-2}.

We observe that the n-type $WS_2(WSe_2)$, and p-type $MoSe_2(WSe_2)$ have the maximum ZT values at room temperature. On the other hand, n-type $WS_2(WSe_2)$, n-type $WS_2(MoS_2)$, and p-type $MoS_2(MoSe_2)$ have larger ZT values at higher temperatures. In Tables 6.2 and 6.3, for comparison, we have listed the room temperature ZT values for pristine 1L TMDCs obtained from Refs. [192, 193]. For the n-type WS_2 1L we observe up to five times larger ZT value with WSe_2 inclusions as compared to a pristine n-type WS_2 1L. Similarly, for p-type $MoSe_2$ with WSe_2 inclusion, we observe an enhancement by a factor of two in the ZT values while compared to a pristine $MoSe_2$ 1L. In general, ZT values increase with temperature, as there is a multiplicative factor of temperature in Eq. (6.1).

The calculated peak value of the PF for n-type $WS_2(WSe_2)$ and $WS_2(MS_2)$ 1L at room temperature is 5.977 mWK^{-2}m^{-1} and 4.565 mWK^{-2}m^{-1}, respectively. These values are about twice the peak PF value observed in pristine TMDC 1L [198]. Moreover, they are of the same order of magnitude as the observed PF in the

1L heterostructure	PF (10^{-3} WK^{-2}m^{-1})			ZT			Pristine 1L (at 300 K)		
A (B)	300 K	500 K	800 K	300 K	500 K	800 K	A	ZT_{1L} [192]	ZT_{1L} [193]
MoS_2 (WS_2)	0.365	0.293	0.181	0.093	0.124	0.125	MoS_2	0.22	0.25
MoS_2 ($MoSe_2$)	0.335	0.256	0.167	0.084	0.109	0.115	MoS_2	0.22	0.25
WS_2 (MoS_2)	4.565	3.896	2.371	0.598	1.231	1.641	WS_2	0.22	0.23
WS_2 (WSe_2)	5.977	4.476	2.470	0.997	1.611	1.806	WS_2	0.22	0.23
$MoSe_2$ (WSe_2)	0.500	0.367	0.200	0.173	0.227	0.205	$MoSe_2$	0.35	0.36
$MoSe_2$ (MoS_2)	0.485	0.362	0.199	0.165	0.223	0.205	$MoSe_2$	0.35	0.36
WSe_2 ($MoSe_2$)	1.929	1.457	0.815	0.485	0.816	0.875	WSe_2	0.33	0.38
WSe_2 (WS_2)	1.954	1.468	0.819	0.488	0.821	0.879	WSe_2	0.33	0.38

Table 6.2: The peak power factor (PF) and the figure-of-merit ZT are listed for n-type monolayer (1L) TMDC heterostructures at temperatures 300 K, 500 K, and 800 K. Here, the notation A(B) represents that the material B inclusions are confined within the matrix of the material A. The material inclusion is equilateral triangle of the side length 8 nm. The density of inclusions is consider to be, $n_d = 10^{12}$ cm^{-2}. For comparison, we have listed the room temperature ZT values for pristine 1L TMDCs obtained in Refs. [192, 193].

1L heterostructure	PF (10^{-3} WK^{-2}m^{-1})			ZT			Pristine 1L (at 300 K)		
A (B)	300 K	500 K	800 K	300 K	500 K	800 K	A	ZT_{1L} [192]	ZT_{1L} [193]
MoS_2 (WS_2)	1.940	1.862	1.315	0.407	0.713	0.871	MoS_2	0.47	0.53
MoS_2 ($MoSe_2$)	4.076	3.213	2.001	0.648	1.115	1.289	MoS_2	0.47	0.53
WS_2 (MoS_2)	0.895	0.779	0.568	0.274	0.407	0.486	WS_2	0.43	0.42
WS_2 (WSe_2)	1.274	1.203	0.873	0.370	0.607	0.736	WS_2	0.43	0.42
$MoSe_2$ (WSe_2)	2.272	1.826	1.060	0.714	1.004	1.045	$MoSe_2$	0.38	0.39
$MoSe_2$ (MoS_2)	2.015	1.554	0.945	0.560	0.861	0.934	$MoSe_2$	0.38	0.39
WSe_2 ($MoSe_2$)	0.034	0.023	0.014	0.015	0.017	0.016	WSe_2	0.34	0.35
WSe_2 (WS_2)	0.023	0.017	0.011	0.011	0.013	0.013	WSe_2	0.34	0.35

Table 6.3: The peak power factor (PF) and the figure-of-merit ZT are listed for p-type monolayer (1L) TMDC heterostructures at temperatures 300 K, 500 K, and 800 K. Here, the notation A(B) represents that the material B inclusions are confined within the matrix of the material A. The material inclusion is considered to be an equilateral triangle of the side length 8 nm. The density of inclusions is consider to be, $n_d = 10^{12}$ cm^{-2}. For comparison, we have listed the room temperature ZT values for pristine 1L TMDCs obtained in Refs. [192, 193].

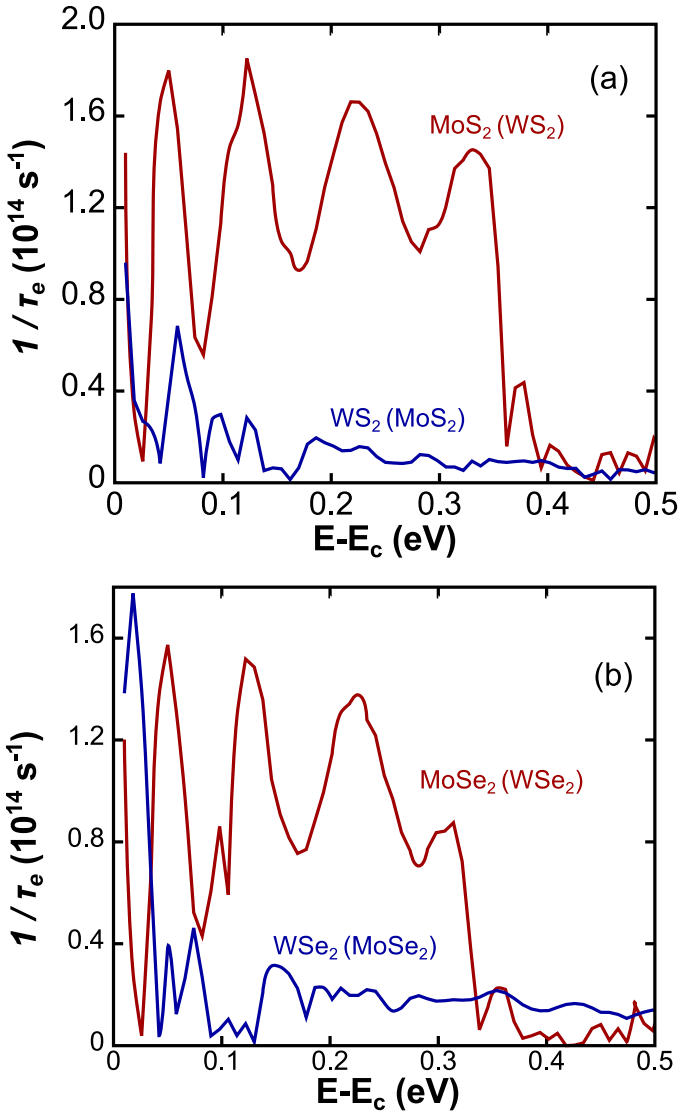

Figure 6.5: The electron scattering rates versus energy for a K-valley electron are plotted for transport in (a) $MoS_2(WS_2)$ & $WS_2(MoS_2)$, and (b) $MoSe_2(WSe_2)$ & $WSe_2(MoSe_2)$ 1L heterostructures.

traditional thermoelectric materials, such as Bi_2Ti_3 ($5.2\,mWK^{-2}m^{-1}$ [202]) and BiSbTe ($5.4\,mWK^{-2}m^{-1}$ [203]) crystals.

In Table 6.2, we observe that n-type $MoS_2(WS_2)$ and $MoS_2(MoSe_2)$ have significantly lower thermoelectric values compared to a pristine MoS_2 1L. Similarly, p-type $WSe_2(WS_2)$ and $WSe_2(MoSe_2)$ have significantly lower thermoelectric values compared to a pristine WSe_2 1L (see Table 6.3). These phenomena can be explained as a direct consequence of band alignment as explained in Sec. 6.3.

Band alignments and the thermoelectric enhancement

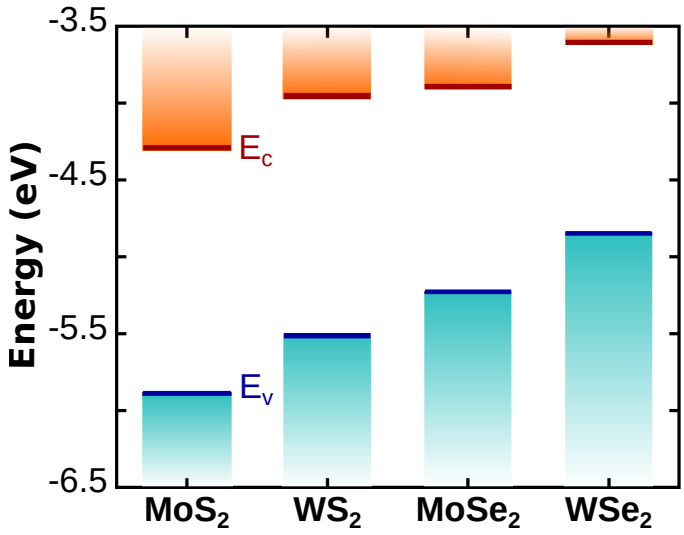

Figure 6.6: The bar chart display the band alignment in the semiconducting TMDC 1L. The conduction band minimum and valance band maximum are represented by E_c and E_v, respectively. These numerical values are listed in Table 6.2.

In Fig. 6.6, we observe that the WS_2 has a higher CB minimum at the K-valley than MoS_2. Hence, MoS_2 inclusions provide additional conduction channels for electrons entering from the n-type WS_2 1L. This will increase the electron scattering time as seen in Fig. 6.5. Whereas in the n-type MOS_2 with WS_2 inclusions scattering occurs through the evanescent modes offered by the WS_2 inclusion. This will significantly decrease the scattering time. Moreover, being real functions the evanescent modes indirectly decrease the probability current by draining the probability of propagating channels. Thereby, significantly reducing the conductance values.

The total scattering time $\tau(E)$ follows the reciprocal sum rule defined in Eq. (6.6). Hence, lower of the two scattering times between τ_{ph} and τ_e will be the dominating contributor to the thermoelectric quantities. For transport in n-type $MoS_2(WS_2)$ 1L, τ_e is an order of magnitude lower than τ_{ph} around the band edge. Hence, we obtain low values of PF and ZT values as shown in Table 6.2.

In p-type heterostructures, the valence band (VB) maxima between the two layers determine the occurance of evanescent modes. In Fig. 6.6, we see that WS_2 has a higher VB maximum than MoS_2. Thus scattering in the p-type $WS_2(MoS_2)$ occurs through evanescent modes. Hence we observe that the p-type WS_2 heterostructures have lower ZT values while compared to the corresponding pristine 1L as seen in Table 6.3. Due to additional conduction channels offered by the WS_2 inclusions, an

enhancement in the ZT and PF values are observed in the p-type $MoS_2(WS_2)$ 1L. An analogous mechanism explains the enhancement observed in p-type $MoSe_2(WSe_2)$, which has the highest room temperature ZT value amongst the p-type heterostructures.

Figure 6.7 displays the conductance, Seebeck coefficient, PF, and electrical thermal conductivity as a function of the reduced Fermi-level $\eta_F = (E - E_c)/k_BT$ for n-type $MoS_2(WS_2)$, and n-type $WS_2(MoS_2)$ 1L heterostructures. Note that σ and κ_e monotonically increase with η_F. Comparing Fig. 6.7(a) and (e), we observe a significant enhancement in σ for $WS_2(MoS_2)$ as reasoned earlier, whereas the Seebeck coefficient remains of the same order for both the heterostructures. Hence we obtain high PF and ZT values for the n-type $WS_2(MoS_2)$ 1L heterostructures. A similar trend is followed by other material combinations as well. We note that the PF increases slightly with increase in the width of material inclusions, and we found it to be optimized for the side length 8 nm. Unlike Schrödinger particles, the massive Dirac particles in TMDC inclusions have a critical length below which they will not occupy any bound states [121]. Below this critical length, heterostructures considered here will have the thermoelectric values similar to that of pristine 1L. In Fig. 6.8, we have displayed the ZT value as a function of the reduced Fermi-level $\eta_F = (E - E_c)/k_BT$ for n-type $MoS_2(WS_2)$, and $WS_2(MoS_2)$ 1L heterostructures. We again see that the ZT is observed to have a maximum value for the side length 8 nm.

6.4 Conclusions

In this chapter, we have investigated the thermoelectric properties of the semiconducting transition metal dichalcogenide lateral heterostructures using a multiscale quantum transport framework. The triangular inclusions were considered here since TMDCs are grown experimentally as triangular flakes. We observed that the n-type WS_2 monolayer with WSe_2 inclusions has the highest room-temperature ZT values, which is about five times larger than the pristine WS_2 monolayer. p-type $MoSe_2$ with WSe_2 inclusions was observed to have a room-temperature ZT value about two times larger than the pristine $MoSe_2$ 1L. The peak PF values calculated in these heterostructures are of the same order as the traditional high-performance thermoelectric materials such as Bi_2Ti_3 and BiSbTe. These PF values obtained here are highest amongst the gapped 2D monolayers. Hence the 2D lateral heterostructures in transition metal dichalcogenides provides exciting new avenues to construct ultra-efficient in-plane thermoelectric devices.

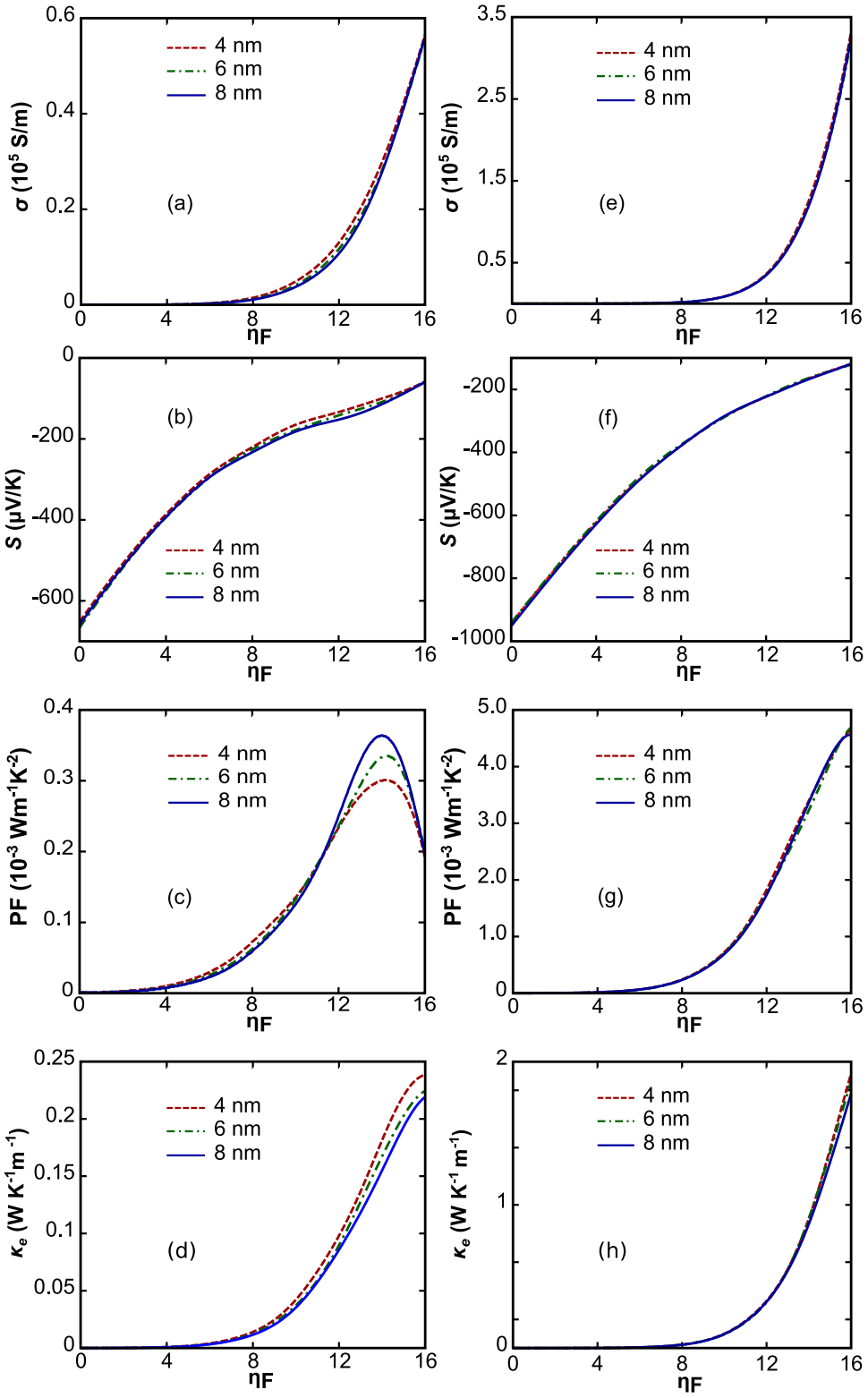

Figure 6.7: The conductance, Seebeck coefficient, power factor, and electrical thermal conductivity are plotted as a function of the reduced Fermi-level $\eta_F = (E - E_c)/k_BT$ for the n-type $MoS_2(WS_2)$, and n-type $WS_2(MoS_2)$ 1L heterostructures. We have considered triangular material inclusions of radius 4, 6, and 8 nm.

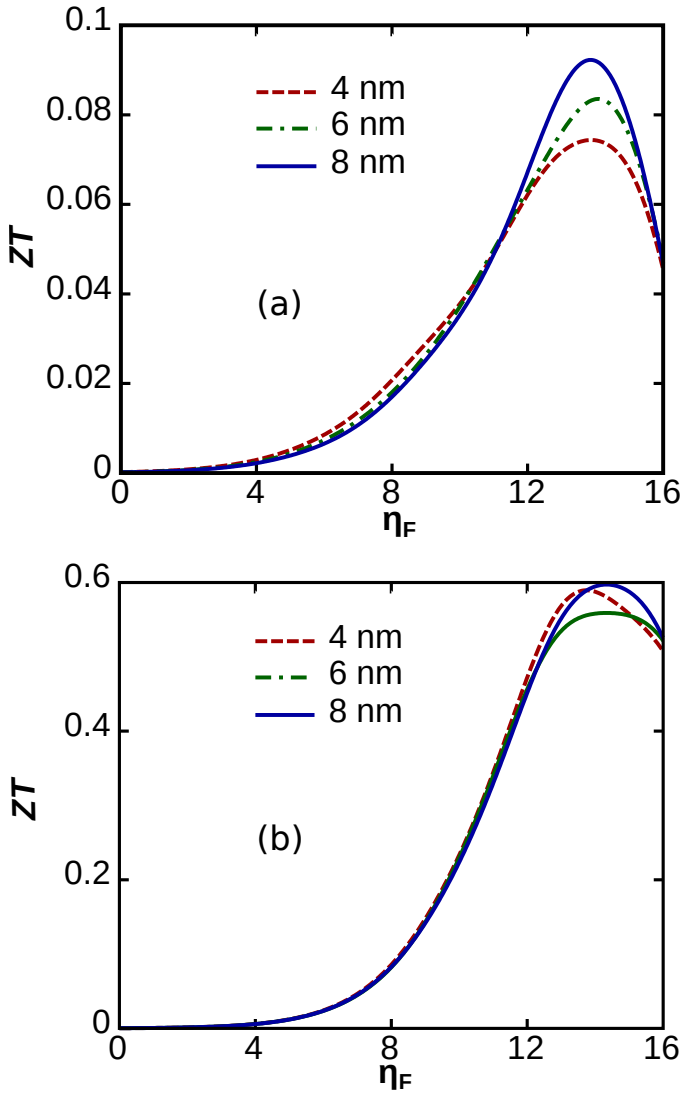

Figure 6.8: The ZT value is plotted as a function of the reduced Fermi-level $\eta_F = (E - E_c)/k_BT$ for the (a) n-type $MoS_2(WS_2)$, and (b) n-type $WS_2(MoS_2)$ 1L heterostructures. We have considered triangular material inclusions of radius 4, 6, and 8 nm.

Chapter 7

SCATTERING THEORY IN THREE-DIMENSIONS USING SOURCES AND ABSORBERS

In this chapter, we set up the framework for the quantum scattering theory in 3D, using our source and absorber scheme. In 3D, we consider a spherical source, and the absorber will be a spherical shell. An incoming plane wave will be of the form

$$e^{i\mathbf{k}\cdot\mathbf{r}} = 4\pi \sum_{l=0}^{\infty} \sum_{m=-l}^{l} i^l \, Y^*_{ml}(k_\theta, k_\phi) Y_{ml}(\theta, \phi) j_l(kr), \tag{7.1}$$

where, Y_{ml} are the Laplace spherical harmonics, $j_l(kr)$ are the spherical Bessel function, and (k_θ, k_ϕ) define the direction of the wavevector $\mathbf{k}$. Following a similar scheme as in Sec. 5.2, we will derive an expression for the source term that can generate plane waves of the form given in Eq. 7.1.

In order to derive this source term, we start with the Green's function equation for the Schrödinger operator in the 3D circular coordinate system given by

$$\left[\nabla^2 + k^2\right] G(\boldsymbol{r}, \boldsymbol{r'}) = S(r', \phi', \theta') \frac{\delta(r - r') \, \delta(\phi - \phi') \, \delta(\theta - \theta')}{r^2 \sin\theta}, \tag{7.2}$$

where $S(r', \phi', \theta')$ is the source term whose form is yet to be determined, the wavevector $k = \sqrt{2m^* E/\hbar^2}$, E is the incoming energy, and m^* is the effective mass. We expand the Green's function in the Fourier form given by

$$G(\boldsymbol{r}, \boldsymbol{r'}) = \sum_{l=0}^{\infty} \sum_{m=-l}^{l} Y^*_{ml}(k_\theta, k_\phi) Y_{ml}(\theta', \phi') g_l(r, r'). \tag{7.3}$$

Substitute this form of the Green's function into Eq. (7.2), multiply by $Y_{ml}(\theta, \phi)$, and integrating over ϕ (from 0 to 2π) & θ (from 0 to π) we obtain

$$\left[\frac{1}{r}\frac{\partial}{\partial r}\left(r^2 \frac{\partial g_l}{\partial r}\right) + \left(k^2 - \frac{l(l+1)}{r^2}\right) g_l\right] = S(r', \phi', \theta') \frac{\delta(r - r')}{r'^2}. \tag{7.4}$$

Here, we have used the orthogonality relations

$$\int_0^{\pi} d\theta \, \sin\theta \int_0^{2\pi} d\phi \, Y^*_{m'l'}(\theta, \phi) Y_{ml}(\theta, \phi) = \delta_{mm'} \delta_{ll'}, \tag{7.5}$$

and

$$\frac{\delta(\phi - \phi') \, \delta(\theta - \theta')}{\sin\theta} = \sum_{l=0}^{\infty} \sum_{m=-l}^{l} Y^*_{ml}(\theta', \phi') Y_{ml}(\theta, \phi). \tag{7.6}$$

The radial part $g_l(r, r')$ is the Green's function for the radial part of Helmholtz equation, and will be of the form

$$g_l(r, r') = A_m \begin{cases} j_l(kr)h_l(kr'), & r \leq r' \\ j_l(kr')h_l(kr), & r > r' \end{cases}, \tag{7.7}$$

where, $j_l(kr)$ and $h_l(kr)$ are the spherical Bessel and Hankel function of first kind, respectively. We determine the coefficient A_m by applying the jump condition at $r = r'$ given by

$$\begin{aligned} \left.\frac{\partial g_l}{\partial r}\right|_{r'+\epsilon} - \left.\frac{\partial g_l}{\partial r}\right|_{r'-\epsilon} &= \frac{S(r', \phi', \theta')}{r'^2}, \\ A_m \mathcal{W}\left[j_l(kr'), h_l(kr')\right] &= \frac{S(r', \phi', \theta')}{r'^2}, \end{aligned} \tag{7.8}$$

where, the Wronskian $\mathcal{W}\left[j_l(kr'), h_l(kr')\right] = i/kr'^2$. Thus

$$A_m = -ik^2\, S(r', \phi', \theta'). \tag{7.9}$$

Substituting Eqs. (7.7) and (7.9) into Eq. (7.3), we obtain the total Green's function of the form

$$\begin{aligned} G(\boldsymbol{r}, \boldsymbol{r'}) = -ik^2\, S(r', \phi', \theta') \times \\ \sum_{l=0}^{\infty} \sum_{m=-l}^{l} Y^*_{ml}(k_\theta, k_\phi) Y_{ml}(\theta', \phi') \begin{cases} j_l(kr)h_l(kr'), & r \leq r' \\ j_l(kr')h_l(kr), & r > r' \end{cases}, \end{aligned} \tag{7.10}$$

To obtain a spherical source we integrate $G(\boldsymbol{r}, \boldsymbol{r'})$ over the solid angle $d\Omega' = sin\theta' d\theta' d\phi'$, where ϕ' goes from 0 to 2π, and θ' goes from 0 to π. Hence the wavefunction emerging from the spherical source is given by

$$\psi_{in}(\rho, \rho') = \int_0^{\pi} d\theta\, \sin\theta \int_0^{2\pi} d\phi' G(\boldsymbol{r}, \boldsymbol{r'}). \tag{7.11}$$

Our aim is to generate plane waves propagating in the forward direction from the spherical source within the region $r \leq r'$. Hence we choose the source term

$$S(r', \theta', \phi') = \frac{4\pi i}{k^2} \sum_{l=0}^{\infty} \sum_{m=-l}^{l} \frac{i^l\, Y^*_{ml}(k_\theta, k_\phi) Y_{ml}(\theta', \phi')}{h_l(kr')}, \tag{7.12}$$

where, $h_l(kr')$ is the spherical Hankel function. With this set up the incoming wavefunction in the absence of external potential is given by

$$\psi_{in} = \begin{cases} e^{i\mathbf{k}\cdot\mathbf{r}} & , r \leq r'; \\ 4\pi \sum_{l=0}^{\infty} \sum_{m=-l}^{l} i^l \, Y^*_{ml}(k_\theta, k_\phi) Y_{ml}(\theta', \phi') \, \dfrac{j_l(kr') h_l(kr)}{h_l(kr')} & \\ & , r > r'. \end{cases}$$

Hence, we obtain plane waves incident on the scattering center from a spherical source at $r = r'$.

With this set up, we can obtain the total wavefunction using finite element analysis as described in earlier chapters. The total wavefunction $\psi = \psi_{in} + \psi_{sc}$, where ψ_{sc} is the scattered wavefunction. In a multiband scattering processes, ψ_{sc} will include both propagating and evanescent mode contributions. We can extend this scattering framework in 3D open domain to multiband processes by using the $\boldsymbol{k}\cdot\boldsymbol{p}$ perturbation theory, as discussed in chapter 5.

Finally, we note that the formalism developed here can be extended to study transport properties in any combination of 3D materials. This will allow us to model transport properties of devices hosted in bulk materials as well. We have previously provided the framework to setup a formalism in 2D open domain as well. Together, these formalism provide a scalable first-principles based quantum transport framework for simulating both two- and three-dimensional nanodevices.

Chapter 8

CONCLUSIONS

In this thesis, we have developed a first-principles-informed multiscale quantum transport theory to study the transport properties of low-dimensional systems. Green's function sources combined with the stealth regions (absorbers) facilitates the construction of a non-asymptotic quantum scattering theory, for confined and open-domains in one, two, and three dimensions. This approach fully accounts for the evanescent solutions that are crucial for determining the scattering properties across heterointerfaces. The geometry discretization scheme employed within our framework, accurately models the transport properties of any complex device geometry. In effect, we have rewritten the traditional scattering treatment with accurate evaluation of the transport properties in proximity to the scattering centers.

This theory is further extended to two-dimensional materials by integrating with $\boldsymbol{k}\cdot\boldsymbol{p}$ perturbation theory, with inputs from *ab-initio* electronic structure calculations. Density functional theory calculations are used to obtain the material parameters, thermal contributions, defect and interfacial potential distributions. Hence, we combine the best of three different numerical methods to obtain a versatile multiscale formalism.

We implement this theory to show a novel Fano q-reversal phenomenon, and a current rectification process in semiconductor quantum waveguides. The current rectification device is expected to find significant applications in quantum transport.

We further analyzed the thermoelectric performance of semiconductor quantum waveguides, and monolayer lateral transition metal dichalcogenide (TMDC) heterostructures. We obtain a significant enhancement in the thermoelectric performance of both the systems, compared to the earlier reported values in their pristine forms. The peak power factor values for the lateral TMDC heterostructures calculated here, are the highest amongst the gapped 2D monolayers reported at room temperature. Hence, our analysis opens new avenues to construct ultra-efficient in-plane thermoelectric devices.

This quantum transport framework developed can also be employed for realizing novel electron optics platforms in molecular junctions, graphene and Van der Waals heterostructures. Our analysis can also be readily extended to study transport in

spintronic, valleytronic, and twistronic devices in layered materials. The fundamental advances in the theory of quantum transport accomplished here will guide us to develop cutting-edge nanodevices and quantum information platforms.

Appendix A

FUNCTION TRANSFORMATIONS AND INTERPOLATION POLYNOMIALS IN FINITE ELEMENT ANALYSIS

This Appendix is organized as follows. Importance of interpolation polynomials in Finite element analysis is briefly discussed in Sec. A.1. A familiarity with function transformation and group theory is required to follow the arguments presented here. A primer on the active and passive transformations is provided in Sec. A.2. A brief introduction to group theory and a transformation by a symmetry operator is discussed in Sec. A.3. In Sec. A.4, the concept of function transformations is introduced with two illustrations. In Sec. A.5, as an example, we formally introduce the scheme based on group representation theory to derive the linear and Hermite interpolation polynomials in one dimension. We further extend this procedure in Sec. A.6 to develop $C^{(2)}$-continuous quintic shape functions *in the element* that can represent an arbitrary function with $C^{(1)}$-continuity for the normal derivative across two triangular elements with a common edge. Transformation of these polynomials to an arbitrary triangular element is discussed in Sec. A.7, so that it is readily applicable in FEA. In Sec. A.8, we summarize the properties of the different choices of interpolation polynomials available on a triangular element. Concluding remarks are presented in Sec. A.9.

A.1 Introduction

Finite element analysis (FEA) has been shown to be a powerful method for the numerical solution of partial differential equations, and is known to be a versatile tool in applications to a wide variety of physical problems including structural mechanics, electromagnetic field modeling, and quantum mechanics [41, 44, 45]. The solution delivered by FEA depends critically on two essential steps. One is the discretization of the physical domain into 1D line elements, 2D rectangles and triangles, or 3D cubes and tetrahedra, that are faithful to the original physical domain. The other is the use of appropriate interpolation polynomials that will represent the solution on each of the discretized regions, or elements, with some level of accuracy over these finite elements. By a choice of using selectively finer and finer mesh refinements for the discretization where the solutions might vary considerably (h-refinement), and using higher order polynomials (p-refinement) for

the interpolation of the solution within each element, it is possible to obtain desired accuracy for the solution. In addition, FEA may be thought of as the discretization of the action integral to directly evaluate the integral. Hence it is very well founded in variational principles which justifies its wide applicability for physical problems.

It is usual to employ linear or quadratic Lagrange interpolation polynomials on the finite elements, so that we have interelement continuity for the solutions, though they may display a "pixelated" form. This is known as $C^{(0)}$-continuity. We can employ $C^{(1)}$- or $C^{(2)}$-continuous polynomials for a better representation of the physical solutions; these correspond to the first or second derivative continuity within and across elements, respectively. We have demonstrated the advantages of such polynomials which are called Hermite interpolation polynomials [41]. In general, Hermite interpolation polynomials can be devised to ensure $C^{(n)}$-continuity across elements. Here $C^{(n)}$-continuity means that the function and its derivatives upto n^{th} order are continuous within each element. The requirements on such polynomials depend on the type of derivative continuity needed in an element of a particular geometry, on the number of nodes per element, and the order of the polynomial derivatives desired at each node.

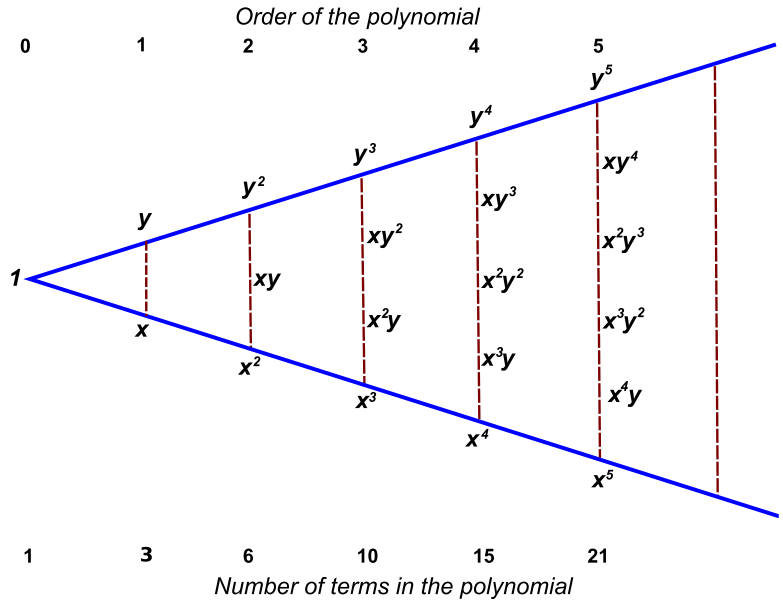

Figure A.1: The two dimensional Pascal triangle.

In the following, we show that group theory provides a beautiful approach for determining the interpolation polynomials on equilateral triangles using their symmetry.

We set the stage by perusing the Pascal triangle of Fig. A.1, which lists the terms in the complete polynomials of a given degree.

For complete 2D quintic polynomials the Pascal triangle shows that 21 terms are present in the polynomials. We will obtain 18 of the parameters by having the nodal values of the function, its first, and second derivatives at the three vertices; this corresponds to the six values (degrees-of-freedom, or DoF) at each vertex node. The remaining three DoF are usually obtained by the normal derivative in the outward direction, with a node at each midpoint of the sides. Polynomials obtained in this manner are not in fashion [215], mainly because the number of DoF at the vertices of the triangle being different as compared with the DoF at the mid-side nodes. Since much of FEA programming involves book-keeping issues anyway, this change in the DoFs from vertices to mid-side nodes should be considered more an irritation than a limitation. However, there are other reasons to avoid using these polynomials. For instance, a side shared by two adjacent triangles will not have continuity of the normal derivative since the polynomials associated with the opposite vertex will influence the value of the function being represented. *Then adjacent triangles sharing a side, but have opposite nodes placed asymmetrically about the shared side will have different normal derivatives*. In addition, such a 21 DoF Hermite triangle will not deliver tangential continuity across adjacent elements since the mid-side nodes seek normal derivative continuity. Alternately, if the tangential derivative is specified at the mid-side nodes, the continuity of the normal derivatives across elements will degrade. A similar limitation arises for the case where all the three nodal degrees of freedom, corresponding to the function value and its two first derivatives, are assigned to a single node at the centroid of the triangle.

A more practical way for finite element programming would be to remove the condition on normal derivatives at the mid-points, thereby making the triangle to be one with 18 DoF. Now, the reduction of the number of parameters from 21 to 18 is achieved imposing a condition that the normal derivative of the *across* the edges of the triangle varies as a cubic rather than a quartic polynomial [216, 217]. In other words, the cubic continuity of the normal derivative of the interpolated function across the edges of the triangle is *implicit* and is enabled without the use of a node on each edge. Meanwhile, tangential continuity across the three sides of the triangle depends on the function value, the first tangential derivative, and the second tangential derivatives, all of which are defined at the two nodes at the

ends of the sides. Such methods of reducing the number of coefficients through combining terms in the 21-term polynomials are not readily generalized to other possible requirements. Thus, the choice of the type of data specified at each node, the number of nodes, and the continuity condition on the polynomial order of the n^{th} derivative will require special schemes to determine the Hermite interpolation polynomials explicitly.

In the following, we present an alternate way in which *group representation theory* can be applied to derive the interpolation polynomials using the symmetry of the element. This method was first proposed by Kassebaum, Boucher and Ram-Mohan (KBR) [73]. Here we provide a detailed account for the derivation of polynomials presented in Ref. [73]. We generalize the formalism to derive new sets of polynomials in three dimensions.

Sets of quintic polynomials on a triangular element obtained through the three methods mentioned above are compared below:

- Polynomials with 21 degrees-of-freedom (DoF) with explicit normal derivatives at the mid-side nodes are computationally efficient except that we need to match the normal derivatives at the common side for 2 adjacent triangles. This is not automatic since the normal derivatives across the shared edge from two adjacent triangles will not agree if these are arbitrary scalene triangles. The alternative choice of a node at the centroid of the triangle with 3 DoF also has non-unique interelement derivative continuity across the sides.

- Polynomials with 18 DoF as presented first by Bell [216], require that the normal derivatives vary as a cubic function across the sides of the triangle. We are thus reducing the number of DoF by three.

- In the KBR method, we obtain 19 conditions on the coefficients of the polynomials using the group representation theory. Additional conditions are obtained for the polynomial by demanding inter-element continuity and Taylor expansion compatibility. These conditions ensure a unique normal across the common side of 2 adjacent triangles, the behavior at and across the shared edge being determined only by the nodal DoFs at the two vertices. The method based on group representation theory can be generalized to obtain shape functions of any order in three and higher dimensions.

A.2 Coordinate transformation

A coordinate transformation is an operation which relates one set of basis vectors to another set of basis vectors. In the current context we will assume it to be a linear transformation.

Given a set of basis vectors $\{\mathbf{e}_i \equiv (\boldsymbol{e}_1, \boldsymbol{e}_2, \boldsymbol{e}_3)\}$, every vector $\boldsymbol{V}$ can be written as a linear combination of these basis vectors

$$\boldsymbol{V} = v_1\boldsymbol{e}_1 + v_2\boldsymbol{e}_2 + v_3\boldsymbol{e}_3. \tag{A.1}$$

Let $\{\mathbf{e}'_i = (\boldsymbol{e}'_1, \boldsymbol{e}'_2, \boldsymbol{e}'_3)\}$ represent the new basis vectors. We can express them in terms of our original set as

$$\begin{aligned}
\boldsymbol{e}'_1 &= a_{11}\boldsymbol{e}_1 + a_{12}\boldsymbol{e}_2 + a_{13}\boldsymbol{e}_3, \\
\boldsymbol{e}'_2 &= a_{21}\boldsymbol{e}_1 + a_{22}\boldsymbol{e}_2 + a_{23}\boldsymbol{e}_3, \\
\boldsymbol{e}'_3 &= a_{31}\boldsymbol{e}_1 + a_{32}\boldsymbol{e}_2 + a_{33}\boldsymbol{e}_3.
\end{aligned} \tag{A.2}$$

And conversely,

$$\begin{aligned}
\boldsymbol{e}_1 &= b_{11}\boldsymbol{e}'_1 + b_{12}\boldsymbol{e}'_2 + b_{13}\boldsymbol{e}'_3, \\
\boldsymbol{e}_2 &= b_{21}\boldsymbol{e}'_1 + b_{22}\boldsymbol{e}'_2 + b_{23}\boldsymbol{e}'_3, \\
\boldsymbol{e}_3 &= b_{31}\boldsymbol{e}'_1 + b_{32}\boldsymbol{e}'_2 + b_{33}\boldsymbol{e}'_3.
\end{aligned} \tag{A.3}$$

Using Einstein's summation convention, we can write Eqs. (A.2, A.3) as

$$\boldsymbol{e}'_i = a_{ij}\boldsymbol{e}_j, \tag{A.4}$$

$$\boldsymbol{e}_j = b_{jk}\boldsymbol{e}'_k, \tag{A.5}$$

where $i, j, k = 1, 2, 3$. Let $\boldsymbol{e}'_i$ and $\boldsymbol{e}_j$ represent two sets of orthonormal bases so that

$$\boldsymbol{e}_i \cdot \boldsymbol{e}_j = \delta_{ij}; \quad \text{and} \quad \boldsymbol{e}'_i \cdot \boldsymbol{e}'_j = \delta_{ij}. \tag{A.6}$$

Substituting Eq. (A.5) in Eq. (A.4) we have,

$$\boldsymbol{e}'_i = a_{ij}b_{jk}\boldsymbol{e}'_k. \tag{A.7}$$

Taking a dot product with $\boldsymbol{e}'_n$ on both sides we have

$$\begin{aligned}
\boldsymbol{e}'_j \cdot \boldsymbol{e}'_n &= a_{ij}b_{jk}\ \left(\boldsymbol{e}'_k \cdot \boldsymbol{e}'_n\right), \\
\delta_{jn} &= a_{ij}b_{jk}\ \delta_{kn}, \\
\delta_{jn} &= a_{ij}b_{jn}.
\end{aligned} \tag{A.8}$$

If we consider a_{ij} and b_{ij} to be the $\{i, j\}$-th elements of the two matrices **A** and **B**, respectively, we have the relation

$$\mathbf{A} \cdot \mathbf{B} = \mathbf{I}, \tag{A.9}$$

where **I** is the identity matrix. Therefore

$$\mathbf{A} = \mathbf{B}^{-1}. \tag{A.10}$$

Rotation matrices in 2D

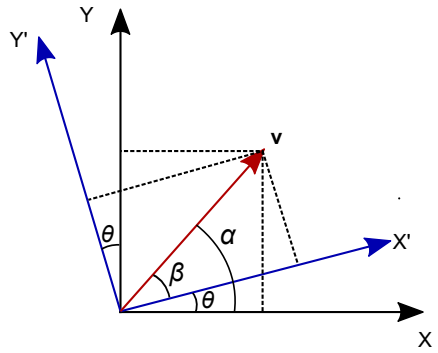

Figure A.2: The passive transformation of a vector is shown. The vector is held fixed while the coordinate system is rotated.

Let us consider a two-dimensional coordinate transformation shown in the Fig. A.2. It is straightforward to determine the matrix elements a_{ij} in this two-dimensional rotation. Since the length of the vector is the same in either of the coordinates (x, y) and (x', y'), $|\boldsymbol{V}| = |\boldsymbol{r}| = |\boldsymbol{r}'|$, we have

$$\begin{aligned} x &= |\boldsymbol{r}| \cos\alpha; \qquad & y &= |\boldsymbol{r}| \sin\alpha; \\ x' &= |\boldsymbol{r}| \cos\beta; \qquad & y' &= |\boldsymbol{r}| \sin\beta. \end{aligned}$$

Now $\alpha = \beta + \theta$, so that

$$\begin{aligned} x' &= |\boldsymbol{r}| \cos(\alpha - \theta) = |\boldsymbol{r}|(\cos\alpha\cos\theta + \sin\alpha\sin\theta), \\ &= x\cos\theta + y\sin\theta. \end{aligned} \tag{A.11}$$

and, similarly

$$\begin{aligned} y' &= |\boldsymbol{r}| \sin(\alpha - \theta) = |\boldsymbol{r}|(-\cos\alpha\sin\theta + \sin\alpha\cos\theta), \\ &= -x\sin\theta + y\cos\theta. \end{aligned} \tag{A.12}$$

We see that the transformation matrix in 2D is given by

$$\begin{bmatrix} x' \\ y' \end{bmatrix} = \begin{bmatrix} \cos\theta & \sin\theta \\ -\sin\theta & \cos\theta \end{bmatrix} \cdot \begin{bmatrix} x \\ y \end{bmatrix}. \tag{A.13}$$

The generalization to 3D is performed using Euler angles defined for rotations about coordinate axes [218, 219]. Two transformation operations in 3D will in general depend on the order in which they are applied; i.e. the reversal of the order of two rotation operations can lead to a different orientation for the resulting axes depending on the order. The transformations are said to be non-commutative.

Note that the transformation matrix

$$B = \begin{bmatrix} \cos\theta & \sin\theta \\ -\sin\theta & \cos\theta \end{bmatrix} = \begin{bmatrix} (\boldsymbol{e}'_1 \cdot \boldsymbol{e}_1) & (\boldsymbol{e}'_1 \cdot \boldsymbol{e}_2) \\ (\boldsymbol{e}'_2 \cdot \boldsymbol{e}_1) & (\boldsymbol{e}'_2 \cdot \boldsymbol{e}_2) \end{bmatrix}, \tag{A.14}$$

has matrix elements that are dot-products of the unit vectors; these entries in the matrix are seen to be the direction cosines of the angles between the coordinate vectors.

Passive Transformation

The transformations discussed in the previous section are called passive transformations. We let the vector $\boldsymbol{V}$ be fixed in coordinate space while the basis set transforms from $\{\boldsymbol{e}_i\}$ to $\{\boldsymbol{e}'_j\}$. Any vector can be represented in terms of components along either of the basis vectors as

$$\boldsymbol{V} = v_i \boldsymbol{e}_i = v'_j \boldsymbol{e}'_j. \tag{A.15}$$

(In matrix form, basis vectors $\{\boldsymbol{e}_i\}$ are represented by a row array and vector components $\{v_i\}$ by a column vector.) Substituting Eq. (A.5) into Eq. (A.15) we relate the vector components in the transformed basis to the components in the earlier basis as

$$\begin{aligned} v'_j \boldsymbol{e}'_j &= v_i (b_{ik} \boldsymbol{e}'_k), \\ v'_j \boldsymbol{e}'_j &= (v_i b_{ik}) \boldsymbol{e}'_k. \end{aligned} \tag{A.16}$$

Taking a dot product with $\boldsymbol{e}'_n$ on both sides we get

$$\begin{aligned} v'_j \boldsymbol{e}'_j \cdot \boldsymbol{e}'_n &= v_i b_{ik} (\boldsymbol{e}'_k \cdot \boldsymbol{e}'_n), \\ v'_j \delta_{jn} &= (v_i b_{ik}) \delta_{kn}, \\ v'_n &= v_i b_{in}, \end{aligned} \tag{A.17}$$

which represents the rule for the transformation of the vector components under a passive transformation. Again, in Fig. A.2, notice that the vector $\boldsymbol{V}$ is fixed in space, but its components are different in the two coordinate systems designated by XY and $X'Y'$.

Active Transformation

In an active transformation, we let the coordinate basis be fixed but transform the physical vectors.[a] After an active transformation we go to a new vector with transformed components with the basis vectors held fixed, in contrast with a passive transformation where we held the vector fixed. Figure A.3 shows the fixed coordinate

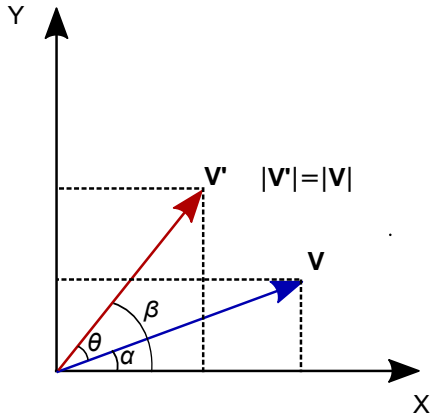

Figure A.3: The active transformation of a vector is shown.

system in which a vector $\boldsymbol{V}$ is rotated by an angle θ in the anti-clockwise sense to a new vector $\boldsymbol{V}'$. The components of $\boldsymbol{V} = \{v_x, v_y\}$ differ from those of $\boldsymbol{V}' = \{v'_x, v'_y\}$ while the magnitude of the two vectors are the same. With $\beta = \alpha + \theta$ and $|\boldsymbol{V}'| = |\boldsymbol{V}| = v$, we have

$$\begin{aligned} v'_x &= v\cos\beta = v\cos(\alpha+\theta), \\ &= (v\cos\alpha)\cos\theta - (v\sin\alpha)\sin\theta; \\ &= v_x\cos\theta - v_y\sin\theta. \end{aligned} \tag{A.18}$$

In a similar manner,

$$\begin{aligned} v'_y &= v\sin\beta = v\sin(\alpha+\theta), \\ &= (v\cos\alpha)\sin\theta + (v\sin\alpha)\cos\theta. \\ &= v_x\cos\theta + v_y\sin\theta. \end{aligned} \tag{A.19}$$

[a]Imagine that we are physically "taking hold" of the vector and rotating it in an active transformation.

Expressing the above equations in matrix notation we have

$$\begin{bmatrix} v'_x \\ v'_y \end{bmatrix} = \begin{bmatrix} \cos\theta & -\sin\theta \\ \sin\theta & \cos\theta \end{bmatrix} \cdot \begin{bmatrix} v_x \\ v_y \end{bmatrix}.$$

In general,

$$v'_i = a_{ij} v_j. \tag{A.20}$$

for $i, j = 1, 2, 3$. Here, a_{ij} is the $(i\,j)^{\text{th}}$ element of the matrix $\boldsymbol{A}$. The transformation matrix $\boldsymbol{A}$ is the transpose (inverse) of the orthogonal matrix $\boldsymbol{B}$ appearing in passive transformations.

Thus we can go from the vector $\boldsymbol{V}$ to $\boldsymbol{V'}$ by doing the transformation of the components, as in above Eq. (A.20) and by keeping the basis vectors fixed. Notice that the transformation law for the active transformation, Eq. (A.20) is the inverse of the passive transformation Eq. (A.17).

In a passive transformation, we always stay in the transforming coordinate (body frame), whereas in the active transformation we work with a fixed (lab frame) coordinate system. Hence, the transforming matrices for the two pictures are inverses of each other.

A.3 Coordinate transformation using symmetry operators

We now present a very brief introduction to *group representation theory* essentially to define the concepts and the notations. The reader is directed to standard books on group representation theory for a more complete treatment [132, 220, 221].
A non-empty set G, with associated operators $(a, b, c \ldots)$, is said to be a "group," when the following four properties are satisfied:

1. *Closure*: The product of any two elements of the group is itself an element of the group.
2. *Associativity*: The operation is associative; that is, $(a \cdot b) \cdot c = a \cdot (b \cdot c)$ for all a, b, c in G.
3. *Identity*: There is an element ϵ in G such that $a \cdot \epsilon = \epsilon \cdot a = a$ for all a in G.
4. *Inverse*: For each element a in G, there is an element a^{-1} in G such that $a \cdot a^{-1} = a^{-1} \cdot a = \epsilon$.

For any given system, the set of all possible operations which leaves the system invariant forms a group known as its 'symmetry group.' Let R be an element of a

symmetry group G. Once we know the way in which the corresponding operator R transforms the given geometry, we can deduce the rule with which the group element will transform the basis vectors (passive perspective) or the coordinates of a vector (active perspective) in space.

For example, the symmetry group of an equilateral triangle, C_{3v} consists of all geometrical transformations that take the triangle to itself. The elements of the group C_{3v} are (see Fig. A.7.

1. the identity ϵ,
2. a rotation by $\pm 2\pi/3$ about the axis perpendicular to the plane of the triangle, denoted by C_3, C_3^{-1},
3. reflection about the planes bisecting the three vertex angles, denoted by $\sigma_1, \sigma_2, \sigma_3$.

Now consider the element C_3 in the symmetry group. Physically, C_3 is an anticlockwise rotation by an angle $2\pi/3$ with respect to the z-axis. Therefore

$$C_3 \cdot \begin{bmatrix} x \\ y \\ z \end{bmatrix} = \begin{bmatrix} \cos\left(\frac{2\pi}{3}\right) & \sin\left(\frac{2\pi}{3}\right) & 0 \\ -\sin\left(\frac{2\pi}{3}\right) & \cos\left(\frac{2\pi}{3}\right) & 0 \\ 0 & 0 & 1 \end{bmatrix} \cdot \begin{bmatrix} x \\ y \\ z \end{bmatrix}, \tag{A.21}$$

$$= \begin{bmatrix} -\frac{1}{2} & \frac{\sqrt{3}}{2} & 0 \\ -\frac{\sqrt{3}}{2} & -\frac{1}{2} & 0 \\ 0 & 0 & 1 \end{bmatrix} \cdot \begin{bmatrix} x \\ y \\ z \end{bmatrix}. \tag{A.22}$$

In general, we may write

$$R \cdot \begin{bmatrix} x \\ y \\ z \end{bmatrix} = \mathbf{D}(R) \cdot \begin{bmatrix} x \\ y \\ z \end{bmatrix}, \tag{A.23}$$

where R is an element in G and $\boldsymbol{D}(R)$ is the corresponding 3×3 matrix. For simplicity, the above expression can be written as

$$R \cdot \boldsymbol{r} = R_{ij}\, x_j. \tag{A.24}$$

Here, R_{ij} is the $(i\,j)^{\text{th}}$ element of the matrix $\boldsymbol{D}(R)$.

A.4 Function transformations

Let us consider a function $f(x_i)$ in coordinate space operated on by a group element R. In an active sense, the transformation takes the coordinates x_j to x_i' given by $x_i' = a_{ij}x_j$. Suppose that the function $f(x_i)$ is acted on by the operator P_R corresponding to the element R thereby yielding a new function $f'(x_j')$. Here we write f' (not f), since the functional form will change due to the coordinate transformation. For example, $f(x) = x^2 + x$ under the reflection operation $x \longrightarrow -x$ will go to a new function $f'(x) = x^2 - x$. Notice that due to the transformation the functional form has changed. Just to be explicit on which transformation is being used, many texts will represent the function $f'(x)$ by $P_R f(x)$. Here $P_R f$ should be considered as a new designation for the transformed function.

Since the function value remains the same after the transformation. We have the relation

$$\begin{aligned} P_R f(x_i') &= f(x_j), \\ P_R f(a_{ik}x_k) &= f(x_j). \end{aligned} \tag{A.25}$$

In vector notation we write

$$P_R f(\boldsymbol{r}') = f(\boldsymbol{r}). \tag{A.26}$$

Here, $\boldsymbol{r}' = R \cdot \boldsymbol{r}$, which is an active transformation.

We can imagine a passive transformation as being on the rotated (transformed) coordinate system and tracing back to the original coordinate system. In the passive sense, we can write the above Eq.(A.26) as

$$P_R f(\boldsymbol{r}) = f(R^{-1} \cdot \boldsymbol{r}). \tag{A.27}$$

In Eq.(A.27) we have exchanged the labels for primed and unprimed coordinate systems. This is because we want to work always with the unprimed coordinate system.

Examples : One of the famous plane curves is the **clothoid** whose curvature is proportional to its arc length. The general form of the clothoid [222] is given in parametric form by

$$clothoid[n, a](t) = a\left(\int_0^t du \sin\left(\frac{u^{n+1}}{n+1}\right), \int_0^t du \cos\left(\frac{u^{n+1}}{n+1}\right)\right). \tag{A.28}$$

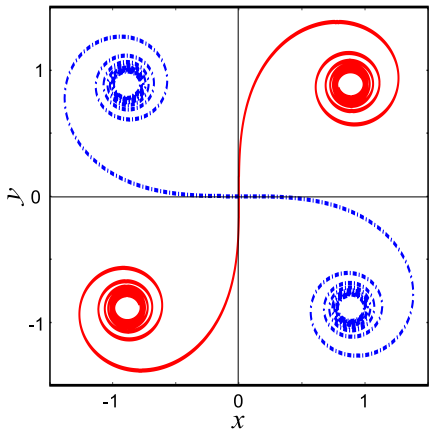

Figure A.4: The $clothoid[1,1]$ (continuous curve) and $clothoid\ '[1,1]$ (dotted curve) obtained through the function transformation of a rotation of $\pi/2$ in the anti-clockwise sense about the z-axis are shown.

For $n = 2$ this is known as Euler's spiral or Cornu's spiral. Under anticlockwise rotation by $\pi/2$ about the z-axis in the passive sense we obtain the new function

$$clothoid\ '[n,a](t) = a\left(-\int_0^t du \cos\left(\frac{u^{n+1}}{n+1}\right), \int_0^t du \sin\left(\frac{u^{n+1}}{n+1}\right)\right). \qquad \text{(A.29)}$$

As one can anticipate, the functional forms of the two clothoids are different. In Fig. A.4, we have shown the functions $clothoid[1,1]$ (continuous curve) and $clothoid\ '[1,1]$ (dotted curve).

As an example of rotation of 2 dimensional surfaces, consider a special hyperbolic paraboloid known as the *monkey's saddle* [222]. On a normal hyperbolic paraboloid a man can easily sit on the saddle as there are indentations for his legs, but not a monkey as there is no space to accommodate its tail. However, a monkey's saddle

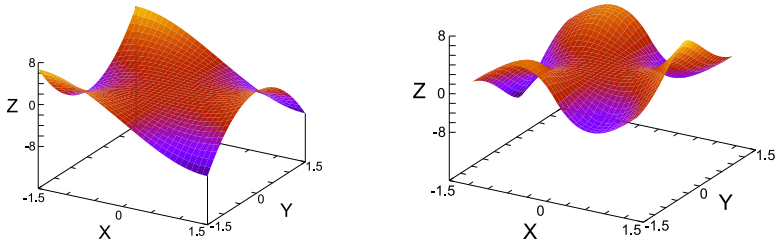

(a) *monkeysaddle(x,y)* **(b)** *monkeysaddlerot(x,y)*

Figure A.5: The function $monkeysaddlerot(x,y)$ is obtained through an anticlockwise passive rotation by $\pi/4$ of the function $monkeysaddle(x,y)$.

would be right for it as shown in the Fig. A.5. Its functional form is given by

$$monkeysaddle(x, y) = x^3 - 3xy^2. \tag{A.30}$$

Under the anticlockwise rotation by an angle of $\pi/4$ about the z-axis, we get the new function

$$\begin{aligned} monkeysaddlerot(x, y) &= monkeysaddle(R^{-1} \cdot \boldsymbol{r}), \\ &= monkeysaddle\left(\frac{(x-y)}{\sqrt{2}}, \frac{(x+y)}{\sqrt{2}}\right), \\ &= \frac{(x-y)^3}{2\sqrt{2}} - \frac{3(x-y)(x+y)^2}{2\sqrt{2}}. \end{aligned} \tag{A.31}$$

These two examples illustrate the idea of function transformation.

As an example of function transformation with a group operator we consider the symmetry group of an equilateral triangle C_{3v}; the group of rotation operators leaving the triangle invariant is

$$G = \left\{E, C_3, {C_3}^{-1}\right\}. \tag{A.32}$$

Clearly, G is a subgroup of C_{3v}. We would like to know the action of the elements of the group G on a function $F(x, y) = xy^2$.

Let $P_E, P_{C_3}, P_{C_3^{-1}}$ be the operators which transforms a function under the rule given by the elements of the group G. Transformation of $F(x, y)$ under the identity element E is given by

$$\begin{aligned} P_E F(x, y) &= F(E^{-1}(x, y)), \\ &= F(x, y) = xy^2. \end{aligned} \tag{A.33}$$

To determine the transformation of $F(x, y)$ under the operation C_3, we write

$$P_{C_3} F(x, y) = F\left({C_3}^{-1}(x, y)\right).$$

We now need the transformation of the coordinate vector under C_3^{-1}. We have

$${C_3}^{-1}\begin{bmatrix} x \\ y \\ z \end{bmatrix} = \begin{bmatrix} -\frac{1}{2} & -\frac{\sqrt{3}}{2} & 0 \\ \frac{\sqrt{3}}{2} & -\frac{1}{2} & 0 \\ 0 & 0 & 1 \end{bmatrix} \cdot \begin{bmatrix} x \\ y \\ z \end{bmatrix} = \begin{bmatrix} -\frac{x}{2} - \frac{\sqrt{3}y}{2} \\ \frac{\sqrt{3}x}{2} - \frac{y}{2} \\ z \end{bmatrix}. \tag{A.34}$$

Therefore

$$P_{C_3}F(x,y) = F\left({C_3}^{-1}(x,y)\right),$$
$$= F\left(-\frac{1}{2}x - \frac{\sqrt{3}}{2}y, \frac{\sqrt{3}}{2}x - \frac{1}{2}y\right),$$
$$= \left(-\frac{x}{2} - \frac{\sqrt{3}y}{2}\right)\left(\frac{\sqrt{3}x}{2} - \frac{y}{2}\right)^2. \tag{A.35}$$

In a similar manner, operation of $P_{{C_3}^{-1}}$ on $F(x,y)$ is given as

$$P_{{C_3}^{-1}}F(x,y) = F\left(C_3(x,y)\right) = \left(-\frac{x}{2} + \frac{\sqrt{3}y}{2}\right)\left(-\frac{\sqrt{3}x}{2} - \frac{y}{2}\right)^2. \tag{A.36}$$

A.5 Interpolation polynomials and symmetry in 1D

We now show how group representation theory can be used to determine the polynomials used for finite element interpolation in one dimension.

Linear interpolation polynomials

Let us first derive the linear Lagrange interpolation polynomials in one dimension through symmetry considerations. The simplest element in one dimension is a line with nodes located at each end at $x_1 = 1$ and $x_2 = -1$. Our "standard element" ranges over $[-1, 1]$.

It is evident that the standard element has a bilateral symmetry about the midpoint, denoted by S_2. The corresponding group elements are, the identity operation denoted by ϵ, and the mirror operation about the origin which is labeled by m. We construct the character table of S_2 in Table A.1 using standard procedures discussed in textbooks on group representation theory [132, 220, 223]. Here S_2 has two irreducible representations given by A_g, for the symmetric, and A_u for the anti-symmetric representation, respectively. (The subscript g is for the German word "gerade" which means "even" and u is for "ungerade" which means "odd.")

An arbitrary scalar, s is invariant under any group operation. Under the mirror operation m, we have $m \cdot s = s$. Thus s belongs to the representation A_g. The function value at a point, a numerical value, must be a scalar, so that it belongs

	ϵ	m	Linear	Quadratic
A_g	1	1	z	x^2, y^2, z^2, xy
A_u	1	-1	x, y	xz, yx
Γ	2	0	$\{x, y\}$	

Table A.1: Character table for the bilateral symmetry group, S_2. We have included the character for the equivalence representation Γ. The entries are the characters of different classes of the group. The last two columns contain the linear and quadratic functions corresponding to the representation in the first column.

to the representation A_g. Similarly, a vector $\boldsymbol{V}$ in one-dimension transforms as $m \cdot \boldsymbol{V} = -\boldsymbol{V}$ under the mirror operation. Hence it, belongs to the representation A_u.

Consider the linear interpolation polynomials with as-yet unknown coefficients in the interval [-1,1]. The polynomials must have the general form

$$N_1(x) = a_1 + b_1 x,$$
$$N_2(x) = a_2 + b_2 x. \tag{A.37}$$

An arbitrary function $\psi(x)$ can be represented by $\psi(x) = \psi_1 N_1(x) + \psi_2 N_2(x)$, where ψ_1, ψ_2 are the values of the function at the node. With nodes located at ± 1 the nodal conditions on these shape functions at the two nodes are

$$N_1(-1) = 1; \quad N_1(1) = 0, \tag{A.38}$$
$$N_2(-1) = 0; \quad N_2(1) = 1. \tag{A.39}$$

Denoting the node at $x = -1$ by x_1 and at $x = +1$ by x_2 (see Fig.A.6) the nodes are

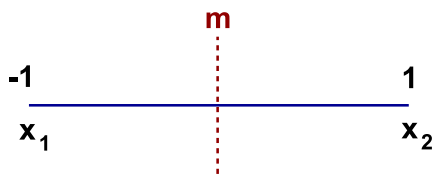

Figure A.6: The standard 1D line element. Nodes are located at $x = 1$ and $x = -1$ which are denoted as x_1 and x_2 respectively.

seen to transform as

$$\epsilon \cdot \begin{bmatrix} x_1 \\ x_2 \end{bmatrix} = \begin{bmatrix} x_1 \\ x_2 \end{bmatrix} = \begin{bmatrix} 1 & 0 \\ 0 & 1 \end{bmatrix} \cdot \begin{bmatrix} x_1 \\ x_2 \end{bmatrix},$$

$$m \cdot \begin{bmatrix} x_1 \\ x_2 \end{bmatrix} = \begin{bmatrix} x_2 \\ x_1 \end{bmatrix} = \begin{bmatrix} 0 & 1 \\ 1 & 0 \end{bmatrix} \cdot \begin{bmatrix} x_1 \\ x_2 \end{bmatrix}. \tag{A.40}$$

These 2×2 coefficient matrices form a representation for the bilateral group which may be called the *nodal equivalence representation*, Γ. Hence, we have the representation

$$\Gamma(\epsilon) = \begin{bmatrix} 1 & 0 \\ 0 & 1 \end{bmatrix}, \quad \Gamma(m) = \begin{bmatrix} 0 & 1 \\ 1 & 0 \end{bmatrix}. \tag{A.41}$$

The traces of these matrices, viz. 2 and 0, are listed in the third row of Table A.1. Clearly, this is a reducible representation as our group has only one dimensional representations. From Table A.1, we see that the equivalence representation can be decomposed as the sum of the 2 irreducible representations

$$\Gamma = A_g + A_u. \tag{A.42}$$

Nodal coordinates, $\{x_1, x_2\}$ transform as per the representation Γ. Hence the linear functions in this space will have components belonging to both the representations A_g and A_u, and these can be determined by operating with the corresponding projection operators.

Let G be a group of order h and Γ^i be an l_i-dimensional representation of G. For a group element R in G, its representation is given by a $l_i \times l_i$ square matrix $\Gamma^i(R)$. Then the projection operator [220], corresponding to the matrix element Γ^i_{mn} for $1 \leq m,\ n \leq l_i$ is given by

$$\mathcal{P}\left(\Gamma^i_{mn}\right) = \frac{l_i}{h} \sum_R \Gamma^i_{mn}(R) \cdot P_R, \tag{A.43}$$

where P_R is the operator corresponding to the element R [220]. From now onward, we denote any group element as R and the corresponding projection operators as P_R. The projection operator $\mathcal{P}\left(\Gamma^i_{mn}\right)$ projects out a function F on to a part f^i_{mn} which belongs to the m^{th} row and n^{th} column of the representation Γ^i. Hence

$$\mathcal{P}\left(\Gamma^i_{mn}\right) F = f^i_{mn}. \tag{A.44}$$

For the group S_2, we have 2 one-dimensional irreducible representations. From Table A.1 the projection operator of the representation A_g is given by

$$\begin{aligned}\mathcal{P}(A_g) &= \frac{1}{2}\left[1.P_\epsilon + 1.P_m\right], \\ &= \frac{1}{2}\left[P_\epsilon + P_m\right]. \end{aligned} \tag{A.45}$$

Let us apply this procedure to find $N_2(x)$. We see that

$$\begin{aligned}\mathcal{P}(A_g)N_2(x) &= \frac{1}{2}\left[P_\epsilon + P_m\right]\left[a_2 + b_2 x\right], \\ &= \frac{1}{2}\left[(a_2 + b_2 x) + (a_2 - b_2 x)\right], \\ &= a_2. \end{aligned} \tag{A.46}$$

$$\begin{aligned}\mathcal{P}(A_u)N_2(x) &= \frac{1}{2}\left[1.P_\epsilon - 1.P_m\right]\left[a_2 + b_2 x\right], \\ &= \frac{1}{2}\left[(a_2 + b_2 x) - (a_2 - b_2 x)\right], \\ &= b_2 x. \end{aligned} \tag{A.47}$$

Hence,

$$N_2(x) = (\mathcal{P}(A_g)N_2(x) + \mathcal{P}(A_u)N_2(x)). \tag{A.48}$$

From Eq. (A.38)

$$N_2(1) = (\mathcal{P}(A_g)N_2(1) + \mathcal{P}(A_u)N_2(1)) = 1. \tag{A.49}$$

$\mathcal{P}(A_g)$ is symmetric and $\mathcal{P}(A_u)$ is antisymmetric under the mirror operation m. Since, the node x_2 can be obtained through the mirror operation on node x_1, we have

$$\begin{aligned}\mathcal{P}(A_u)N_2(-1) &= m \cdot \mathcal{P}(A_u)N_2(1), \\ &= -\mathcal{P}(A_u)N_2(1), \\ &= -b_2. \end{aligned} \tag{A.50}$$

Therefore, we have the relation

$$\mathcal{P}(A_u)N_2(-1) = -\mathcal{P}(A_u)N_2(1). \tag{A.51}$$

From Eq. (A.48) and (A.50),

$$\begin{aligned}N_2(-1) &= m \cdot \left[\mathcal{P}(A_g)N_2(1) + \mathcal{P}(A_u)N_2(1)\right], \\ &= \left[\mathcal{P}(A_g)N_2(1) - \mathcal{P}(A_u)N_2(1)\right] = 0. \end{aligned} \tag{A.52}$$

We solve Eqs. (A.49) and (A.52) to obtain self-consistency conditions as

$$\begin{aligned} \mathcal{P}(A_g)N_2(1) &= \frac{1}{2}, \\ \mathcal{P}(A_u)N_2(1) &= \frac{1}{2}. \end{aligned} \tag{A.53}$$

Using the above Eq.(A.53) we have

$$a_2 = \frac{1}{2},\ b_2 = \frac{1}{2}. \tag{A.54}$$

Hence our shape function is given by

$$N_2(x) = \frac{1}{2}\left(1 + x\right). \tag{A.55}$$

To get $N_1(x)$, we can use the existence of mirror symmetry between x_1 and x_2.

$$N_1(x) = m \cdot N_2(x) = \frac{1}{2}\left(1 - x\right). \tag{A.56}$$

This example illustrates the method for the simplest of shape functions. This procedure can be easily generalized to higher dimensions as discussed in the subsequent sections.

1D Hermite interpolation polynomials and group theory

The Hermite interpolation polynomials on a straight side element give us the freedom to impose derivative continuity at the nodes. As an example, let us determine the one dimensional cubic interpolation polynomials for an element having two nodes, with two degrees-of-freedom at each node. Let, $N_i^{(0)}(x)$, $N_i^{(1)}(x)$ be the polynomials associated with node i, having nodal conditions

$$N_i^{(0)}(x_j) = \delta_{ij}; \quad \frac{d}{dx}N_i^{(0)}(x_j) = 0; \tag{A.57}$$

$$N_i^{(1)}(x_j) = 0; \quad \frac{d}{dx}N_i^{(1)}(x_j) = \delta_{ij}, \tag{A.58}$$

where $i, j = 1, 2$. The superscripts 0 and 1 represent the order of the derivative that is normalized to unity at one of the nodes, i. As before, we derive the interpolation polynomials defined over the range, $[-1, 1]$. We can represent the interpolated function $\psi_{i_{el}}(x)$, whose values and derivatives at nodes are known in the form

$$\psi_{i_{el}}(x) = \sum_{i=1}^{2}\left[N_i^{(0)}(x)\psi_i + N_i^{(1)}(x)\psi_i'\right]. \tag{A.59}$$

The subscript i_{el} provides the index for the element of interest. We have to assign values of two parameters ψ_i and ψ_i' at each node, hence we have 2 degrees of freedom at each node.

It is known that the symmetry of a function is specified by the symmetry of the boundary conditions that are imposed [224]. The boundary conditions must be satisfied by each of the components of the function that belong to the separate irreducible representations of the symmetry group of the boundary conditions. For the Lagrange interpolation polynomials in the above, decomposition into different irreducible representations at the boundary can be seen explicitly in the Eqs. (A.46, A.47).

A general polynomial over the range $[-1, 1]$ for the case of two nodes with 2 DoF at each node is a cubic function. (We have 2 DoF $\times$ 2 nodes=4 as the number of conditions needed to specify the polynomial. So we need to determine 4 coefficients, hence we choose a cubic polynomial which has 4 terms.) As before we denote the node at $x = -1$ as x_1 and the node at $x = 1$ as x_2.

Let us derive the shape function, $N_2^{(0)}(x)$ using group theory considerations. Let

$$N_2^{(0)}(x) = a_1 + b_1 x + c_1 x^2 + d_1 x^3. \tag{A.60}$$

Here, a_1, b_1, c_1 and d_1 are as yet undetermined coefficients. Nodal conditions on this polynomial are

$$N_2^{(0)}(1) = 1,\ N_2^{(0)}(-1) = 0; \tag{A.61}$$

$$\frac{dN_2^{(0)}}{dx}(x = 1) = \frac{dN_2^{(0)}}{dx}(x = -1) = 0. \tag{A.62}$$

We noted in the earlier section that the shape functions in this standard element will be in the equivalence representation Γ, which decomposes as $A_g + A_u$. We can write the A_g and A_u part of the shape function as

$$\mathcal{P}(A_g)N_2^{(0)}(x) = \frac{1}{2}\left[P_\epsilon N_2^{(0)}(x) + P_m N_2^{(0)}(x)\right] = \frac{1}{2}(a_1 + c_1 x^2), \tag{A.63}$$

$$\mathcal{P}(A_u)N_2^{(0)}(x) = \frac{1}{2}\left[P_\epsilon N_2^{(0)}(x) - P_m N_2^{(0)}(x)\right] = \frac{1}{2}(b_1 x + d_1 x^3). \tag{A.64}$$

Nodal conditions for the value of the shape function, $N_2^{(0)}(x)$, given in Eq. (A.61) are rewritten as

$$\mathcal{P}(A_g)N_2^{(0)}(1) + \mathcal{P}(A_u)N_2^{(0)}(1) = 1, \tag{A.65}$$

$$\mathcal{P}(A_g)N_2^{(0)}(-1) + \mathcal{P}(A_u)N_2^{(0)}(-1) = 0, \tag{A.66}$$

Since, $m \cdot x_2 = x_1$, we can simplify Eq. (A.66) as

$$\begin{aligned}\mathcal{P}(A_g)N_2^{(0)}(-1) + \mathcal{P}(A_u)N_2^{(0)}(-1) &= m \cdot \left[\mathcal{P}(A_g)N_2^{(0)}(1) + \mathcal{P}(A_u)N_2^{(0)}(1)\right], \\ &= \mathcal{P}(A_g)N_2^{(0)}(1) - \mathcal{P}(A_u)N_2^{(0)}(1) = 0, \end{aligned} \tag{A.67}$$

Here we have used the fact that $\mathcal{P}(A_g)$ is even and $\mathcal{P}(A_u)$ is odd under mirror operation. We solve the Eq. (A.65) and (A.67) to get

$$\mathcal{P}(A_g)N_2^{(0)}(1) = \frac{1}{2}(a_1 + c_1) = \frac{1}{2}, \tag{A.68}$$

$$\mathcal{P}(A_u)N_2^{(0)}(1) = \frac{1}{2}(b_1 + d_1) = \frac{1}{2}. \tag{A.69}$$

We wish to obtain the representation for the derivative of the shape functions. For that purpose, we introduce the concept of *direct product* between two representations. Let, Γ^1 and Γ^2 are m- and n-dimensional representations of the same group G.Then the direct product [220] of these two representations is defined as

$$\Gamma = \Gamma^1 \otimes \Gamma^2, \tag{A.70}$$

where Γ is a $m \times n$-dimensional representation of the group G.

Under the mirror operation the derivative operator transforms as

$$m \cdot \frac{d}{dx} = -\frac{d}{dx}. \tag{A.71}$$

Hence derivative operator is in the representation A_u. Therefore, the derivatives of the shape functions belonging to the representation $A_g + A_u$ transform as

$$A_u \otimes (A_g + A_u) = A_u + A_g. \tag{A.72}$$

The derivative nodal conditions in Eq. (A.62) decompose at the node x_1 as

$$\mathcal{P}(A_g)\frac{dN_2^{(0)}}{dx}(1) + \mathcal{P}(A_u)\frac{dN_2^{(0)}}{dx}(1) = 0, \tag{A.73}$$

and at x_2 as

$$\begin{aligned}\mathcal{P}(A_g)\frac{dN_2^{(0)}}{dx}(-1) + \mathcal{P}(A_u)\frac{dN_2^{(0)}}{dx}(-1) &= 0, \\ m \cdot \left[\mathcal{P}(A_g)\frac{dN_2^{(0)}}{dx}(1) + \mathcal{P}(A_u)\frac{dN_2^{(0)}}{dx}(1)\right] &= 0, \\ \mathcal{P}(A_g)\frac{dN_2^{(0)}}{dx}(1) - \mathcal{P}(A_u)\frac{dN_2^{(0)}}{dx}(1) &= 0. \end{aligned} \tag{A.74}$$

Solving the Eqs. (A.73, A.74) we have

$$\mathcal{P}(A_g)\frac{dN_2^{(0)}}{dx}(1) = b_1 + 3d_1 = 0, \tag{A.75}$$

$$\mathcal{P}(A_u)\frac{dN_2^{(0)}}{dx}(1) = 2c_1 = 0. \tag{A.76}$$

The self-consistency conditions in Eqs. (A.68), (A.69), (A.75) and (A.76) can be cast into the matrix form

$$\begin{bmatrix} 1 & 1 & 0 & 0 \\ 0 & 2 & 0 & 0 \\ 0 & 0 & 1 & 1 \\ 0 & 0 & 1 & 3 \end{bmatrix} \cdot \begin{bmatrix} a_1 \\ c_1 \\ b_1 \\ d_1 \end{bmatrix} = \begin{bmatrix} 1 \\ 0 \\ 1 \\ 0 \end{bmatrix}. \tag{A.77}$$

Here the coefficients are rearranged in such a way that 4×4 matrix will take the block-diagonal form. We have two blocks each of dimension 2, which are consistent with the representations given in the Eq. (A.42,A.72). We invert the above matrix equation to determine the coefficient values,

$$\begin{bmatrix} a_1 \\ c_1 \\ b_1 \\ d_1 \end{bmatrix} = \begin{bmatrix} 1 & -\frac{1}{2} & 0 & 0 \\ 0 & \frac{1}{2} & 0 & 0 \\ 0 & 0 & \frac{3}{2} & -\frac{1}{2} \\ 0 & 0 & -\frac{1}{2} & \frac{1}{2} \end{bmatrix} \cdot \begin{bmatrix} 1 \\ 0 \\ 1 \\ 0 \end{bmatrix}, \tag{A.78}$$

and obtain the shape function

$$N_2^{(0)}(x) = \frac{1}{4}\left(2 + 3x - x^3\right). \tag{A.79}$$

Before we proceed to obtain other shape functions, we introduce a new classification for the shape function or the interpolation polynomials depending on the nodal conditions.

The functions whose values are set to 1 at a node and 0 at all the other nodes are called scalar shape functions. Hence, $N_1^{(0)}(x)$ and $N_2^{(0)}(x)$ are scalar shape functions as their values are set to 1 at the node $x = -1$ and $x = 1$, respectively.

The functions whose first derivative value is set to 1 at a node and 0 at all the other nodes are called vector shape functions. Hence, $N_1^{(1)}(x)$ and $N_2^{(1)}(x)$ are vector shape functions as their x derivative values are set to 1 at the node $x = -1$ and $x = 1$,

respectively. This classification will be useful when we discuss the transformation properties of these shape functions from one node to an another, as well as from the standard element to an arbitrary element.

Next, we derive $N_2^{(1)}(x)$ using a similar procedure. Let

$$N_2^{(1)}(x) = a_2 + b_2 x + c_2 x^2 + d_2 x^3. \tag{A.80}$$

The nodal conditions on this polynomial are

$$N_2^{(1)}(1) = N_2^{(1)}(-1) = 0.$$

$$\frac{dN_2^{(1)}}{dx}(x = 1) = 1, \ \frac{dN_2^{(1)}}{dx}(x = -1) = 0.$$

Nodal conditions on the value of $N_2^{(1)}$ are invariant under the mirror operation. Hence $N_2^{(1)}$ has components in irreducible representations of the group S_2. Hence, at $x = 1$ we write

$$\mathcal{P}(A_g)\frac{dN_2^{(1)}}{dx}(1) + \mathcal{P}(A_u)\frac{dN_2^{(1)}}{dx}(1) = 1, \tag{A.81}$$

and at $x = -1$ we have

$$\mathcal{P}(A_g)\frac{dN_2^{(1)}}{dx}(-1) + \mathcal{P}(A_u)\frac{dN_2^{(1)}}{dx}(-1) = 0,$$

$$m \cdot \left[\mathcal{P}(A_g)\frac{dN_2^{(1)}}{dx}(1) + \mathcal{P}(A_u)\frac{dN_2^{(1)}}{dx}(1)\right] = 0,$$

$$\mathcal{P}(A_g)\frac{dN_2^{(1)}}{dx}(1) - \mathcal{P}(A_u)\frac{dN_2^{(1)}}{dx}(1) = 0. \tag{A.82}$$

Solving the Eqs.(A.81) and (A.82) we have

$$\mathcal{P}(A_g)\frac{dN_2^{(1)}}{dx}(1) = b_2 + 3d_2 = \frac{1}{2},$$

$$\mathcal{P}(A_u)\frac{dN_2^{(1)}}{dx}(1) = 2c_2 = \frac{1}{2}. \tag{A.83}$$

Similarly, for the shape function values of $N_2^{(1)}(x)$ we can deduce the conditions as

$$\mathcal{P}(A_g)\frac{dN_2^{(1)}}{dx}(1) = a_2 + c_2 = 0,$$

$$\mathcal{P}(A_u)\frac{dN_2^{(1)}}{dx}(1) = b_2 + d_2 = 0. \tag{A.84}$$

We can cast the above four equations in matrix form as

$$\begin{bmatrix} 0 & 4 & 0 & 0 \\ 1 & 1 & 0 & 0 \\ 0 & 0 & 2 & 6 \\ 0 & 0 & 1 & 1 \end{bmatrix} \cdot \begin{bmatrix} a_2 \\ c_2 \\ b_2 \\ d_2 \end{bmatrix} = \begin{bmatrix} 1 \\ 0 \\ 1 \\ 0 \end{bmatrix}, \tag{A.85}$$

and invert the matrix to determine the coefficients a_2, b_2, c_2 and d_2. We then have

$$N_2^{(1)}(x) = \frac{1}{4}\left(-1 - x + x^2 + x^3\right). \tag{A.86}$$

Shape functions associated with node x_2 are now obtained through appropriate symmetry group transformations. We deduce $N_1^{(0)}(x)$ through the mirror operation on $N_2^{(0)}(x)$ to get

$$\begin{aligned} m \cdot\ N_2^{(0)}(x) &= N_2^{(0)}\left(\xi(x)\right), \\ &= N_2^{(0)}(-x), \\ m \cdot N_2^{(0)}(x) &= N_1^{(0)}(x), \\ &= \frac{1}{4}\left(2 - 3x + x^3\right). \end{aligned} \tag{A.87}$$

where $\xi(x) = m^{-1} \cdot x = -x$. Under the group transformation from the node x_2 to x_1, the shape functions $N_1^{(1)}$ and $N_2^{(1)}$ transform from one to the other as the component of a vector in one-dimensional space. Hence we call $N_2^{(1)}$ and $N_1^{(1)}$ as vector shape functions.[b] While transforming to $N_1^{(1)}$ from $N_2^{(1)}$ we will have the *Jacobian* associated with the transformation as a coefficient. We write

$$N_1^{(1)}(x) = N_2^{(1)}\left(\xi(x)\right)\ \frac{dx}{d\xi} = \frac{1}{4}(-1 + x + x^2 - x^3). \tag{A.88}$$

Let us verify that the above expression satisfies the required boundary conditions. We see that

$$\begin{aligned} N_1^{(1)}(1) &= N_2^{(1)}(-1)\frac{dx}{d\xi} = 0, \\ N_1^{(1)}(1) &= N_2^{(1)}(1)\frac{dx}{d\xi} = 0. \end{aligned} \tag{A.89}$$

Using the chain rule for differentiation we have

$$\begin{aligned} \frac{dN_1^{(1)}(x)}{dx} &= \frac{dN_2^{(1)}\left(\xi(x)\right)}{d\xi}\ \frac{d\xi}{dx}\ \frac{dx}{d\xi}, \\ &= \frac{dN_2^{(1)}\left(\xi(x)\right)}{d\xi}. \end{aligned} \tag{A.90}$$

[b] We will explain this concept in more detail in Sec. A.6.

Hence

$$\frac{dN_1^{(1)}}{dx}(1) = \frac{dN_2^{(1)}}{d\xi}(\xi(1)) = \frac{dN_2^{(1)}}{d\xi}(-1) = 0.$$

$$\frac{dN_1^{(1)}}{dx}(-1) = \frac{dN_2^{(1)}}{d\xi}(\xi(-1)) = \frac{dN_2^{(1)}}{d\xi}(1) = 1. \tag{A.91}$$

First, we note that for vector shape functions transformation from one node to an another will involve the *Jacobian* factor $\frac{dx}{d\xi}$ as the coefficient. Second, notice that for scalar and vector shape functions have different transformation properties. A list of all 4 DoF cubic polynomials on a 1D line element that support $C^{(1)}$-continuity across the element are listed in Table B.1.2. It is straightforward to derive the 6 DoF $C^{(2)}$-continuous quintic Hermite polynomials in 1D in a similar manner. These are displayed in Table B.1.3. *One of the highlights of our formalism is that once we determine all the polynomials at a node, we can easily generate the polynomials associated with the other nodes in the element by group transformations.*

A.6 Shape functions for a triangular element

Now consider the interpolation polynomials in two dimensions specifically on a triangular element with nodes located at the vertices. The data at its vertices provide a total of 18 DoF with which to describe an arbitrary function over the triangle, with 6 DoF values at each of the three vertices. From Fig. A.1, we see that the next higher complete polynomial with more than 18 terms is the quintic polynomial which has 21 parameters.

Here the nodal conditions will have two types of symmetries. For example, let a function $f(x)$ be a constant f_1 at the vertex 1 and zero at vertices 2 and 3 of an equilateral triangle. A mirror operation which takes vertex 2 to 3 leave $f(x)$ invariant. Hence, $f(x)$ has S_2 symmetry. Let $\partial_x f$ is set to 0 at all the three vertices. Any operation in the symmetry group C_{3v} leave the $\partial_x f$ value invariant. Hence, $\partial_x f(x)$ is invariant under the operators of the group C_{3v}.

Let the desired shape function be written as an arbitrary complete fifth order polynomial

$$N_i^{(m,n)}(x, y) = \sum_{j=1}^{21} c_j^{(i)} x^a y^b, (i = 1, 2, 3), \qquad \text{such that } a + b \leq 5, \tag{A.92}$$

	ϵ	$2C_3$	$3m$	Linear	Quadratic
A_1	1	1	1	z	x^2+y^2, z^2
A_2	1	1	-1	-	-
E	2	-1	0	$\{x, y\}$	$\{x^2-y^2, xy\}, \{xz, yz\}$
Γ^{eq}	3	0	1	$\{x, y, z\}$	

Table A.2: Character table for the symmetry group of an equilateral triangle. We have included the character for the reducible representation Γ^{eq}, which is explained in the section A.6. The last two columns contains the linear and quadratic basis functions of the corresponding representation in the first column.

where $c_j^{(i)}$ are real coefficients to be determined.

The superscripts on N_i denote the derivative order necessary for the shape function to be equal to unity at its associated node and they have the values

$$\{(m,n) = (0,0), (0,1), (1,0), (2,0), (1,1), (0,2)\}\,. \tag{A.93}$$

The indices m and n are associated with the order of the x and y derivative of N_i which is set to 1 at the associated node.

For example, $N_1^{(0,0)}$ is the polynomial whose value is set 1 at the node $\boldsymbol{r}_1$ and 0 at all other nodes (see Fig. A.7). Similarly, $N_1^{(1,0)}$ and $N_1^{(0,1)}$ are the polynomial whose x and y derivative is set to 1 at the node $\boldsymbol{r}_1$ and zero at all other nodes, respectively. Similarly $N_1^{(2,0)}$, $N_1^{(1,1)}$ and $N_1^{(0,2)}$ are the polynomial corresponding to second derivative ∂_{xx}, ∂_{xy} and ∂_{yy} respectively. Since we require, values of the function, its two first derivatives and three second derivatives to be defined at each node, we have 6 conditions $\times$ 3 nodes=18 Hermite interpolation polynomials on the equilateral triangle.

Scalar shape functions $N_i^{(0,0}$ are normalized to unity at a specified vertex, i, and zero at the other two vertices. They have bilateral symmetry in the function value at the nodes. Since, all of its derivatives are set to zero at all 3 vertices, derivatives of scalar shape functions will have the symmetry of an equilateral triangle.

Let us derive the expression for $N_1^{(0,0)}$ which is the shape function associated with the node at $\boldsymbol{r}_1$. The polynomial expansion is projected into the irreducible representations of the bilateral group S_2 and the group of the equilateral triangle C_{3v}. Character table for S_2 and for C_{3v} are given in Table A.1 and A.2 respectively. The triangle can be constructed from one of its halves using the operations of S_2, so the

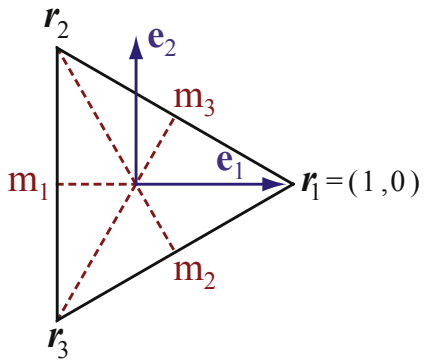

Figure A.7: The equilateral triangular element and the mirror operations of the group C_{3v}.

nodal conditions can be applied to just two nodes that belong to one of the halves. Similarly, the nodal conditions that are symmetric with respect to C_{3v} can be applied at just one vertex. The conditions on other two nodes are imposed implicitly through group theoretical operations.

As noted before, irreducible representations of S_2 are A_g and A_u. The nodal conditions on the symmetry components are provided using in the projection operator in Eq. (A.43) as Note that we are putting these conditions manually in such a way that $N_1^{(0,0)}$ is normalized to unity at $\boldsymbol{r}_1$ and zero at $\boldsymbol{r}_2$ or $\boldsymbol{r}_3$, as per our original nodal conditions.

$$\mathcal{P}(A_g)N_1^{(0,0)}(\boldsymbol{r}_1) = 1; \qquad \mathcal{P}(A_u)N_1^{(0,0)}(\boldsymbol{r}_1) = 0, \tag{A.94}$$

$$\mathcal{P}(A_g)N_1^{(0,0)}(\boldsymbol{r}_2) = 0; \qquad \mathcal{P}(A_u)N_1^{(0,0)}(\boldsymbol{r}_2) = 0. \tag{A.95}$$

From Fig. A.7 we note that

$$\begin{aligned} \mathcal{P}(A_g)N_1^{(0,0)}(x,y) &= \frac{1}{2}\left[P_\epsilon N_1^{(0,0)}(x,y) + P_m N_1^{(0,0)}(x,y)\right], \\ &= \frac{1}{2}[N_1^{(0,0)}(x,y) + N_1^{(0,0)}(x,-y)], \end{aligned} \tag{A.96}$$

and

$$\begin{aligned} \mathcal{P}(A_u)N_1^{(0,0)}(x,y) &= \frac{1}{2}\left[P_\epsilon N_1^{(0,0)}(x,y) - P_m N_1^{(0,0)}(x,y)\right], \\ &= \frac{1}{2}[N_1^{(0,0)}(x,y) - N_1^{(0,0)}(x,-y)]. \end{aligned} \tag{A.97}$$

We use the notation

$$N_1^{(0,0)} = \sum_{n=1}^{21} c_n p_n(x,y), \tag{A.98}$$

where $p_n(x, y) = x^a y^b$, for all possible a, b such that $a + b \leq 5$. So Eq. (A.96) and Eq. (A.97) become

$$\begin{aligned}\mathcal{P}(A_g)N_1^{(0,0)}(x, y) = c_{21}x^5 + c_{19}x^4 + c_{18}x^3y^2 + c_{16}x^3 + c_{14}x^2y^2 + c_{12}x^2 \\ +c_{11}xy^4 + c_9xy^2 + c_7x + c_5y^4 + c_3y^2 + c_1,\end{aligned} \tag{A.99}$$

$$\begin{aligned}\mathcal{P}(A_u)N_1^{(0,0)}(x, y) = c_{20}x^4y + c_{17}x^3y + c_{15}x^2y^3 + c_{13}x^2y + c_{10}xy^3 \\ +c_8xy + c_6y^5 + c_4y^3 + c_2y.\end{aligned} \tag{A.100}$$

Now we can use Eqs. (A.94, A.95) to get 4 equations to determine the coefficients $\{c_i\}$.

The rest of the nodal conditions equate the derivatives of the shape function $N_i^{(0,0)}$ to zero at all the three nodes, which have the symmetry of the equilateral triangle. Therefore, these nodal conditions decompose as per the irreducible representations of the symmetry group C_{3v}. To get these conditions we need the concept of *"Equivalence Representation"* which is introduced in the next section.

Equivalence Representation

We noted earlier that the group representation theory has reduced the problem of finding shape functions associated with each node in an element to that of finding shape functions that belong only to those nodes that cannot be transformed from other nodes under operations of the symmetry group of the element. Nodes that can be transformed into each other under an element of the symmetry group we call them to be *equivalent*. The notion is motivated from group theory applied to covalent molecules [132, 221]. Two bonds in a molecule are said to be *equivalent* if they transform to one another under an operation in the symmetry group of the molecule. For example, the shape of the ammonia molecule (NH_3) is a trigonal pyramid. Three hydrogen (H) atoms are at the vertices of the triangle and the nitrogen (N) atom is at the top vertex of the pyramid. Hence it has C_{3v} symmetry. All three N-H bonds can be brought into each other under the symmetry operations of the group C_{3v}. Therefore, we say that all the three N-H bonds are equivalent.

In case of the equilateral triangle element (see Fig. A.7), node at $\boldsymbol{r}_2$ and $\boldsymbol{r}_3$ can be brought into the node at $\boldsymbol{r}_1$ by rotation and reflection operations of the symmetry group C_{3v} respectively. Hence all these three nodes are equivalent. Therefore, once we determine the shape function $N_1^{(0,0)}$, we can determine $N_2^{(0,0)}$ and $N_3^{(0,0)}$ by simply applying the symmetry operations on $N_1^{(0,0)}$. The shape functions associated with the derivative DoFs at $\boldsymbol{r}_1$ are treated in a similar manner once we account for the vector

nature of $\{\partial_x, \partial_y\}$ and the tensor nature of the second derivatives $\{\partial_{xx}, \partial_{xy}, \partial_{yy}\}$ under a coordinate transformation.

Nodal equivalence representation

The transformation that takes one equivalent node into the other generates a representation for the symmetry group that we call as the *nodal equivalence representation* [73]. The matrix components, D_{ij}^{eq} of the nodal equivalence representation $\Gamma^{eq}(R)$ is given by

$$R \cdot x_i = \sum_{j=1}^{3} D_{ij}^{eq}\, x_j. \tag{A.101}$$

Let us obtain the nodal equivalence representation for the equilateral triangle element. From Fig. A.7, we see that under the mirror operation m_1, the node at $\boldsymbol{r}_1$ remain invariant. Whereas, the node at $\boldsymbol{r}_2$ and $\boldsymbol{r}_3$ transform into one another. Therefore

$$m_1 \cdot \begin{bmatrix} x_1 \\ x_2 \\ x_3 \end{bmatrix} = \begin{bmatrix} x_1 \\ x_3 \\ x_2 \end{bmatrix} = \begin{bmatrix} 1 & 0 & 0 \\ 0 & 0 & 1 \\ 0 & 1 & 0 \end{bmatrix} \cdot \begin{bmatrix} x_1 \\ x_2 \\ x_3 \end{bmatrix}, \tag{A.102}$$

and the nodal equivalence representation of m_1 is given by

$$\Gamma^{eq}(m_1) \equiv \begin{bmatrix} 1 & 0 & 0 \\ 0 & 0 & 1 \\ 0 & 1 & 0 \end{bmatrix}. \tag{A.103}$$

We can use a similar procedure to obtain the representation Γ^{eq} for rest of the operators in the group C_{3v}. Notice that this representation will have only one's and zero's as its components. As in molecular symmetry and molecular bonds we say that the trace or character of the nodal equivalence representation of a group operator R is equal to the number of nodes which remain invariant under R.

Γ^{eq} is a 3-dimensional representation of the group C_{3v}. For the group C_{3v}, we have two one-dimensional representations and one two-dimensional representation as seen in Table A.2. Hence, the nodal equivalent representation is reducible. We can decompose Γ^{eq} in terms of the irreducible representations as

$$\Gamma^{eq} = A_1 + E. \tag{A.104}$$

The nodal equivalence representation determines the projection operator components to which we need to apply the consistency conditions. From Eq. (A.104), we

$\mathcal{P}(A_1)\left[\partial_x N_1^{(0,0)}\right]_{\boldsymbol{r}_2} = 0;$	$\mathcal{P}(A_1)\left[\partial^2_{xx} N_1^{(0,0)}\right]_{\boldsymbol{r}_2} = 0;$
$\mathcal{P}(E_{11})\left[\partial_x N_1^{(0,0)}\right]_{\boldsymbol{r}_2} = 0;$	$\mathcal{P}(E_{11})\left[\partial^2_{xx} N_1^{(0,0)}\right]_{\boldsymbol{r}_2} =; 0$
$\mathcal{P}(E_{22})\left[\partial_x N_1^{(0,0)}\right]_{\boldsymbol{r}_2} = 0;$	$\mathcal{P}(E_{22})\left[\partial^2_{xx} N_1^{(0,0)}\right]_{\boldsymbol{r}_2} = 0;$
$\mathcal{P}(A_1)\left[\partial_y N_1^{(0,0)}\right]_{\boldsymbol{r}_2} = 0;$	$\mathcal{P}(A_1)\left[\partial^2_{yy} N_1^{(0,0)}\right]_{\boldsymbol{r}_2} = 0;$
$\mathcal{P}(E_{11})\left[\partial_y N_1^{(0,0)}\right]_{\boldsymbol{r}_2} = 0;$	$\mathcal{P}(E_{11})\left[\partial^2_{yy} N_1^{(0,0)}\right]_{\boldsymbol{r}_2} = 0,$
$\mathcal{P}(E_{22})\left[\partial_y N_1^{(0,0)}\right]_{\boldsymbol{r}_2} = 0;$	$\mathcal{P}(E_{22})\left[\partial^2_{yy} N_1^{(0,0)}\right]_{\boldsymbol{r}_2} = 0,$
	$\mathcal{P}(A_1)\left[\partial^2_{xy} N_1^{(0,0)}\right]_{\boldsymbol{r}_2} = 0,$
$\mathcal{P}(E_{22})\left[\partial^2_{xy} N_1^{(0,0)}\right]_{\boldsymbol{r}_2} = 0;$	$\mathcal{P}(E_{11})\left[\partial^2_{xy} N_1^{(0,0)}\right]_{\boldsymbol{r}_2} = 0.$

Table A.3: Self-consistent nodal conditions for first and second derivatives of the polynomial $N_1^{(0,0)}$.

see that only A_1 and E contribute to the representation. Hence, we need to apply the self-consistency conditions only for the projection operators of A_1 and E.

We know that the nodal conditions on the first and second derivatives of $N_1^{(0,0)}$ have C_{3v} symmetry. Hence we need to apply the self-consistency conditions for derivatives at any one of the nodes. We set each projected component of derivatives of $N_1^{(0,0)}$ to zero at $\boldsymbol{r}_2$. Thus, we get 15 remaining nodal conditions, 6 corresponding to the first and 9 to the second derivatives as shown in Table A.3. The components of $\mathcal{P}(A_2)$ for the first and second derivatives vanish as A_2 does not appear the Eq. (A.104).

The natural basis $\boldsymbol{e}_1, \boldsymbol{e}_2$ are chosen to represent the two dimensional E irreducible representation of C_{3v}, which comprises of the column vector along x- and y- axis respectively. We know that the character of a representation $\chi_i(R)$ for an element R, is equal to the sum of the diagonal elements of the matrix representation $\Gamma^{(i)}(R)$. *It is well known that for an arbitrary function, the sum of the diagonal projection operators* [c] *of a representation projects out the part belonging to that representation.*

[c] See p. 42 in Ref. [220].

Hence it is sufficient to apply the self-consistency conditions for diagonal projection operators $\mathcal{P}(E_{11}), \mathcal{P}(E_{22})$. Off-diagonal projection operators $\mathcal{P}(E_{12}), \mathcal{P}(E_{21})$ will not contribute any additional conditions.

Tensor equivalence representation

We stated earlier that the shape functions can be classified according to their nodal conditions. Shape functions whose value is set to unity at a node are called scalar shape functions. In the current case, $N_i^{(0,0)}$ for $i = 1, 2, 3$ are scalar shape functions. Similarly, $N_i^{(1,0)}$, $N_i^{(0,1)}$ are called as vector shape functions as one of their first derivatives is set to 1 at the i^{th} node. The shape functions with one of the second derivatives is set to 1 at a node are called rank-2 tensor shape functions. Here, $\left\{N_i^{(2,0)}, N_i^{(1,1)}, N_i^{(0,2)}\right\}$ for $i = 1, 2, 3$ are rank-2 shape functions. Transformation rules from one node to another are different for the scalar, vector, and rank-2 tensor shape functions. We wish to obtain the representation for the group C_{3v} with scalar, vector and rank-2 shape functions as its basis.

The scalar shape functions transform under a coordinate transformation individually as a scalar. Since scalars belong to the representation A_1, the equivalence representation for scalar shape functions is given by

$$\begin{aligned} A_1 \otimes \Gamma^{eq} &= A_1 \otimes (A_1 + E), \\ &= A_1 + E. \end{aligned} \tag{A.105}$$

Note that the dimension of the representation is 3, same as the number of scalar shape functions in our set. The irreducible representation A_1 provides the scalar nature of the shape functions under transformation and the equivalent representation Γ^{eq} includes the contribution from all the three nodes. Hence we need to take their *direct product*, which incorporates both the scalar nature of the shape functions and the nodal equivalence.

Vector shape functions transform pairwise. We can treat $\left\{N_i^{(1,0)}, N_i^{(0,1)}\right\}$ as a vector in a 2-dimensional vector space and deduce the appropriate transformation properties. Since $\{x, y\}$ form a basis for the representation E of the group C_{3v} (see Table A.2), and the pair $\{x, y\}$ transforms as a vector, vector shape functions are in the representation

$$E \otimes \Gamma^{eq} = A_1 + A_2 + 2E, \tag{A.106}$$

a 6 dimensional representation, since we have 2 nodes × 3 vertices = 6 vector shape functions. Similarly, rank-2 tensor shape functions are in the representation

$$(E \otimes E)_{ord} \otimes \Gamma^{eq} = 2A_1 + A_2 + 3E, \tag{A.107}$$

where, we define $(E \otimes E)_{ord}$ to be a 3 dimensional representation of C_{3v} formed by the basis $\{x^2, xy, y^2\}$. (The direct product, $E \otimes E$ is a 4-dimensional reducible representation. Since, we need a 3-dimensional representation (as there are only 3 rank-2 shape functions at each node) we work with the representation $(E \otimes E)_{ord}$.)

We obtain another condition on the polynomial $N_1^{(0,0)}$ by taking the mirror symmetry of the nodal conditions with respect to the e_1-axis. The irreducible representation E has four projection operators corresponding to the four matrix element components, E_{11}, E_{12}, E_{21} and E_{22}. From Eq. (A.43) we see that,

$$\mathcal{P}(E_{11}) = \left[\frac{1}{3}\left(2P_\epsilon - P_{c_3} - P_{c_3^2} + 2P_{m_1} - P_{m_2} - P_{m_3}\right)\right].$$

Under the mirror operation m_1, $\mathcal{P}(E_{11})$ remain invariant. Hence

$$\begin{aligned} m_1 \cdot \mathcal{P}(E_{11}) &= m_1 . \left[\frac{1}{3}\left(2P_\epsilon - P_{c_3} - P_{c_3^2} + 2P_{m_1} - P_{m_2} - P_{m_3}\right)\right], \\ &= \frac{1}{3}\left[2P_\epsilon - P_{c_3} - P_{c_3^2} + 2P_{m_1} - P_{m_2} - P_{m_3}\right], \end{aligned} \tag{A.108}$$

implies that $\mathcal{P}(E_{11})$ is even. Similarly, the projection operator $\mathcal{P}(E_{12})$ is even, and the projection operators $\mathcal{P}(E_{21})$, $\mathcal{P}(E_{22})$ are odd with respect to the group operation m_1 (reflection through the e_1-axis).

Since boundary conditions for $N_1^{(0,0)}$ are symmetric with respect to the mirror operation m_1, $N_1^{(0,0)}$ has to be a even function. Hence, it only comprise of components in A_1 and E_{11}. From Eq. (A.106), $N_1^{(1,0)}$ contains components in A_1 and E_{11}, and $N_1^{(0,1)}$ contains components in A_2 and E_{22}. Similarly from Eq. (A.107), $N_1^{(2,0)}$ has components in A_1 and E_{11}, $N_1^{(1,1)}$ has components in A_2 and E_{22}, and $N_1^{(0,2)}$ has components in A_1 and E_{11}.

We have 18 nodal conditions from Eqs. (A.94, A.95) and from Table A.3 to determine the coefficients of terms in the polynomial $N_1^{(0,0)}$. By applying these 18 *self-consistency conditions* for the projected components, we can express all the 21 coefficients in terms of the polynomial $N_1^{(0,0)}$ in terms of 3 as yet unknown coefficients. These 3 coefficients are taken arbitrarily to be c_{14}, c_{15} and c_{18}. For this choice of coefficients the projected component for the element E_{22} is

$$\mathcal{P}(E_{22})N_1^{(0,0)}(x, y) = -\frac{1}{12}c_{15}(1 + 2x)^2 y(1 - 2x + x^2 - 3y^2). \tag{A.109}$$

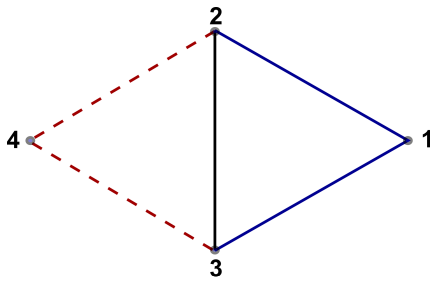

Figure A.8: Two adjacent triangles with nodes at $\{1, 2, 3\}$ and$\{2, 3, 4\}$ share a common side $\{23\}$. The polynomials associated with the node at 1 and4 may have different values along the side $\{23\}$. In order to remove this inconsistency, we impose a condition that the polynomials associated with the node 1 and 4 and their corresponding normal derivatives are zero along the side $\{23\}$.

Since $\mathcal{P}(E_{22})$ is odd with respect to the mirror operation m_1 and $N_1^{(0,0)}$ is an even function, the projected component $\mathcal{P}(E_{22})N_1^{(0,0)}$ should vanish. Hence, c_{15} must be set to zero. This is the 19^{th} condition for the polynomial.

Inter-element continuity

Each side in the interior of the discretized physical region is shared by two triangular elements. We will face inconsistency if the opposite nodes to the shared side from the two adjacent triangles influence the value of the shape functions along this side (see Fig. A.8). One way to remove this inconsistency is by requiring that the value of the shape functions associated with a node is zero along its opposite side. Since we desire $C^{(1)}$-continuity across an element, we impose that even the normal derivative of the shape functions associated with a node is zero on the opposite side. This is the 20^{th} condition. It so happens that for $N_1^{(0,0)}(x, y)$, with 19 conditions imposed through group theory are sufficient to make its value vanish at the opposite side. From Fig. A.7 we see that for the vertex $\boldsymbol{r}_1$, normal at the opposite side is $\boldsymbol{e}_1$. Hence,

$$\partial_x N_1^{(0,0)}(-\frac{1}{2}, y) = -\frac{1}{16}c_{14}(3 - 4y^2)^2 = 0. \tag{A.110}$$

This implies that the coefficient, c_{14}=0. With this condition, in Fig. A.8 we see that along $\{23\}$ only the DoFs at 2 and 3 affect the inter-element properties.

We have fixed 20 of the 21 undermined coefficients by the above mentioned conditions. As the shape function along the edge depends only on the vertices at the ends of the edge, we have built in the tangential derivative continuity along each edge. We deduce the last constraint by noting that the shape function must be compatible with the Taylor expansion of the normal derivative along an edge containing the

vertex, as discussed in the following section.

Taylor expansion compatibility

Let us suppose that the function which we express in terms of the shape functions is $f(x, y)$. A Taylor series expansion of the function away from a node $\{x_1, y_1\}$ and along one of the two edges is

$$\begin{aligned} f(x,y) = f(x_1,y_1) &+ \left[\frac{\partial f}{\partial x}\right]_{(x_1,y_1)}(x-x_1) + \left[\frac{\partial f}{\partial y}\right]_{(x_1,y_1)}(y-y_1) \\ &+ \left[\frac{\partial^2 f}{\partial x^2}\right]_{(x_1,y_1)}\frac{1}{2}(x-x_1)^2 + \left[\frac{\partial^2 f}{\partial y^2}\right]_{(x_1,y_1)}\frac{1}{2}(y-y_1)^2 \\ &+ \left[\frac{\partial f}{\partial x}y\right]_{(x_1,y_1)}(x-x_1)(y-y_1) + \dots . \end{aligned} \tag{A.111}$$

But according to the finite element Hermite interpolation scheme, we should be able to express the same function in the basis of interpolation polynomials given as

$$f(x,y) = f(x_1,y_1)N_1^{(0,0)} + \left[\frac{\partial f}{\partial x}\right]_{(x_1,y_1)}N_1^{(1,0)} + \left[\frac{\partial f}{\partial y}\right]_{(x_1,y_1)}N_1^{(0,1)} + \dots . \tag{A.112}$$

Let us take the normal derivative of the function $f(x, y)$. Using Eq. (A.111) we obtain

$$\begin{aligned} \partial_{\boldsymbol{n}} f(x,y) = &\left[\frac{\partial f}{\partial x}\right]_{(x_1,y_1)}n_1 + \left[\frac{\partial f}{\partial y}\right]_{(x_1,y_1)}n_2 + \left[\frac{\partial^2 f}{\partial x^2}\right]_{(x_1,y_1)}(x-x_1)n_1 \\ &+ \left[\frac{\partial^2 f}{\partial y^2}\right]_{(x_1,y_1)}(y-y_1)n_2 + \left[\frac{\partial f}{\partial x}y\right]_{(x_1,y_1)}(x-x_1)n_2 \\ &+ \left[\frac{\partial f}{\partial x}y\right]_{(x_1,y_1)}(y-y_1)n_1 + \dots . \end{aligned} \tag{A.113}$$

where $\boldsymbol{n} = n_1\boldsymbol{e}_1 + n_2\boldsymbol{e}_2$ is the normal to an edge containing the vertex 1. Alternatively, using Eq. (A.112) we obtain

$$\partial_{\boldsymbol{n}} f(x,y) = f(x_1,y_1)\partial_{\boldsymbol{n}}N_1^{(0,0)} + \left[\frac{\partial f}{\partial x}\right]_{(x_1,y_1)}\partial_{\boldsymbol{n}}N_1^{(1,0)} + \left[\frac{\partial f}{\partial y}\right]_{(x_1,y_1)}\partial_{\boldsymbol{n}}N_1^{(0,1)} + \dots . \tag{A.114}$$

Since function value at the node $f(x_1, y_1)$ does not appear in the above equation, by comparing with Eq. (A.112) we find the desired additional constraint on that the normal derivative of $N_1^{(0,0)}$ vanishes along the edge

$$\partial_{\boldsymbol{n}}N_1^{(0,0)}(\Sigma) = 0, \tag{A.115}$$

where Σ is the set of points on the side connected to the vertex 1. From the Fig. A.7 we note that the normal vector for the edge containing vertices 1 and 2 is

$$\begin{aligned} \boldsymbol{n} &= \cos\left(\frac{\pi}{6}\right)\boldsymbol{e}_1 + \sin\left(\frac{\pi}{6}\right)\boldsymbol{e}_2, \\ &= \frac{1}{2}\boldsymbol{e}_1 + \frac{\sqrt{3}}{2}\boldsymbol{e}_2. \end{aligned} \tag{A.116}$$

Eq. (A.115) now takes the form

$$\begin{aligned} \frac{1}{2}\left(\partial_x + \sqrt{3}\partial_y\right) N_1^{(0,0)}\left(x, \frac{1}{\sqrt{3}}(1-x)\right) &= \frac{27}{81}\left(c_{18} - \frac{40}{27}\right)(1-x)^2(1+2x)^2 \\ &= 0. \end{aligned} \tag{A.117}$$

This implies, $c_{18} = 40/27$. In Fig. A.8 we see that the polynomials associated with the node 1 are made quartic along the sides $\{12\}$ and $\{13\}$.

With all 21 conditions applied to the complete fifth order polynomial in two-–dimensions, $N_1^{(0,0)}$ is fully specified to be

$$N_1^{(0,0)} = \frac{1}{27}\left(9 + 30x + 10x^2 - 30x^3 + 8x^5 - 10y^2 - 30xy^2 + 40x^3y^2\right). \tag{A.118}$$

The scalar shape function at node $\boldsymbol{r}_2$ can be obtained by an anti-clockwise rotation by an angle $2\pi/3$ on $N_1^{(0,0)}$.

$$\begin{aligned} N_2^{(0,0)} &= C_3 \cdot N_1^{(0,0)}(x,y), \\ &= N_1^{(0,0)}\left(C_3^{-1}(x,y)\right), \\ &= N_1^{(0,0)}\left(\frac{1}{2}(-x+\sqrt{3}y), \frac{1}{2}(-\sqrt{3}x - y)\right). \end{aligned} \tag{A.119}$$

On substitution into Eq. (A.118) we have

$$N_2^{(0,0)} = \frac{1}{54}(x-1)(1+2x)^2(11 - x(2+3x) - 15y^2). \tag{A.120}$$

Similarly, we obtain $N_3^{(0,0)}$ through an appropriate group operation in C_{3v}. As yet we have determined the shape functions whose values are normalized at a particular node. They are classified as scalar shape functions. To determine the shape functions whose derivatives are normalized at a node we need to take care of their tensor nature under a coordinate transformation. For the 18 DoF polynomials on an equilateral triangular element we have rank-0 (scalar), rank-1 (vector) and rank-2 tensor shape functions.We would like to obtain rank-1 and rank-2 tensor shape functions associated with the node $\boldsymbol{r}_2$ and $\boldsymbol{r}_3$ (see Fig. A.7) by transforming the shape functions associated with the node $\boldsymbol{r}_1$, which we have already obtained through group theory.

Interpolation of a constant function A constant function, $\psi(x, y) = \psi$ can be represented using Hermite interpolation polynomials as

$$\psi = \sum_{i=1}^{4} \psi_i N_i^{(0,0)}(x, y). \tag{A.121}$$

Derivatives of ψ are zero throughout. Hence, vector and rank-1 shape functions will not contribute in the above interpolation. The function value at the i^{th} node, $\psi_i = \psi$. *Therefore, we require a condition that the sum of the scalar interpolation polynomials add up to unity.* This condition is true in any dimension. For example, the sum of 1D linear interpolation polynomials on the standard line element (see Sec. A.5) is given by

$$N_1(x) + N_2(x) = \frac{1+x}{2} + \frac{1-x}{2} = 1. \tag{A.122}$$

For the set of 18 DoF polynomials on a triangular element, we know that the scalar shape functions associated with node r_2 and r_3 are obtained through anti-clockwise and clockwise rotation by an angle $2\pi/3$ on $N_1^{(0,0)}$, respectively. Therefore

$$\begin{aligned} N_1^{(0,0)}(\boldsymbol{r}) + N_2^{(0,0)}(\boldsymbol{r}) + N_3^{(0,0)}(\boldsymbol{r}) &= N_1^{(0,0)}(\boldsymbol{r}) + N_1^{(0,0)}\left(C_3^{-1} \cdot \boldsymbol{r}\right) + N_1^{(0,0)}(C_3 \cdot \boldsymbol{r}), \\ &= 1. \end{aligned} \tag{A.123}$$

If we use the above relation instead of the condition through the Taylor expansion (see Eq. (A.117)), we obtain the same expression for the shape function, $N_1^{(0,0)}(x, y)$ as before.

Creating Equivalent Shape functions

We know that

$$\boldsymbol{r_2} = C_3 \cdot \boldsymbol{r_1}, \tag{A.124}$$

where, C_3 give rise to an anticlockwise rotation by an angle $2\pi/3$. The transformation rule for the scalar shape function is given by

$$N_2^{(0,0)}(\boldsymbol{r}_2) = N_1^{(0,0)}\left(C_3^{-1}\boldsymbol{r}_1\right), \tag{A.125}$$

as explained in Sec. A.4. Whereas under group transformation the shape functions $N_1^{(1,0)}$ and $N_1^{(0,1)}$ transform like x and y components of a vector in $x - y$ plane,

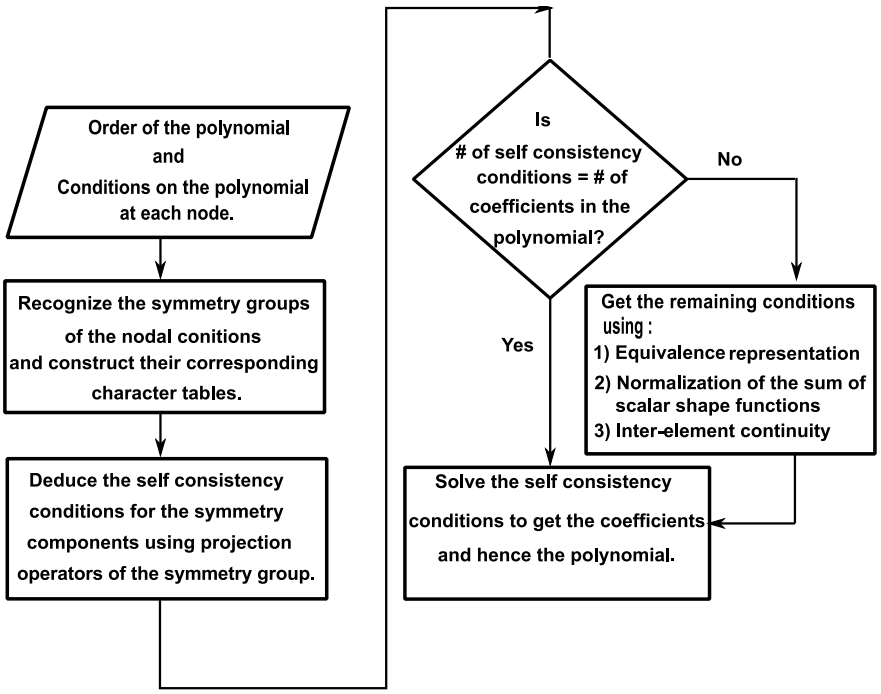

Figure A.9: A flowchart representing the steps for deriving the interpolation polynomial

respectively. The active transformation rule for coordinates of a vector $\boldsymbol{V}$ under C_3 rotation is given by

$$\begin{bmatrix} v'_x \\ v'_y \end{bmatrix} = \begin{bmatrix} a_{11} & a_{12} \\ a_{21} & a_{22} \end{bmatrix} \cdot \begin{bmatrix} v_x \\ v_y \end{bmatrix}, \tag{A.126}$$

where a_{ij} are the matrix components of the group operation C_3. The transformation rule for the vector shape functions associated with vertex 2 is given by

$$\begin{bmatrix} N_2^{(1,0)}(\boldsymbol{r}) \\ N_2^{(0,1)}(\boldsymbol{r}) \end{bmatrix} = \begin{bmatrix} a_{11} & a_{12} \\ a_{21} & a_{22} \end{bmatrix} \cdot \begin{bmatrix} N_1^{(1,0)}\left(C_3^{-1}\boldsymbol{r}\right) \\ N_1^{(0,1)}\left(C_3^{-1}\boldsymbol{r}\right) \end{bmatrix}. \tag{A.127}$$

In component form we have

$$\begin{aligned} N_2^{(1,0)}(x,y) &= a_{11}N_1^{(1,0)}(b_{11}x + b_{12}y, b_{21}x + b_{22}y) && \text{(A.128)} \\ &\quad + a_{12}N_2^{(0,1)}(b_{11}x + b_{12}y, b_{21}x + b_{22}y); \end{aligned}$$

$$\begin{aligned} N_2^{(0,1)}(x,y) &= a_{21}N_1^{(1,0)}(b_{11}x + b_{12}y, b_{21}x + b_{22}y) && \text{(A.129)} \\ &\quad + a_{22}N_2^{(0,1)}(b_{11}x + b_{12}y, b_{21}x + b_{22}y), && \text{(A.130)} \end{aligned}$$

where b_{ij} are the components of the rotation matrix, C_3^{-1}.

The rank-2 shape functions are composed of 3 shape functions, $\left\{N_i^{(2,0)}, N_i^{(1,1)}, N_i^{(0,2)}\right\}$, for $i = 1, 2, 3$. A general rank-2 tensor $\boldsymbol{T}_1$ in 2-dimensional space has 3 parameters. $\boldsymbol{T}_1$ is represented by a 2×2 square matrix as

$$\boldsymbol{T_1} = \begin{bmatrix} p_1 & p_3 \\ p_3 & p_2 \end{bmatrix}, \tag{A.131}$$

where, p_1, p_2 and p_3 are real numbers. Under a group transformation the general rank-2 tensor transforms as

$$\boldsymbol{T'} = \boldsymbol{A} \cdot \boldsymbol{T} \cdot \boldsymbol{A}^{-1}. \tag{A.132}$$

Since C_3^{-1} is the inverse of rotation C_3, we have $a_{ik} b_{kj} = \delta_{ij}$. Hence, transformation rule for rank-2 tensor shape functions associated with vertex 2 is given by

$$\begin{bmatrix} N_2^{(2,0)}(\boldsymbol{r}) & N_2^{(1,1)}(\boldsymbol{r}) \\ N_2^{(1,1)}(\boldsymbol{r}) & N_2^{(0,2)}(\boldsymbol{r}) \end{bmatrix} = \begin{bmatrix} a_{11} & a_{12} \\ a_{21} & a_{22} \end{bmatrix} \cdot \begin{bmatrix} N_1^{(2,0)}\left(C_3^{-1}\boldsymbol{r}\right) & N_1^{(1,1)}\left(C_3^{-1}\boldsymbol{r}\right) \\ N_1^{(1,1)}\left(C_3^{-1}\boldsymbol{r}\right) & N_1^{(0,2)}\left(C_3^{-1}\boldsymbol{r}\right) \end{bmatrix} \cdot \begin{bmatrix} b_{11} & b_{12} \\ b_{21} & b_{22} \end{bmatrix}. \tag{A.133}$$

In a similar manner, we can derive the transformation rules for the shape functions associated with the vertex 3.

Vector shape functions

The shape functions whose first derives are set to unity at a vertex are called *vector shape functions*. The labeling is based on the fact that $\left\{N_1^{(1,0)}, N_1^{(0,1)}\right\}$ transforms like a vector under a symmetry operation of the group C_{3v}. As an exercise, let us apply the above mentioned procedures to derive the polynomial $N_1^{(0,1)}(x, y)$.

At vertex 1, the partial derivative of $N_1^{(0,1)}$ with respect to y is set to unity and its function value and the other first and all the three second derivatives are set to zero. Therefore, $\partial_y N_1^{(0,1)}$ will have bilateral symmetry. Hence

$$\mathcal{P}(A_g)\frac{\partial N_1^{(0,1)}}{\partial y}(\boldsymbol{r}_1) = 1; \quad \mathcal{P}(A_u)\frac{\partial N_1^{(0,1)}}{\partial y}(\boldsymbol{r}_1) = 0,$$

$$\mathcal{P}(A_g)\frac{\partial N_1^{(0,1)}}{\partial y}(\boldsymbol{r}_2) = 0; \quad \mathcal{P}(A_u)\frac{\partial N_1^{(0,1)}}{\partial y}(\boldsymbol{r}_2) = 0.$$

Furthermore, $N_1^{(0,0)}$, $\partial_x N_1^{(0,0)}$, $\partial_{xx} N_1^{(0,0)}$, $\partial_{xy} N_1^{(0,0)}$ and $\partial_{yy} N_1^{(0,0)}$ are zero at all the three nodes. Hence they have C_{3v} symmetry. We know that, nodal equivalence

$\mathcal{P}(A_1)N_1^{(0,1)}(\boldsymbol{r}_2) = 0,$	$\mathcal{P}(A_1)\partial_x N_1^{(0,1)}(\boldsymbol{r}_2) = 0;$
$\mathcal{P}(E_{11})N_1^{(0,1)}(\boldsymbol{r}_2) = 0,$	$\mathcal{P}(E_{11})\partial_x N_1^{(0,1)}(\boldsymbol{r}_2) = 0;$
$\mathcal{P}(E_{22})N_1^{(0,1)}(\boldsymbol{r}_2) = 0,$	$\mathcal{P}(E_{22})\partial_x N_1^{(0,1)}(\boldsymbol{r}_2) = 0;$
$\mathcal{P}(A_1)\partial_{xx}^2 N_1^{(0,1)}(\boldsymbol{r}_2) = 0;$	$\mathcal{P}(A_1)\partial_{yy}^2 N_1^{(0,1)}(\boldsymbol{r}_2) = 0;$
$\mathcal{P}(E_{11})\partial_{xx}^2 N_1^{(0,1)}(\boldsymbol{r}_2) = 0;$	$\mathcal{P}(E_{11})\partial_{yy}^2 N_1^{(0,1)}(\boldsymbol{r}_2) = 0,$
$\mathcal{P}(E_{22})\partial_{xx}^2 N_1^{(0,1)}(\boldsymbol{r}_2) = 0;$	$\mathcal{P}(E_{22})\partial_{yy}^2 N_1^{(0,1)}(\boldsymbol{r}_2) = 0,$
$\mathcal{P}(A_1)\partial_{xy}^2 N_1^{(0,1)}(\boldsymbol{r}_2) = 0;$	$\mathcal{P}(E_{11})\partial_{xy}^2 N_1^{(0,1)}(\boldsymbol{r}_2) = 0.$
$\mathcal{P}(E_{22})\partial_{xy}^2 N_1^{(0,1)}(\boldsymbol{r}_2) = 0;$	

Table A.4: Self-consistent nodal conditions for the polynomial $N_1^{(0,1)}$ through C_{3v} symmetry.

representation is $\Gamma^{eq} = A_1 + E$. Hence we obtain 3 nodes $\times$ 5 DoF =15 self-consistency conditions as listed in Table A.4. We solve for these self-consistency conditions to obtain the polynomial in terms of 3 undetermined coefficients.

$$\begin{aligned} N_1^{(0,1)}(x,y) &= \frac{1}{108}(2x+1)\,[27c_{18}(2x+1)y^3 \\ &\quad +27(x-1)y^2(c_{15}(2x+1)+2c_{14})+3(x-1)^3(-2c_{14}(x+2) \\ &\quad -3c_{15}(2x+1))+54c_{14}y^4 \\ &\quad +(2x+1)y\left(4(3-4(x-1)x)-9c_{18}(x-1)^2\right)]. \end{aligned} \tag{A.134}$$

From Eq. (A.106) we see that $N_1^{(1,0)}$ will have components in A_1 and E_{11}, and $N_1^{(0,1)}$ will have components in A_2 and E_{22}. Therefore the component of $N_1^{(0,1)}$ in A_1 and E_{11} should vanish.

$$\begin{aligned} \mathcal{P}(A_1)N_1^{(0,1)} &= -\frac{1}{36}(4c_{14}+3c_{15})(2x+1)\left((x-1)^2-3y^2\right)\left(x^2+y^2-1\right), \\ &= 0. \end{aligned} \tag{A.135}$$

$$\begin{aligned} \mathcal{P}(E_{11})N_1^{(0,1)} &= \frac{1}{72}(2c_{14}-3c_{15})(2x+1)\left((x-1)^2-3y^2\right)\left((x-1)x-y^2\right), \\ &= 0. \end{aligned} \tag{A.136}$$

Solving these two simultaneous equations we see that, $c_{14} = c_{15} = 0$. So we are left with just one undetermined coefficient.

To have the inter-element continuity as explained in Sec. A.6, the polynomial and its normal derivative along $\{23\}$ has to be zero along the side opposite to the vertex 1 (see Fig. A.8). This is indeed true.

To obtain another condition on the polynomial we impose the condition that the normal derivative along the sides containing the vertex 1 is a cubic function. We see that

$$\begin{aligned}\frac{1}{2}\left[\partial_x + \sqrt{3}\partial_y\right] N_1^{(0,1)}\left(x, \frac{1}{\sqrt{3}}(1-x)\right) &= \frac{4c_{18}x^4}{3\sqrt{3}} - \frac{4c_{18}x^3}{3\sqrt{3}} - \frac{c_{18}x^2}{\sqrt{3}} \\ &+ \frac{2c_{18}x}{3\sqrt{3}} + \frac{c_{18}}{3\sqrt{3}} + \frac{8x^4}{27\sqrt{3}} \\ &- \frac{32x^3}{27\sqrt{3}} + \frac{4x^2}{9\sqrt{3}} + \frac{40x}{27\sqrt{3}} + \frac{25}{54\sqrt{3}}.\end{aligned} \tag{A.137}$$

After grouping terms we set the coefficients of quartic terms to zero, leading to

$$c_{18}\frac{4}{3\sqrt{3}} + \frac{8}{27\sqrt{3}} = 0, \tag{A.138}$$

Hence,

$$c_{18} = -\frac{2}{9}. \tag{A.139}$$

Hence the required interpolation polynomial is given by

$$N_1^{(0,1)}(x,y) = \frac{1}{54}(2x+1)^2 y\left((6-7x)x - 3y^2 + 7\right). \tag{A.140}$$

In a similar manner, we get the functional form for the polynomial $N_1^{(1,0)}$ as

$$N_1^{(1,0)}(x,y) = -\frac{1}{54}(x-1)(2x+1)^2\left(x(3x+2) + 15y^2 - 11\right). \tag{A.141}$$

To get $N_2^{(0,1)}$ and $N_2^{(0,1)}$ we need to consider the vectorial nature of the transformation. From Eq. (A.127) we have

$$\begin{bmatrix} N_2^{(0,1)}(x,y) \\ N_2^{(1,0)}(x,y) \end{bmatrix} = \begin{bmatrix} -\frac{1}{2} & -\frac{\sqrt{3}}{2} \\ \frac{\sqrt{3}}{2} & -\frac{1}{2} \end{bmatrix} \cdot \begin{bmatrix} N_1^{(1,0)}\left(\frac{\sqrt{3}y}{2} - \frac{x}{2}, -\frac{\sqrt{3}x}{2} - \frac{y}{2}\right) \\ N_1^{(0,1)}\left(\frac{\sqrt{3}y}{2} - \frac{x}{2}, -\frac{\sqrt{3}x}{2} - \frac{y}{2}\right) \end{bmatrix}. \tag{A.142}$$

Substituting appropriate functions we get

$$N_2^{(0,1)}(x,y) = \frac{(2x+1)}{108}\left(-x+\sqrt{3}y+1\right)^2\left(11-6x^2-\sqrt{3}(3-2x)y-5x\right), \quad \text{(A.143)}$$

$$\begin{aligned} N_2^{(1,0)}(x,y) = \frac{1}{108}\left(-x+\sqrt{3}y+1\right)^2 &\left(4\sqrt{3}x^3+2x^2\left(5\sqrt{3}-4y\right)\right. \\ &+x\left(-8y\left(\sqrt{3}y-3\right)-3\sqrt{3}\right) \\ &\left.+y\left(6\left(\sqrt{3}-2y\right)y+23\right)-11\sqrt{3}\right). \end{aligned} \quad \text{(A.144)}$$

From Fig. A.8, the polynomials associated with the node 1 and their normal derivatives are set to zero along the side {23}. But the second normal derivatives of such polynomials associated with the node 1and 4 may have different values along the side {23}. Hence, we say that the 18 DoF polynomials are $C^{(1)}$-continuous across the element. All 18 quintic Hermite interpolation polynomials in the standard equilateral triangular element that support $C^{(1)}$-continuous quartic polynomials across shared sides of elements are listed in Table B.2.3.

Shape functions on a right triangle

In a typical finite element calculation the integration of the Lagrange density is carried out by transforming from the general triangular element, defined in the "global" coordinate system, into a standard element. This "local" finite element can be an equilateral triangle as in Fig. A.7, or a right triangle (see Fig. A.12). This is dictated by the availability of Gauss quadrature points and weights on the local element. So it is useful to map the shape functions accordingly from the local to the global element.

To begin with, we would like to show that the geometrical transformation from the coordinates of a right triangle to an arbitrary triangle is a linear transformation. The standard right triangle with vertices at $P_1 = (0,0), P_2 = (1,0)$ and $P_3 = (0,1)$ is chosen. Let us consider an arbitrary triangular element with vertices located at the coordinates (ξ_i, η_i), $i = 1,2,3$. Let $\boldsymbol{\rho} = (\xi, \eta)$ represent the coordinates on an arbitrary triangle and $\boldsymbol{r} = (x, y)$ are the variables on the standard right triangle.

The linear shape functions on the standard right triangle are given by

$$\begin{aligned} M_1(x,y) &= 1-x-y, \\ M_2(x,y) &= x, \\ M_3(x,y) &= y. \end{aligned} \quad \text{(A.145)}$$

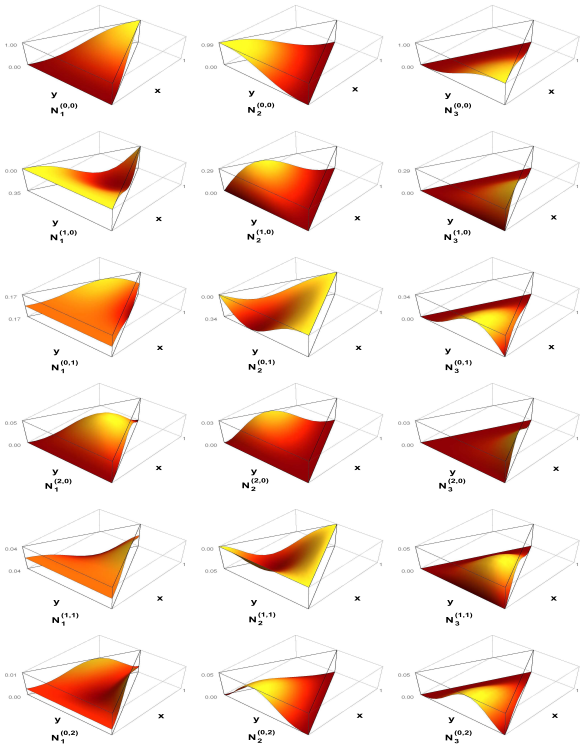

Figure A.10: The $C^{(2)}$-continuous 18 DoF quintic Hermite interpolation polynomials that have $C^{(1)}$-continuous normal derivatives across the element are plotted on the standard equilateral triangle.

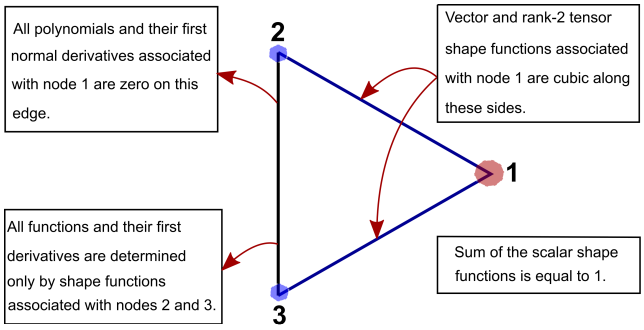

Figure A.11: Pictorial representation of additional conditions applied to determine 18 DoF polynomials on an equilateral triangle.

A general function $\psi(\xi, \eta)$, with the given values ψ_i at the three vertices of the arbitrary triangle can be interpolated as

$$\psi(\xi, \eta) \approx \sum_{i=1}^{3} \psi_i M_i(x, y). \tag{A.146}$$

We can represent the coordinates ξ and η themselves in terms of linear shape

functions as

$$\begin{aligned}\xi &= \xi_1 M_1(x,y) + \xi_2 M_2(x,y) + \xi_3 M_3(x,y),\\ &= \xi_1\ (1-x-y) + \xi_2\ x + \xi_3\ y,\\ &= (\xi_2-\xi_1)x + (\xi_3-\xi_2)y + \xi_1,\end{aligned} \tag{A.147}$$

and

$$\begin{aligned}\eta &= \eta_1 M_1(x,y) + \eta_2 M_2(x,y) + \eta_3 M_3(x,y),\\ &= \eta_1\ (1-x-y) + \eta_2\ x + \eta_3\ y,\\ &= (\eta_2-\eta_1)x + (\eta_3-\eta_2)y + \eta_1.\end{aligned} \tag{A.148}$$

This is an isoparametric mapping. Equations (A.147) and (A.148) can be written as a 2×2 matrix of the form

$$\begin{bmatrix}\xi-\xi_1\\ \eta-\eta_1\end{bmatrix} = \begin{bmatrix}\xi_2-\xi_1 & \xi_3-\xi_1\\ \eta_2-\eta_1 & \eta_3-\eta_1\end{bmatrix}\cdot\begin{bmatrix}x\\ y\end{bmatrix},$$

$$\boldsymbol{\rho}-\boldsymbol{\rho}_1 = \boldsymbol{J}\cdot\boldsymbol{r}. \tag{A.149}$$

This is a linear mapping between the variables (x,y) and (ξ,η). The determinant of the matrix $\boldsymbol{J}$ is the *Jacobian* of the transformation. For example, consider the transformation from the coordinates (x,y) in the standard triangular element (see Fig. A.12) to the coordinates (ξ,η) in our equilateral triangle (see Fig. A.7). From Eq. (A.149), the corresponding transformation is given by

$$\begin{bmatrix}\xi-1\\ \eta\end{bmatrix} = \begin{bmatrix}-\frac{3}{2} & -\frac{3}{2}\\ \frac{\sqrt{3}}{2} & -\frac{\sqrt{3}}{2}\end{bmatrix}\cdot\begin{bmatrix}x\\ y\end{bmatrix}, \tag{A.150}$$

where the Jacobian of the transformation is given by

$$\boldsymbol{J} = \begin{bmatrix}-\frac{3}{2} & -\frac{3}{2}\\ \frac{\sqrt{3}}{2} & -\frac{\sqrt{3}}{2}\end{bmatrix}. \tag{A.151}$$

Hence

$$\begin{bmatrix}\xi\\ \eta\end{bmatrix} = \begin{bmatrix}-\frac{3}{2} & -\frac{3}{2}\\ \frac{\sqrt{3}}{2} & -\frac{\sqrt{3}}{2}\end{bmatrix}\cdot\begin{bmatrix}x\\ y\end{bmatrix} + \begin{bmatrix}1\\ 0\end{bmatrix}, \tag{A.152}$$

and the inverse transformation is given by

$$\begin{bmatrix}x\\ y\end{bmatrix} = \begin{bmatrix}-\frac{1}{3} & \frac{1}{\sqrt{3}}\\ -\frac{1}{3} & -\frac{1}{\sqrt{3}}\end{bmatrix}\cdot\begin{bmatrix}\xi\\ \eta\end{bmatrix} + \begin{bmatrix}\frac{1}{3}\\ \frac{1}{3}\end{bmatrix}. \tag{A.153}$$

Let us consider the transformation of the linear shape functions labeled by $\{M_i(x, y) \| i = 1, 2, 3\}$ on the right triangle (see Eq. (A.145)) to obtain the linear shape functions $\{N_i(\xi, \eta) |\ i = 1, 2, 3\}$ on our standard equilateral triangle. The corresponding passive coordinate transformation is obtained by inverting the Jacobian matrix in Eq. (A.151). Hence

$$\begin{aligned}\begin{bmatrix} x \\ y \end{bmatrix} &= \begin{bmatrix} -\frac{3}{2} & -\frac{3}{2} \\ \frac{\sqrt{3}}{2} & -\frac{\sqrt{3}}{2} \end{bmatrix}^{-1} \cdot \begin{bmatrix} \xi - 1 \\ \eta \end{bmatrix}, \\ &= \begin{bmatrix} \frac{1-\xi}{3} + \frac{\eta}{\sqrt{3}} \\ \frac{1-\xi}{3} - \frac{\eta}{\sqrt{3}}. \end{bmatrix}. \end{aligned} \tag{A.154}$$

Since we have only scalar shape functions, transformation rule at the i^{th} node is given by

$$\begin{aligned} N_i(\xi, \eta) &= M_i\left(x(\xi, \eta), y(\xi, \eta)\right), \\ &= M_i\left(\frac{1-\xi}{3} + \frac{\eta}{\sqrt{3}}, \frac{1-\xi}{3} - \frac{\eta}{\sqrt{3}}\right). \end{aligned} \tag{A.155}$$

Substituting Eq. (A.145) in Eq. (A.155) we get

$$\begin{aligned} N_1(\xi, \eta) &= \frac{2(\xi - 1)}{3} + 1, \\ N_2(\xi, \eta) &= \frac{\eta}{\sqrt{3}} + \frac{1-\xi}{3}, \\ N_3(\xi, \eta) &= \frac{1-\xi}{3} - \frac{\eta}{\sqrt{3}}. \end{aligned} \tag{A.156}$$

Transformation rules for the Hermite shape functions

Let us consider the concrete case of mapping our Hermite shape functions from the equilateral triangle into a right angled triangle. Transformation properties closely follow our discussion in Sec. A.6. Let $M_i^{(m,n)}(x, y)$ be the shape functions on the right triangle, with $i = 1, 2, 3$. The possible combinations of (m, n) are $\{(0, 0), (1, 0), (0, 1), (2, 0), (1, 1), (0, 2)\}$. Transformation properties for scalar shape functions follow simply as

$$M_i^{(0,0)}(x, y) = N_i^{(0,0)}\left(\xi(x, y), \eta(x, y)\right), \tag{A.157}$$

given the shape functions $N_i^{(0,0)}$ on the equilateral triangle. For example,

$$\begin{aligned} M_1^{(0,0)}(x, y) &= N_1^{(0,0)}\left(\xi(x, y), \eta(x, y)\right), \\ &= N_1^{(0,0)}\left(\frac{1}{2}(-3x - 3y + 2), \frac{1}{2}\sqrt{3}(x - y)\right). \end{aligned} \tag{A.158}$$

Therefore,

$$M_1^{(0,0)}(x,y) = -(x+y-1)^2\Big(6x^3 + 3x^2(y-1) + x(3(y-2)y-2) + (y-1)\left(6y^2+3y+1\right)\Big). \tag{A.159}$$

We can derive $M_2^{(0,0)}(x,y)$ and $M_3^{(0,0)}(x,y)$ in a similar fashion.

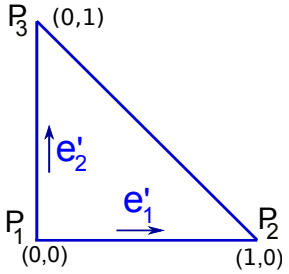

Figure A.12: The right triangular element typically used in Finite element analysis.

In the case of vector shape functions $M_i^{(1,0)}$, $M_i^{(0,1)}$, the transformation properties are given by

$$\begin{bmatrix} M_i^{(1,0)}(x,y) \\ M_i^{(0,1)}(x,y) \end{bmatrix} = \begin{bmatrix} -\frac{1}{3} & \frac{1}{\sqrt{3}} \\ -\frac{1}{3} & -\frac{1}{\sqrt{3}} \end{bmatrix} \cdot \begin{bmatrix} N_i^{(1,0)}\left(\xi(x,y),\eta(x,y)\right) \\ N_i^{(0,1)}\left(\xi(x,y),\eta(x,y)\right) \end{bmatrix}. \tag{A.160}$$

For example,

$$M_1^{(1,0)}(x,y) = -\frac{1}{3}N_1^{(1,0)}\left(\xi(x,y),\eta(x,y)\right) + \frac{1}{\sqrt{3}}N_1^{(0,1)}\left(\xi(x,y),\eta(x,y)\right). \tag{A.161}$$

Substituting Eq. (A.152) into the above equation we get

$$M_1^{(1,0)}(x,y) = -\frac{1}{3}N_1^{(1,0)}\left(\frac{1}{2}(-3x-3y+2),\frac{1}{2}\sqrt{3}(x-y)\right) + \frac{1}{\sqrt{3}}N_1^{(0,1)}\left(\frac{1}{2}(-3x-3y+2),\frac{1}{2}\sqrt{3}(x-y)\right). \tag{A.162}$$

Hence

$$M_1^{(1,0)}(x,y) = -\frac{1}{2}x(x+y-1)^2\left[x(6x+3y-4)-4y-2\right]. \tag{A.163}$$

Derivations of the rest of the vector shape functions follow the same steps. Transformation properties for the rank-2 shape functions follow from the discussion above and from Sec. A.6. In Table B.2.4 we list a set of 18 DoF quintic Hermite polynomials on the right triangle that support $C^{(1)}$-continuous quartic polynomials across shared sides of elements. These interpolation polynomials were reported for the first time by Kassebaum *et al.*, [73] where they also compared and contrasted these new polynomials with previously reported 18 DoF polynomials by Bell [216].

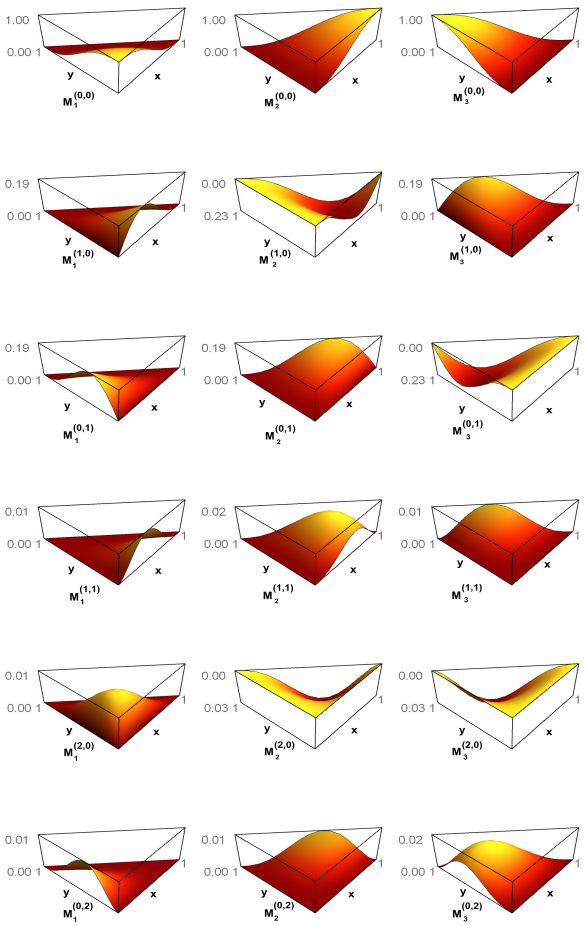

Figure A.13: The $C^{(2)}$-continuous 18 DoF quintic Hermite interpolation polynomials that have $C^{(1)}$-continuous normal derivatives across the element are plotted on the standard right triangle.

A.7 Transformation to an arbitrary triangular element

In finite element analysis, the central idea is to express the solution as a linear combination of a set of shape functions multiplied by as-yet undetermined coefficients.

We can always find such polynomials for an arbitrary element. However having to find the explicit form in global coordinates in every element is very inefficient. Thus we seek to develop a method to obtain the shape functions on an arbitrary element given a set of shape functions on a standard element.

We choose the standard element as before to be the equilateral triangle with vertices $P_1 = (1,0), P_2 = (-1/2, \sqrt{3}/2), P_3 = (-1/2, -\sqrt{3}/2)$. Let us suppose that an arbitrary triangular element has vertices located at $V_1 = (x_1, y_1), V_2 = (x_2, y_2)$ and $V_3 = (x_3, y_3)$ in the global coordinate system. The transformation of coordinates $\boldsymbol{\rho} = (\xi, \eta)$ from the points in standard equilateral triangle, to the global coordinates $\boldsymbol{r} = (x, y)$ in the arbitrary triangle is given by

$$\begin{aligned}\begin{bmatrix} x \\ y \end{bmatrix} &= \begin{bmatrix} \frac{1}{3}(2x_1 - x_2 - x_3) & \frac{1}{3}\left(\sqrt{3}x_2 - \sqrt{3}x_3\right) \\ \frac{1}{3}(2y_1 - y_2 - y_3) & \frac{1}{3}\left(\sqrt{3}y_2 - \sqrt{3}y_3\right) \end{bmatrix} \cdot \begin{bmatrix} \xi \\ \eta \end{bmatrix} + \begin{bmatrix} \frac{1}{3}(x_1 + x_2 + x_3) \\ \frac{1}{3}(y_1 + y_2 + y_3) \end{bmatrix}, \\ &= \begin{bmatrix} \frac{\partial x}{\partial \xi} & \frac{\partial x}{\partial \eta} \\ \frac{\partial y}{\partial \xi} & \frac{\partial y}{\partial \eta} \end{bmatrix} \cdot \begin{bmatrix} x \\ y \end{bmatrix} + \begin{bmatrix} x_0 \\ y_0 \end{bmatrix}. \end{aligned} \tag{A.164}$$

In vector notation

$$\boldsymbol{r} = \boldsymbol{J} \cdot \boldsymbol{\rho} + \boldsymbol{r}_0, \tag{A.165}$$

where $\boldsymbol{r}_0$ is the position vector of the center of the triangular element. This is a linear transformation as in Eq. (A.149). The Jacobian matrix of the above transformation is given by

$$\boldsymbol{J} = \begin{bmatrix} J_{11} & J_{12} \\ J_{21} & J_{22} \end{bmatrix} = \begin{bmatrix} \frac{\partial x}{\partial \xi} & \frac{\partial x}{\partial \eta} \\ \frac{\partial y}{\partial \xi} & \frac{\partial y}{\partial \eta} \end{bmatrix}. \tag{A.166}$$

Let $\left\{M_i^{(m,n)}\right\}$ be the set of shape functions on the triangular element in the global coordinates, which are to be determined given the shape function $\left\{N_i^{(m,n)}\right\}$ in the standard equilateral element. Equation (A.165) transforms the vertex P_i of the standard equilateral triangle to the vertex V_i of the arbitrary triangle. Hence the nodal conditions for the corresponding shape functions should remain the same. The nodal conditions for the scalar shape functions is written as

$$\begin{aligned} M_i^{(0,0)}(x_j, y_j) &= N_i^{(0,0)}\left(\xi_j, \eta_j\right), \\ &= N_i^{(0,0)}\left(\boldsymbol{J}^{-1} \cdot (\boldsymbol{r_j} - \boldsymbol{r}_0)\right), \\ &= \delta_{ij}, \end{aligned} \tag{A.167}$$

where, $i, j = 1, 2, 3$. Therefore,the transformation rule for the scalar shape function associated with the i^{th} node is simply given by

$$M_i^{(0,0)}(x, y) = N_i^{(0,0)}\left(\boldsymbol{J}^{-1} \cdot (\boldsymbol{r} - \boldsymbol{r}_0)\right). \tag{A.168}$$

To obtain the transformation rules for the vector and rank-2 tensor shape functions, we need to take into account of their tensorial nature under transformation (see Sec. A.6). Nodal conditions on the vector shape functions is written as[d]

$$\begin{bmatrix}\partial_x \\ \partial_y\end{bmatrix} \otimes \begin{bmatrix}M_i^{(1,0)}(x_i, y_i) & M_i^{(0,1)}(x_i, y_i)\end{bmatrix} = \begin{bmatrix}\partial_\xi \\ \partial_\eta\end{bmatrix} \otimes \begin{bmatrix}N_i^{(1,0)}(\xi_i, \eta_i) & N_i^{(0,1)}(\xi_i, \eta_i)\end{bmatrix} = \boldsymbol{I}_2. \tag{A.169}$$

Let us consider

$$\begin{aligned}\begin{bmatrix}\partial_\xi \\ \partial_\eta\end{bmatrix} \otimes \begin{bmatrix}M_i^{(1,0)}\left(x_i(\xi,\eta), y_i(\xi,\eta)\right) & M_i^{(0,1)}\left(x_i(\xi,\eta), y_i(\xi,\eta)\right)\end{bmatrix} \\ = \begin{bmatrix}\frac{\partial x}{\partial \xi} & \frac{\partial y}{\partial \xi} \\ \frac{\partial x}{\partial \eta} & \frac{\partial y}{\partial \eta}\end{bmatrix} \cdot \begin{bmatrix}\partial_x \\ \partial_y\end{bmatrix} \otimes \begin{bmatrix}M_i^{(1,0)}(x_i, y_i) & M_i^{(0,1)}(x_i, y_i)\end{bmatrix},\end{aligned} \tag{A.170}$$

Substituting Eq. (A.169) in Eq. (A.170) we obtain

$$\begin{aligned}\begin{bmatrix}\partial_\xi \\ \partial_\eta\end{bmatrix} \otimes \begin{bmatrix}M_i^{(1,0)}(x_i, y_i), & M_i^{(0,1)}(x_i, y_i)\end{bmatrix} = \begin{bmatrix}\frac{\partial x}{\partial \xi} & \frac{\partial y}{\partial \xi} \\ \frac{\partial x}{\partial \eta} & \frac{\partial y}{\partial \eta}\end{bmatrix} \cdot \\ \begin{bmatrix}\partial_\xi \\ \partial_\eta\end{bmatrix} \otimes \begin{bmatrix}N_i^{(1,0)}(\xi_i, \eta_i), & N_i^{(0,1)}(\xi_i, \eta_i)\end{bmatrix} \\ = \boldsymbol{J}^{\mathrm{T}} \begin{bmatrix}\partial_\xi \\ \partial_\eta\end{bmatrix} \otimes \begin{bmatrix}N_i^{(1,0)}(\xi_i, \eta_i), & N_i^{(0,1)}(\xi_i, \eta_i)\end{bmatrix}.\end{aligned} \tag{A.171}$$

The operator $\left[\partial_\xi, \partial_\eta\right]^T$ is acting on both the left and right side of Eq. (A.171). If we remove this operator in Eq. (A.171), we get a transformation rule for the vector

[d]Here, the direct product $\begin{bmatrix}\partial_x \\ \partial_y\end{bmatrix} \otimes \begin{bmatrix}M_i^{(1,0)}(x_i, y_i) & M_i^{(0,1)}(x_i, y_i)\end{bmatrix}$ is defined to be $\begin{bmatrix}\partial_x M_i^{(1,0)} & \partial_x M_i^{(0,1)} \\ \partial_y M_i^{(1,0)} & \partial_x M_i^{(0,1)}\end{bmatrix}$, where all the derivatives are evaluated at the point (x_i, y_i).

shape functions on the arbitrary triangular element in terms of the vector shape functions on the standard equilateral triangle. Hence we write

$$\begin{aligned}&\left[M_i^{(1,0)}(x,y) \quad M_i^{(0,1)}(x,y)\right]\\&= \boldsymbol{J}^{\mathrm{T}} \cdot \left[N_i^{(1,0)}\left(\xi(x,y),\eta(x,y)\right) \quad N_i^{(0,1)}\left(\xi(x,y),\eta(x,y)\right)\right].\end{aligned} \tag{A.172}$$

Transposing the above relation we have

$$\begin{aligned}\begin{bmatrix}M_i^{(1,0)}(x,y)\\ M_i^{(0,1)}(x,y)\end{bmatrix} &= \boldsymbol{J} \cdot \begin{bmatrix}N_i^{(1,0)}\left(\xi(x,y),\eta\,(x,y)\right)\\ N_i^{(0,1)}\left(\xi(x,y),\eta(x,y)\right)\end{bmatrix}\\&= \boldsymbol{J} \cdot \begin{bmatrix}N_i^{(1,0)}\left(\boldsymbol{J}^{-1}\cdot(\boldsymbol{r}-\boldsymbol{r}_0)\right)\\ N_i^{(0,1)}\left(\boldsymbol{J}^{-1}\cdot(\boldsymbol{r}-\boldsymbol{r}_0)\right)\end{bmatrix}.\end{aligned} \tag{A.173}$$

Now the nodal conditions on the second derivatives of the rank-2 tensor shape functions evaluated at the vertex (x_i, y_i) is written as

$$\begin{aligned}&\begin{bmatrix}\partial_{xx}\\ \partial_{xy}\\ \partial_{yy}\end{bmatrix} \otimes \begin{bmatrix}M_i^{(2,0)} & M_i^{(1,1)} & M_i^{(0,2)}\end{bmatrix} =\\&\qquad\qquad \begin{bmatrix}\partial_{\xi\xi}\\ \partial_{\xi\eta}\\ \partial_{\eta\eta}\end{bmatrix} \otimes \begin{bmatrix}N_i^{(2,0)} & N_i^{(1,1)} & N_i^{(0,2)}\end{bmatrix} = \mathbf{I}_3.\end{aligned} \tag{A.174}$$

Let us consider

$$\begin{bmatrix}\partial_{\xi\xi}\\ \partial_{\xi\eta}\\ \partial_{\eta\eta}\end{bmatrix} \otimes \begin{bmatrix}M_i^{(2,0)} & M_i^{(1,1)} & M_i^{(0,2)}\end{bmatrix} \tag{A.175}$$

$$= \begin{bmatrix}\left(\dfrac{\partial x}{\partial \xi}\partial_x + \dfrac{\partial y}{\partial \xi}\partial_y\right)\cdot\left(\dfrac{\partial x}{\partial \xi}\partial_x + \dfrac{\partial y}{\partial \xi}\partial_y\right)\\ \left(\dfrac{\partial x}{\partial \xi}\partial_x + \dfrac{\partial y}{\partial \xi}\partial_y\right)\cdot\left(\dfrac{\partial x}{\partial \eta}\partial_x + \dfrac{\partial y}{\partial \eta}\partial_y\right)\\ \left(\dfrac{\partial x}{\partial \eta}\partial_x + \dfrac{\partial y}{\partial \eta}\partial_y\right)\cdot\left(\dfrac{\partial x}{\partial \eta}\partial_x + \dfrac{\partial y}{\partial \eta}\partial_y\right)\end{bmatrix} \otimes \begin{bmatrix}M_i^{(2,0)} & M_i^{(1,1)} & M_i^{(0,2)}\end{bmatrix}.$$

The above equation, Eq. (A.176), can be expanded to write

$$\begin{bmatrix}\partial_{\xi\xi}\\ \partial_{\xi\eta}\\ \partial_{\eta\eta}\end{bmatrix} \otimes \begin{bmatrix} M_i^{(2,0)} & M_i^{(1,1)} & M_i^{(0,2)}\end{bmatrix} \tag{A.176}$$

$$= \begin{bmatrix} \left(\frac{\partial x}{\partial \xi}\right)^2 & 2\frac{\partial x}{\partial \xi}\frac{\partial y}{\partial \xi} & \left(\frac{\partial y}{\partial \xi}\right)^2 \\ \frac{\partial x}{\partial \xi}\frac{\partial x}{\partial \eta} & \frac{\partial x}{\partial \xi}\frac{\partial y}{\partial \eta} + \frac{\partial x}{\partial \eta}\frac{\partial y}{\partial \xi} & \frac{\partial y}{\partial \eta}\frac{\partial y}{\partial \xi} \\ \left(\frac{\partial x}{\partial \eta}\right)^2 & 2\frac{\partial x}{\partial \eta}\frac{\partial y}{\partial \eta} & \left(\frac{\partial y}{\partial \eta}\right)^2 \end{bmatrix} \cdot \begin{bmatrix}\partial_{xx}\\ \partial_{xy}\\ \partial_{yy}\end{bmatrix} \otimes \begin{bmatrix} M_i^{(2,0)} & M_i^{(1,1)} & M_i^{(0,2)}\end{bmatrix}.$$

Using Eq. (A.174) we have

$$\begin{bmatrix}\partial_{\xi\xi}\\ \partial_{\xi\eta}\\ \partial_{\eta\eta}\end{bmatrix} \otimes \begin{bmatrix} M_i^{(2,0)} & M_i^{(1,1)} & M_i^{(0,2)}\end{bmatrix} \tag{A.177}$$

$$= \begin{bmatrix} \left(\frac{\partial x}{\partial \xi}\right)^2 & 2\frac{\partial x}{\partial \xi}\frac{\partial y}{\partial \xi} & \left(\frac{\partial y}{\partial \xi}\right)^2 \\ \frac{\partial x}{\partial \xi}\frac{\partial x}{\partial \eta} & \frac{\partial x}{\partial \xi}\frac{\partial y}{\partial \eta} + \frac{\partial x}{\partial \eta}\frac{\partial y}{\partial \xi} & \frac{\partial y}{\partial \eta}\frac{\partial y}{\partial \xi} \\ \left(\frac{\partial x}{\partial \eta}\right)^2 & 2\frac{\partial x}{\partial \eta}\frac{\partial y}{\partial \eta} & \left(\frac{\partial y}{\partial \eta}\right)^2 \end{bmatrix} \cdot \begin{bmatrix}\partial_{\xi\xi}\\ \partial_{\xi\eta}\\ \partial_{\eta\eta}\end{bmatrix} \otimes \begin{bmatrix} N_i^{(2,0)} & N_i^{(1,1)} & N_i^{(0,2)}\end{bmatrix}.$$

Hence we can write down the transformation rule for the rank-2 tensor shape functions as

$$\begin{bmatrix} M_i^{(2,0)} & M_i^{(1,1)} & M_i^{(0,2)}\end{bmatrix} = \begin{bmatrix} \left(\frac{\partial x}{\partial \xi}\right)^2 & 2\frac{\partial x}{\partial \xi}\frac{\partial y}{\partial \xi} & \left(\frac{\partial y}{\partial \xi}\right)^2 \\ \frac{\partial x}{\partial \xi}\frac{\partial x}{\partial \eta} & \frac{\partial x}{\partial \xi}\frac{\partial y}{\partial \eta} + \frac{\partial x}{\partial \eta}\frac{\partial y}{\partial \xi} & \frac{\partial y}{\partial \eta}\frac{\partial y}{\partial \xi} \\ \left(\frac{\partial x}{\partial \eta}\right)^2 & 2\frac{\partial x}{\partial \eta}\frac{\partial y}{\partial \eta} & \left(\frac{\partial y}{\partial \eta}\right)^2 \end{bmatrix} \cdot \begin{bmatrix} N_i^{(2,0)} & N_i^{(1,1)} & N_i^{(0,2)}\end{bmatrix}. \tag{A.178}$$

Transposing the above relation we obtain

$$\begin{bmatrix} M_i^{(2,0)}(x,y) \\ M_i^{(1,1)}(x,y) \\ M_i^{(0,2)}(x,y) \end{bmatrix} = \begin{bmatrix} \left(\frac{\partial x}{\partial \xi}\right)^2 & 2\frac{\partial x}{\partial \xi}\frac{\partial y}{\partial \xi} & \left(\frac{\partial y}{\partial \xi}\right)^2 \\ \frac{\partial x}{\partial \xi}\frac{\partial x}{\partial \eta} & \frac{\partial x}{\partial \xi}\frac{\partial y}{\partial \eta} + \frac{\partial x}{\partial \eta}\frac{\partial y}{\partial \xi} & \frac{\partial y}{\partial \eta}\frac{\partial y}{\partial \xi} \\ \left(\frac{\partial x}{\partial \eta}\right)^2 & 2\frac{\partial x}{\partial \eta}\frac{\partial y}{\partial \eta} & \left(\frac{\partial y}{\partial \eta}\right)^2 \end{bmatrix}^{\boldsymbol{T}} \cdot \begin{bmatrix} N_i^{(2,0)}\left(\boldsymbol{J}^{-1}\left(\boldsymbol{r}-\boldsymbol{r}_0\right)\right) \\ N_i^{(1,1)}\left(\boldsymbol{J}^{-1}\cdot\left(\boldsymbol{r}-\boldsymbol{r}_0\right)\right) \\ N_i^{(0,2)}\left(\boldsymbol{J}^{-1}\cdot\left(\boldsymbol{r}-\boldsymbol{r}_0\right)\right) \end{bmatrix}. \tag{A.179}$$

Hence the transformation rule for rank-1 shape functions in terms of the entries of the Jacobian matrix $\boldsymbol{J}$ is given by

$$\begin{bmatrix} M_i^{(2,0)} \\ M_i^{(1,1)} \\ M_i^{(0,2)} \end{bmatrix} = \begin{bmatrix} J_{11}^2 & J_{11}J_{12} & J_{12}^2 \\ 2J_{11}J_{21} & J_{12}J_{21}+J_{11}J_{22} & 2J_{12}J_{22} \\ J_{21}^2 & J_{21}J_{22} & J_{22}^2 \end{bmatrix} \cdot \begin{bmatrix} N_i^{(2,0)} \\ N_i^{(1,1)} \\ N_i^{(0,2)} \end{bmatrix}. \tag{A.180}$$

The set of 18 DoF polynomials contains scalar, vector and rank-2 tensor shape functions. Hence the transformation for the polynomials associated with i^{th} node is given by

$$\begin{bmatrix} M_i^{(0,0)} \\ M_i^{(1,0)} \\ M_i^{(0,1)} \\ M_i^{(2,0)} \\ M_i^{(1,1)} \\ M_i^{(0,2)} \end{bmatrix}(x,y,z) = \begin{bmatrix} 1 & & & & & \\ & J_{11} & J_{12} & & & \\ & J_{21} & J_{22} & & & \\ & & & J_{11}^2 & J_{11}J_{12} & J_{12}^2 \\ & & & 2J_{11}J_{21} & J_{12}J_{21}+J_{11}J_{22} & 2J_{12}J_{22} \\ & & & J_{21}^2 & 2J_{21}J_{22} & J_{22}^2 \end{bmatrix}_{6\times 6} \cdot \begin{bmatrix} N_i^{(0,0)} \\ N_i^{(1,0)} \\ N_i^{(0,1)} \\ N_i^{(2,0)} \\ N_i^{(1,1)} \\ N_i^{(0,2)} \end{bmatrix}\left(\boldsymbol{J}^{-1}\left(\boldsymbol{r}-\boldsymbol{r}_0\right)\right), \tag{A.181}$$

where $i = 1, 2, 3$.

A.8 Summary

Properties of different sets of polynomials on a triangle

It is very appropriate at this stage to summarize the properties of the different sets of Hermite interpolation polynomials we have considered here. This provides an overview of the properties of these polynomials in 2D triangles, allowing us to make choices as to which set would be applicable and natural for a given problem.

18 DoF

1. Complete quintic polynomials with 21 coefficients are treated with group representation theory.
2. Nodes are at the vertices of the triangle, and f, $\partial_x f$, $\partial_y f$, $\partial_{xx} f$, $\partial_{xy} f$, and $\partial_{yy} f$ are defined at each vertex.
3. Polynomials and their normal derivatives are set to zero at the opposite side of the given node.
4. Supports $C^{(2)}$-continuous quintic polynomials in each element.
5. The set of 18 DoF polynomials first derived by KBR [73] supports tangential $C^{(2)}$- and normal derivative $C^{(1)}$-continuity across the element.

21 DoF

1. Coefficients of quintic polynomials with 21 terms are obtained through the matrix inversion method.
2. Nodes are located at the vertices and at the centroid of the triangle. We define $f, \partial_x f, \partial_y f, \partial_{xx} f, \partial_{xy} f, \partial_{yy} f$ at each vertex and f, $\partial_x f$, $\partial_y f$ at the centroid of the triangle.
3. Polynomials are zero at the side opposite to a given node. But their normal derivatives do not have unique values across the interface between two elements. Hence the inter-element normal derivative continuity is not guaranteed.
4. 18 DoF polynomials are preferred over 21 DoF polynomials for any finite element calculations.

A.9 Concluding remarks

We have presented a new method based on the group representation theory to derive interpolation polynomials that satisfy the requirement of $C^{(n)}$-continuity across elements using the symmetry of the finite element. We have applied this method to derive linear interpolation polynomials and cubic Hermite interpolation polynomials in one dimensional straight element. For an equilateral triangular finite element, the 18 DoF $C^{(2)}$-continuous quintic Hermite interpolation polynomials with $C^{(1)}$-continuous normal derivatives across the element were derived. Transformation of these polynomials to a right triangle element and to an arbitrary triangular element is discussed.

We have shown in our earlier work that the 18 DoF finite elements yields better accuracy by several orders of magnitude, with a smoother representation of fields than the vector finite element methods for electromagnetic field calculations in waveguides [227], photonic crystals [228], and three-dimensional cavities [229, 230]. Hermite finite elements presented here do not generate any spurious solutions that afflict Lagrange finite elements, even though both are scalar in nature. These polynomials are shown to provide an efficient and accurate means of solving Maxwell's equations in a variety of systems, potentially offering a computationally inexpensive means of designing devices for optoelectronics and plasmonics of increasing complexity. The development of $C^{(1)}$- and $C^{(2)}$-continuous set of Hermite interpolating polynomials in three dimension will make this method a feasible option for a large number of engineering applications. These finite elements provide a robust method for quantum mechanical calculations as well [231]. Simulations based on these scalar finite elements are applicable to a broad class of physical systems, e.g., to semiconducting lasers which require simultaneous modeling of transitions in nanoscale quantum wells or dots together with EM cavity calculations, to modeling plasmonic structures in the presence of EM field emissions, and to on-chip propagation within monolithic integrated circuits in high frequency electronics.

In conclusion, Hermite finite elements presented here provide significant advantages in both electromagnetic and quantum mechanical modeling of complex systems that should attract their more universal usage in physics and engineering applications.

Appendix B

LIST OF INTERPOLATION POLYNOMIALS

In this appendix, we list the set of shape functions on a 1D line element, and the 18 DoF quintic polynomials on the standard equilateral and right triangular elements.

B.1 List of polynomials on a 1D line element

$$N_1(x) = \frac{1}{2}(1-x); \qquad N_2(x) = \frac{1}{2}(1+x).$$

Table B.1.1: Linear interpolation polynomials on a 1D line element with vertices at $x = -1$ and $x = 1$.

$$N_1^{(0)}(x) = \frac{1}{4}\left(x^3 - 3x + 2\right); \qquad N_1^{(1)}(x) = \frac{1}{4}(x-1)^2(x+1);$$
$$N_2^{(0)}(x) = \frac{1}{4}\left(-x^3 + 3x + 2\right); \qquad N_2^{(1)}(x) = \frac{1}{4}(x-1)(x+1)^2.$$

Table B.1.2: Cubic Hermite interpolation polynomials on a 1D line element with vertices at $x = -1$ and $x = 1$ that support $C^{(1)}$-continuity across the element.

$$
\begin{aligned}
N_1^{(0)}(x) &= \frac{1}{16}(1-x)^3(3x(x+3)+8),\\
N_1^{(1)}(x) &= \frac{1}{16}(1-x)^3(x+1)(3x+5),\\
N_1^{(2)}(x) &= \frac{1}{16}(1-x)^3(x+1)^2,\\
N_2^{(0)}(x) &= \frac{1}{16}(x+1)^3(3(x-3)x+8),\\
N_2^{(1)}(x) &= \frac{1}{16}(1-x)(x+1)^3(3x-5),\\
N_2^{(2)}(x) &= \frac{1}{16}(x-1)^2(x+1)^3.
\end{aligned}
$$

Table B.1.3: Quintic Hermite interpolation polynomials on a 1D line element with vertices at $x = -1$ and $x = 1$ that support $C^{(2)}$-continuity across the element.

B.2 List of polynomials on a triangular element

$$
\begin{aligned}
N_1(x,y) &= 1 + \frac{2}{3}(x-1); \qquad ,\\
N_2(x,y) &= \frac{1}{3}(1-x) + \frac{y}{\sqrt{3}},\\
N_3(x,y) &= \frac{1}{3}(1-x) - \frac{y}{\sqrt{3}}.
\end{aligned}
$$

Table B.2.1: Linear interpolation polynomials on the standard equilateral triangular element. Coordinates of the vertices are located at $(1,0)$, $(-1/2,\sqrt{3}/2)$ and $(-1/2,-\sqrt{3}/2)$ which are labeled as the vertex 1, 2 and 3, respectively.

$$M_1(x, y) = 1 - x - y,$$
$$M_2(x, y) = x,$$
$$M_3(x, y) = y.$$

Table B.2.2: Linear interpolation polynomials on the standard right triangular element. Coordinates of the vertices are located at $(0, 0)$, $(1, 0)$ and $(0, 1)$ which are labeled as the vertex 1, 2 and 3, respectively.

$$
\begin{aligned}
N_1^{(0,0)}(x,y) &= \tfrac{1}{27}(1+2x)^2(9-10y^2-2x(3+(1-x)x-5y^2)).\\
N_1^{(1,0)}(x,y) &= \tfrac{1}{54}(x-1)(1+2x)^2(11-x(2+3x)-15y^2).\\
N_1^{(0,1)}(x,y) &= \tfrac{1}{54}(1+2x)^2y(7+x(6-7x)-3y^2).\\
N_1^{(2,0)}(x,y) &= \tfrac{1}{72}(1-x)(1+2x)^2(3-x(2+x)-5y^2).\\
N_1^{(1,1)}(x,y) &= \tfrac{1}{108}(2x+1)^2y\left(x(7x-2)+3y^2-5\right).\\
N_1^{(0,2)}(x,y) &= \tfrac{1}{216}(1+2x)^2((7+5x)y^2-(1-x)^3).
\end{aligned}
$$

$$
\begin{aligned}
N_2^{(0,0)}(x,y) = \tfrac{1}{27}(&-4x^5+10\sqrt{3}x^4y+5x^3\left(3-4y^2\right)-5x^2\left(3\sqrt{3}y+1\right)\\
&-5x\left(-3y^2+2\sqrt{3}y+3\right)+y(y\left(3\sqrt{3}y\left(2y^2-5\right)+5\right)\\
&+15\sqrt{3})+9).\\
N_2^{(1,0)}(x,y) = \tfrac{1}{108}&(1+2x)(1-x+\sqrt{3}y)^2(11-5x-6x^2-\sqrt{3}(3-2x)y).\\
N_2^{(0,1)}(x,y) = \tfrac{1}{108}&(1-x+\sqrt{3}y)^2(4\sqrt{3}x^3+2x^2(5\sqrt{3}-4y)\\
&+y(23+6(\sqrt{3}-2y)y)-x(3\sqrt{3}-8y(3-\sqrt{3}y))-11\sqrt{3}).\\
N_2^{(2,0)}(x,y) = \tfrac{1}{432}&(1+2x)^2(1-x+\sqrt{3}y)^2(3-3x+\sqrt{3}y).\\
N_2^{(1,1)}(x,y) = \tfrac{1}{216}&(1+2x)(1-x+\sqrt{3}y)^2(11y+x(3\sqrt{3}+2\sqrt{3}x-2y)-5\sqrt{3}).\\
N_2^{(0,2)}(x,y) = -\tfrac{1}{432}&\left(-x+\sqrt{3}y+1\right)^2(4(1-4x)y^2-4\sqrt{3}(x-3)xy\\
&+x(4x(x+3)-3)-8\sqrt{3}y^3+13\left(\sqrt{3}y-1\right)).
\end{aligned}
$$

$$
\begin{aligned}
N_3^{(0,0)}(x,y) = \tfrac{1}{27}&(1-x-\sqrt{3}y)^2(x(3-4x(2+x))\\
&+2\sqrt{3}(2-x)xy-4(1-x)y^2-2\sqrt{3}y^3+3(3+\sqrt{3}y)).\\
N_3^{(1,0)}(x,y) = \tfrac{1}{108}&(1+2x)(1-x-\sqrt{3}y)^2(11-5x-6x^2+\sqrt{3}(3-2x)y).\\
N_3^{(0,1)}(x,y) = \tfrac{1}{108}&(1-x-\sqrt{3}y)^2(11\sqrt{3}-4\sqrt{3}x^3-2x^2(5\sqrt{3}+4y)\\
&+y(23-6y(\sqrt{3}+2y))+x(3\sqrt{3}+8y(3+\sqrt{3}y))).\\
N_3^{(2,0)}(x,y) = \tfrac{1}{432}&(1+2x)^2(1-x-\sqrt{3}y)^2(3-3x-\sqrt{3}y).\\
N_3^{(1,1)}(x,y) = \tfrac{1}{216}&(1+2x)(1-x-\sqrt{3}y)^2(\sqrt{3}(1-x)(5+2x)+(11-2x)y).\\
N_3^{(0,2)}(x,y) = \tfrac{1}{432}&(1-x-\sqrt{3}y)^2(13-4x^3+13\sqrt{3}y-4y^2\\
&-8\sqrt{3}y^3-4x^2(3+\sqrt{3}y)+x(3+4y(3\sqrt{3}+4y))).
\end{aligned}
$$

Table B.2.3: Quintic Hermite interpolation polynomials in the equilateral triangular reference element with vertices at $(1,0)$, $(-1/2,\sqrt{3}/2)$ and $(-1/2,-\sqrt{3}/2)$ that support $C^{(1)}$-continuous quartic polynomials across shared sides of elements [73].

$$
\begin{aligned}
&M_1^{(0,0)}(x,y) = (1-x-y)^2(3x^2(1-y)-6x^3+x(2+3(2-y)y)\\
&+(1-y)(1+3y+6y^2)).\\
&M_1^{(1,0)}(x,y) = \tfrac{1}{2}x(1-x-y)^2(2+4y+x(4-6x-3y)).\\
&M_1^{(0,1)}(x,y) = \tfrac{1}{2}y(1-x-y)^2(x(4-3y)+2(1-y)(1+3y)).\\
&M_1^{(2,0)}(x,y) = \tfrac{1}{4}x^2(1-x-y)^2(2-2x-y).\\
&M_1^{(1,1)}(x,y) = xy(1-x-y)^2.\\
&M_1^{(0,2)}(x,y) = \tfrac{1}{4}y^2(1-x-y)^2(2-2y-x).
\end{aligned}
$$

$$
\begin{aligned}
&M_2^{(0,0)}(x,y) = x^2(x(10-3x(5-2x))+15(1-x)^2y-15(1-x)y^2).\\
&M_2^{(1,0)}(x,y) = \tfrac{1}{2}x^2(1-x)(6x^2-15(1-y)y-x(8-15y)).\\
&M_2^{(0,1)}(x,y) = \tfrac{1}{2}x^2y(x(3y-4)+3(2-y-y^2)).\\
&M_2^{(2,0)}(x,y) = \tfrac{1}{4}x^2(x-1)(2(x-1)x-5(1-x)y+5y^2).\\
&M_2^{(1,1)}(x,y) = \tfrac{1}{2}x^2y(y^2+y+x(2-y)-2).\\
&M_2^{(0,2)}(x,y) = \tfrac{1}{4}x^2(1+x-y)y^2.
\end{aligned}
$$

$$
\begin{aligned}
&M_3^{(0,0)}(x,y) = y^2(15x^2(y-1)+15x(1-y)^2+y(10-3y(5-2y))).\\
&M_3^{(1,0)}(x,y) = \tfrac{1}{2}xy^2(6-3x(1+x-y)-4y).\\
&M_3^{(0,1)}(x,y) = \tfrac{1}{2}y^2(1-y)(15(x-1)x-(8-15x)y+6y^2).\\
&M_3^{(2,0)}(x,y) = \tfrac{1}{4}x^2y^2(1-x+y).\\
&M_3^{(1,1)}(x,y) = \tfrac{1}{2}xy^2(x+x^2+2y-xy-2).\\
&M_3^{(0,2)}(x,y) = \tfrac{1}{4}y^2(y-1)(5x^2-5x(1-y)-2(1-y)y).
\end{aligned}
$$

Table B.2.4: Quintic Hermite interpolation polynomials derived in the equilateral triangular reference element that support $C^{(1)}$-continuous quartic polynomials across shared sides of elements mapped into the right triangle with vertices at $(0,0)$, $(1,0)$ and $(0,1)$ which are labeled as the vertex 1, 2 and 3, respectively.

BIBLIOGRAPHY

[1] G. Gamow, Z. Phys. **51**, 204–212 (1928); Nature **122**, 805–806 (1928); Z. Phys. **52**, 510 (1928); *ibid.* **53**, 601 (1929).

[2] D. Bohm, *Quantum Theory* (Dover, NY, 1989).

[3] J. J. Sakurai, *Modern Quantum Mechanics* (Addison-Wesley, Reading, MA, 1994).

[4] N. F. Mott and H. S. W. Massey, *The Theory of Atomic Collisions* (Oxford University Press, London, 1949).

[5] M. L. Goldberger and K. M. Watson, *Collision Theory* (J. Wiley and Sons, NY, 1964).

[6] J. R. Taylor, *Scattering Theory: The Quantum Theory of Nonrelativistic Collisions* (Dover, NY, 2006).

[7] R. G. Newton, *Scattering Theory of Waves and Particles*, 2nd Ed. (Springer-Verlag, NY, 1982).

[8] C. C.-Tannoudji, B. Diu, and F. Laloe, *Quantum Mechanics*, Vol. **2** (John Wiley & Sons Inc, New York, NY, 1991).

[9] S. K. Adhikari, Am. J. Phys. 54, 362–367 (1986).

[10] A. Sommerfeld, *Partial Differential Equations in Physics* (Academic Press, New York, NY, 1949); Ch. 4, p. 98–101.

[11] J. W. Strutt and B. Rayleigh,*The theory of sound*, Vol. **2** (Macmillan and Co., Ltd., New York, 1896); Ch. 17, p. 236–284.

[12] H. Faxen and J. P. Holtsmark, Zeits. f. Physik **45**, 307 (1927).

[13] T. Liu, W-.D Li, and W-.S. Dai, J. High Energy Phys. **2014**, 87 (2014).

[14] W-.D Li, and W-.S. Dai, J. Phys. A: Math. Theor. **49**, 465202 (2016).

[15] Sathwik Bharadwaj, and L. R. Ram-Mohan, J. Appl. Phys. **125**, 164307 (2019).

[16] J. Schwinger and D. S. Saxon, *Discontinuities in waveguides: Notes on lectures by Julian Schwinger* (Gordon and Breach, New York, 1968). Also see: K. A. Milton and J. Schwinger, *Electromagnetic Radiation: Variational Methods, Waveguides and Accelerators* (Springer-Verlag, Berlin, Germany, 2006).

[17] K. Kalikstein, J. Math. Phys. **22**, 1433-1437 (1981).

[18] W. Kohn, Phys. Rev. **74**, 1763–1772 (1948).

[19] S. I. Rubinow, Phys. Rev. **98**, 183–187 (1955).

[20] L. Hulthén, Ark. Mat. Astron. Fys. A **35**, 25 (1948).

[21] C. Schwartz, Phys. Rev. **124**, 1468–1471 (1961); Ann. Phys. **16**, 36–50 (1961).

[22] J. Schwinger, Phys. Rev. **72**, 742 (1947).

[23] B. L. Moiseiwitsch, *Variational Principles* (Interscience, London, 1966).

[24] B. A. Lippmann and J. Schwinger, Phys. Rev. **79**, 469–480 (1950).

[25] R. K. Nesbet, *Variational methods in electron-atom scattering theory* (Plenum Press, New York, 1980).

[26] S. K. Adhikari, *Variational Principles and the Numerical Solution of Scattering Problems* (Wiley Inter-Science, NY, 1998).

[27] M-Y. Li, S-K. Su, H.-S. P. Wong and L.-J. Li, Nature **567**, 169–170 (2019)

[28] J. M. Shalf and R. Leland, Computer **48**, 14–23 (2015)

[29] F. Schwierz, Nat. Nanotechnol. **5**, 487–496 (2010).

[30] L. Tao, E. Cinquanta, D. Chiappe, C. Grazianetti, M. Fanciulli, M. Dubey, A. Molle and D. Akinwande, Nat. Nanotechnol. **10**, 227–231 (2015).

[31] L. Li, Y. Yu, G. Jun Ye, Q. Ge, X. Ou, H. Wu, D. Feng, X. H. Chen and Y. Zhang, Nat. Nanotechnol. **9**, 372–377 (2014).

[32] Y. Yoon, K. Ganapathi, S. Salahuddin, Nano Lett. **11**, 3768–3773 (2011).

[33] Y. Cui, R. Xin, Z. Yu, Y. Pan, Z-Y. Ong, X. Wei, J. Wang, H. Nan, Z. Ni, Y. Wu, T. Chen, Y. Shi, B. Wang, G. Zhang, Y-W. Zhang, X. Wang, Adv. Mater. **27**, 5230–5234 (2015).

[34] A. D. Bartolomeo, F. Urban, M. Passacantando, N. McEvoy, L. Peters, L. Iemmo, G. Luongo, F. Romeo, and F. Giubileo, Nanoscale, **11**, 1538–1548 (2019).

[35] J. Lee, D. Wong, J. Velasco, Jr., J. F. Rodriguez-Nieva, S. Kahn, H.-Z. Tsai, T. Taniguchi, K. Watanabe, A. Zettl, F. Wang, L. S. Levitov, and M. F. Crommie, Nat. Phys. **12**, 1032–1037 (2016).

[36] C. Gutiérrez, L. Brown, C.-J. Kim, J. Park, and A. N. Pasupathy, Nature Phys. **12**, 1068-1076 (2016).

[37] H. Alon, C. Stern, M. Kirshner, O. Sinai, M. Wasserman, R. Selhors, R. Gasper, A. Ramasubramaniam, T. E. Orcid, and D. Naveh, ACS Nano **12**, 1928–1933 (2018).

[38] S. Carr, S. Fang, Z. Zhu, and E. Kaxiras, Phys. Rev. Research **1**, 013001 (2019).

[39] E. Margapoti, J. Li, O. Ceylan, M. Seifert, F. Nisic, T. Le Anh, F. Meggendorfer, C. Dragonetti, C.-A. Palma, J. V. Barth, and J. J. Finley, Adv. Mater. **27**, 1426 (2015).

[40] D. M.-Gustin, L. Cabral, M. P. Lima, J. L. F. Da Silva, E. Margapoti, S. E. Ulloa,, Phys. Rev. B. **98**, 241403(R) (2018).

[41] L. R. Ram-Mohan, *Finite Element and Boundary Element applications in Quantum Mechanics* (Oxford University Press Inc., New York, 2002).

[42] M. Born, E. Wolf, A. B. Bhatia, P. C. Clemmow, D. Gabor, A. R. Stokes, A. M. Taylor, P. A. Wayman, and W. L. Wilcock, *Principles of Optics: Electromagnetic Theory of Propagation, Interference and Diffraction of Light,* 7th ed. (Cambridge University Press, Cambridge, 1999).

[43] D. BenDaniel and C. Duke, Phys. Rev. **152**, 683–692 (1966).

[44] O. C. Zienkiewicz and Y. K. Cheung, *Finite Element Methods in Structural and Continuum Mechanics* (McGraw-Hill, New York, 1967); O. C. Zienkiewicz, *The Finite Element Method* (McGraw-Hill, New York, 1977).

[45] J. Jin, *The Finite Element Method in Electromagnetics*, 2nd ed. (Wiley, New York, 2002).

[46] B. Chen, M. Lazzouni, L. R. Ram-Mohan, Phys. Rev. B **45**, 1204–1212 (1992).

[47] Satish Balay *et al.*, Argonne National Laboratory, ANL-95/11 - Revision 3.7, 2016. *PETSc Users Manual.*

[48] P. R. Amestoy, I. S. Duff, J.-Y. L'Excellent and, J. Koster, SIAM J. Matrix Anal. Appl. **23**, 15–41 (2006).

[49] P. R. Amestoy, A. Guermouche, J.-Y. L'Excellent and, S. Pralet, Parallel Comput. **32**, 136–156 (2006).

[50] X. S. Li and J. W. Demmel, ACM Trans. Math. Software, **29**, 2, 110–140 (2003).

[51] Sathwik Bharadwaj, Andrei lyashenko, Anthony Gianfrancesco, and L. R. Ram-Mohan, Trans. JASCOME **17**, 22, 107–112 (2017).

[52] D. Dossa, Lok C. Lew Yan Voon, L. R. Ram-Mohan, C. Parks, R. G. Alonso, A. K. Ramdas, and M. R. Melloch, Appl. Phys. Lett. **59**, 2706–2708 (1991).

[53] F. C. Zhang, N. Dai, H. Luo, N. Samarth, M. Dobrowolska, J. K. Furdyna, and L. R. Ram-Mohan, Phys. Rev. Lett. **68**, 3220–3223 (1992).

[54] C. Parks, A. K. Ramdas, M. R. Melloch, G. Steblovsky, L. R. Ram-Mohan, and H. Luo, Solid State Commun. **92**, 563–567 (1994). See also, N. Dai, L. R. Ram-Mohan, H. Luo, G. L. Yang, F. C. Zhang, M. Dobrowolska, and J. K. Furdyna, Phys. Rev. B **50**, 18153–18166 (1994).

[55] C. Parks, A. K. Ramdas, M. R. Melloch, G. Steblovsky, L. R. Ram-Mohan, and H. Luo, J. Vac. Sci. Technol. B **13**, 657–659 (1995).

[56] R. Tsu and L. Esaki, Appl. Phys. Lett. **22**, 562–564 (1973).

[57] S. Datta, *Quantum Phenomena* (Addison-Wesley, Reading, 1989).

[58] C.W.J. Beenakker and H. van Houten, Solid State Phys. **44**, 1–228 (1991).

[59] A. Ohtomo and H. Y. Hwang, Nature **427**, 423-–426 (2004). See also, S. Thiel, G. Hammerl, A. Schmehl, C. W. Schneider, and J. Mannhart, Science **313**, 1942–1945 (2006).

[60] W. Liang, M. Bockrath, D. Bozovic, J. H. Hafne, M. Tinkham, and H. Park, Nature **411**, 665–669 (2001).

[61] Y. Li, and Z. L. Cendes, IEEE Trans. Magn. **29**, 1835–1838 (1993).

[62] R. Goloskie, J. W. Kramer, and L. R. Ram-Mohan, Comput. Phys. **8**, 679–686 (1994).

[63] H. K. Harbury and W. Porod, J. Appl. Phys. **75**, 5142–5149 (1994).

[64] A. Askar, *Finite Elements Method for Quantum Scattering,* in *Numerical Grid Methods and their Applications to Schrödinger's Equation,* NATO ASI Series, edited by C. Cerjan (Kluwer Academic, New York, 1993).

[65] P. F. Bagwell, Phys. Rev. B. **41**, 10354–10357 (1990).

[66] M. Tinkham, *Group Theory and Quantum Mechanics* (Dover Publications, New York, 2003).

[67] M. S. Dresselhaus, G. Dresselhaus and A. Jorio, *Group Theory: Application to the Physics of Condensed Matter* (Springer, Berlin, 2008).

[68] D. Boese, M. Lischka, and L. E. Reichl, Phys. Rev. B **61**, 5632–5636 (2000).

[69] H. Lee, H. Hsu, and L. E. Reichl, Phys. Rev. B **71**, 045307–1–9 (2005).

[70] T. Ueta, Phys. Rev. B **60**, 8213–8217 (1999).

[71] Y. Miyagawa and T. Ueta, Thin Solid Films, **505**, 57–59 (2006).

[72] Sathwik Bharadwaj, and L. R. Ram-Mohan, J. Appl. Phys. **125**, 164306 (2019).

[73] P. G. Kassebaum, C. R. Boucher and L. R. Ram-Mohan, J. Comp. Physics. **231**, 5747—5760 (2012).

[74] U. Fano, Phys. Rev. **124**, 1866–1878 (1961); U. Fano, and J. W. Cooper, *ibid* **137**, A1364–A1379 (1965).

[75] E. Tekman, and P. F. Bagwell, Phys. Rev. B. **48**, 2553–2559 (1993).

[76] Y. S. Joe, A. M. Satanin and C. S. Kim, Phys. Scr. **74**, 259–266 (2006).

[77] A. E. Miroshnichenko, S. Flach, and Y. S. Kivshar, Rev. Mod. Phys. **82**, 2257–2298 (2010).

[78] A R P Rau, Phys. Scr. **69**, 1, C10–13 (2004).

[79] C. S. Kim, A. M. Satanin, Y. S. Joe, and R. M. Cosby, Phys. Rev. B **60**, 10962–10970 (1999).

[80] C. S. Kim, O. N. Roznova, A. M. Satanin, and V. B. Stenberg, J. Exp. Theor. Phys. **94**, 992–1007 (2002).

[81] Y. S. Joe and A. M. Satanin, J. Supercond. Nov. Magn. **20**, 2 (2007).

[82] S. Flügge, *Practical quantum mechanics* (Springer-Verlag, Berlin, 1971).

[83] V. Vargiamidis, P. Komninou, and H. M. Polatoglou, Phys. Stat. Sol. (c) **5**, 3813–3817 (2008).

[84] V. Vargiamidis and H. M. Polatoglou, Phys. Rev. B **72**, 195333–1–12 (2005).

[85] S. A. Gurvitz and Y. B. Levinson, Phys. Rev. B **47**, 10578 (1993). See also, A. A. Clerk, X. Waintal, and P. W. Brouwer, Phys. Rev. Lett. **86**, 4636–4639 (2001).

[86] J. Göres, D. Goldhaber-Gordon, S. Heemeyer, and M. A. Kastner, Phys. Rev. B **62**, 2188–2194 (2000).

[87] J. Kim, J.-R. Kim, J.-O. Lee, J. W. Park, H. M. So, N. Kim, K. Kang, K.-H. Yoo, and J.-J. Kim, Phys. Rev. Lett. **90**, 166403–1–4 (2003).

[88] Kensuke Kobayashi, Hisashi Aikawa, Akira Sano, Shingo Katsumoto, and Yasuhiro Iye, Phys. Rev. B **70**, 035319–1–6 (2004).

[89] A. C. Johnson, C. M. Marcus, M. P. Hanson, and A. C. Gossard, Phys. Rev. Lett. **93**, 106803–1–4 (2004).

[90] H. Feshbach, Ann. Phys. **5**, 357 (1958); Ann. Phys. **19**, 287–313 (1962).

[91] J. U. Nöckel and A. D. Stone, Phys. Rev. B **50**, 17415–17432 (1994).

[92] C. Berthod, F. Gagel, and K. Maschke, Phys. Rev. B **50**, 18299–18311 (1994).

[93] J.-P Connerade and A M Lane, Rep. Prog. Phys. **51**, 1439-1478 (1988), and references within.

[94] J.-P Connerade and A M Lane, J. Phys. B: At. Mol. Phys. **20**, 1757-1769 (1987).

[95] S. Klaiman, N. Moiseyev, and H. R. Sadeghpour, Phys. Rev. B **75**, 113305–1–4 (2007).

[96] R. Landauer, IBM J. Res. Dev. **1**, 223 (1957).

[97] R. Landauer, Philos. Mag. **21**, 863 (1970).

[98] M. Büttiker, Phys. Rev. Lett. **57**, 1761 (1986); see also, IBM J. Res. Dev. **32**, 317 (1988).

[99] M. Büttiker, Y. Imry, R. Landauer, and S. Pinhas, Phys. Rev. B **31**, 6207 (1985).

[100] D. S. Fisher and P. A. Lee, Phys. Rev. B **23**, 6851–6854(R) (1981).

[101] U. Sivan and Y. Imry, Phys. Rev. B **33**, 1, 551–558 (1986).

[102] S. Datta, *Electronic Transport in Mesoscopic Systems* (Cambridge University Press, Cambridge, 1995).

[103] C. R. Proetto, Phys. Rev. B **44**, 16, 9096–9099 (1991).

[104] N. F. Mott and E. A. Davis, *Electronic processes in non-Crystalline materials* (Oxford University Press, Oxford, 2012).

[105] A. A. Gorbatsevich and V. V. Kapaev, Russ. Microelectron. **36**, 1, 1–13 (2005).

[106] C. S. Chu and R. S. Sorbello, Phys. Rev. B **40**, 5941–5949 (1989).

[107] M. Zebarjadi, K. Esfarjani, A. Shakouri, J.-H. Bahk, Z. Bian, G. Zeng, J. Bowers, H. Lu, J. Zide, and A. Gossard, Appl. Phys. Lett. **94**, 202105–1–3 (2009).

[108] T. Zhu, K. Swaminathan-Gopalan, K. Stephani, and E. Ertekin, Phys. Rev. B **97**, 174201 (2018).

[109] B. Wang, J. Zhou, R. Yang, and B. Li, New J. Phys. **16**, 065018 (2014).

[110] L. R. Ram-Mohan, K. H. Yoo, J. Moussa, J. Appl. Phys. **95**, 3081–3092 (2004).

[111] J. Goldstone and R. L. Jaffe, Phys. Rev. B **45**, 14100–14107 (1992).

[112] R. L. Schult, D. G. Ravenhall, and H. W. Wyld, Phys. Rev. B **39**, 5476–5479 (1989).

[113] Z.-M. Bai, X. Chen, X.-T. An, Physica B **407**, 4293—4297 (2012).

[114] O. Olendski and L. Mikhailovska, Phys. Rev. B **67**, 035310–1–13 (2003).

[115] J. D. Walls, J. Huang, R. M. Westervelt, and E. J. Heller, Phys. Rev. B **73**, 035325–1–17 (2006).

[116] T. Ueta and Y. Miyagawa, Phys. Rev. E **86**, 026707–1–8 (2012).

[117] G. Dresselhaus, Phys. Rev. **100**, 580–586 (1955).

[118] E. I. Rashba, Sov. Phys. Solid. State, **1**, 368–380 (1959). See also, G. Bihlmayer, O. Rader, and R. Winkler, New J. Phys. **17**, 050202–1–8 (2015).

[119] See Ref. [4], Ch. 8, p. 184–194.

[120] H. Friedrich, *Theoretical Atomic Physics* (Springer-Verlag, Berlin, 1990).

[121] C. C. PriceNathan C. Frey, D. Jariwala, V. B. Shenoy, ACS Nano **13**, 8303-8311 (2019).

[122] W. Kohn and L. J. Sham, Phys. Rev. **140**, A1133–A1138 (1965).

[123] C. W. Groth, M. Wimmer, A. R. Akhmerov, X. Waintal, New J. Phys. **16**, 063065 (2014).

[124] M. L. Van de Put , M. V. Fischetti, W. G. Vandenberghe, Comput. Phys. Commun. **244**, 156–169 (2019).

[125] J. Taylor, H. Guo, and J. Wang, Phys. Rev. B **63**, 245407 (2001).

[126] M. Brandbyge, J. L. Mozos, P. Ordejón, J. Taylor, and K. Stokbro, Phys. Rev. B **65**, 1654011 (2002).

[127] H. Gan, P. L. Levin, and R. Ludwig, J. Acoust. Soc. Am. **94**, 1651–1662 (1993).

[128] P.M. Morse, H. Feshbach, *Methods of theoretical physics* (McGraw-Hill Book Company, New York, NY, 1953).

[129] J. M. Luttinger and W. Kohn, Phys. Rev. **97**, 869–883 (1955).

[130] J. M. Luttinger, Phys. Rev. **102**, 1030–1041 (1956).

[131] G. Bir and G. Pikus, *Symmetry and Strain-Induced Effects in Semiconductors* (Wiley, New York, NY, 1974).

[132] M. S. Dresselhaus, G. Dresselhaus, and A. Jorio, *Group Theory Application to the Physics of Condensed Matter* (Springer, Berlin, 2008).

[133] S. Haastrup, M. Strange, M. Pandey, T. Deilmann, P. S. Schmidt, N. F. Hinsche, M. N. Gjerding, D. Torelli, P. M. Larsen, A. C. Riis-Jensen, J. Gath, K. W. Jacobsen, J. J. Mortensen, T. Olsen, K. S. Thygesen, 2D Materials **5**, 042002 (2018).

[134] P. O. Lowdin, J. Chem. Phys. **19**, 1396–1401 (1951).

[135] E.O.Kane, J. Phys. Chem. Solids **6**, 236 (1958).

[136] E. O. Kane, *Semiconductors and Semimetals*, vol. 1, ed. R. K. Willardson, and A. C. Beer (Academic, New York, NY, 1966). See also, E. O. Kane, *Handbook on Semiconductors*, vol. 1, ed. W. Paul (North-Holland, Amsterdam,1982) p. 193.

[137] L. R. Ram-Mohan and K.-H. Yoo, J. Phys.: Condens. Matter **18**, R901–R917 (2006).

[138] M. Gell-Mann, and M. Levy, Nuovo Cimento **16** 53 (1960).

[139] R. L. Liboff, *Kinetic Theory: Classical, Quantum, and Relativistic Descriptions* (Springer, Berlin, 2003).

[140] J. Bardeen and W. Shockley, Phys. Rev. **80**, 72–80 (1950).

[141] K. Kaasbjerg, K. S. Thygesen, and K. W. Jacobsen, Phys. Rev. B **85**, 115317 (2012).

[142] Z. Jin, X. Li, J. T. Mullen, and K. W. Kim, Phys. Rev. B **90**, 045422 (2014).

[143] X. Li, J. T. Mullen, Z. Jin, K. M. Borysenko, M. B. Nardelli, and K. W. Kim, Phys. Rev. B **87**, 115418 (2013).

[144] B. Radisavljevic, A. Radenovic, J. Brivio, V. Giacometti, and A. Kis, Nat. Nanotechnol. **6**, 147 (2011).

[145] A. Ovchinnikov, A. Allain, Y.-S. Huang, D. Dumcenco, and A. Kis , ACS Nano **8**, 8174 (2014).

[146] B. Radisavljevic and A. Kis, Nat. Mater. **12**, 815 (2013).

[147] D. M.-Gustin, S. E. Ulloa, and V. L.-Richard, Phys. Rev. B **98**, 125301 (2018)

[148] H. Zeng, J. Dai, W. Yao, D. Xiao, and X. Cui, Nature Nanotech. **7**, 490–493 (2012).

[149] Y. Ye, J. Xiao, H. Wang, Z. Ye, H. Zhu, M. Zhao, Y. Wang, J. Zhao, X. Yin and X. Zhang, Nature Nanotech. **11**, 598–602 (2016).

[150] A. Kormányos, V. Zólyomi, N. D. Drummond, and G. Burkard, Phys. Rev. X **4**, 011034 (2014).

[151] G.-B. Liu, H. Pang, Y. Yao, and W. Yao, New J. Phys. **16**, 105011 (2014).

[152] Y. Wu, Q. Tong, G.-B. Liu, H. Yu, and W. Yao, Phys. Rev. B **93**, 045313 (2016).

[153] J. Pawlowski, D. Zebrowski, and S. Bednarek, Phys. Rev. B **97**, 155412 (2018).

[154] R. Pisoni, Z. Lei, P. Back, M. Eich, H. Overweg, Y. Lee, K. Watanabe, T. Taniguchi, T. Ihn, and K. Ensslin, Appl. Phys. Lett. **112**, 123101 (2018).

[155] O. A-Ovando, D. Mastrogiuseppe, and S. E. Ulloa Phys. Rev. B **99**, 035107 (2019).

[156] C. Huang, S. Wu, A. M. Sanchez, J. J. P. Peters, R. Beanland, J. S. Ross, P. Rivera, W. Yao, D. H. Cobden, and X. Xu, Nat. Mater. **13**, 1096 (2014).

[157] Y. Gong, J. Lin, X. Wang, G. Shi, S. Lei, Z. Lin, X. Zou, G. Ye, R. Vajtai, B. I. Yakobson, H. Terrones, M. Terrones, B. K. Tay, J. Lou, S. T. Pantelides, Z. Liu, W. Zhou, and P. M. Ajayan, Nat. Mater. **13**, 1135 (2014).

[158] X. Duan, C. Wang, J. C. Shaw, R. Cheng, Y. Chen, H. Li, X. Wu, Y. Tang, Q. Zhang, A. Pan, J. Jiang, R. Yu, Y. Huang, and X. Duan, Nat. Nanotechnol. **9**, 1024 (2014).

[159] X.-Q. Zhang, C.-H. Lin, Y.-W. Tseng, K.-H. Huang, and Y.-H. Lee, Nano Lett. **15**, 410 (2015).

[160] M.-Y. Li, Y. Shi, C.-C. Cheng, L.-S. Lu, Y.-C. Lin, H.-L. Tang, M.-L. Tsai, C.-W. Chu, K.-H. Wei, J.-H. He, W.-H. Chang, K. Suenaga, and L.-J. Li, Science **349**, 524 (2015).

[161] C. Zhang, Y. Chen, J.-K. Huang, X. Wu, L.-J. Li, W. Yao, J. Tersoff, and C.-K. Shih, Nat. Commun. **7**, 10349 (2016).

[162] C. Zhang, M.-Y. Li, J. Tersoff, Y. Han, Y. Su, L.-J. Li, D. A. Muller, and C.-K. Shih, Nat. Nanotechnol. **13**, 152 (2018).

[163] P. K. Sahoo, S. Memaran, Y. Xin, L. Balicas, and H. R. Gutiérrez, Nature **553**, 63 (2018).

[164] S. Xie, L. Tu, Y. Han, L. Huang, K. Kang, K. U. Lao, P. Poddar, C. Park, D. A. Muller, R. A. DiStasio, and J. Park, Science **359**, 1131 (2018).

[165] J. Wang, Z. Li, H. Chen, G. Deng, X. Niu, Nano-Micro Lett. **11**, 48 (2019).

[166] A. Kormányos, G. Burkard, M. Gmitra, J. Fabian, V. Zólyomi, N. D. Drummond, and V. I. Fal'ko, 2D Mater. **2**, 022001 (2015). See also, A. Kormányos, V. Zólyomi, N. D. Drummond, G. Burkard, and V. I. Fal'ko, Phys. Rev. B **88** 045416 (2013).

[167] B. A. Foreman, Phys. Rev. B **56**, R12748 (1997).

[168] Sathwik Bharadwaj, Ashwin Ramasubramaniam and L. R. Ram-Mohan (Submitted for publication).

[169] K. Kaasbjerg , T. Low, and A.-P. Jauho, Phys. Rev. B **100**, 115409 (2019).

[170] I. R. Lapidus, Am. J. Phys. **54**, 459–461 (1986).

[171] S. McAlinden and J. Shertzer, Am. J. Phys. **84**, 764–769 (2016).

[172] M. S. Dresselhaus, G. Chen, M. Y. Tang, R. G. Yang, H. Lee, D. Z. Wang, Z. F. Ren, J. P. Fleurial, P. Gogna, *New Directions for Low-Dimensional Thermoelectric Materials*, Adv. Mater. **19**, 1043–1053 (2007).

[173] G. Chen, M. S. Dresselhaus, G. Dresselhaus, J. P. Fleurial, and T. Caillat, *Recent developments in thermoelectric materials*, International Materials Reviews **48**, 45–66 (2003).

[174] C. J. Vineis, A. Shakouri, A. Majumdar, and M. G. Kanatzidis, *Nanostructured Thermoelectrics: Big Efficiency Gains from Small Features*, Adv. Mater. **22**, 3970–3980 (2010).

[175] R. Franz and G. Wiedemann, *Über die Wärme-Leitungsfähigkeit der Metalle*, Annalen der Physik **165**, 497–531 (1853).

[176] D. M. Rowe, *Thermoelectrics Handbook: Macro to Nano*, (CRC Press, Boca Raton, Florida, 2005).

[177] L. D. Hicks and M. S. Dresselhaus, *Thermoelectric figure of merit of a one-dimensional conductor*, Phys. Rev. B **47**, 16631–16634 (1993).

[178] L. D. Hicks and M. S. Dresselhaus, *Effect of quantum-well structures on the thermoelectric figure of merit*, Phys. Rev. B **47**, 12727-12731 (1993).

[179] L. D. Hicks, T. C. Harman, X. Sun and M. S. Dresselhaus, *Experimental study of the effect of quantum-well structures on the thermoelectric figure of merit*, Phys. Rev. B **53**, R10493–R10496 (1996).

[180] N. T. Hung, E. H. Hasdeo, A. R. T. Nugraha, M. S. Dresselhaus and R. Saito, *Quantum Effects in the Thermoelectric Power Factor of Low-Dimensional Semiconductors*, Phys. Rev. Lett. **117**, 036602 (2016).

[181] A. Majumdar, *Thermoelectricity in Semiconductor Nanostructures*, Science **303**, 777–778 (2004) .

[182] Y. Pei, H. Wang and G.J. Snyder, *Band Engineering of Thermoelectric Materials*, Adv. Mater. **24**, 6125–6135 (2012).

[183] T. Koga, X. Sun, S. B. Cronin, and M. S. Dresselhaus, *Carrier pocket engineering to design superior thermoelectric materials using GaAs/AlAs superlattices*, Appl. Phys. Lett. **73**, 2950–2952 (1998).

[184] J.-H. Bahk, Z. Bian, and A. Shakouri, *Electron energy filtering by a nonplanar potential to enhance the thermoelectric power factor in bulk materials*, Phys. Rev. B **87**, 075204 (2013).

[185] Y.-M. Lin, O. Rabin, S. B. Cronin, J. Y. Ying, and M. S. Dresselhaus, *Semimetal–semiconductor transition in $Bi_{(1-x)}Sb_x$ alloy nanowires and their thermoelectric properties*, Appl. Phys. Lett. **81**, 2403–2405 (2002).

[186] M. Zebarjadi, *An Overview of 2D Materials for Thermoelectric Applications*, Celebrating Millie (2018). Available from: https://millie.pubpub.org/pub/b0fn884z

[187] F. Bonaccorso, L. Colombo, G. Yu, M. Stoller, V. Tozzini, A. C. Ferrari, R. S. Ruoff, and V. Pellegrini, *Graphene, related two-dimensional crystals, and hybrid systems for energy conversion and storage*, Science **347**, 1246501 (2015).

[188] J. Duan, X. Wang, X. Lai, G. Li, K. Watanabe, T. Taniguchi, M. Zebarjadi, and E. Y. Andrei, *High thermoelectric power factor in graphene/hBN devices*, Proc. Natl Acad. Sci. **113**, 14272–14276 (2016).

[189] S. Chen, A.L. Moore, W. Cai, J.W. Suk, J. An, C. Mishra, C. Amos, C.W. Magnuson, J. Kang, L. Shi, and R.S. Ruoff, *Raman Measurements of Thermal Transport in Suspended Monolayer Graphene of Variable Sizes in Vacuum and Gaseous Environments*, ACS Nano **5**, 321 (2010).

[190] S. Chen, Q. Wu, C. Mishra, J. Kang, H. Zhang, K. Cho, W. Cai, A.A. Balandin, R.S. Ruoff, *Thermal conductivity of isotopically modified graphene*, Nat Mater **11**, 203 (2012).

[191] Y. Cai, J. Lan, G. Zhang, and Y.-W. Zhang, *Lattice vibrational modes and phonon thermal conductivity of monolayer MoS_2*, Phys. Rev. B **89**, 035438 (2014).

[192] G. Ozbal , R. T. Senger, C. Sevik, and H. Sevincli, *Ballistic thermoelectric properties of monolayer semiconducting transition metal dichalcogenides and oxides*, Phys. Rev. B **100**, 085415 (2019).

[193] W. Huang, H. Da, and G. Liang, *Thermoelectric performance of MX_2 (M: Mo,W; X: S,Se) monolayers*, J. Appl. Phys. **113**, 104304 (2013).

[194] W. Huang, X. Luo, C. K. Gan, S. Y. Quek, and G. Liang, *Theoretical study of thermoelectric properties of few-layer MoS_2 and WSe_2*, Phys. Chem. Chem. Phys. **16**, 10866 (2014).

[195] D. Wickramaratne, F. Zahid, and R. K. Lake, *Electronic and thermoelectric properties of few-layer transition metal dichalcogenides*, J. Chem. Phys. **140**, 124710 (2014).

[196] H. Babaei, J. M. Khodadadi, and S. Sinha, *Large theoretical thermoelectric power factor of suspended single-layer MoS_2*, Appl. Phys. Lett. **105**, 193901 (2014).

[197] B. Ouyang, S. Chen, Y. Jing, T. Wei, S. Xiong, and D. Donadio, *Enhanced thermoelectric performance of two dimensional MS_2 (M = Mo, W) through phase engineering*, J. Materiomics **4**, 329–337 (2018).

[198] K. Hippalgaonkar, Y. Wang, Y. Ye, D. Y. Qiu, H. Zhu, Y. Wang, J. Moore, S. G. Louie, and X. Zhang, *High thermoelectric power factor in two-dimensional crystals of MoS_2*, Phys. Rev. B **95**, 115407 (2017).

[199] M. Kayyalha, J. Maassen, M. Lundstrom, L. Shi, and Y. P. Chen, *Gate-tunable and thickness-dependent electronic and thermoelectric transport in few-layer MoS_2*, J. Appl. Phys. **120**, 134305 (2016).

[200] Y. Zhang, and G. D. Stucky, *Heterostructured Approaches to Efficient Thermoelectric Materials*, Chem. Mater. **26**, 837–848 (2014).

[201] R. Venkatasubramanian, E. Siivola, T. Colpitts, and B. O'Quinn, *Thin-film thermoelectric devices with high room-temperature figures of merit*, Nature **413**, 597 (2001).

[202] C. Satterwaithe and R. Ure JR., *Electrical and Thermal Properties of Bi_2Te_3* Phys. Rev. **108**, 1164–1170 (1957).

[203] T. Caillat, M. Carle, P. Pierrat, H. Scherrer, and S. Scherrer, *Thermoelectric properties of $(Bi_xSb_{1-x})_2Te_3$ single crystal solid solutions grown by the T.H.M. method*, J. Phys. Chem. Solids **53**, 1121 (1992).

[204] J.-H. Lee, G. A. Galli, and J. C. Grossman, *Nanoporous Si as an Efficient Thermoelectric Material*, Nano Lett. **8**, 3750 (2008).

[205] G. Kresse, J. Furthmüller, *Efficiency of Ab-Initio Total Energy Calculations for Metals and Semiconductors Using a Plane-Wave Basis Set*, Comput. Mater. Sci. **6**, 15–50 (1996)

[206] G. Kresse, J. Furthmüller, *Efficient Iterative Schemes for Ab Initio Total-Energy Calculations Using a Plane-Wave Basis Set* Phys. Rev. B **54**, 11169–11186 (1996)

[207] P. E. Blöchl, *Projector Augmented-Wave Method* Phys. Rev. B **50**, 17953–17979 (1994)

[208] G. Kresse, D. Joubert, *From Ultrasoft Pseudopotentials to the Projector Augmented-Wave Method* Phys. Rev. B **59**, 1758–1775 (1999)

[209] D. M. Ceperley and B. J. Alder, *Ground State of the Electron Gas by a Stochastic Method*, Phys. Rev. Lett. **45**, 566 (1980).

[210] J. P. Perdew and A. Zunger, *Self-interaction correction to density-functional approximations for many-electron systems*, Phys. Rev. B **23**, 5048 (1981).

[211] B. Schönfeld, J. J. Huang, and S. C. Moss, *Anisotropic mean-square displacements (MSD) in single-crystals of 2H- and 3R-MoS_2* Acta Cryst. **B39**, 404–407 (1983).

[212] P. B. James and M. T. Lavik, *The crystal structure of $MoSe_2$*, Acta Cryst. **16**, 1183 (1963).

[213] W. J. Schutte, J. L. De Boer, F. Jellinek, *Crystal structures of tungsten disulfide and diselenide*, J. Solid State Chem. **70**, 207–209 (1987).

[214] Sathwik Bharadwaj, Ashwin Ramasubramaniam, and L. R. Ram-Mohan, *Scalable first-principles informed quantum transport theory in two-dimensional materials* (Submitted for publication).

[215] H. R. Schwarz, *Finite Element Methods* (Academic Press Inc., San Diego, 1988). p. 134–137.

[216] K. Bell, A refined triangular plate bending finite element, International Journal for Numerical Methods Engineering **1** (1969) 101-–122.

[217] J. H. Argyris, I. Fried, D. W. Scharpf, *The TUBA family of plate elements for the matrix displacement method*, Aeronautical Journal of Royal Aeronautical Society **72** (1968)701-–709.

[218] H. Goldstein, C. Poole, J. Safko, *Classical Mechanics*, 3rd. Ed. (Addison-Wesley, New York, 2002).

[219] M. E. Rose, *Elementary theory of angular momentum* (Dover Publications, New York, 1995).

[220] M. Tinkham, *Group Theory and Quantum Mechanics* (Dover Publications Inc., New York, 2003).

[221] M. Lax, *Symmetry Principles in Solid State and Molecular Physics* (J. Wiley and Sons, New York, 1974).

[222] Alfred Gray, *Modern Differential Geometry of Curves and Surfaces* (CRC Press, Inc., 2000).

[223] R. McWeeny, *Symmetry, an Introduction to Group Theory and its Applications* (Pergamon Press, Oxford, 1963).

[224] A. Bossavit, *Boundary value problems with symmetry and their approximation by finite elements,* SIAM Journal of Applied Mathematics **53**, 1352-–1380 (1993).

[225] R. Courant and D. Hilbert, *Methods of Mathematical Physics*, Vol. 1 (Interscience, New York, 1953).

[226] G. Dhatt, G. Touzot, G. Cantin, *The Finite Element Method Displayed* (John Wiley & Sons, New York, 1984); p. 99.

[227] C. R. Boucher, Z. Li, C. I. Ahheng, J. D. Albrecht, and L. R. Ram-Mohan, Journal of Applied Physics **119**, 143106 (2016).

[228] C. R Boucher, Z. Li, J. D. Albrecht, L. R. Ram-Mohan, Journal of Applied Physics **115**, 1-10 (2014).

[229] S. Pandey, Sathwik Bharadwaj, M. Santia, M. Hodek, J. D. Albrecht, and L. R. Ram-Mohan, Journal of Applied Physics **124**, 213106 (2018).

[230] S. Pandey, Sathwik Bharadwaj, and L. R. Ram-mohan, *Method and Apparatus for Modelling Electromagnetic Fields Using Hermite Finite Elements*, United States Patent Application 20190392099. http://www.freepatentsonline.com/y2019/0392099.html

[231] Sathwik Bharadwaj, Siddhant Pandey, and L. R. Ram-Mohan, Phys. Rev. B **96**, 195305 (2017).

⋆ Parts of this thesis have appeared in the following publications:

Sathwik Bharadwaj and L. R. Ram-Mohan, *Electron scattering in quantum waveguides with sources and absorbers. I. Theoretical Formalism*, Journal of Applied Physics **125**, 164306 (2019).

Sathwik Bharadwaj and L. R. Ram-Mohan, *Electron scattering in quantum waveguides with sources and absorbers. II. Applications*, Journal of Applied Physics **125**, 164307 (2019).

INDEX

LIST OF PUBLICATIONS

1. Sathwik Bharadwaj, Siddhant Pandey, and L. R. Ram-Mohan, *Removal of accidental degeneracy in semiconductor quantum dots*, Physical Review B **96**, 195305 (2017).

2. Sathwik Bharadwaj, A. lyashenko, A. Gianfrancesco, and L. R. Ram-Mohan, *Quantum scattering theory and stealth finite element analysis*, Transractions of JASCOME **17**, 107–112 (2017).

3. Siddhant Pandey, Sathwik Bharadwaj, M. Santia, M. Hodek, J. D. Albrecht, and L. R. Ram-Mohan, *Cavity electrodynamics with Hermite interpolation: Role of symmetry and degeneracies*, Journal of Applied Physics **124**, 213106 (2018).

4. Sathwik Bharadwaj, and L. R. Ram-Mohan, *Electron scattering in quantum waveguides with sources and absorbers. I. Theoretical formalism*, Journal of Applied Physics **125**, 164306 (2019).

5. Sathwik Bharadwaj, and L. R. Ram-Mohan, *Electron scattering in quantum waveguides with sources and absorbers. II. Applications*, Journal of Applied Physics **125**, 164307 (2019).

6. Dung N. Pham, Sathwik Bharadwaj, and L. R. Ram-Mohan, *Tuning spatial entanglement in interacting two-electron quantum dots*, Physical Review B **101**, 045306 (2020).

7. Leo Rodriguez, Shanshan Rodriguez, Sathwik Bharadwaj, L. R. Ram-Mohan, *Exploration of the duality between generalized geometry and extraordinary magnetoresistance*, Physical Review B **101**, 174417 (2020).

8. Sathwik Bharadwaj, Ashwin Ramasubramaniam, and L. R. Ram-Mohan, *Scalable first-principles informed quantum transport theory in two-dimensional materials* (Submitted, 2020).

9. Sathwik Bharadwaj, Ashwin Ramasubramaniam, and L. R. Ram-Mohan, *Ultra-high thermoelectric performance in lateral transition metal dichalcogenide heterostructures* (Submitted, 2020).

10. Dung N. Pham, Sathwik Bharadwaj, and L. R. Ram-Mohan, *Spatial entanglement in two-dimensional artificial atoms* (Submitted, 2020).

11. Dung N. Pham, Sathwik Bharadwaj, Zehao Li, and L. R. Ram-Mohan, *Accurate calculations of very high electromagnetic fields in regions withre-entrant peripheries* (Submitted, 2020).